ISSN
2712-8172

Magazine of Civil Engineering

123(7), 2023

Magazine of Civil Engineering

ISSN 2712-8172

Online peer-reviewed open-access scientific journal in the field of Civil and Construction Engineering

Founder and Publisher: Peter the Great St. Petersburg Polytechnic University

This journal is registered by the Federal Service for Supervision of Communications, Information Technology, and Mass Media (ROSKOMNADZOR) in 2020. Certificate El No. FS77-77906 issued February 19, 2020.

Periodicity: 8 issues per year

Publication in the journal is open and free for all authors and readers.

Indexing: Scopus, Web of Sceince (ESCI, RSCI), DOAJ, Compendex, Google Academia, Index Copernicus, ProQuest, Ulrich's Serials Analysis System, CNKI

Corresponding address: 29 Polytechnicheskaya st., Saint Petersburg, 195251, Russia

Chief science editor: associate member of RAS, D.S. in Engineering, Vitaly V. Sergeev

Deputy chief science editors:
D.S. in Engineering, Galina L. Kozinetc

D.S. in Engineering, Sergey V. Korniyenko

Executive editor: Ekaterina A. Linnik

Translator, editor: Darya Yu. Alekseeva

DT publishing specialist:
Anastasiya A. Kononova

Contacts:
E-mail: mce@spbstu.ru
Web: http://www.engstroy.spbstu.ru

Date of issue: 13.11.2023

Contents

Magazine of Civil Engineering

ISSN 2712-8172

journal homepage: http://engstroy.spbstu.ru/

Research article

UDC 681.7:624.012

DOI: 10.34910/MCE.123.1

Fiber optics based system of monitoring load-bearing building structures

A.D. Mekhtiyev[1], ***M.Yu. Narkevich***[2], ***Y.G. Neshina***[3], ***A.K. Kozhas***[4], ***R.Zh. Aimagambetova***[5], ***B.B. Aubakirova***[6], ***Y.Zh. Sarsikeyev***[1]

[1] *Kazakh Agrotechnical University named after S. Seifullin, Astana, Republic of Kazakhstan*

[2] *Nosov Magnitogorsk State Technical University, Magnitogorsk, Russian Federation*

[3] *Karaganda Technical University, Karaganda, Republic of Kazakhstan*

[4] *L.N. Gumilyov Eurasian National University, Astana, Republic of Kazakhstan*

[5] *Kazakhstan Institute of Standardization and Metrology, Astana, Republic of Kazakhstan*

[6] *North Kazakhstan University named after Manash Kozybayev, Petropavlovsk, Republic of Kazakhstan*

✉ *Narkevich_MU@mail.ru*

Keywords: building and construction, mechanical safety, information systems, signal processing, management and systems engineering, stress-strain state, monolithic reinforced concrete structures, buildings and structures, defect, crack, structural failure, optical

Abstract. Inspection of the technical condition of load-bearing structural elements of buildings and structures in the process of their construction and operation is an important issue at the present time. A fiber-optic monitoring system is proposed as a solution to the problem of early diagnostics of defects and damage to load-bearing building structures. We developed a scheme for testing fiber-optic sensors, which make it possible to control the stress-strain state of monolithic reinforced concrete structures. For testing, a series of monolithic concrete beams of rectangular cross section were reinforced with fiber optics during their manufacturing. The values of mechanical stresses and deformations arising in beams under loading were determined. Using the tested samples as an example, it was established that the proposed fiber-optic monitoring system (FOMS) makes it possible to control stresses and deformations (and to predict the appearance and growth of cracks) in various building structures. The main element of the system is a hardware-software complex capable of estimating the parameters of a light wave at the output of the optical fiber. The distance from the installation site of the data processing unit to the measurement point can cover the area of 30 km. At this, fiber-optic sensors operate without additional power supply from a laser with the power of up to 30 mW. The proposed monitoring system has a low cost of one measurement point, it is easy to install, which is a good alternative to the electronic beacon-recorder device and the development of optical digital technologies in construction.

Citation: Mekhtiyev, A.D., Narkevich, M.Yu., Neshina, Y.G., Kozhas, A.K., Aimagambetova, R.Zh., Aubakirova, B.B., Sarsikeyev, Y.Zh. Fiber optics based system of monitoring load-bearing building structures. Magazine of Civil Engineering. 2023. 123(7). Article no. 12301. DOI: 10.34910/MCE.123.1

1. Introduction

At present, as the number of buildings and houses are increasing it is important to provide their sustainability. Possible solution to this task is the development of the integrity monitoring system. The improvement of the semiconductor and digital technologies made the building of the monitoring system easier and more effective. The relevance lies in the fact that there is well-known problem of sudden collapse of structures after their long-term operation. The solution requires developing methods and tools for diagnosing the state of building structures. In addition, with the consideration of the Industry 4.0 objectives the proposed technologies must be digital and energy efficient. This is a rather serious challenge for scientists and developers who create new diagnostic and monitoring tools in construction.

The operation of the buildings depends on many factors. From the practice it is known that every integrity deviation in the monolithic reinforced concrete elements and structures can lead to the potential destruction of the whole building. Visual inspections, as well as with the use of nondestructive testing means, showed the presence of hidden slowly developing or already formed and growing cracks in the body of the building structure. The technical inspection can establish the parameters of the defects and identify the causes of their occurrence. Cracks have certain geometric dimensions and are also characterized by the speed of development, which is quite important when assessing the danger to the integrity of the structure of a building or structure.

Therefore, it is much more efficient not to control already formed cracks but to take preventive measures for determining the state of stress and deformation changes in structures and identifying emergency zones where cracks arise from stress concentration.

The simplest method of crack opening control is installing gypsum, cement, glass beacons on the cleared surface on both sides of the crack that is currently used but is obsolete and does not meet present day requirements.

The unique properties of optical fiber allow its use, as a distributed sensor, and the optical fiber (OF) must be built into the monolithic reinforced concrete structure at the stage of its manufacture. The OF application provides a number of advantages [1]. In contrast to the copper wire OF is energetically passive, because it does not transmit electrical signals. An important point is that OF should contain a protective sheath of plastic to protect the glass filament from moisture, which may be contained in the reinforced concrete building structure, such as foundations. The selected object of research is optical fiber of G.652 standard, which is quite common in telecommunications systems and mass-produced by various countries, which provides a fairly low cost per linear meter. The OF also has sufficiently high reliability and durability, it is not susceptible to electromagnetic interference. The main hypothesis is the research of the G.652.D standard optical fiber application as a tool for the early diagnostics of the building structural elements destruction, because of the propagating inside its core light wave parameters dependance from mechanical impact. The obtained data can be further fixed using a hardware-software complex and converted into numerical values of the crack growth.

As shown by the analysis of the literature and the results of various years of research, the problem of cracking in monolithic reinforced concrete structures remains unsolved and creates many problems in the operation of buildings and structures [1–9]. The source of cracks is quite a serious danger, since it can be hidden from visual control, and the process and speed of crack growth can be quite rapid. It may also be noted that in the world there are enough examples of destruction of buildings and structures with cracks, sometimes, unfortunately, with tragic consequences. So far there are no effective tools to ensure monitoring of the cracks in monolithic reinforced concrete structures in real time for a long time without interruption. This will allow revealing the centers of crack formation at early stages, to identify their location and to take measures for their elimination. The analysis of the literature also showed that in some cases the cause of failure of monolithic reinforced concrete structures are errors made by designers. In the source [1] the collapse of buildings at the stage of construction connected with the violation of the technology of concrete production, weak reinforcement or incorrectly chosen distance between the columns are considered. There are examples when fully constructed buildings collapsed with terrible consequences and loss of life. The author does not give an example that a monitoring system was used, capable of detecting the danger of collapse at an early stage.

The analysis of the literature and the results of research in different years demonstrates that the problem of cracking in monolithic reinforced concrete structures remains unresolved and creates many problems in the operation of buildings and structures [1–9]. The source of cracks is a serious danger, because it can be hidden from visual inspection, and the process and the rate of crack growth can be fast. It may also be noted that in the world there are enough examples of destruction of buildings and structures by cracks, sometimes, unfortunately, with tragic consequences. In addition, currently, there are no effective means for continuous real-time monitoring of the technical condition of monolithic reinforced concrete structures without interruption in long periods. This will allow to reveal the centers of cracking at early stages, to determine their location and to take measures on their elimination. The analysis of the literature has also shown that in some cases the cause of failure of monolithic reinforced concrete structures is errors made by designers. Source [1] considers the problems associated with the collapse of buildings at the construction stage due to violation of the technology of concrete production, weak reinforcement or improperly chosen spacing between the columns. There are examples where fully constructed buildings have collapsed with terrible consequences and loss of life due to saving construction materials and their poor quality, as well as the lack of technical supervision and control over the constructed buildings. In Turkey, where residential buildings with reinforced concrete frame are mainly located in seismically active areas, design errors in building structural systems including low reinforcement and low column height, high beam reinforcement, non-seismic connections of steel parts and poor concrete quality have resulted in thousands of deaths and huge economic losses in earthquakes (1999 and 2011) [2].

On the other hand, in the Gaza Strip (Israel) many construction projects are being built in a short time, especially after the Gaza war in 2014 [3]. The analysis of this source revealed that the leading factors of the building destruction are primarily the human factor that can be described as violations of construction technology or the use of low-quality materials. The violation of the technology can be distinguished to preparation of the foundations and deviations from the vertical axis of the building; insufficient reinforced concrete structures; absence of technical supervision and the use of expired materials, using rusty or reused reinforcing steel or materials that are not suitable for the application. In the work [4], authors analyzed the sources of the bridge damages. The most valuable ones are wrong calculations of the wind load and errors in the technology of construction or repair work. Paper [5] describes the problem of defects, failures and accidents in the construction of buildings in the Czech Republic. Particular attention is paid to defects and malfunctions that have resulted in death or serious injury (to people or animals), safety hazards or serious property damage. There are considered failures of load-bearing structures, i.e. such states of structures that do not meet their functional requirements during their operation.

The analysis of defects and damages to public buildings in Botswana [6] showed that structural defects in building structures accounted for 73 % of total repair costs. To prevent building structures defects and damages, authors recommend implementation of quality assurance programs throughout the life cycle of building objects, especially at the design and construction stages. In work [7], studies were carried out to identify factors contributing to the occurrence of structural defects in load-bearing structures that occur during construction in Malaysia, especially in the Penang region, to minimize the time and cost. In article [8], the authors consider the hidden defects of the building, the causes of their occurrence and ways to prevent them. As the possible main factors, the human factor during the design stage as well as load created by people, environmental conditions, water concentration and leaks in the premises and violation of the governmental rules and standards are considered.

The analysis of defects and damages in the building structures made of monolithic reinforced concrete in the Republic of Kazakhstan appeared due to several reasons. First of them is practical absence of the domestic regulatory framework for the design and construction of high-rise and unique buildings including those with multifunctional purposes. Second is the little experience in the design and construction of high-rise buildings. Third is the violation of the technologies of concrete, formwork, construction and installation works, including those under extreme conditions; low quality of building materials, structures and products; deviation from the project [9]. Roof collapses of such underground structures as tunnels, mine roads, power plants and oil storage facilities can result in catastrophic injury, loss of life and significant financial loss. Major accidents have occurred in such civilian infrastructures as the collapse of the West Virginia rail tunnel in 2009, the collapse of the tunnel in Hangzhou, China in 2008, and the collapse of the subway tunnel in Cologne, Germany in 2009 [10].

To assess the strength and continuity of concrete and reinforced concrete structures, various non-destructive testing devices are used. The existing methods of continuous diagnostics of the strength of reinforced concrete structures have a certain complexity and require a certain amount of expensive preparatory work [11–13]. For instrumental inspection of buildings and non-destructive testing. One of them can be called a fairly well-known method of instrumental examination using non-destructive flaw detector IPS-MG4, this device allows to set the strength parameters of reinforced concrete and masonry structures, and also has a number of functions to control the homogeneity of concrete. There are several analogues with identical functions and almost similar technical characteristics used for the express quality control of concrete and mortar with the shock-pulse method (GOST 22690).

The relevance consists in developing and searching for new methods of the early diagnostics of deviations from standard working parameters of the building structures based on fiber-optic technologies and methods of computer processing the images of color spots using a hardware-software complex. This will allow real-time informing of the building structure technical condition and taking timely measures to prevent emergencies. The possible solution to the problem can be the early diagnostics of defects and damages of building structures with the application of a fiber-optic monitoring system (FOSM).

In the age of digital technologies, various electronic monitoring systems have been developed, which, among other things, allow detecting integrity faults of buildings and structures for the growth of cracks in monolithic concrete and reinforced concrete structures. This problem is quite serious and occurs in various cases, especially when construction technology is violated. Accordingly, the development of effective tools for early diagnostics of distributed and significant objects is very relevant.

The goal of this article is to research the conditions of the building to further develop the a real-time monitoring system based on the fiber-optic sensor for monolithic reinforced concrete structures. This will detect the centers of crack formation and establish their dislocation place in the foundation structure.

The task is to develop a monitoring system of the distributed or quasi-distributed type that in comparison does not use electricity in sensitive elements, with the lowest possible cost of one point-by-point measurement instrument. The cost is important for the subsequent implementation of the monitoring system in the construction industry. At this, a single-mode fiber is used as a guiding system for transmitting the measurement data and a sensor simultaneously over a greater distance with the lowest energy consumption compared to the existing systems of monitoring the building structure technical condition.

To monitor the technical condition of buildings and structures, tensometric, acoustic piezoelectric transducers, molecular-electronic, fiber-optic strain gauges [14] are successfully used. Among them the most widespread are electrical sensors: strain gauges in the form of thin rectangular foil strips with labyrinth wiring diagrams. The disadvantages of strain gauges are limited length (up to 800 m), a large number of cables, and the cost.

Fiber optic strain sensors (FOSS) have been developed based on the improving the technical characteristics of optical gauges. The principle of this system operation is refraction of a light beam in an optical fiber that has a sharp bend.

One solution of the problem is early diagnosis of defects and damages of building structures is a fiber-optic monitoring system (FOMS). The idea is to use G.652.D standard single-mode optical fiber as a distributed sensor, as it has several advantages in comparison with twisted-pair copper and its cost is several times lower. The task is to develop a monitoring system of a distributed or quasi-distributed type without applying electric signals, with the lowest possible cost for point-by-point measurement instrument. The cost of implementing a monitoring system in the construction industry is a crucial consideration. Specifically, the use of a single-mode fiber as both a guiding measurement data transmission system and a sensor is being explored in this case.

Optical fiber (OF) allows to transmit signals with high efficiency over long distances with a low attenuation coefficient at minimal energy consumption. OF has also sufficiently high reliability and durability, it is not susceptible to electromagnetic interference.

A scientific analysis of the works of foreign authors who work with optical fiber and develop fiber-optic sensors has been carried out. Similar problems exist in the mines of China, Russia and India, where rock displacement and pressure must be controlled. At the moment, a lot of research is related to the developing monitoring systems to control the geotechnical condition of mine workings, where optical fiber is used as a sensor. The condition of the coal mines can be inspected by different values, for example the temperature of the coal seams or pressure of mine water in the rocks. The system proposed by researchers from China for coal mine has been successfully tested and proved to work in coal mine conditions. In their development, Bragg gratings are used [15]. The application of FOS with Bragg gratings is not always economically justified, primarily due to the cost of the elements, such as an optical spectroanalyzer.

There is an example of a fiber-optic monitoring system capable of measuring the pressure on the coal face. The article [16] presents a detailed description of this system and the results of its testing. In the source [17] a distributed fiber-optic sensor and data processing unit are considered. The sensor is designed to monitor the stress-strain state of rocks of coal mine workings, capable of automatically monitoring the geotechnical condition of underground workings. The rock pressure can reach the value of 400–500 MPa. There is no need to use this sensor because the racks are already equipped with rock pressure monitoring system and this sensor performs a duplicate function. However, there is no information about its performance. In [18] information about the use of Bragg gratings for the creation of distributed fiber-optic sensors capable of measuring the deformation of the rock massif is presented. It may be noted that there is no example of their use in the coal industry because of the complexity and high cost. There are two interesting publications [19] and [20], which are devoted to the use of Bragg gratings to create a distributed FOS (DFOS). These articles contain only theoretical information without the results of practical research and testing in mine conditions, but the basis of any scientific work must be a well-planned and set experiment. In this case, the experiment was not conducted, and the system was not tested in practice. The very idea of using optical fiber as a sensor for monitoring the geotechnical condition of coal mine rocks is very relevant, as it allows to achieve a high level of safety. The light wave propagating along the core cannot become a source of fire or explosion of the mine atmosphere. In [21] the information on tests of already ready-to-use fiber-optic sensors based on Bragg gratings, which allow to measure deformations of the rock mass, is presented. The authors claim to have conducted tests in coal mines and received positive results. Tests were conducted in a coal mine in China.

There is a similar article [22], which also mentions that there were successful tests of DFOS based on Bragg gratings. This sensor allows monitoring the geotechnical condition of mine workings of coal mines of one of the Chinese mining companies, but there is no information about its practical application yet. Despite the high cost of sensors based on Bragg grids, some researchers continue to work, although other directions have already appeared. For example, research is already underway into the use of long-period optical gratings, which would be unambiguously more advantageous to use due to the absence of devices for analyzing the optical spectrum in the measurement chain. There are papers that consider only Bragg gratings [23], and the proposed developments are only at the stage of laboratory samples, which are not subject to commercialization due to the problems discussed above. Therefore, it is necessary to look for a way to simplify the fiber-optic sensor and reduce its cost. An optical interferometer could be a feasible solution as it is relatively inexpensive for both the sensor and data processing unit, yet offers high measurement accuracy. However, this method faces several significant issues that prevent its utilization in monitoring the structural integrity of monolithic reinforced concrete foundations in buildings. Since the measurement process is greatly and adversely affected by the temperature changes of the optical fiber [24]. The influence of temperature is also characteristic of sensors based on Bragg gratings and it is quite a serious problem of occurrence of noise in the measuring channel and output of false measured values [25]. There is also a mention of attempts to solve these problems arising during the application of the FOS with Bragg gratings. In the mentioned work to measure the mechanical parameters with the various strain gauges. On the other hand, the system cannot be used for long time and the main information carriers are electrical signals. In the work [27] authors suggest using fiber optic sensors instead of them, while some problems of using optical fiber are considered. According to the known literature, the foundation of the system for developing the computational device of the monitoring system can be formed for any application [28]. In the source [29] some issues on the use of Bragg gratings and problems in their use are considered. An article [30] proposes a simplified design of a pressure sensor. There are several articles that contain the results of research related to the control of displacement of rocks in a mine, using fiber-optic sensors [31], refers to the OF application to inspect the pads of the quarry [32].

The industry produces an electric string load cell "Autograph-1.2", which is installed already in the place of the formed crack. The length of the wire from the sensor to the data processing unit is not more than 800 meters, which sometimes limits the scope of its application, also the sensor itself has a rather high cost for a single point of measurement.

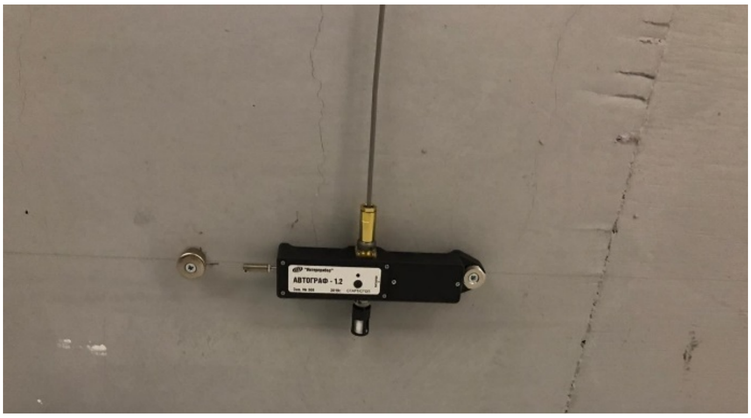

Figure 1. Electronic beacon-recorder “Autograph-1.2” mounted in the beam crack.

Many articles, papers are discovering the problem of the technical condition monitoring for the monolithic reinforced concrete building structures. Timely detection of cracks and crack growth monitoring are important [33]. A publication devoted to the description of methods for assessing the destruction of reinforced concrete was found [34].

There is a problem of effective control of monolithic structures including foundations in which cracks form (Fig. 2). In many cases, extended objects are not available for inspection. The growth of cracks in the foundation is the reason of the building walls destruction that in future threats with the collapse. The experience of using OF to control rock displacement demonstrated the possibility of the determination of the stress-strain state change in the structure at the early stages of the stress concentrators formation and initiation of cracks. OF can be built into the body of the foundation and stay in it during the entire service life. In contrast to the copper pair of a string sensor, in which the length of the guide system is limited to 800 meters, OF can transmit measurement data over the distance of more than 50 km, while energy consumption is only a few milliwatts. The FOMS can use existing fiber-optic telecommunication networks to transmit data within the city or over longer distances. The design of the FOS is simpler, and it will have a lower cost compared to a string sensor.

Figure 2. Cracks in the foundation.

If to install the FOSs in the body of the foundation during its mounting or to fix them on its surface, then there can be timely detected the centers of destruction. The problem of diagnosing the state of concrete structures is relevant and is considered by various researchers. It is especially important to detect the problem at the early stages of crack development. There are works [35] and [36], connected with the development of methods of monitoring the technical condition of reinforced concrete electrical signals and magnetic fields. As a result of the review, it can be said that at the present moment the greatest interest and relevance is acquired not by electrical, but by optical measurement systems. There are the results of similar studies of fiber-optic sensors, which are buried in the ground and used in security systems [37]. The main advantage of the proposed system in comparison to the existing ones is integration of the G.652.D standard single-mode optical fiber with the hardware and software complex [38]. Another differentiating factor lies in the methods employed for processing signals from the FOS. Additionally, preliminary testing of fiber-optic sensors embedded in reinforced concrete beams has been carried out [39]. The fundamental of the process of the fiber-optic sensors have also been discussed and presented in an earlier source [40].

2. Methods

Given the need to develop highly efficient means of remote monitoring load-bearing reinforced concrete structures including columns, floor slabs and coatings, walls, flights of stairs and foundations, the aim of the experimental studies were solving the problems discussed above [12, 33–36]. The basis of The proposed monitoring system that inspects the condition of the monolithic reinforced concrete structures including floors with pre-stressed beams is the fiber-optic technology based on monitoring changes in the parameters of a light wave passing through an optical fiber under mechanical action. Fiber-optic sensors that are based on the optical fiber standard G.652.D allows to simultaneously solve two important problems: reduce the cost and ensure the length of the measurement channel within 30 km. The advantages of fiber-optic sensors have already been discussed previously and outlined [37–40]. The diameter of the glass filament is 125 µm, which is covered by a protective layer of acrylic and plastic. The final diameter is about 1 mm.

The experiment was carefully planned, first of all the fiber optic sensor test scheme was prepared. A data processing unit was specially designed, to which the sensors were connected. The idea was to simulate the real situation when the optical fiber is inside a monolithic reinforced concrete structure to reproduce as accurately as possible the real conditions of foundation loading and load measurement. The optical fiber was placed inside the concrete beam, and it was secured to the reinforcement with plastic clamps. The optical fiber was impacted mechanically as the beam was destroyed with the all parameters of the of the propagating light wave were recorded using a hardware-software complex. The method proposed below makes it possible to control the stress-strain state of a concrete structure and, in this case, of a concrete beam. Before a crack forms, a zone of mechanical stress concentration is formed, which can be fixed by means of a fiber-optic sensor and also establish the place of the crack formation, which is very important, since the foundation may be hidden under the soil layer and inaccessible for visual inspection. This method implies that the optical fiber will be installed inside the foundation structure at the stage of its erection, and the fiber ends should have optical connectors to connect the measuring device. In [40, 41] there is already information on how measurements are made and how the fiber takes the load. The hardware-software complex (HSC) receives information from fiber-optic sensors, then processes it and outputs a numerical value of load changes on the beam, as well as changes in its stress-strain state. The mechanical action on the OF changes the parameters of the light wave passing through the OF and falling on the sensitive multi-pixel photodetector. The HSC processes the data according to the algorithm developed and converts the changes in the parameters of the light wave into changes in the pattern of pixels. The higher the load on the beam, the greater the transition of pixels from black to white state. Further the microprocessor outputs the numerical value of the measured value.

Fig. 3 shows a general view of reinforced concrete beams laboratory samples that simulate various monolithic reinforced concrete structures. The beams use G.652.D standard optical fiber that is identical in its characteristics and was attached to the reinforcement at the stage of its manufacturing. Its ends were released to the outside. The fabricated samples are made with transverse dimensions of 40x40 mm, the length of 160 mm, using cement of PC-400 D.0 grade, Volsky sand. Concrete beams were stored within 28 days in water according to the GOST. The hardening conditions are natural.

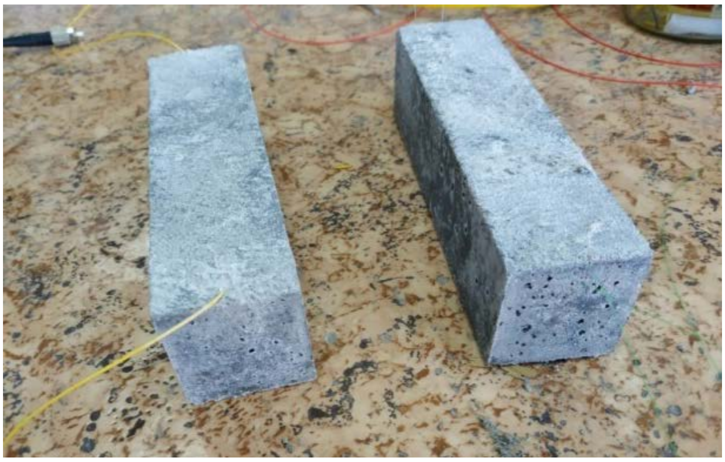

Figure 3. Laboratory samples.

The result of the research was the establishment of numerical values of mechanical stresses and strains that occurred in the body of the beam when the load increased. The beam was subjected to fracture and a crack was formed in it, this process was also recorded by the APC. The beam was divided into three equal parts and contained three sensors. The determination of the crack formation place was considered.

Accordingly, 6 optical fibers, three working and three reserve, were embedded in the reinforced concrete beam at the manufacturing stage. Optical connectors of the SC PhysicalContact type are installed at both ends of the fiber optic sensors, which facilitates switching with the guiding system for transmitting optical signals and control devices.

The proposed method implies that an optical OTDR (Optical Time Domain Reflectometer) is used to obtain a more accurate distance to the location of the formed crack in extended objects. The scheme of the experiment and measurement is shown in Fig. 4. The diagram shows that the beam was terminated into three zones, which are marked with Roman numerals I-III. The use of the reflectometer is economically justified only on long objects over a distance of 500 meters, in other cases the HSC is able at a distance of 200 meters to ensure an accuracy of crack detection within 3 meters. At a distance of 100 meters it is already 1.5 meters. The main disadvantage of the measurement scheme is the inability to determine the exact location of the crack without the use of a reflectometer (Fig. 4). HSC monitors various parameters, including additional losses of optical power, which according to a linear function increased proportionally to the increase of the mechanical load. The fiber optic sensors were pre-calibrated using an automatic strain gauge with AID-4 strain gauges. The HSC performs all measurements in real time and saves the results in the computer memory. As a source of loading was used testing machine MII-100, which is used to conduct static bending tests (serial number 239, inv. number 2235, certificate of verification GVL-2-03-1800003). The bending strength parameter of the beam was measured in kgf/cm^2. Load rise rates of 5 kg/s were selected. Concrete beams of rectangular section of 40x40 mm and length of 160 mm participated in the tests. A VIAVI (JDSU) Smart Pocket OLP-38 optical wattmeter and a Smart Pocket OLS-34 light wave emitter were used as measuring instruments. Switching with fiber-optic sensors is made by means of optical connectors and optical connectors of CS type. Optical wavelength of 1310 and 1550 nm is used.

During the experiments the load applied to the center of the concrete beam was increasing smoothly until its destruction or a crack was formed in it. The appearance of the test bench is shown in Fig. 5. The generator of the coherent light is the semiconductor laser 1 (SmartPocket OLS-34/35/36) connected through the optical connector to optical fiber 2. The optical fiber is inside beam body 3, and its ends go out for connection to the measuring system. MII-100 is capable of developing pressure up to 100 kgf/cm^2, in the Figure it is marked by position 4. The direction of the force vector application is indicated by the F arrow. The pressure on the beam is carried out through device 5. The beam is located on two stationary supports 6, thereby forming two support points for fracture tests. The fracture of the beam occurs in its middle. One end of the optical fiber is connected with the optical connector to the SmartPocket OLP-38 optical power meter, indicated by position 7, which measures the level of additional losses that occur when exposed to the optical fiber. The mechanical impact on the center of the beam causes the development of mechanical stress and deformation, this impact is transmitted respectively to the optical fiber, in which the refractive index changes and the phase of the light wave propagates, which is recorded by photo-detector 4.

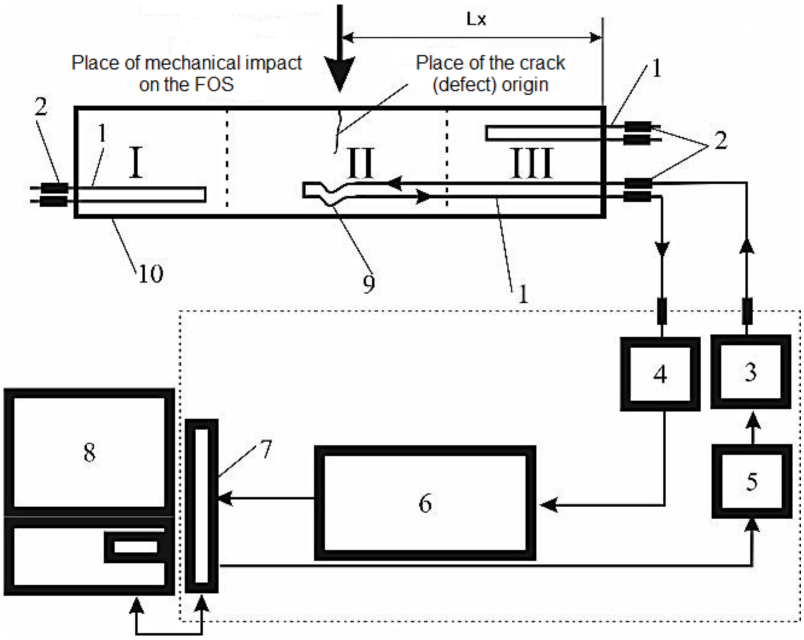

Figure 4. The structural scheme for the mechanical stresses values measurement and determination of the defect location: 1 – optical fiber, 2 – optical connectors of the SC brand, 3 – semiconductor laser with a system of controlling its pumping, 4 – photo-detector, 5 – device for controlling laser pumping, 6 – device for preliminary processing of the received data, 7 – device for matching, 8 – personal computer, 9 – place of microbending, 10 – beam.

Figure 5. Testing machine MII – 100 (two-support bend): 1 – radiation source; 2 – optical single-mode fiber in a protective sheath; 3 – beam; 4 – testing machine MII-100; 5 – area of pressure application; 6 – stationary support; 7 – optical power meter.

It was recorded that when the load on the concrete beam increased, the value of additional optical losses in the OF increased in proportion to the increase of the load, with a linear law predominating. Mechanical impact on the OF caused a change in the properties of the light wave passing through the OF, and changes in light intensity were also recorded.

Part of the optical power is lost when microbending occurs [41]. This makes it possible to detect the magnitude of mechanical effects on the beam with sufficiently high accuracy through changing the magnitude of additional losses. One important fact can be noted that the OF remained undamaged and continued to perform its functions, while in the place of the formed crack a slight deformation of the fiber is preserved, it will allow using a refractometer to accurately determine the location of the beam damage.

During the experiments, some conditions were set. The magnitude of loading should not exceed 16 kgf/cm^2, with a load of 0 to kgf/cm^2 at the beginning of the experiment. Two ranges of light wave 1310 and 1550 nm) were used. The temperature in the room where the experiments were conducted was fixed at 25 °C. The movement of the beam was excluded (OX = 0 m; OY = 0 m; OZ = 0 m). To process and approximate the data, the capabilities of Microsoft Excel were used. Each measurement during the experiment was carried out 30 times. The number of necessary repetitions of experiments to achieve a sufficient reliability equal to 0.95 was chosen according to the recommendations of the source [43]. The coefficient of variation was also determined. Also to process the results of the experiments was used Wolframalpha program, which is publicly available and is an interactive system for processing the results of various experiments, as well as helps in working with arrays of data.

The main limitation of the proposed system is the need to install sensors directly in the body of the foundation structure itself. In this regard, the use of this system for other building structures requires the use of another type of sensors. The SNO can be installed directly in the body of the foundation or attached to its side surfaces. When using the HSC in practice it should be understood that for each building structure it is necessary to configure the HSC separately and to calibrate it. The proposed monitoring system can be adapted to monitor the technical parameters of any monolithic reinforced concrete structures, such as walls, bridge abutments, slabs and hydraulic structures. At the moment this system represents a laboratory specimen, on which positive results are received, which allow to assume its practical introduction, but for this purpose comprehensive industrial tests are required which will be realized in the future. The main purpose of the research was not to determine the strength characteristics of concrete, but to investigate the response of the optical fiber to the deformation of concrete. The limitations of the test machine, as well as the purpose of the experiment, were taken into account in conducting the experiment.

3. Results and Discussion

The results of the experiments were processed and presented in the graphs of Fig. 6 and 7. These graphs represent only part of the data obtained. Different values were obtained in different wavelength ranges of 1310 and 1550 nm, but the principle of linearity of measurement was maintained in both occasions. The results were obtained by measuring the additional losses in the OF when it is deformed. It should be understood that the fiber is subjected to microbending and the well-known photoelastic effect occurs, which was recorded. The measurement scheme is presented earlier in Fig. 4. In the graphs of Fig. 6 and 7, which show how the additional optical power loss varied with the step-by-step increase in the load on the concrete beam during its bending tests. It is known that loading in the center of the beam causes changes in mechanical stresses and deformations, and the beam begins to deflect, concrete layers and reinforcing bars affect the fiber-optic sensor located inside the beam. The step-by-step increase in load leads to the failure of the beam and the formation of a crack. The instrumentation and the HSC recorded that at the moment of failure there is a small spike in additional losses and a short-term increase in losses. This moment remains in the memory of the HSC and if necessary, can be retrieved from it. The graph of Fig. 6 reflects the dependence of the additional losses at a wavelength of 1310 nm, the graph in Fig. 7 reflects the growth of additional losses at a wavelength of 1550 nm. At the same time, loading in both cases was performed in the same way and with the same step. The experiments with OF without a protective shell showed its greater sensitivity to a lower load, but at the same time there was a big problem of its damage, since the glass filament is quite fragile. Therefore, the use of protective sheathless fiber is not recommended because the sensor can be easily damaged. In all cases, the fiber with the protective sheath remained intact and without visible damage.

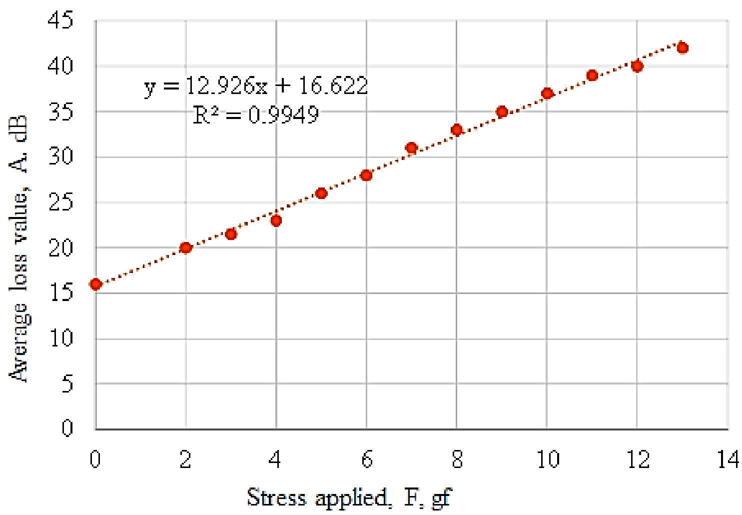

Figure 6. Optical fiber with the wavelength of 1310 nm loss value with a step-by-step increase of bending load.

For each experiment, the reliability and accuracy evaluation criteria were selected. Using the recommendations of the source [43], the necessary number of measurements was selected. The parameters at which the required reliability was achieved were selected. For example, for the graph in Fig. 6, the Student coefficient has a value of 2.098 with a confidence interval of 0.94. In addition, the calculation of the accuracy of the measurements was performed and the absolute error was determined to be 2.32 and the value of the relative error was 3.87 %.

As it was mentioned before, the difference of the graph presented in Fig. 7 consists in other values of additional losses, formed in OF from mechanical impact on it. Analyzing the dependence of the optical power loss presented in Fig. 7, which is called additional, because it is formed during microbending of the OF and differs from the straight section of the OF not affected by the mechanical impact. The experiment was performed using a wavelength of 1550 nm. The load was identical and increased in steps similar to the experiment with a wavelength of 1310 m. A pattern was found that as the wavelength increased, the losses decreased with the same mechanical load on the OF.

For example, for the graph in Fig. 7, the Student coefficient has a value of 2.091 with a confidence interval of 0.94. The measurement accuracy was also calculated and the absolute error was determined to be 3.01, as well as the relative error, which was 2.97 %.

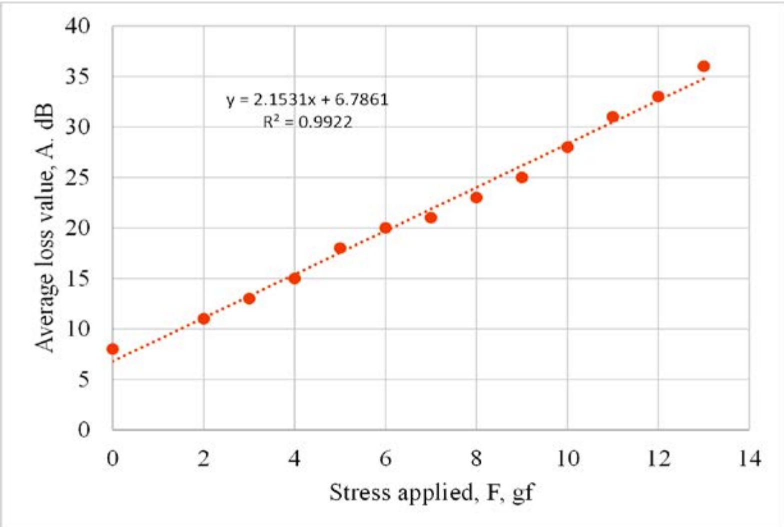

Figure 7. Optical fiber with the wavelength of 1550 nm loss value with a step-by-step increase of bending load.

The FOMS presented below is able to control the loading and growth of cracks in various building structures. The FOMS is able to work with monolithic reinforced concrete and steel building structures. So far, the laboratory sample is capable of registering a change in the loading of the structure only at four points. Fig. 8 shows the program window, which allows controlling four sensors simultaneously. The number of measuring channels and sensors is theoretically unlimited, but in practice there are limitations associated with the number of cores of the fiber optic cable. As stated above, an important element of the monitoring system is the HSC, which performs an assessment of the parameters of the light wave passing through the core, when a microbend occurs, the properties of the light wave change and, first of all, the phase of propagation of the intensity. When a microbend occurs, part of the light wave travels beyond the shell into the environment. The greater the microbending or mechanical impact on the OF, the more energy of the light wave escapes to the outside. A multi-pixel photodetector is installed at the end of the fiber, which captures all changes in the light spot and converts them into a numerical value of the measured quantity, such as mechanical load or pressure. As the graphs in Fig. 6 and 7 have shown, the higher the load, the greater the additional losses of optical power, which was recorded by the HSC program.

HSC monitors many parameters of the light spot falling on the surface of the sensitive photodetector. The program analyzes the shape of the light spot, its reduction with increasing load, the change in shape in each segment and the number of formed white pixels, which grew with proportional to the load on the beam. After processing all the data and making certain adjustments for external interference, numerical values are given. The HSC also has an alarm function, in case of changes in the parameters and their growth, the operator is given a signal indicating the zone of load change. The APC window shown in Fig. 8 contains a number of important functions, which can be used to perform its adjustment. Designed and used in experiments HSC contains four independent channels capable of working at a distance of up to 5 km. In the experiments only two channels were used to achieve a certain guarantee of reliability of the obtained results. Measured parameters are displayed in various forms. The instantaneous value of the measured quantity and the averaged value are displayed. There are also two information windows with the oscillogram of the measurement process and the representation of the measured value as a separate bar. The operator manually sets the measurement limits and starts the monitoring system in operation. The individual bursts are specifically recorded and shown. As can be seen on the screen, external vibrations from the machine are also recorded. Each channel reacts differently because of the different settings and sensitivity. The instrument readings, the swashplate is sufficiently successful in interference control that even with a deliberate impact on the beam there is no interference and the difference between the averages is negligible. The HSC is able to recognize interference and perform averaging of the measured values.

All the measurement parameters are stored in the computer memory. On the right there is an enlarged view of the measuring channel during operation, which shows the case of oscillations during the appearance of noise and subsequent impact on the sensor. It is seen that the noise generated by the laser presents a single peak, and the effect presents a more stable and time-consuming section of the diagram.

Figure 8. Program interface: 1 – threshold value, 2 – number of triggers, 3 – trigger time period, 4 – average amplitude value, 5 – instantaneous amplitude value, 6 – response time fixation window.

Separate bursts in the measurement data array appear due to the vibro-acoustic effect on the OF from the electromechanical part of the MII-100N testing machine. The program has a number of settings that allow dealing with incoming external interference, which can affect the accuracy of the measurement, as well as the results reliability.

The program window in the setup mode, where the image of the light spot is on the left, and the results of the analysis of changing the pixel pattern are on the right, is presented on the Fig. 9. The left part of the figure shows the light spot, which is formed on the surface of the Full HD photomatrix, which is the measurement body. The photodetector is a matrix, which is installed on the end of the optical fiber. On the surface of the photomatrix a light spot is formed, which can be referred to the well-known Poisson's spot. This spot of light has a fairly bright central part and a darker part closer to the edge of the spot. The middle is very bright and usually has, as observations have shown, about one-third of the entire area of the spot. The rest of the light spot profile looks darker. The transformation process is rather complicated and is performed by the program automatically, but some moments should be explained separately. The photodetector records all changes of the light spot. It also converts the image into a negative and then analyzes the number of white pixels formed on the background of the OF shell. The more the load on the beam and therefore directly on the sensor itself, the more changes in the light spot. The spot loses intensity and becomes less bright with increasing mechanical impact on the OM. In the negative image the white zone increases, unlike when there was no load, the spot was completely black. When the load increases, the transition of pixels from black to white is observed. As shown in Fig. 9, the left side shows a positive image of the spot, but the right side is its negative. With increasing load on the screen in the right part the white ring increases in size and at the break of the OV becomes the maximum occupying almost the entire window.

This is a rather serious problem that has to be dealt with. At the output, a stepped profile is formed that is described by the Gaussian distribution.

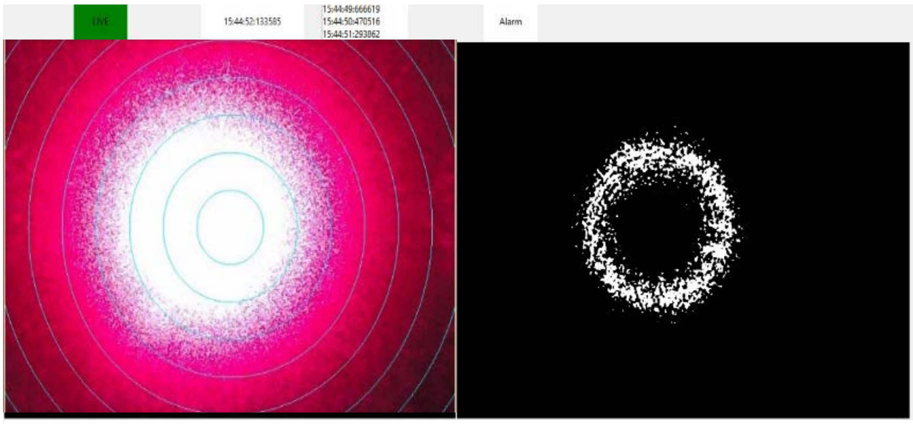

Figure 9. The program window in the setup mode.

From the output of the optical fiber the light spot falls on the high-resolution television matrix surface. The core glows more intensely, and the shell is less intense. The spot can slightly change its shape with changes in temperature and fluctuations in the light generator frequency. In order to negate all the noise from laser is the coherency and the possible error of 5 nm and the varying power from 10 to 30 mW. With increasing the load on the structure, the pressure on the OF increases proportionally. As the result the propagating light wave properties changes. The measurement of the values were performed by the television matrix, and the hardware-software complex converts them into numerical measured value. Fig. 10 shows changing pressure on the OF that is converted into changing the pixelized image of the light spot. In comparison with the previous Figure, there is observed increasing the number of white pixels and decreasing the number of black ones. Additionally, the graph of the white pixels number dependence from the pressure on the OF is presented on the Figure. The number of dark pixels unlike the white ones decreases with the pressure growth. If the load is removed from the optical fiber, then the white pixels amount will decrease as presented in Fig. 10.

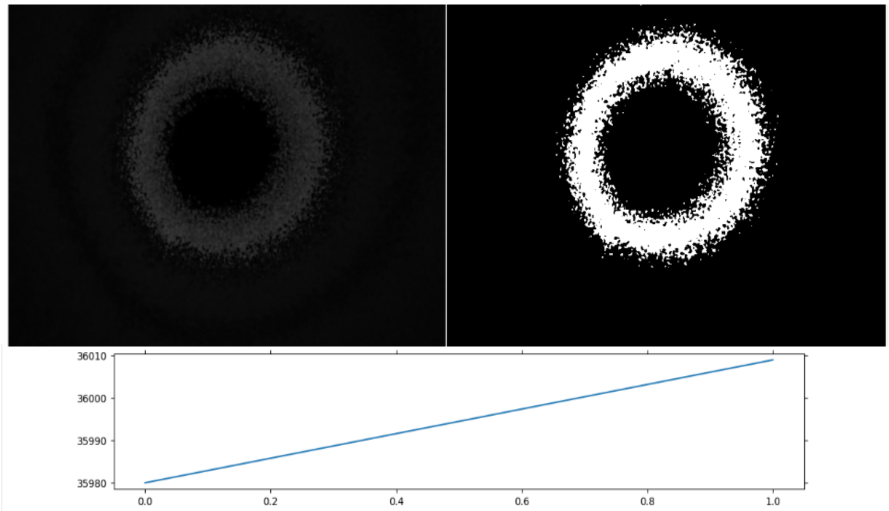

Figure 10. Changing the spot with increasing pressure on the OF.

When the laser is unstable, the operation of the entire FOMS is disrupted. For this occasion, the HSC has the function of learning and distinguishing time peaks, when the frequency of the radiation source light wave deviates. When mechanical impact is done on the optical fiber, the pixel pattern changes in the direction of increasing white color, and additional losses that can be converted into numerical values of the displacement or deformation parameters increase, respectively.

Fig. 11 shows a photo of a FOMS laboratory specimen in the setup mode. The presented specimen has four measuring channels but only two were used in the experiment to compare the results and to refine them. The Figure also shows that both channels produce the same parameters and diagrams. Preliminary adjustment of the program made the elimination of the reaction to changing the frequency of the radiation source possible.

During the increase of the pressure, a uniform increase in the deformation parameters of the beam is observed. Because of the occurrence of a photo-elastic effect caused by microbending additional losses in the OF increase. Theoretically, there is limitations of the number of channels by the number of strands of the fiber-optic communication cable. The approximate maximum number of measurement channels is 64.

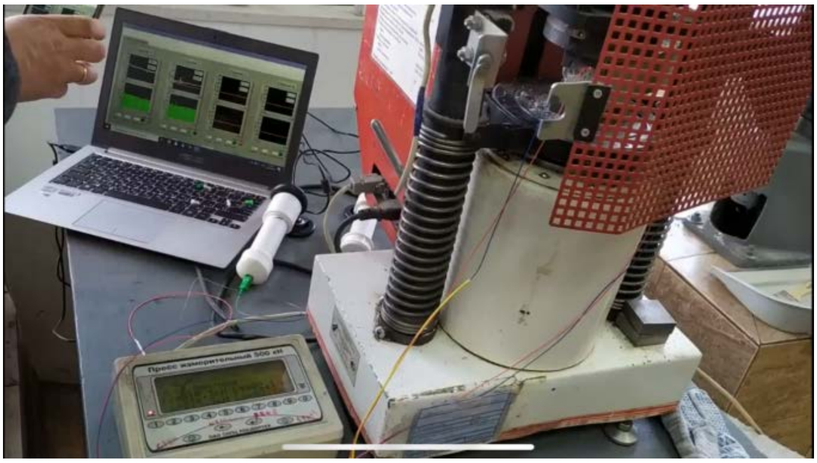

Figure 11. FOMS laboratory specimen.

The FOMS is used in testing concrete beams for compression and bending. When the beam is broken, the optical fiber in most cases remains undamaged and makes it possible to determine the parameters of further crack growth and its dislocation. Thus, it is possible to use this system for monitoring the technical condition of monolithic reinforced concrete structures. In contrast to the known methods of constructing FOS based on interferometers, reflectometers, and Bragg gratings, the proposed FOMS has a simpler design and a lower cost per measurement point. This system has lower energy consumption compared to electric string sensors. The radiation source is common for all the measuring channels, and the television matrix is installed separately for each channel. The hardware-software complex is installed on a personal computer.

Experiments have shown that the G.652.D standard single-mode optical fiber is capable of handling a measurement channel length of up to 30 km, in contrast to the G.651 standard multimode fiber, which was experimented with earlier. The 30 km long sensor can cover almost any need in the construction industry, as there are no such long foundations. Industry-proposed strain gauge monitored cracks can operate at distances up to 800 meters from the data processing unit, which is not always convenient in real construction conditions. The use of the previously considered strain gauge is limited, since it is installed over the already formed crack. Also, this sensor is much more expensive to produce. As for the OV standard G.651 is earlier in its production and is suitable for use at distances up to 1 km. Losses in this type of fiber are quite significant in contrast to the OF standard G.652, and it was excluded from further development as unpromising. The fiber optic sensor at a length of 30 km consumes power equal to 30 mV. Measured attenuation of OF standard G.652 does not exceed 0.22 dB per km. The use of fiber-optic sensors will make it possible to build a distributed or quasi-distributed system for monitoring the technical condition of monolithic building structures. To create a fully distributed monitoring system, an OTDR must be added to the existing HSC. The lower cost is provided using the OF, low energy consumption, a simpler sensor design.

Compared to the other methods of periodic control that are currently used and discussed earlier, the FOMS works in real time, therefore, it can control the process of crack formation at the early stages of their development, because fiber optic sensors are built into the design itself.

An important difference is also the development of an original hardware-software complex that uses intelligent processing of the data received from fiber-optic sensors, which reduces the likelihood of obtaining false data when the temperature changes or when some other external interference occurs. This work is based on the preliminary scientific groundwork and the results obtained in the development of the system for monitoring the technical condition of the reinforced concrete lining of mine workings and used out-of-the-box work is the modernization of the already considered HSC in [41]. In the process of research a number of upgrades and improvements were made, which improved the noise immunity of the measurement channels. The results of the research coincided with previous studies, which were carried out earlier and concerned the development of the monitoring system of the technical condition of the reinforced concrete lining of mine workings [42]. The proposed monitoring system is able to recognize at an early stage the process of load changes and the occurrence of stress concentration in the monolithic building structure. Accordingly, at an early stage to inform the user of the beginning of the process of formation and growth of cracks in the foundation. The use of fiber-optic sensors makes it possible to create a distributed and quasi-distributed monitoring system, which is unattainable when using string strain gauges, which are able to monitor parameters only in one point.

4. Conclusions

1. The above experimental studies allowed developing a test scheme and a laboratory prototype of the system for monitoring the technical condition of monolithic building structures made of reinforced concrete.

2. Concrete beams with embedded fiber-optic strands of G.652.D standard were used in the experiments. The values of mechanical stresses and deformations arising in the beam during its loading were determined and places of defect (crack) appearance were established.

3. The research was conducted to study in detail the processes of propagation of light waves with lengths of 1310 and 1550 nm through the core of an optical fiber at the moment of application of external mechanical load to a concrete beam into which an optical fiber of standard G.652 was embedded at the pouring stage. We also measured additional losses of optical power during step-by-step loading. The experiments showed that it is possible to measure, with sufficient accuracy and linearity, the magnitude of the load on the concrete beam, through the measurement of the additional optical power loss in the OV formed by microbending.

4. The developed HSC is the fundamental basis of the monitoring system, which is intelligent and capable of learning. The HSC can transform and convert the values of mechanical impact on the beam into the numerical value of mechanical stress–strain parameters with high accuracy. Future studies will be done to improve the HSC in the field of machine learning algorithms, to increase the level of its adaptation to various conditions of operation of monolithic reinforced concrete structures and to increase the level of noise immunity of measurement channels.

5. A limitation of using the proposed system is the need to install sensors directly inside the structure, so to assess the technical condition of other load-bearing monolithic reinforced concrete structures, which will require adaptation and small changes in the technical characteristics of the sensors.

6. In the process of the experiment, it was found that the use of single-mode fiber optics of G.652 standard makes it possible to significantly increase the distance from the sensor to the data processing unit within 30 km, which increases the capabilities of this method and determines its present relevance. Switching from 650 nm to 850 nm wavelength will increase the distance from the data processing unit to the FOS.

7. Presented FOMS is a new generation monitoring system, based on fiber-optic technology, where OF is both a means of data transmission and a sensitive element at the same time.

8. FOMS are relatively simple and cheap, as they do not use fiber-optic measuring systems based on interferometer, reflectometer and Bragg gratings.

References

1. Kioko, J.M. Causes of building failures in Africa: A case study on collapsing structures in Kenya. IOSR Journal of Mechanical and Civil Engineering. 2014. 11(3). Pp. 09–10. DOI: 10.9790/1684-11370910
2. Cogurcu, M.T. Construction and design defects in the residential buildings and observed earthquake damage types in Turkey. Natural Hazards and Earth System Sciences. 2015. 15. Pp. 931–945. DOI: 10.5194/nhess-15-931-2015
3. Allotey, S.E. An evaluation of the impact of defects in public residential buildings in Ghana. Civil and Environmental Research. 2014. 6(11). Pp. 58–64.
4. 4. Ovchinnikov, I.G., Ovchinnikov, I.I. Analysis of the causes of accidents and damage to transport structures. Transport Construction. M. 2010. 7. Pp. 2–5.
5. Kraus, M., Vondráčková T., Ņývlt, V. Defects, faults and accidents of contemporary constructions. MATEC Web of Conferences. 8th International Scientific Conference Building Defects (Building Defects 2016). 2017. 93. Aticle no. 03004. DOI: 10.1051/matecconf/20179303004
6. Ssegawa, J., Lugwisha, G. Defects as a quality problem in newly constructed public buildings in Botswana. Journal of Civil Engineering Research and Practice. 2006. 3(1). Pp. 31–40. DOI: 10.4314/jcerp.v3i1.29149
7. Ahzahar, N., Karim, N., Hassan, S., Eman, J. A study of contribution factors to building failures and defects in construction industry. Procedia Engineering. 2011. 20. Pp. 249–255. DOI: 10.1016/j.proeng.2011.11.162
8. Chong, W.K., Low, S.P. Latent Building Defects: Causes and Design Strategies to Prevent Them. Journal of Performance of Constructed Facilities. 2006. 20(3). Pp. 213–221. DOI: 10.1061/(ASCE)0887-3828(2006)20:3(213)
9. Kozhas, A.K., Baltabaeva, N., Kapbasova, A. Defects and damages during the construction of high-rise objects of monolithic reinforced concrete in Kazakhstan and the causes of their occurrence. Proceedings of the University. 2014. 1. Pp. 70–72.
10. Palei, S., Das, S. Sensitivity analysis of support safety factor for predicting the effects of contributing parameters on roof falls in underground coal mines. International Journal of Coal Geology. 2008. 75.Pp. 241–247. DOI: 10.1016/j.coal.2008.05.004
11. Ledenev, V.V., Odnolko, V.G. Analysis of the causes of accidents in buildings and ways to improve their reliability. Bulletin of Tambov State Technical University. 2012. 18(2). Pp. 449–457.
12. Berbekov, J.V. Nondestructive methods of concrete strength control. Young Scientist. 2012. 11. Pp. 20–23.
13. Mekhtiyev, A.D., Yurchenko, A.V., Neshina, Y.G., Alkina, A.D., Kozhas, A.K., Zholmagambetov, S.R. Nondestructive Testing for Defects and Damage to Structures in Reinforced Concrete Foundations Using Standard G.652 Optical Fibers Russian Journal of Nondestructive Testing. 2020. 56(7). Pp. 179–190. DOI: 10.1134/S1061830920020072

14. Zaprudnov, V.I., Seregin, N.G. Methods and means of monitoring the technical condition of building structures. Lesnoy vestnik. 2019. 23(5). Pp. 108–115. DOI: 10.18698/2542-1468-2019-5-108-115
15. Liu, X., Wang, C., Liu, T., Wei, Y., Lv, J. Fiber Grating Water pressure sensor and system for mine. ACTA Photonica Sinica. 2009. 38. Pp. 112–114.
16. Kumar, A., Kumar, D., Singh, U.K., Gupta, P.S., Shankar, G. Optimizing fibre optics for coal mine automation. – International Journal of Control and Automation. 2011. Vol. 3. Pp. 63–70.
17. Naruse, H., Uehara, H., Deguchi, T., Fujihashi, K., Onishi, M., Espinoza, R., Pinto, M. Application of a distributed fibre optic strain sensing system to monitoring changes in the state of an underground mine. Measurement Science and Technology. 2007. 18(10). Pp. 3202–3210. DOI: 10.1088/0957-0233/18/10/S23.
18. Chotchaev, Kh.O. Control of the stress-strain state of a rock massif by sound-metric and geophysical methods. Geology and Geophysics in the South of Russia. 2016. 3. Pp. 129–140.
19. Buymistruk, G.Ya. Principles of construction of intelligent fiber-optic sensors. Foton-Express. 2011. 6(43). Pp. 38–39.
20. Buymistruk, G. Fiber-optic sensors for extreme conditions. Control engineering. Russia. 2013. 3(45). Pp. 34–40.
21. Kim, S.T., Park, Y.H., Park, S.Y., Cho, K., Cho, J.R. A sensor-type PC strand with an embedded FBG sensor for monitoring prestress forces. Sensors (Switzerland). 2015. 15(1). Pp. 1060–1070. DOI: 10.3390/s150101060
22. Liu, T., Wei, Y., Song, G., Li, Y., Wang, J., Ning, Y., Lu, Y. Advances of optical fiber sensors for coal mine safety monitoring applications. Proceedings of the 2013 International Conference on Microwave and Photonics, 2013. Pp. 102–111.
23. Yiming, Z., Nong Z. and Guang-yao Si. A fiber bragg grating-based monitoring system for roof safety control in underground coal mining. Sensors (Switzerland). 2016. 16(10). Pp. 112–117. DOI: 10.3390/s16101759.
24. Volchikhin, V.I., Murashkina, T.I. Sensors and systems. Measurement, control, automation. 2001. 7. Pp. 54–58.
25. Liu, J., Chai, J., Wei, S., Li, Y., Zhu, L., Qiu, B. Theoretical and Experimental Study on Fiber Bragg Grating Sensing of Rock Strata Settlement Deformation. Journal of Coal Science & Engineering. 2008. 14(3). Pp. 394–398.
26. Kamenev, O.T., Kulchin, Y.N., Petrov, Y.S., Khizhnyak, R.V. Application of a fiber-optic Mach-Zender interferometer for creation of long-base deformometers. Letters in ZhTF. 2014. 40(3). Pp. 49–56.
27. Kulchin, Yu.N., Kamenev, O.T., Petrov, Yu.S., Kolchinsky, V.A. Fiber-optic interferometric receivers of weak seismic signals. Bulletin of the Far Eastern Branch of the Russian Academy of Sciences. 2016. 4. Pp. 56–59.
28. Nguyen, W., Duncan, J.F., Jen, G., Ostertag, C.P. Influence of matrix cracking and hybrid fiber reinforcement on the corrosion initiation and propagation behaviors of reinforced concrete. Corrosion Science. 2018. 140. Pp. 168–181. DOI: 10.1016/j.corsci.2018.06.004
29. Fan, L., Bao, Y., Meng, W., Chen, G. In-situ monitoring of corrosion-induced expansion and mass loss of steel bar in steel fiber reinforced concrete using a distributed fiber optic sensor. Composites Part B: Engineering. 2019. 165. Pp. 679–689.
30. Jonas, H. Osório, et al. Simplifying the Design of Microstructured Optical Fibre Pressure Sensors. Scientific Reports. 2017. 7. Article no. 2990. DOI: 10.1038/s41598-017-03206-w
31. Zhao, Z., Zhang, Y., Li, C., Wan, Z., Li, Y., Wang, K., Xu, J. Monitoring of coal mine roadway roof separation based on fiber Bragg grating displacement sensors. International Journal of Rock Mechanics and Mining Sciences. 2015. 74. Pp. 128–132. DOI: 10.1016/j.ijrmms.2015.01.002
32. Bin, T., Hua, C. Application of Distributed Optical Fiber Sensing Technology in Surrounding Rock Deformation Control of TBM-Excavated Coal Mine Roadway. Journal of Sensors. 2018. Article no. 8010746. DOI: 10.1155/2018/8010746
33. Fursa, T.V., Petrov, M.V., Dann, D.D. Developing a Nondestructive Method for Revealing Defective Areas in Reinforced Concrete Under Bending Conditions. Russian Journal of Nondestructive Testing. 2019. 55(4). Pp. 293–298. DOI: 10.1134/S1061830919040065
34. Fursa, T.V., Petrov, M.V., Dann, D.D. A method for evaluating failure in reinforced concrete under bending based on the response of electrical parameters to an impact action. Russian Journal of Nondestructive Testing. 2018. 54(7). Pp. 519–527. DOI: 10.1134/S1061830918070033
35. Guo, F., Yu, Z., Liu, P., Shan, Z. Practical issues related to application of electromechanical impedance-based method in concrete structural health monitoring. Research in Nondestructive Evaluation. 2015. 27(1). Article no. 150610064754006. DOI: 10.1080/09349847.2015.1044587
36. Morareskul, N.N. Arrangement of foundations in peat soils (peculiarities of technology). Geotechnics: Science and Practice: Collection of Scientific Works. Ministry of Education of the Russian Federation. Saint-Petersburg State Architectural and Construction University. Saint-Petersburg, 2000. Pp. 47–51.
37. Polyakov, A.V. Quasi-distributed recirculation fiber-optic temperature sensor. Optical Memory and Neural Networks. 2009. 18(4). Pp. 271–277.
38. Yurchenko, A.V., Mekhtiyev, A.D., Neshina, Y.G., Alkina, A.D., Madi, P.Sh. Physical Principles of Developing Pressure Sensors Using Refractive Index Changes in Optical Fiber Microbending. Russian Physics Journal. 2020. 63. Pp. 323–331. DOI: 10.1007/s11182-020-02038-y
39. Mekhtiyev, A.D., Yurchenko, A.V., Alkina, A.D. Nondestructive Testing for Defects and Damage to Structures in Reinforced Concrete Foundations Using Standard G.652 Optical Fibers. Russian Journal of Nondestructive Testing. 2020. 56(7). Pp. 179–190. DOI: 10.1134/S1061830920020072
40. Mekhtiyev, A., Bulatbayev, F., Neshina, Y., Siemens, E., Alkina, A., Shaigarayeva, T. The external mechanical effects on the value of additional losses in the telecommunications fiber optic cables under operating conditions. Proceedings of the 6th International Conference on Applied Innovation in IT, Koethen: Anhalt University of Applied Sciences. 2018. 1(6). Pp. 123–127.
41. Yurchenko, A.V., Mekhtiyev, A.D., Bulatbayev, F.N., Neshina, Y.G., Alkina, A.D. The Model of a Fiber-Optic Sensor for Monitoring Mechanical Stresses in Mine Working. Russian Journal of Nondestructive Testing. 2018. 54(7). Pp. 528–533. DOI: 10.1134/s1061830918070094
42. Yurchenko, A., Mekhtiyev, A., Alkina, A., Yugai, V. Passive Perimeter Security Systems Based On Optical Fibers Of G 652 Standard. Proceedings of International Conference on Applied Innovation in IT. 2019. 7(1). Pp. 31–36.
43. Yiming, Z.. Nong, Z., Guangyao, S. A fiber bragg grating-based monitoring system for roof safety control in underground coal mining. Sensors. 2016. 16(10). Pp. 112–117. DOI: 10.3390/s16101759

Information about authors:

Ali Mekhtiyev, *PhD in Technical Sciences*
ORCID: https://orcid.org/0000-0002-2633-3976
E-mail: barton.kz@mail.ru

Mikhail Narkevich, *PhD in Technical Sciences*
ORCID: https://orcid.org/0000-0001-6608-8293
E-mail: Narkevich_MU@mail.ru

Yelena Neshina, *PhD in Technical Sciences*
ORCID: https://orcid.org/0000-0002-8973-2958
E-mail: 1_neg@mail.ru

Aigul Kozhas, *PhD in Technical Sciences*
ORCID: https://orcid.org/0000-0002-5039-9529
E-mail: kozhas@bk.ru

Raushan Aimagambetova,
ORCID: https://orcid.org/0000-0002-4429-953X
E-mail: rauwan2012@mail.ru

Bakhytkul Aubakirova,
ORCID: https://orcid.org/0000-0002-7205-6455
E-mail: aubakirova_68@mail.ru

Yermek Sarsikeyev, *PhD*
ORCID: https://orcid.org/0000-0002-7209-5024
E-mail: sarsikeyev.ermek@yandex.ru

Received 14.02.2022. Approved after reviewing 15.02.2023. Accepted 15.09.2023.

Magazine of Civil Engineering. 2023. 123(7). Article No. 12302

Magazine of Civil Engineering

ISSN 2712-8172

journal homepage: http://engstroy.spbstu.ru/

Research article

UDC 691.3

DOI: 10.34910/MCE.123.2

Self-healing concrete utilizing low calcium fly ash, recycled aggregate, and macro synthetic fibers: autogenous behavior and properties

***M.M. Sabri*[1]**, ***F. Javed Muhammad*[2]**, ***M. Arslan*[2]**

[1] Peter the Great St. Petersburg Polytechnic University, St. Petersburg, Russian Federation

[2] Department of Civil Engineering, COMSATS University Islamabad, Islamabad, Pakistan

✉ *mohanad.m.sabri@gmail.com*

Keywords: self-healing concrete, hydrostructures, fly ash, macro synthetic fibers, recycled aggregates

Abstract. This study aims to develop a self-healing concrete solution that addresses the issues of high maintenance and repair costs, limited durability, and reduced service life of concrete structures. To achieve this, low calcium Fly Ash and partially replaced recycled aggregate were utilized, resulting in decreased concrete strength. To counteract this issue, macro synthetic fibers were introduced at 0.5 % and 1 %. The samples were then cracked and left to self-heal over a five-week period. The outcomes indicated that incorporating 60 % Fly Ash was the most effective method of healing cracks within the given timeframe. Moreover, the addition of 0.5 % macro synthetic fibers showed substantial enhancement in mechanical properties without compromising workability. This study highlights the potential of self-healing concrete as a sustainable and cost-effective solution to enhance the performance and durability of concrete structures.

Funding: This research was supported by a grant from the Russian Science Foundation No. 22-79-10021, https://rscf.ru/project/22-79-10021/

Citation: Sabri, M.M., Javed Muhammad, F., Arslan, M. Self-healing concrete utilizing low calcium fly ash, recycled aggregate, and macro synthetic fibers: autogenous behavior and properties. Magazine of Civil Engineering. 2023. Article no. 12302. DOI: 10.34910/MCE.123.2

1. Introduction

Concrete is a widely used construction material that can be designed to have a service life of several decades [1–4]. It is a crucial component in the construction of many infrastructures, and its annual global production in 2011 was estimated at 3.5 billion tons, which highlights the significant demand for cement [5]. Emerging markets are investing in new infrastructure to sustain their rapid economic development and growing populations, and it is projected that emerging Asian markets will require $776 billion in annual investments between 2010 and 2020 to meet the increasing infrastructure demand [6]. Due to its moldable nature, concrete is a versatile construction material that can be cast into any shape within a proper framework, and its physical attributes can be utilized in various structural applications. However, concrete's highly brittle behavior makes it vulnerable to cracking, which reduces its lifespan and sustainability. Extreme loading, earthquakes, and adverse environmental factors are the leading causes of cracks in concrete, weakening its strength, exposing it to harsh environmental agents, and decreasing its service life. These cracks result in higher maintenance and repair costs and reduced strength and service life of concrete structures [1–4].

The occurrence of cracking-related issues increases the maintenance and repair costs of civil infrastructure and reduces its service life, rendering concrete infrastructure unsustainable. Consequently, research and development have shifted towards developing new technologies that can enhance the material properties of concrete and construct new infrastructure that can withstand multiple hazards [7]. The development of concrete that can recover from any performance loss caused by cracking is highly desirable. The hydration of concrete has been shown in several research studies and practical experiences to repair its structural cracks on its own. This has led material scientists to explore the concept of "self-healing," which was inspired by biomimicry, such as the natural healing of broken bones or blood coagulation. However, applying this idea to industrial materials was challenging due to the complexities involved in the healing process. Nonetheless, this concept has proven to be a revolutionary approach to the maintenance and repair of concrete.

The self-healing capability of concrete was first identified by Abrams in 1925 [8]. In his study, concrete samples that had cracks after a compression test were repaired when left outdoors for eight days, and their compressive strength was twice as high as that in 28 days. Further research has revealed that freeze-thaw damage to concrete samples can also self-heal after curing. Ettringite crystals and calcium hydroxide crystals were found in the cracks, and parts of the resonant frequencies were restarted [9]. Subsequent studies on crack healing in concrete can be classified into two self-healing techniques: intrinsic healing and extrinsic healing. Intrinsic healing can occur through several mechanisms, including carbonation of $Ca(OH)_2$ to generate $CaCO_3$ precipitation, further hydration of un-hydrated cementitious particles, closing cracks caused by water impurities or loosened concrete particles, and matrix swelling (Calcium Silicate Hydration) products (C-S-H). The formation of calcium carbonate $CaCO_3$ precipitates has been identified as the main cause of autogenous self-healing [10]. The second self-healing approach is subdivided into vascular and capsule-based healing methods, which rely on incorporating adhesive reserves inside the matrix to detect deterioration with or without human involvement [11, 12]. However, technical flaws emerged when the chemical substances were not simultaneously present at the affected locations, leading to long-lasting voids inside the concrete and a decline in durability. Among all potential strategies, only intrinsic healing investigations have resulted in a considerable reduction in fracture width, less water permeability, and improved or recovered mechanical characteristics [13–16].

Autogenous self-healing is the ability of concrete to repair itself using its own matrix potential. This phenomenon is common in water-retaining structures, culverts, and pipelines and has been extensively studied since it was first identified by the French Academy of Science in 1836, particularly in relation to water-retaining structures. To promote autogenous self-healing in concrete, mineral admixtures such as Fly Ash and Blast Furnace Slag, expansive minerals, and crystalline admixtures can be used. High-activity mineral admixtures, such as Fly Ash and slag, can improve the mechanical properties of concrete by enhancing pore structure, compactness, and durability, and also reduce cement consumption and lower the temperature rise during hydration. This can have a positive impact on the environment by reducing carbon dioxide production from cement production [17, 18].

Recycling and processing concrete waste into new aggregates can enhance the geotechnical and chemical properties of concrete, and recycled aggregates can also improve soil characteristics [19]. In a recent study, Fly Ash was added as a mineral admixture at different volumes to induce autogenous self-healing in concrete, while recycled aggregates were used to partially replace natural aggregates and make the concrete more environmentally friendly and improve its mechanical properties. Furthermore, 0.5 % of macro synthetic fibers were added to the concrete matrix to further enhance its durability and mechanical properties [20].

To enhance the self-healing capability of cement-based materials, fibers are typically used in combination with clinker substitutes such as Fly Ash and silica fume, as well as with crystalline admixtures [21]. The ultimate aim of this research is to develop new techniques that can promote self-healing capabilities in concrete using Fly Ash as a cement autogenous self-healing addition. This method has the potential to revolutionize the concrete industry by creating more durable, sustainable, and long-lasting structures while significantly reducing repair and maintenance costs [20].

2. Materials and Methods

2.1. Materials

The focus of this study is on the utilization of Class F Fly Ash, a supplementary cementing material, in concrete to explore its self-healing capabilities when combined with recycled aggregate and macro fibers.

In this research, Ordinary Portland cement grade 53 was employed, with a claimed fineness of about 301 m^2/kg and a specific gravity of 3.15 g/cm^3. The chemical composition of the cement used in the investigation is presented in Table 1.

Table 1. Chemical composition of cement.

Chemical composition (% by weight)	
SiO_2	21.24
Al_2O_3	5.56
Fe_2O_3	3.24
CaO	63.53
MgO	0.93
Na_2O	0.13
K_2O	0.62
SO_3	2.55
Free lime	0.55
Insoluble residue	0.64
Loss on ignition	1.24

2.1.1. Concrete

Mix design is a critical step in concrete research, involving the determination of the appropriate proportions of cement, aggregates, water, and additives to achieve desired properties. The outcome of the mixed design process directly affects the performance of the concrete, including its strength, durability, and workability. Thus, a well-designed concrete mix is essential for the success of any substantial research project. For the preparation of M30 concrete, various quantities of cement aggregates and water content were evaluated.

In the present study, a cubic (6in*6in) concrete of 30 MPa strength was designed as a control group, as shown in Table 2.

Table 2. Mix design of control group.

Description	Cement, (kg)	Fine aggregate (kg)	Coarse aggregate (kg)	Water Content (kg)
Ratio	1	1.725	2.416	0.46
Per Cube (6in × 6in)	1.60	3.17	3.7	0.784
Per m^3	420.23	724.92	1015.11	193.3

2.1.2. Fly Ash

Fly Ash is a residual substance that is generated during the combustion of coal in industrial settings. It comprises fine particles carried away by the exhaust gases, with those that do not ascend being referred to as base ashes. The composition of Fly Ash is heterogeneous and typically consists of Silicon dioxide (SiO_2), Aluminum oxide (Al_2O_3), Ferric oxide (Fe_2O_3), Calcium oxide (CaO), and Magnesium oxide (MgO).

Fly Ash is a versatile material offering substantial performance benefits in concrete and non-concrete applications. When treated with sodium hydroxide in high-temperature pyrolysis, it can act as a catalyst for converting polyethylene into a substance similar to crude oil. Due to the hardening of Fly Ash particles during their suspension in exhaust gases, they tend to have a round shape and range in size from 0.5 to 300 micrometers.

In the construction industry, Fly Ash is classified as a supplementary cementitious material (SCM) and can replace binders in cement. The use of SCMs in concrete provides several environmental benefits, as waste materials are used to reduce the amount of cement required, which is a significant source of carbon emissions that contribute to global warming.

Figure 1. Fly Ash.

Moreover, modern research has shown that SCMs like Fly Ash can induce self-healing of cracks when exposed to moisture, making them increasingly sought after. When combined with lime in concrete, Fly Ash enhances its strength, with a typical usage rate of 15–35 % by weight of cement in structural concrete and up to 70 % in mass concrete for dam construction, roller-compacted concrete pavements, parking lots, and low-strength concrete applications. The chemical composition of Class F Fly Ash used in this research is detailed in Table 3.

Table 3. The chemical Composition of Class F Fly Ash.

Analysis	Result
	II
Loss on ignition (LOI) (%)	1.53
Chloride (as Cl) (%)	0.011
Sulphate (as SOs) (%)	0.51
Free CaO (%)	Nil
Reactive CaO (%)	4.06
Total CaO (%)	4.42
SiO_2 (%)	51.55
Al_2O_3 (%)	33.32
Fe_2O_3 (%)	3.34
SiO_2+ Al_2O_3+ Fe_2O_3 (%)	88.21
Na_2O (%)	0.51
MgO (%)	0.75
Phosphate (as P_2O_5) mg/kg	6.22

2.1.3. Macro Synthetic Fibres

Macro synthetic fibers, referred to as "structural" synthetic fibers, are composed of a blend of polymers and were originally developed to serve as a substitute for steel fibers in specific applications. These fibers are preferred over steel fibers due to their lightweight nature, resulting in less dense concrete when used in reinforced concrete. While initially investigated as a potential replacement for steel fibers in shotcrete, subsequent research and development has demonstrated their effectiveness in the design and construction of ground-supported slabs and various other applications. Macro synthetic fibers have multiple important uses and are characterized by their embossed structure and length of approximately 3 inches.

Figure 2. Macro Synthetic Fibers.

The physical properties of embossed macro synthetic fibers used for this project are explained in Table 4.

Table 4. Physical properties of MSF.

Characteristic	Property
Material	100% virgin polypropylene
Surface Texture	Continuously Embossed
Appearance	White
Water Absorbency	Nil
Tensile Strength	500-700Mpa
Elastic Modulus	>9000Mpa
Length	55mm
Density	0.91 g/cm^3
Melting Point	160–170°C
Resistance to Acid & Alkali	Excellent

2.1.4. Recycled Aggregate

Cement recycling is a straightforward process that involves breaking down, removing, and crushing existing cement to create a particular size and quality material. Recycled aggregate is produced by crushing concrete and, in some cases, asphalt, to recover the aggregate. This research collected large lumps of recycled concrete aggregate (RCA) from a demolished site in Mirpur Abbottabad. These large lumps were then crushed into smaller sizes of 4.75 mm – 19 mm using an aggregate crusher machine.

Figure 3. Recycled coarse aggregate.

2.2. Methods and Mixing design

The methodology for this study involved a three-stage process. In the first stage, control samples of mixed design were prepared and tested for strength to establish a baseline. In the second stage, various modifications were made to the concrete mix, including replacing 50 % of the coarse aggregate with recycled aggregate, replacing 60 % of the cement with Fly Ash, and adding macro synthetic fibers at volumes of 0.5 % and 1 % individually, with a specific focus on the effects of the 0.5 % volume addition of macro synthetic fibers. Finally, in the third stage, the results of the final concrete samples were analyzed, which included the replacement of cement with Fly Ash, replacing 50 % of the coarse aggregate with recycled aggregate, and adding macro synthetic fibers at a volume of 0.5 %.

3. Results and Discussion

3.1. Compressive Strength of Natural Concrete

The compressive strength of the reference concrete samples was obtained using a compression testing machine after 7, 14, and 28 days respectively. The compressive strength values post-testing are given in Table 5.

Table 5. Compressive strength of the reference concrete.

SAMPLE	7 DAYS (N/mm^2)	14 DAYS, (N/mm^2)	28 DAYS (N/mm^2)
NC 1	19.01	23.13	29.17
NC2	18.65	22.56	28.84
NC3	17.94	21.92	28.65

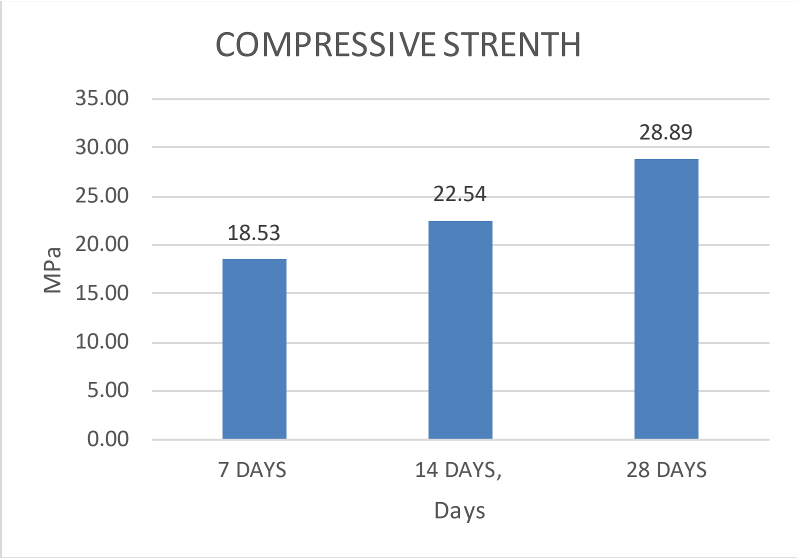

Figure 4. Average values of '7,14- and 28-days' compressive strength reference concrete.

3.2. Replacement of Coarse Aggregate with 50 % RCA

The coarse aggregate in the concrete mixture was partially substituted with recycled aggregate, representing 50 % of the total coarse aggregate used. The recycled aggregate was obtained by crushing large lumps of recycled concrete and producing 19 mm down recycled aggregate. The recycled aggregate was incorporated as a partial replacement for the natural aggregate in the concrete mixture. Compression tests were conducted on the concrete specimens using a testing machine after 28 days to determine their strength. The outcomes of the compression tests are presented in Table 6.

Table 6. Compressive strength of 50%RCA replaced concrete after 28 days.

SAMPLES	28 DAYS
RA1	20.83
RA2	20.68
RA3	23.49

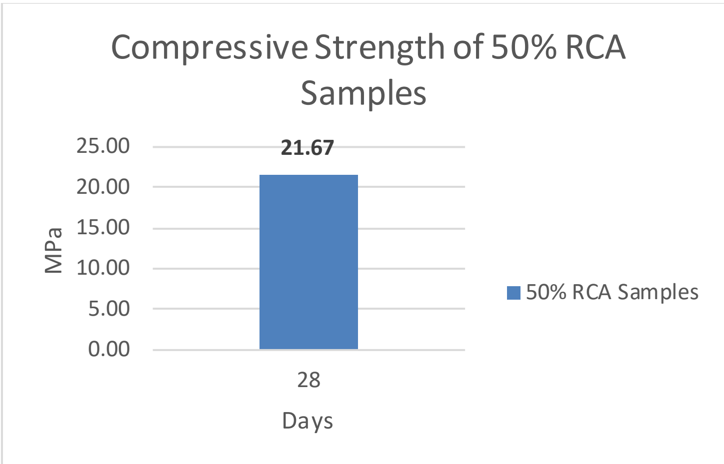

Figure 5. Average compressive strength of 50 % RCA samples at 28 days.

3.3. Addition of Macro Synthetic Fibers (0.5 % & 1 %)

As part of the research, we used macro synthetic fibers to increase the mechanical properties of concrete as we lost strength due to the usage of Fly Ash and recycled aggregate. The volume used macro synthetic fibers on two percentages, 0.5 %, and 1 %, respectively.

Compressive strength of 28 days was obtained using a compression testing machine, the values of which are presented in Table 7.

Table 7. Compressive strength of concrete with fibres at 1 % and 0.5 %.

SAMPLE	50%RA+ 0.5% FIBERS (N/mni²)	50% RA + 1 % FIBERS (N/mm²)
1	21.41	23.13
2	23.5	23.92
3	21.87	24.09

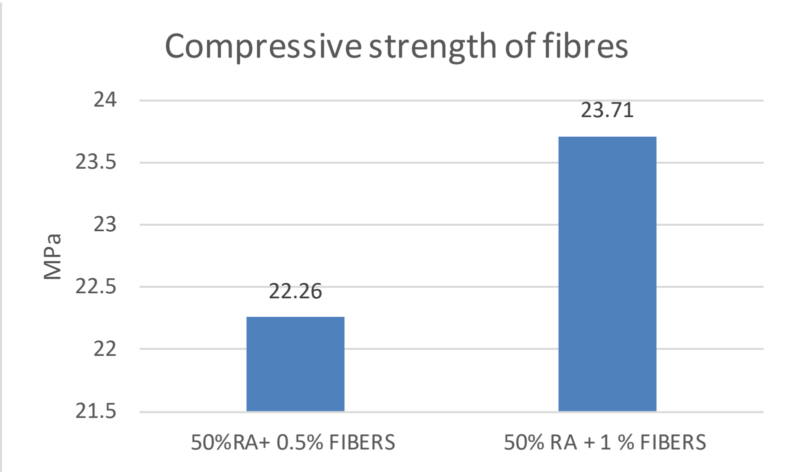

Figure 6. Compressive strength of fibres with concrete at 28 days.

3.4. Replacement of Fly Ash + RCA & addition of MSF in Concrete

Following the successful autogenous self-healing in Fly Ash based RCA concrete, the next objective was to enhance the mechanical properties of concrete by incorporating macro synthetic fibers, as a decrease in the strength was observed due to the use of Class F Fly Ash and 50 % replaced recycled aggregate. For this purpose, concrete samples were prepared by replacing 50 % of the coarse aggregate with recycled aggregate and utilizing Fly Ash at a proportion of 60 %. Macro synthetic fibers were then added to these samples at a volume percentage of 0.5 %. These samples were subsequently cured for 28 days and subjected to various loading conditions to induce cracking. The resulting crack widths under each loading condition are presented in Table 9.

Table 9. Different cracking loads for Fly Ash, RCA, and MSF concrete.

SAMPLE	FA %age + 50% RCA+0.5% Fibres	PEAK (KN)
1	60%	147.7
2	60%	164.0
3	60%	152.8

Following the induction of cracks in the concrete samples, they were subjected to autogenous self-healing by being submerged in water. The initial observation was made after three weeks, and the second and final observations were made after five weeks, so cracking widths and details are in Table 10.

Table 10. Cracking details with healing behavior of Fly Ash, RCA, and MSF concrete after 3 and 5 weeks, respectively.

Concrete samples	Crack width (mm)	Healing status (after three weeks)	Healing status (after five weeks)
SAMPLE (60% FLY ASH + 50% RA + 0.5% FIBERS)			
C11	0.6	Completely healed	
C12	0.63	Completely healed	
C2I	0.57	Completely healed	
C31	0.48	Completely healed	

3.5. The healing in the concrete of 60% Fly Ash + 50% RA + 0.5% Fibers

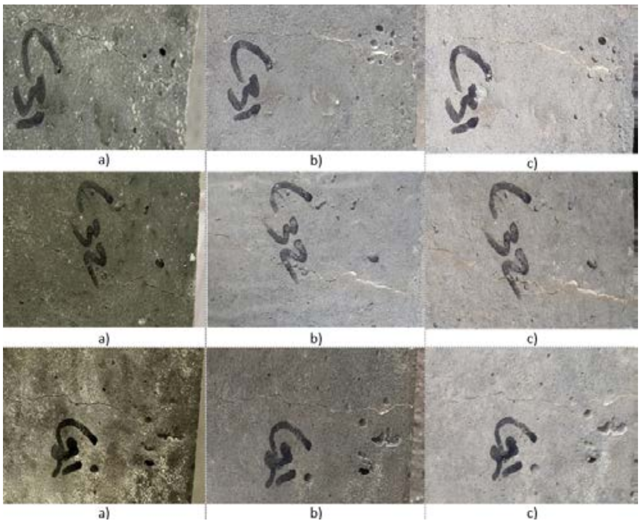

Figure 8: Healing in concrete having 60% Fly Ash + 50% RA + 0.5% fibres.
a) initial, b) after three weeks, c) after five weeks.

After observing successful healing in the samples, their compressive strength was evaluated using a compression testing machine. The resultant values are presented in Table 11.

Table 11. Compressive strength of samples of FA+50%RCA+fibres after healing

SAMPLE	FA %age+50% RA+ 0.5% Fibers	STRENGTH(N/mm^2)
1	60%	14.8
2	60%	15.91
3	60%	14.36

4. Conclusions

This study investigated the autogenous self-healing properties of concrete containing varying volumes of low calcium Class F Fly Ash with partially replaced recycled aggregate and the incorporation of macro synthetic fibers to improve mechanical properties. The following conclusions can be drawn from this investigation:

1. The use of recycled aggregate and fibers in concrete reduced the workability of concrete, which was rectified by using a higher water-cement ratio.

2. The use of partially replaced recycled aggregate resulted in a decrease in the strength of concrete. However, the incorporation of macro synthetic fibers led to an increase in the mechanical properties of the concrete.

3. The self-healing behavior of Fly Ash was observed to be significant within the first two weeks after the cracking of 28-day strength samples.

4. The self-healing behavior of concrete generally increased with the increasing volume of Fly Ash up to 60 percent replacement, beyond which a decrease in self-healing ability was observed.

5. Future recommendation

Based on the results of this study investigating the self-healing behavior of concrete with partially replaced recycled aggregate and the addition of macro synthetic fibers, the following recommendations can be made:

1. The use of calcium-treated Class F Fly Ash with $CaCl_2$ could potentially enhance the healing ability of concrete and should be further explored to heal larger crack widths.

2. Increasing the volume of replaced recycled aggregate to 75 % and 100 % may provide a more economical solution for the production of self-healing concrete, and this possibility warrants further investigation.

3. Other supplementary cementitious materials (SCMs), such as blast furnace slag, could be combined with recycled aggregate to enhance the autogenous self-healing of concrete and should be considered in future research.

References

1. Huang, C. Evaluating the self healing behavior of the fiber-reinforced cementitious composite incorporating the internal curing agents. Purdue University Graduate School, 2020.
2. Qaidi, S., Najm, H.M., Abed, S.M., Özkılıç, Y.O., Al Dughaishi, H., Alosta, M., Sabri, M.M.S., Alkhatib, F., Milad, A. Concrete Containing Waste Glass as an Environmentally Friendly Aggregate: A Review on Fresh and Mechanical Characteristics. Materials 2022, 15, DOI: 10.3390/ma15186222
3. Huang, J., Sabri, M.M.S., Ulrikh, D.V., Ahmad, M., Alsaffar, K.A.M. Predicting the Compressive Strength of the Cement-Fly Ash–Slag Ternary Concrete Using the Firefly Algorithm (FA) and Random Forest (RF) Hybrid Machine-Learning Method. Materials 2022, 15, DOI: 10.3390/ma15124193
4. El-said, A., Awad, A., Ahmad, M., Sabri, M.M.S., Deifalla, A.F., Tawfik, M. The Mechanical Behavior of Sustainable Concrete Using Raw and Processed Sugarcane Bagasse Ash. Sustainability (Switzerland) 2022, 14, DOI: 10.3390/su141811181
5. Sherir, M.A. Self-healing cementitious composites incorporating innovative materials. Ph. D. thesis, Dept. of Civil Engineering, Ryerson Univ, 2016.
6. Milla, J.E. Performance Evaluation and Characterization of Encapsulated Calcium Nitrate for Self-Healing Concrete Applications. 2017.
7. Giannaros, P., Kanellopoulos, A., Al-Tabbaa, A. Sealing of cracks in cement using microencapsulated sodium silicate. Smart Materials and Structures 2016, 25, 084005, DOI: 10.1088/0964-1726/25/8/084005
8. Rajczakowska, M., Habermehl-Cwirzen, K., Hedlund, H., Cwirzen, A. Autogenous self-healing: A better solution for concrete. Journal of Materials in Civil Engineering 2019, 31, 03119001.
9. Zhang, Z., Qian, S., Ma, H. Investigating mechanical properties and self-healing behavior of micro-cracked ECC with different volume of fly ash. Construction and Building Materials 2014, 52, 17–23.
10. Xu, J., Du, Y., Jiang, Z., She, A. Effects of calcium source on biochemical properties of microbial CaCo3 precipitation. Frontiers in Microbiology 2015, 6, DOI: 10.3389/fmicb.2015.01366
11. Zhang, W., Zheng, Q., Ashour, A., Han, B. Self-healing cement concrete composites for resilient infrastructures: A review. Composites Part B: Engineering 2020, 189, DOI: 10.1016/j.compositesb.2020.107892
12. Li, W., Jiang, Z., Yang, Z., Yu, H. Effective mechanical properties of self-healing cement matrices with microcapsules. Materials & Design 2016, 95, 422-430, DOI: 10.1016/j.matdes.2016.01.124
13. Huseien, G.F., Faridmehr, I., Baghban, M.H. Self-Healing Cementitious Materials. Self-Healing Cementitious Materials 2022, 21–40, DOI: 10.1201/9781003195764-3
14. Zhang, W., Wang, D., Han, B. Self-healing concrete-based composites. Self-Healing Composite Materials 2020, 259–284, DOI: 10.1016/b978-0-12-817354-1.00015-6
15. Tziviloglou, E., Wiktor, V., Jonkers, H., Schlangen, E. Performance requirements to ensure the crack sealing performance of bacteria-based self-healing concrete. In Proceedings of the Proceedings of the 9th International Conference on Fracture Mechanics of Concrete and Concrete Structures, 2015/05/29, 2015.
16. Zhu, Y., Yang, Y., Yao, Y. Autogenous self-healing of engineered cementitious composites under freeze–thaw cycles. Construction and Building Materials 2012, 34, 522–530, DOI: 10.1016/j.conbuildmat.2012.03.001
17. Edvardsen, C. Water permeability and autogenous healing of cracks in concrete. In Innovation in concrete structures: Design and construction; Thomas Telford Publishing: 1999; pp. 473–487.
18. Zhou, Z.H., Li, Z.Q., Xu, D.Y., Yu, J.H. Influence of slag and fly ash on the self-healing ability of concrete. In Proceedings of the Advanced Materials Research, 2011, pp. 1020–1023.
19. Karkush, M.O., Yassin, S. Using sustainable material in improvement the geotechnical properties of soft clayey soil. Journal of Engineering Science and Technology 202, 15, 2208–2222.
20. Navas, F.O., Navarro-Gregori, J., Herdocia, G.L., Serna, P., Cuenca, E. An experimental study on the shear behaviour of reinforced concrete beams with macro-synthetic fibres. Construction and Building Materials 2018, 169, 888–899.
21. Ortega, J.M., Sánchez, I., Antón, C., de Vera, G., Climent, M.A. Influence of Environment on Durability of Fly Ash Cement Mortars. ACI Materials Journal 2012, 109.

Information about authors:

Mohanad Sabri, *PhD*
ORCID: https://orcid.org/0000-0003-3154-8207
E-mail: mohanad.m.sabri@gmail.com

Faisal Javed Muhammad,
E-mail: arbabfaisal@cuiatd.edu.pk

Muhammad Arslan,
E-mail: ars918158@gmail.com

Received 15.02.2023. Approved after reviewing 10.04.2023. Accepted 26.09.2023.

Magazine of Civil Engineering. 2023. 123(7). Article No. 12303

Magazine of Civil Engineering

ISSN 2712-8172

journal homepage: http://engstroy.spbstu.ru/

Research article

UDC 626.01

DOI: 10.34910/MCE.123.3

Hoek–Brown model for ice breaking simulation

S.A. Andreeva[1] ✉, ***D. Sharapov***[2]

[1] *Admiral Makarov State University of Maritime and Inland Shipping, St. Petersburg, Russian Federation*

[2] *Peter the Great St. Petersburg Polytechnic University, St. Petersburg, Russian Federation*

✉ *Cofiaand16@gmail.com*

Keywords: Hoek–Brown model, ice model, ice failure, ice bending, finite-element analysis

Abstract. Arctic is an important region for science and economic projects. New infrastructure is required for the sustainable development of this region. The water transport infrastructure in Arctic is subject to extreme environmental impacts. One of the main loads on such structures is the ice load. Conventional way to assess ice loads is to use empirical equations from normative documents. Nowadays with the increasing complexity of designs the numerical calculations became more important. Modern software and material models become more common in design. Ice model is not incorporated in the common engineering software, therefore engineers have to choose among available models. The Hoek–Brown model of ice is considered as one of the most suitable preinstalled material models in the Plaxis software package. As of today, the authors found no studies proving the applicability of the Hoek–Brown model to the destruction of ice by bending, so this problem is of interest. The Hoek–Brown model was examined by using available results of the field ice bending tests. The authors compared the ice strength from the numerical calculation and field tests. Young's modulus was estimated with Vaudrey equation. The calculation results from Hoek–Brown model showed the possibility of the model application in general case. The convergence of the results was revealed, with an error that in most cases does not exceed 20 %. Bigger discrepancy for some result points can be explained by the presence of the excessive brine volume in ice.

Funding: The project is carried out with the support of the Russian Ministry of Education and Science "Study of statistical patterns of ice loads on engineering structures and development of a new method for their stochastic modeling (FSEG 2020-2021)" No. 0784-2020-0021

Citation: Andreeva, S.A., Sharapov, D. Hoek–Brown model for ice breaking simulation. Magazine of Civil Engineering. 2023. 123(7). Article no. 12303. DOI: 10.34910/MCE.123.3

1. Introduction

The development of the Arctic territories is one of the priorities for scientific research and economic development. It is important for a number of reasons: rich deposits of minerals, natural resources of animal and plant origin, traffic routes (including Europe–Asia), climate study, and others. Meanwhile, construction in harsh Arctic conditions inevitably faces a number of challenges, primarily related to low temperatures and ice impacts. The transport infrastructure of the Arctic region in some areas is inevitably limited to sea and river ports. These berthing complexes are subject to considerable ice loads and must be designed against ice actions. To determine ice loads in the modern world, software programs are usually used. Not all programs have a wide range of material models, so it is important to understand the possibilities of replacing complex ice models with simple standard ones. Plaxis is widely used by hydraulic engineers, but it does not have a special ice model. The object of the investigation is to evaluate the applicability of the most suitable material model in the Plaxis program (Hoek–Brown model) for modeling of the ice destruction by bending.

The calculation of ice loads is usually carried out with the help of normative documents [1-4], and can be confirmed by modeling. Computer modeling of ice as a material is a separate problem in software systems [5-7] and usually, the material "ice" is not in the database of popular engineering calculation systems [8, 9]. The user is invited to select the general model and introduce the characteristics of ice for the given calculation tasks. The relevance of the topic of this work is related to the lack of verification data about the Hoek–Brown model for breaking ice by bending in the Plaxis software package. The breaking of ice by bending is the subject of many articles describing the theoretical approach to determining strength [10-15], as well as physical field experiments [12]. The modeling of ice failure by bending is described in detail in the work of L. Li [15]. L. Li carried out strength analyses and comparisons with D.S. Sodhi experiments [13] to calculate ice loads on ocean and marine hydrotechnical constructions. The authors used a dynamic approach to modeling ice destruction using the LS-Dyna program. This approach deserves attention but uses a different problem statement as well as models that are not available in the Plaxis software package. The work of S.V. Godetsky on the assessment of ice strength in the Sea of Okhotsk [16] deserves a special attention as it well describes the strength properties of ice. However, the Hoek–Brown model is not considered in the work by S.V. Godetsky. The authors O.V. Yakimenko and S.A. Matveev in their work "Modeling the stress state of reinforced specimens" [17] developed a mathematical model of the stress state of ice reinforced with geosynthetic materials. In this model, using the finite difference method, normal and shear stresses in the samples are calculated. However, the Hoek–Brown model is missing in the work [8]. There are several methods for thermodynamic modeling of ice; for example, the article by Y. Fang describes the model based on the Winton model, which takes into account the influence of snow cover, vertically changing ice salinity, and an increased number of layers considered [18]. Also, a thermodynamic model was considered in the article by J. Zhao on the effect of snow cover on the thickness of sea ice in Prydz Bay, East Antarctica [19]. In the article by M. Prasanna about laboratory experiments on the destruction of floating salt ice blocks in contact with ice, an experimental system for studying the nature of ice destruction is considered [20]. Thermodynamic modeling of the consolidated ice hummock layer using the Comsol Multiphisics software package is described in the articles by E. Salganik [21, 22]. This model also can be found in some works about structure “freeze-in the ice” [23, 24]. In C. Pang's article, the determination of the initial nature of the fracture during ice bending was considered and the numerical model of the ice field “Fixed effects” model was considered [25]. M. Mokhtari modeled ice in the computer program “VUMAT” and “Crushable Foam” to analyze its plastic properties during crushing [26]. There are several natural experiments to determine ice loads on structures, such as the article by Å. Ervik on the interaction of hummocks with lighthouses and the assessment of global ice loads [27]; in the article by M. van den Berg, a study was conducted on the interaction of ice with vertical-type structures [28]. T. Kärnä considered numerical modeling to determine the ice load on structures [29].

The relevance of the study lies in the lack of practical information on applying the Hoek–Brown model to solving problems of ice destruction by bending. There was no Hoek–Brown model considered for calculating the strength characteristics of ice in the known literature above. The most common models that should be taken into account when choosing a material model in general case are (using the Plaxis software package): linear model, Mohr-Coulomb model, Hardening soil model, Soft soil model, Jointed rock model, Hoek–Brown model. It should be noted that there are other models [30], but they are not presented by default in the considered software package. Linear elasticity model: this model assumes that the behavior of the material is linear and elastic, which means that the relationship between stress and strain is proportional and that the ice returns to its original state after the load is removed. Mohr-Coulomb model: this model is used for a material under shear loads, and it takes into account the relationship between shear stress and normal stress. Hardening Soil Model: this model assumes the strengthening effect of both compressive and shear soil. The stiffness characteristics of the material model increase with increasing pressure. Model of Weakly(small) Hardening soil takes into account the elastic behavior of the material during unloading and its reloading at small deformations. The Rock model is an anisotropic model of the behavior of fractured rock and is a linearly elastic and ideally plastic model. Reduced elastic and plastic properties can only occur in shear planes. The Hoek–Brown model, an isotopically ideal-plastic linear elastic model, which is characterized by the Hoek–Brown strength criterion, which consists in a nonlinear dependence of stresses, characterizes the moment of occurrence of plastic deformations. The described material models use different initial data, which must also be taken into account when preparing the calculation. A comparison of the initial data required for the calculation is given in Table 1.

Table 1. Initial data for different material models.

Model variable	Linear elastic	Mohr-Culomb	Hardening soil	Soft (weak) hardening soil	Rock	Hoek–Brown
E is Young's modulus, (for some models: E_{50ref}, $E_{ref\,oed}$, $E_{ref\,ur}$)	+	+	+	+	+	+
ν is Poisson's ratio	+	+	+	+	+	+
φ is angle of friction or effective angle of friction		+	+	+	+	
c is cohesion coefficient or effective cohesion coefficient		+	+	+	+	
ψ is dilatancy angle		+	+	+	+	+
σ_t is tensile limit and tensile strength		+	+	+	+	
Σc_i is uniaxial compressive strength of undisturbed soil						+
m_i is intact rock parameter						+
GSI is Geological strength index						+
D is disturbance factor						+
N is number of crack directions					+	
$\alpha_{1,i}$ is dip angle (-180°≤ α_{1i}≤180°)					+	
α_{2i} is stretch (-180°≤ $\alpha_{1,i}$≤180°), (α_{2i}=90° PLAXIS 2D)					+	
$G_{0\,ref}$ is shear modulus at ultrasmall strains				+		
$\gamma_{0.7}$ is strain threshold (G_s=0.722G_0)				+		
m is exponent for the dependence of stiffness on the stress level			+			

The data presented in the table clearly demonstrate that some material models have a minimum amount of initial data. The Hoek–Brown model, in comparison with the linear model, also takes into account: the uniaxial compressive strength of the undisturbed soil, the parameter of the undisturbed soil, the geological strength index, the coefficient of disturbance as input data. There are practical and theoretical methods of analysis to select the appropriate material model. Theoretical ones include the analysis of the mathematical model of the behavior of the ice material and the selection of the maximum correspondence with the known model in the given boundary conditions. A practical way of analysis includes comparing models with the results of natural experiments. When choosing a theoretical approach, it makes sense to consider the Brugers model, Fig. 1 [31]. This model consists of "Maxwell Units" and "Kelvin Units". The Maxwell unit is responsible for the viscoplastic behavior of the material, and the Kelvin unit is responsible for the partial recovery after loading. This model makes it possible to take into account the rate of ice deformation, which is an important factor for a certain category of tasks.

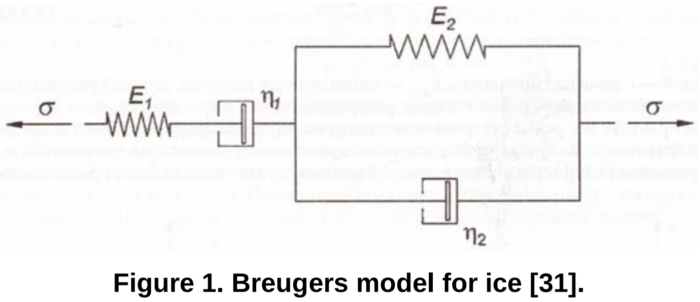

Figure 1. Breugers model for ice [31].

In the Fig. 1: E_1 is Young's modulus for "Maxwell Unit", E_2 is Young's modulus for "Kelvin Units", η_1 and η_2 are viscosity factor for the corresponding unit.

The Brueger model describes the behavior of ice; however, in practical calculations, it makes sense to reduce the number of degrees of freedom by setting certain restrictions and assumptions, such as a known strain rate, which makes it possible to significantly simplify the model. When choosing a practical approach to model selection based on direct experiments, it is important to have a sufficient amount of initial experimental data. For further analysis, the work used the initial data based on the experiments of M. Karulina [11, 12] presented in Table 2.

Table 2. Initial data for analysis.

No.	Length, m	Width, m	Thickness, m	Salinity, ppt	Temperature, °C	Bending strength, kPa	Date	Place
1	1.97	0.64	0.23	5.57	-8.00	346.7	05.03.2010	Tempel fjord
2	1.27	0.58	0.22	5.57	-8.00	258.3		
3	1.40	0.56	0.22	5.57	-8.00	302.6		
4	1.38	0.56	0.22	5.57	-8.00	256.7		
5	1.90	0.74	0.35	5.57	-5.18	310.5	06.03.2010	
6	1.98	0.68	0.35	5.57	-5.18	281.8		
7	2.50	0.51	0.51	6.03	-3.77	213.2	07.03.2010	
8	2.53	0.58	0.49	5.78	-3.90	282.3	19.02.2011	
9	3.39	0.50	0.45	3.50	-2.10	169.0	03.05.2010	Van Mijen fjord
10	2.13	0.48	0.40	2.70	-1.40	149.8		
11	2.30	0.46	0.39	2.70	-1.60	186.1		
12	2.27	0.45	0.37	5.70	-2.20	131.6		
13	3.02	0.60	0.49	3.90	-2.10	128.1		
14	1.22	0.25	0.23	7.72	-3.20	202.0	25.02.2011	Advent fjord
15	1.33	0.27	0.25	7.72	-3.20	160.8		
16	1.59	0.45	0.31	5.96	-2.30	193.0		
17	2.40	0.68	0.40	6.98	-2.00	205.0	21.03.2012	Sveagruva
18	2.22	0.45	0.31	8.38	-2.20	178.0		
19	3.40	0.63	0.63	4.53	-6.50	186.0	26.03.2012	
20	3.18	0.63	0.65	3.30	-3.30	328.0	28.03.2012	

These results were obtained during experiments in the fjords of Svalbard and published in the journal [3]. The values presented in the table were used to justify the possibility of using the Hoek–Brown model to calculate the destruction of ice by bending in the Plaxis software package, which was the purpose of this work.

The goals of this work are:

1. Analyze the Hoek–Brown model for calculations related to the flexural stiffness of ice.
2. Analyze the possibility of calculation using the Plaxis software product (Hoek–Brown model in the list of available standard models).
3. Carry out a series of numerical calculations using the Hoek–Brown model and compare them with the results of physical experiments carried out in the field. Assess the error/convergence of numerical and field experiments.
4. Assess the possibility of using the Vaudrey equation [32] for ice models.

2. Methods

Numerical models were created in a finite element software package for the verification of the Hoek–Brown model for the calculations of the flexural strength of ice. The calculation results were analyzed and compared with the actual results of physical experiments.

The flexural test of ice is a classic traditional field test for hydrological surveys. During experiments to determine the strength of ice in bending in the field, the ice beam is sawn from three sides (one side is connected to the original ice level), then loads are applied to one end of the beam, and deformations are fixed until the moment of destruction, Fig. 2 [11].

Figure 2. Field experiment to determine the bending strength of a beam [12].

It is assumed that the embedment of the beam is rigid and that the Archimedes force does not affect the result of the experiment. There are “MAGI” recommendations, which regulate the dimensions of beams depending on their thickness in order to reduce the effect of shift/variations on the result [33]. The ‘rate of load increase’ is chosen in such a way that no more than 1–2 seconds elapse from the beginning of the process of applying the load to the destruction of the beam. The advantage of this test method is undisturbed structure of the sample; the disadvantage of this method is the possible formation of stress concentrations at the site of the ice beam.

Fig. 3 shows an example of a graph of the dependence of the beam deformation on the load [12].

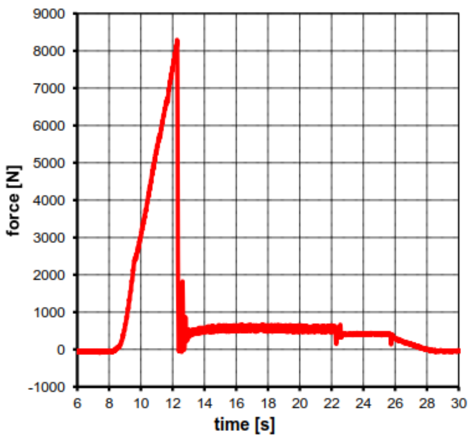

Figure 3. Force dependence on time for determining the bending strength of a beam [12].

The numerical formulation of the experiment was implemented in the Plaxis software package in 2D. Plaxis is a modern software package for performing calculations, mainly related to soil and foundations. The program is based on the finite element method. The entire computational area (within the given boundaries) is divided into a certain number of connected mesh elements, and the required values are determined at the nodes (depending on the type of element) of the mesh. The mesh element size was determined by practical considerations, taking into account the necessary absence of influence on the result. The default recommended model boundary conditions were used, which restrict horizontal movements at the lateral boundaries of the model and restrict vertical movements at the bottom boundary of the model. For a 2D setting, the boundary conditions take the following form (x is the horizontal axis, y is the vertical axis).

The vertical boundaries of the model allow vertical displacements, but they are fixed in the direction normal to the vertical side boundary [9].

$$u_x = 0, \quad u_y = free. \tag{1}$$

The “bottom” of the model is fixed in all directions.

$$u_x = u_y = 0. \tag{2}$$

The "top surface" is free in all directions.

$$u_x = free,\ u_y = free. \tag{3}$$

Fig. 4 shows the calculation model in the software package.

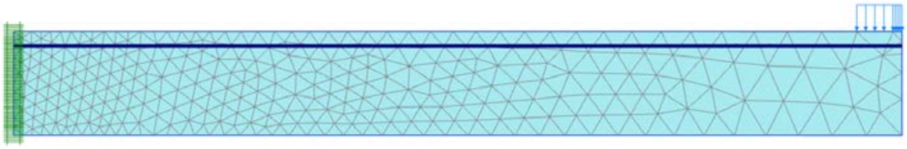

Figure 4. Calculation model.

The presented model contains: 579 elements, 4851 nodes. The dimensions of the simulated beam were selected according to known field test results.

The following parameters were used in the calculation:

Young's modulus (E) is a physical quantity that characterizes the ability of a material to resist compression and tension during elastic deformation. In the Hoek–Brown model, Young's modulus is determined depending on the quality of the rock.

Poisson's ratio (v) characterizes the ratio of transverse deformation of the material during its tension or compression.

Undisturbed uniaxial compressive strength (σ_{ci}) is the ratio of the vertical load applied to a material sample at which its destruction occurs to its cross-sectional area.

Undisturbed rock parameter (m_i) is an empirical parameter that depends on the type of rock being tested.

The Geological Strength Index (GSI) is a parameter that takes into account the nature of the fracture of the rock and the "blockiness" of the massif.

Disturbance coefficient (D) is a parameter characterizing the degree of rock damage as a result of mechanical impact.

The geological strength index and the failure coefficient were taken as GSI = 100, D = 0, taking into account the fact that the beams were sawn in natural conditions and should not undergo changes in temperature and salinity during testing.

The m_i parameter was selected taking into account the greatest convergence with the experimental data, $m_i = 7$.

The load at which the ultimate bending strength of the beam was calculated is derived from the equation:

$$\sigma_f = \frac{6Pl}{bh^3}, \tag{4}$$

where σ_f is beam bending strength limit, P is load applied to the beam, kN; l is beam length, m; b is beam width, m; h is beam height, m.

Formula (4) represents the ratio of the load to the moment of resistance, resulting in the ultimate bending stress that the material can withstand.

Young's modulus of elasticity (E) for sea ice was determined by the Vaudrey equation [32], according to experimental data. This equation is included in ISO 19906 [2]:

$$E = 5.31 - 0.436\sqrt{\nu_b}, \tag{5}$$

where ν_b is liquid brine content of sea ice, ‰.

The brine volume is calculated depending on the temperature, T, °C and salinity of sea ice, S, ‰ [34]:

$$\nu_b = S\left(\frac{49.185}{|T|} + 0.532\right). \quad (6)$$

Poisson's ratio was calculated as a function of temperature according to the equation proposed by Wicks and Assour:

$$\nu = 0.33 + 0.06105 \exp\left(\frac{T}{5.48}\right). \quad (7)$$

The density of ice depends on temperature, pressure, salinity and other factors. The dependence of ice density on temperature T and pressure P is given by the following empirical equation:

$$\rho(P,T) = \rho_0\left[1 + 0.94\cdot 10^{-7}\left(\frac{P}{1.01\cdot 10^5} - 1\right)\right]\left(1 - 1.53\cdot 10^{-4}T\right). \quad (8)$$

The strength of ice for uniaxial compression was obtained according to Russian normative document SP 38.13330.2018 [3] depending on the temperature and salinity of the ice. The type of ice crystal structure was assumed to be granular.

The load specified in the software package is calculated from equation (4) based on experimental data.

Initial data doesn't have pressure details for each sample therefore the pressure is assumed to be constant and equal to normal atmospheric pressure.

The PLAXIS software package solves a two-dimensional problem, taking into account the fact that the load was recalculated for the beam of a certain width. The specified load was reduced to a value of one meter, taking into account the width of the beams. In the calculation model, the water level is set at a ratio of 0.9 from the thickness of the surrounded level ice. An example of a calculation scheme is shown in Fig. 4. An example of the characteristics used for the Hoek–Brown model is given in Table 3.

Table 3. Example of characteristics used for the Hoek–Brown model.

Characteristic	Value	Units
γ	8.99	kN/m³
E	2650000	kN/m²
ν	0.347	–
σ_{ci}	2054	kN/m²
m_i	7.0	–
GSI	100.0	–
D	0.00	–

A data array was prepared for the calculation model based on the described expressions, Table 4.

Table 4. Data for the calculation model

No	Length, m	Width, m	Thickness, m	Salinity, S, ‰	Temperature, T °C	Strength, σ_f, kPa	Load, P, kN	Recalculated load, P, kN/m	Brine volume, ν_b,‰	Modulus of elasticity, E, GPa	Poisson's ratio, ν	Ice density, ρ, kg/m³	σ_{ci}, MPa
1	1.97	0.64	0.23	5.57	-8.00	346.70	0.993	1.552	37.208	2.650	0.347	916.80	2.054
2	1.27	0.58	0.22	5.57	-8.00	258.30	0.952	1.641	37.208	2.650	0.347	916.80	2.054
3	1.40	0.56	0.22	5.57	-8.00	302.60	0.976	1.744	37.208	2.650	0.347	916.80	2.054
4	1.38	0.56	0.22	5.57	-8.00	256.70	0.840	1.501	37.208	2.650	0.347	916.80	2.054
5	1.90	0.74	0.35	5.57	-5.18	310.50	2.469	3.337	55.851	2.052	0.357	916.80	1.512

No	Length, m	Width, m	Thickness, m	Salinity, S, ‰	Temperature, T °C	Strength, σ_f, kPa	Load, P, kN	Recalculated load, P, kN/m	Brine volume, ν_b,‰	Modulus of elasticity, E, GPa	Poisson's ratio, ν	Ice density, ρ, kg/m^3	σ_{ci}, MPa
6	1.98	0.68	0.35	5.57	-5.18	281.80	1.976	2.906	55.851	2.052	0.357	916.80	1.512
7	2.50	0.51	0.51	6.03	-3.77	213.20	1.885	3.697	81.878	1.365	0.364	916.80	1.195
8	3.39	0.50	0.45	3.50	-2.10	169.00	0.841	1.683	83.837	1.318	0.375	916.80	1.253
9	2.13	0.48	0.40	2.70	-1.40	149.80	0.900	1.875	96.293	1.032	0.380	916.80	1.603
10	2.30	0.46	0.39	2.70	-1.60	186.10	0.944	2.051	84.436	1.304	0.379	916.80	1.644
11	2.27	0.45	0.37	5.70	-2.20	131.60	0.595	1.323	130.466	0.330	0.374	916.80	0.925
12	3.02	0.60	0.49	3.90	-2.10	128.10	1.018	1.697	93.418	1.096	0.375	916.80	1.135
13	2.53	0.58	0.49	5.78	-3.90	282.30	2.590	4.465	75.970	1.510	0.363	916.80	1.247
14	1.22	0.25	0.23	7.72	-3.20	202.00	0.365	1.460	122.766	0.479	0.367	916.80	0.777
15	1.33	0.27	0.25	7.72	-3.20	160.80	0.340	1.259	122.766	0.479	0.367	916.80	0.777
16	1.59	0.45	0.31	5.96	-2.30	193.00	0.875	1.944	130.624	0.327	0.373	916.80	0.917
17	2.40	0.68	0.40	6.98	-2.00	205.00	1.549	2.278	175.369	-0.464	0.375	916.80	0.715
18	2.22	0.45	0.31	8.38	-2.20	178.00	0.578	1.284	191.808	-0.728	0.374	916.80	0.539
19	3.40	0.63	0.63	4.53	-6.50	186.00	2.280	3.619	36.688	2.669	0.352	916.80	1.925
20	3.18	0.63	0.65	3.30	-3.30	328.00	4.576	7.263	50.941	2.198	0.366	916.80	1.576

Remark: Colored rows correspond to the values with significant relative mistake obtained

3. *Results and Discussion*

The calculations were carried out for a previously prepared data array based on the initial data from the experiments of M. Karulina [11, 12]. Fig. 5 shows the deformed scheme of the calculation model. Fig. 6 shows the bending moment in a cantilever beam.

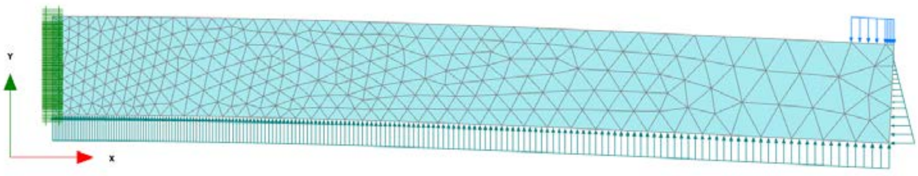

Figure 5. Deformed scheme of the model.

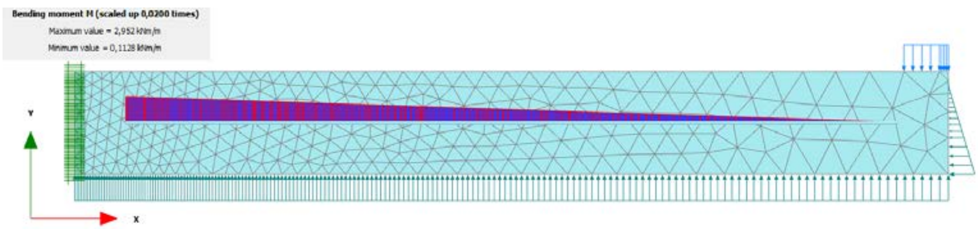

Figure 6. Bending moment in a beam.

The resulting nature of displacements and the dependence of the moment correspond to the expected ones, which were published in the work [11, 12]. The bending moment per one meter length was recalculated to the experimental width of the beam, and the strength was calculated by formula (4).

Table 5 shows the results of calculations and the variation between the strength characteristics obtained empirically and modeled in the software package [8]. In Fig. 7, the results are presented in the form of graphs.

Table 5. Comparisons of results.

No	Bending moment, kNm /m	Recalculated moment, kNm	Strength, kPa	Strength, kPa (experimental data)	Variation
1	2.952	1.889	334.82	346.70	4%
2	1.878	1.089	232.81	258.30	11%
3	2.342	1.312	290.33	302.60	4%
4	1.968	1.102	243.97	256.70	5%
5	5.491	4.063	268.95	310.50	15%
6	4.952	3.367	242.55	281.80	16%
7	8.318	4.242	191.88	213.20	11%
8	5.750	2.875	170.37	169.00	1%
9	3.569	1.713	133.84	149.80	12%
10	4.051	1.863	159.80	186.10	16%
11	2.725	1.226	119.43	131.60	10%
12	4.701	2.821	117.48	128.10	9%
13	4.372	2.536	109.25	282.30	158%
14	1.047	0.262	118.75	202.00	70%
15	1.224	0.330	117.50	160.80	37%
16	2.570	1.157	160.46	193.00	20%
17	2.883	1.960	108.11	205.00	90%
18	1.433	0.645	89.47	178.00	99%
19	11.160	7.031	168.71	186.00	10%
20	16.580	10.445	235.46	328.00	39%

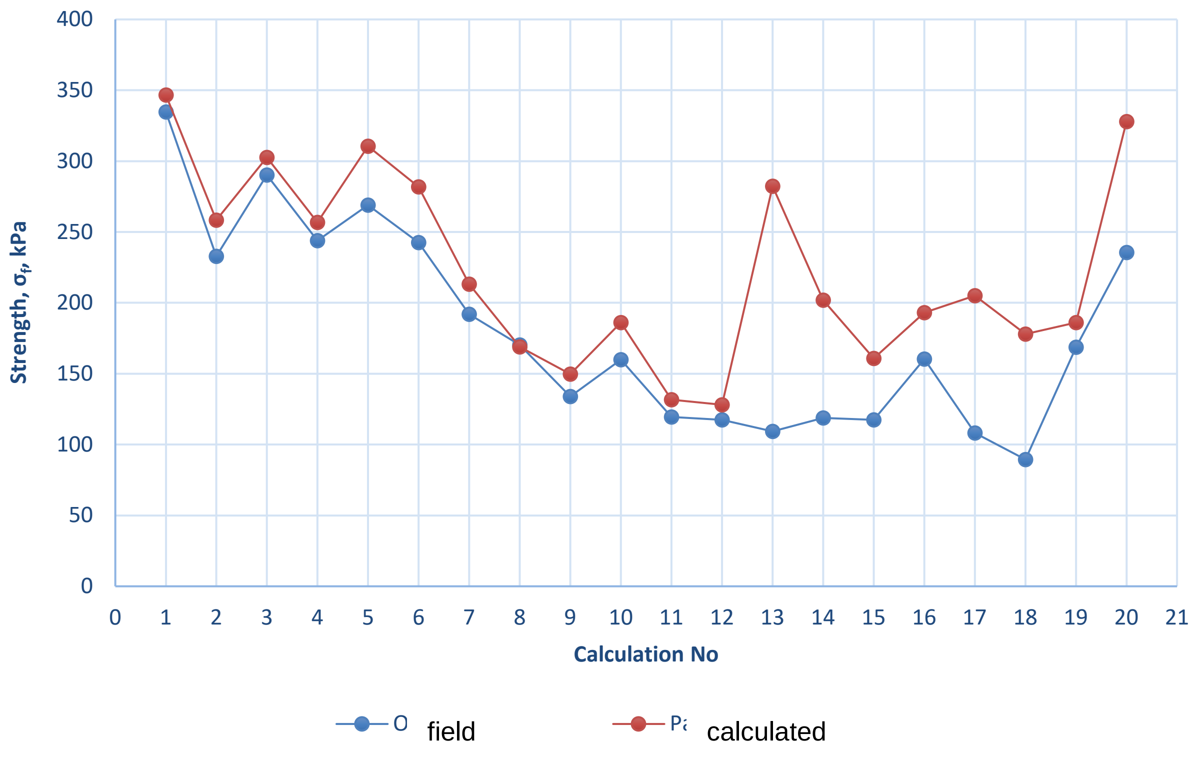

Figure 7. Comparison of the strength of ice based on the calculation results.

An analysis of the results shows that some of the deformation modulus obtained with Vaudrey equation (5) [2] have a negative value, which is associated with a large volume of brine contained in the sea ice.

The density of sea ice does not change when determining by using formula (8) [34], which takes into account temperature and pressure.

The largest variation of results was for the experiments No. 13,14,18,20 (Table 5). Possible error reaches a value of 50 %.

Some results of experiments (No 17, 18) can be explained by the deviation of the deformation modulus, which is probably associated with a large volume of brine in the ice structure, since the results were obtained at a relatively high ice temperature and high salinity.

In Karulina's experiments [11, 12], a comparison was made to determine the bending strength of ice obtained experimentally with empirical formulas depending on the volume of brine. There is also a discrepancy in some results, which is due to the internal structure of the ice depending on a certain region [2]. This could be an explanation for big discrepancy of the experiment No 13, as the location of the data sample is different. Location and brine volume influence on the result was also discussed by Marchenko in the article “Experimental studies of sea ice elastic behavior” [31]. The study revealed the dependence of the deformation modulus on the volume of brine in ice, which explains the big variation for experiment No 13.

4. Conclusions

1. In the work, the Hoek–Brown model for calculations related to the flexural stiffness of ice was analyzed. The results of the Hoek–Brown model showed the possibility of its application in the general case; however, it is necessary to carefully monitor the deviation of the initial and resulting data; one of the reasons for the result discrepancy could be a variation of the brine volume in ice. Arctic engineering projects generally include a field research stage when the properties of ice in situ could be examined and a correction to the material model could be introduced.

2. Plaxis software product was used, and therefore calculations were limited to the available models and functions in this software. The study showed that the Hoek–Brown model available in the Plaxis software package can be used. No fundamental limitations were found in the program. However, ice has a significant variation of properties (including brine volume), which should be considered in the model. Therefore, it is difficult to build a simple unique ice model for all locations.

3. A significant series of numerical experiments was carried out and compared with the results obtained in the field. In most cases, the convergence of the results was revealed, with an error that in most cases does not exceed 20 %. The bigger discrepancy (40 %) for some result points can be explained due to the presence of excessive brine volume in ice. Variations in the field data are a subject of separate studies of statistical inhomogeneity. The present deviation was considered acceptable for the purpose of this work. It should be noted that for field experiments related to the properties of ice, the results often vary by several times [12].

4. Based on the analyzed data, it can be seen that the dependence of the Young's modulus on the Vaudrey equation [32] is not applicable to all ice models. However, it is a convenient calculation method, which provides acceptable results for most cases. Based on the results obtained, it is possible to estimate a variation of the result to introduce a correction factor, which will allow using the described model with the prescribed level of reliability.

References

1. API-RP-2N Recommended practice for planning, designing, and constructing structures and pipelines for arctic conditions. American Petroleum Institute, 1995.
2. DS/ISO 19906-2019 Petroleum and natural gas industries – Arctic offshore structures. International Organization for Standardization, 2010.
3. Russian Code Specification SP 38.13330.2018 Loads and impacts on hydraulic structures (from wave, ice and ships). – Moscow: Ministry of Regional Development of Russia, 2018.
4. NORSOK STANDARD N-003 Actions and action effects. 2007.
5. Timco, G.W., Croasdale, K.R. How well can we predict ice loads. Proceedings oh the 18th IAHR International Symposium on Ice. 2006. Pp. 167–174.
6. Frederking, R. Comparison of standards for predicting ice forces on arctic offshore structures. Proceedings of the Tenth (2012) ISOPE Pacific/Asia Offshore Mechanics Symposium. Vladivostok, Russia, 2012.
7. Shkhinek, K., Blanchet, D., Croasdale, K., Matskevitch, D.G., Bhat, S. Comparison of the Russian and foreign codes and methods for global load estimation. Book Comparison of the Russian and Foreign Codes and Methods for Global Load Estimation. 1994. Pp. 75–81.
8. Material Models Manual PLAXIS CONNECT Edition V20, Build 10265. Bentley, 2020.
9. Scientific Manual PLAXIS CONNECT Edition V20, Build 10265. Bentley, 2020.

10. Peng, C. Eksperimental'nyye issledovaniya i analiz kharakteristik predela prochnosti morskogo l'da na izgib vdol' poberezh'ya Bokhayskogo zaliva [Experimental studies and analysis of the characteristics of the bending strength of sea ice along the coast of the Bohai Bay]. Molodoy uchonyy. 2017. 27 (161). Pp. 39–46. (rus)
11. Karulina, M., Marchenko, A., Karulin, E., Sodhi, D., Sakharov, A., Chistyakov, P. Full-scale flexural strength of sea ice and freshwater ice in Spitsbergen Fjords and North-West Barents Sea. Applied Ocean Research. 2019. 90 (C10). 101853. DOI: 10.1016/j.apor.2019.101853
12. Karulina, M., Karulin, E., Marchenko, A. Field investigations of first year ice mechanical properties in North-West Barents Sea. Proceedings of the International Conference on Port and Ocean Engineering under Arctic Conditions. POAC 2013, 2013.
13. Sodhi, D.S. Vertical penetration of floating ice sheets. International Journal of Solid and Structures. 1998. 35 (32–32). Pp. 4275–4294.
14. Vasiliev, N.K., Karulina, M.M., Marchenko, A.V., Sakharov, A.N., Chistyakov, P.V. Ispytaniya konsoley armirovannogo morskogo l'da [Reinforced sea ice cantilever testing]. Izvestiya VNIIG im. B.E. Vedeneeva. 2015. 277. Pp. 46–55.
15. 1Li, L., Shkhinek, K. The ultimate bearing capacity of ice beams. Magazine of Civil Engineering. 2013. 1 (36). Pp. 65–74. DOI: 10.5862/MCE.36.8
16. Godetsky, S.V., Kokin, O.V., Kuznetsova, O.A., Tsvetsinsky, A.S., Arhipov, V.V. Estimation of ice strength limits for uniaxial compression in the Sea of Okhotsk according to measurements and calculations. Ice and Snow. 2021. 61 (4). Pp. 561–570. (rus). DOI: 10.31857/S2076673421040108
17. Yakimenko, O.V., Matveev, S.A. Modelirovaniye napryazhenogo sostoyaniya armirovannykh ledovykh obraztsov-balok [Simulation of the stress state of reinforced ice specimens-beams]. Vestnik SibADI. 2011. 3 (21). Pp. 39–44. (rus)
18. Fang, Yo., Wu, T., Hu, A., Chu., M. A modified thermodynamic sea ice model and its application. Ocean Modelling. 2022. 178 (1). 102096. DOI: 10.1016/j.ocemod.2022.102096
19. Zhao, J., Cheng, B., Vihma, T., Yang, Q., Hui, F., Zhao, B., Hao, G., Shen, H., Zhang, L. Observation and thermodynamic modeling of the influence of snow cover on landfast sea ice thickness in Prydz Bay, East Antarctica. Cold Regions Science and Technology. 2019. 168 (C11). 102869. DOI: 10.1016/j.coldregions.2019.102869
20. Prasanna, M., Wei, M., Polojärvi, A., Cole, D.M. Laboratory experiments on floating saline ice block breakage in ice-to-ice contact. Cold Regions Science and Technology. 2021. 189. 103315. DOI: 10.1016/j.coldregions.2021.103315
21. Salganik, E., Høyland, K.V., Shestov, A. Medium-scale experiment in consolidation of an artificial sea ice ridge in Van Mijenfjorden, Svalbard. Cold Regions Science and Technology. 2021. 181. 103194. DOI: 10.1016/j.coldregions.2020.103194
22. Salganik, E., Høyland, K.V., Maus, S. Consolidation of fresh ice ridges for different scales. Cold Regions Science and Technology. 2020. 171. 102959. DOI: 10.1016/j.coldregions.2019.102959
23. Sharapov, D., Shkhinek, K., DelValls, T.Á. Ice collars, development and effects. Ocean Engineering. 2016. 115. Pp. 189–195. DOI: 10.1016/j.oceaneng.2016.02.026
24. Sharapov, D., Shkhinek, K. Numerical calculation of the ice grow and empirical calculation results. Advanced Materials Research, Proceedings of 3rd International Conference on Materials and Products Manufacturing Technology (ICMPMT 2013). September 25-26, Changsha, China, 2013.
25. Pan, C., Peng, D., Xu, N., Wang, Y. Determination of initial breaking pattern in the bending failure of a semi-infinite ice sheet. Polar Science. 2022. 34. 100869. DOI: 10.1016/j.polar.2022.100869
26. Mokhtari, M., Kim, E., Amdahl, J. Pressure-dependent plasticity models with convex yield loci for explicit ice crushing simulations. Marine Structures. 2022. 84. 103233. DOI: 10.1016/j.marstruc.2022.103233
27. Ervik, Å., Nord, T.S., Høyland, K.V., Samardzija, I., Li, H. Ice-ridge interactions with the Norströmsgrund lighthouse: Global forces and interaction modes. Cold Regions Science and Technology. 2019. 158. DOI: 10.1016/j.coldregions.2018.08.020
28. Berg, M., Owen, C.C., Hendrikse, H. Experimental study on ice-structure interaction phenomena of vertically sided structures. Cold Regions Science and Technology. 2022. 201. DOI: 10.1016/j.coldregions.2022.103628
29. Kärnä, T., Kamesaki, K., Tsukuda, H. A numerical model for dynamic ice–structure interaction. Computers & Structures. 72 (4–5). Pp. 645–658.
30. Schulson, E.M. Brittle failure of ice. Engineering Fracture Mechanics. 2001. 68 (17–18). Pp. 1839–1887.
31. Marchenko A. V., Karulin Y. B., Chistyakov P. V. Experimental studies of sea ice elastic behavior. Vesti Gazovoy Nauki: collected scientific technical papers. 2020. 3 (45). Pp. 129–140.
32. Vaudrey, K. Ice engineering – study of related properties of floating sea ice sheets and summary of elastic and viscoelastic analysis: Rep. TR860. Port Huenem, CA: U.S. Naval Civil Engineering Lab., 1977.
33. Maattanen, M. On the flexural strength of brackish water ice by in situ tests. Mar. Sci. Comuns. 1976. 2 (2). Pp. 125–138.
34. Sharapov D. Freezing into ice of sea and river hydraulic engineering structures. Saint-Petersburg: Peter the Great St.Petersburg Polytechnic University, 2023. P.167. DOI: 10.18720/SPBPU/2/i23-240

Information about authors:

Sofiya Andreeva,
E-mail: Cofiaand16@gmail.com

Dmitry Sharapov, *PhD*
ORCID: https://orcid.org/0000-0001-8650-2375
E-mail: sharapov.dm@gmail.com

Received 08.03.2023. Approved after reviewing 24.08.2023. Accepted 24.08.2023.

Magazine of Civil Engineering

ISSN 2712-8172

journal homepage: http://engstroy.spbstu.ru/

Research article

UDC 539.3

DOI: 10.34910/MCE.123.4

Stabilization of kaolinitic soil using crushed tile column

M.S.I. Zaini* , *M. Hasan* ✉ , *K.A. Masri

Universiti Malaysia Pahang, Pahang, Malaysia

✉ *muzamir@ump.edu.my*

Keywords: crushed tile, granular column, lateral load capacity, kaolinitic clay, ground improvement

Abstract. Kaolinitic soil is a problematic soil that causes poor carrying capacity and excessive settlement, resulting in significant damage to buildings and foundations. Therefore, soil enhancements were introduced to improve the engineering characteristics of the soil. Crushed tiles were taken from the construction area to substitute aggregate or natural sand. Hence, the purpose of the study is to investigate the lateral load capacity of the crushed tile column on the kaolin clay at various column dimensions. Reinforced kaolin clay samples were tested via several laboratory tests, including Particle Size Distribution, Atterberg limits test, Relative Density, Compaction test, Permeability test, Unconfined Compression Test, and Unconsolidated Undrained Triaxial Test with encapsulated crushed tile with geotextile encasement. The authors investigated the effects of column diameter, height, area replacement ratio, height penetration ratio, height to column diameter ratio, volume replacement ratio, and confining pressures on the shear strength of the encapsulated crushed tile columns at a diameter of 6 mm and 8 mm and at a height of 25.33 mm, 38 mm, and 76 mm. The findings showed that using crushed tile columns at various above listed parameters can enhance the soil's shear strength up to 52.00 % at the optimal utilization of a single enveloped crushed tile column with a diameter of 6 mm and height of 76 mm. The crushed tile granular column is practical to be implemented to enhance the strength of the problematic soil. However, the limitation of utilizing this approach is that the crushed tile granular column may not be suitable for deeper soil layers. Hence, the study demonstrated the significant enhancement of the lateral load capacity of soft kaolin clay soil by utilizing crushed tile waste as a granular column.

Funding: International Grant (UIC201503), UMP Matching Grant (RDU202701, RDU223309)

Citation: Zaini, M.S.I., Hasan, M., Masri, K.A. Stabilization of kaolinitic soil using crushed tile column. Magazine of Civil Engineering. 2023. 123(7). Article no. 12304. DOI: 10.34910/MCE.123.4

1. Introduction

In the process of construction, the biggest problem faced by contractors as well as other workers is the foundation settlements. The use of kaolinitic soil in construction projects presents a complex challenge [1]. This type of soil is known for its problematic characteristics that result from changes in moisture content, which cause volumetric alterations [2]. The engineering characteristics issues linked with this type of soil include settlement, insufficient plasticity, greater compressibility, and susceptibility to climate variables [3]. The resulting disasters and costs of recovering and reconstructing structures built on problematic soils are a matter of national concern [4]. Kaolin is one of the most common clay minerals, and it is distributed sensitively among other high-resistance clays [5, 6]. Therefore, unstable soils, such as soft clay soils, are altered to improve their technical properties and increase their cutting strength [7]. Most of the researchers have suggested various methods, including soil stabilization and improvement [8–11], to alter the characteristics of kaolinitic soils.

The use of concrete or granular materials for ground improvement techniques has become increasingly popular in both partially and fully saturated conditions to enhance ground strength, reduce settlement, and control ground movement. This technique has been employed to improve the load-bearing capacity of kaolinitic clay and expedite the consolidation process. The application of granular column ground improvement presents benefits, including reduced compressibility and instability risk, alongside amplified durability and permeability. Bagriacik [3] and Zaini and Hasan [12] conducted thorough investigations on these subjects.

Several factors, such as column width, arrangement, and spacing, properties of the granular material used, degree of pillar material compression, and the lateral restraints offered by the soil beneath, have an impact on the efficacy of granular columns as a ground improvement method. Nonetheless, the application of granular columns may not be efficient in soils with a shear strength endurance below 15 kPa because of insufficient lateral support from the underlying soft soil [13]. To address this issue, it is possible to encase the granular column using materials like bottom ash, masonry, or steel slag, which provides extra support and allows for the use of more robust shear endurance without excessive column swelling. Thus, it is crucial to establish a strong basis for the creation of solutions for dehydrated soil by incorporating imperforate columns. Studies by Zaini et al., [14], Hosseinpour et al. [15], Zhang et al., [16], Supian et al. [17], and Hilal & Hadzima-Nyarko [18] have explored these aspects in detail.

The use of solid waste as a replacement component has been increasing in the last 30 years, and ceramic waste is a significant contributor to this waste stream. However, recycling options for this waste are often overlooked, and the waste is instead shipped to landfills. In the construction industry, powder and fine particle ceramic waste have potential as replacement components. The recycling of ceramic tile waste has been explored in previous research, such as the groundbreaking work of Zanelli et al. [19], and the ceramic industry has also begun recycling its own waste since the early 1990s. However, the lack of information on the effects of residues in the production of ceramic tiles is a significant barrier to widespread recycling.

Incorporating crushed tile waste as a substitute for fragile aggregates in construction projects presents environmental advantages, such as obviating the necessity to discard the waste in landfills and furnishing an alternate source of raw materials. The utilization of crushed tile waste as an eco-friendly option to stabilize soft clay soils is becoming increasingly popular, but it is essential to comprehensively comprehend the characteristics of crushed tile and its effects on problematic soils before adopting it.

The study is conducted to achieve the aim of identifying the role of crushed tile waste as a kaolinitic clay stabilization method whereas to enhance the compressibility and shear strength of consolidated clayey soils. Besides, the used of crushed tile waste column as a gravelly material is to enhance the bearing capacity, reduce settlement and to accelerate the consolidation. This is realized by using the crushed tile waste in stabilizing the kaolinitic clay soil in regard to the specific gravity, particle size distribution (PSD), compaction parameters, Atterberg limits, unconfined compressive strength and shear strength parameters.

2. Materials and Methods

2.1. Materials

Kaolinite is a type of clay mineral that possesses a hydrophobic polymer structure and has a tendency to combine and interact with water to create a consistent soft clay. The kaolinitic clay samples utilized in this investigation were obtained from Kaolin (M) Sdn. Bhd, situated in Malaysia at coordinates 4°9'48.6"N, 101°16'25.32"E. Homogeneous soft clay samples were created using the S300 grade of kaolin powder. Table 1 presents the fundamental properties of the soil that were employed in this investigation. Moreover, the crushed tile is collected from Nico Ceramic Premium Factory Outlet (3°3’35.0”N, 101°31’24.0”E) at Selangor, Malaysia. The company have been established since 2008. In this study, the crushed tile was encased in an open-pore material that possesses significantly wide pore diameter. The substitution technique was used to place the crushed tile in the soft clay. For encapsulating the kaolinitic clay reinforced with the crushed tile column, the MTS 130 Polyester Non-woven Geotextile Needle punched Fabric was chosen.

Table 1. Basic engineering properties of kaolinitic clay

Properties	Unit	Result
Gravel	%	0
Sand	%	46
Clay and Silt	%	54
USCS classification		ML
AASHTO classification		A-7-6b
Initial moisture content	%	0.97
Specific gravity, G_s		2.62
Liquid limit, LL	%	41.30
Plastic limit, PL	%	31.25
Plasticity index, PI	%	10.05
MDD, $\rho_{d(max)}$	g/cm^3	1.55
OMC, W_{opt}	%	18.00
UCS, q_u	kN/m^2	10.46
USS, S_u	kN/m^2	5.23
Cohesion, c	kN/m^2	14.1
Internal Friction Angle, φ	°	23.8

Note: MDD refers to Maximum Dry Density; OMC refers to Optimum Moisture Content; UCS refers to Unconfined Compression Strength; USS refers to Undrained Shear Strength

2.2. Samples Preparation

The experimental procedures in this study were conducted in accordance with both ASTM and British standards. Various tests were carried out as highlighted in Table 2. The crushed tile columns used in the strength tests were prepared with uniform density by filling the same volume with the same mass of crushed tile. The cylindrical specimens for UU and UCT tests had a diameter of 38 mm and height of 76 mm, with a density of 3.597 g/cm^3 (Mass = 310 g, Volume = 86.19 cm^3). The kaolinitic clay was admixed with 18.40 % water, which was determined to be the optimum moisture content from the compaction test. Each specimen had a constant mass of 310 g and was compacted in three layers using a customized steel mold with a diameter of 38 mm and height of 76 mm. The mold was designed to compress the kaolin clay into a uniform specimen. The crushed tile column was remoulded to enhance the soil layer and mimic the conditions in the construction section, where soil undulations, tilt, and uneven subsidence can occur due to liquefaction of underlying soil layers.

Table 2. Type of Test in accordance to the standard

Material	Tests	Standard/ Method
Kaolin	Atterberg Limit	ASTM D4318-17
	Sieve Analysis	BS 1377: Part 5: 1990
	Compaction	ASTM D4253-16
	Specific Gravity	ASTM D854-14
	Permeability - Falling Head	ASTM D 2434
Crushed Tile	Sieve Analysis	BS 1377: Part 5: 1990
	Specific Gravity	ASTM D854-14
	Compaction	ASTM D4253-16
	Permeability - Constant Head	BS 1377: Part 5: 1990
Crushed Tile Reinforced Kaolin	Unconfined Compression	ASTM D 2166
	Unconsolidated Undrained Triaxial	BS 1377: Part 7: 1990

The process for reinforcing the kaolinitic clay samples with crushed tile columns followed the same procedure as the unreinforced sample, including mixing the kaolin clay and compacting it in three layers with free-fall blows using a customized steel hammer. Before removing the samples from the mold, holes were drilled with diameters of either 6 mm or 8 mm to prevent the specimens being extruded out of the mold. The crushed tile column was inserted into the pre-drilled hole to maintain a uniform density in all the crushed tile. The mass used to fill the hole was based on the volume of the pre-drilled hole. After the crushed tile installation, the specimens were taken out for the Unconfined Compression Test (UCT). The kaolin specimens were arranged with a single diameter of 6 mm or 8 mm and heights of 25.33 mm, 38 mm, and 76 mm, as shown in Fig. 1.

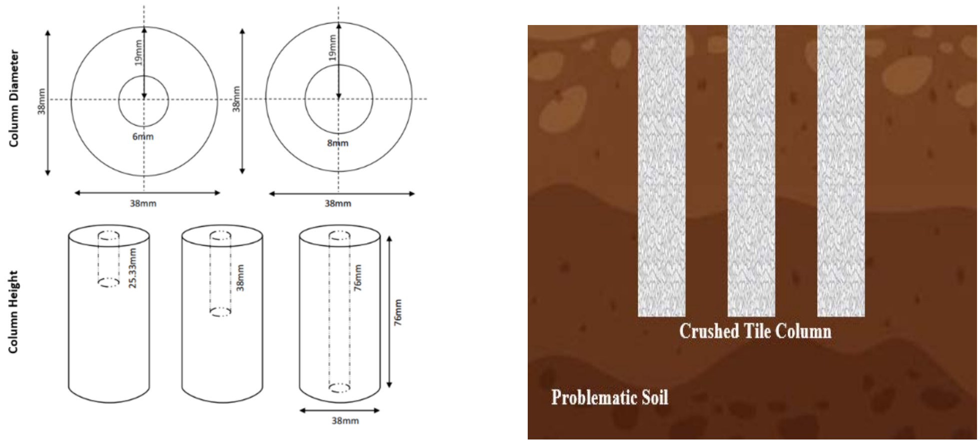

(a) (b)

Figure 1. Variation of crushed tile column dimension and arrangement; a) Lab scale; b) On-site Application.

To prevent excessive bulging of the crushed tile column, a geotextile was used to encapsulate it. The geotextile was sewn into a cylinder shape to fit the diameter of the borehole and carefully placed inside it [14, 20]. Based on multiple pilot test results, the raining method was concluded to be the most effective technique for producing homogeneous crushed tile columns in kaolinitic clay specimens by the researchers.

2.3. Samples Testing

The laboratory tests were carried out on the kaolinitic clay, and crushed tile waste. The samples were tested for basic geotechnical properties (i.e. specific gravity, Atterberg limit and compaction), unconfined compressive strength and unconsolidated undrained. Three replicates were used for each test for basic engineering properties, unconsolidated undrained and five replicates for unconfined compression test.

2.3.1. Specific Gravity

The specific gravity of the kaolinitic clay soil samples was determined with the small pycnometer method. For the kaolinitic soil, the pycnometer was filled to the brim with distilled water and the mass of the pycnometer filled with water was also measured. From these measurements, the specific gravity of the kaolinitic clay specimen was calculated. The same procedure was repeated for crushed tile samples to determine their specific gravity. Specific gravity is an important property to determine the soil-water content, soil-air content, and soil particle density.

After weighing the mould with the material, the material was transferred into a gas jar, which was then filled with distilled water until the water level reached the overflow spout. The volume of the water displaced by the material was measured and recorded. The relative density of the material was calculated as the ratio of the mass of the material to the mass of an equal volume of water. The gas jar method is commonly used for coarse-grained materials with particle sizes between 0.6 mm and 2.36 mm.

2.3.2. Atterberg Limit

The Atterberg limit of a sample was determined through the cone penetration method. The liquid limit will be first determined, followed by the determination of the plastic limit. Then, the plasticity index was calculated.

2.3.3. Standard Proctor Test

Standard Proctor Compaction Test was adopted in this study. The correlation of dry density of soil and moisture content obtained from the compaction test is plotted in a graph to determine the Optimum Moisture Content (OMC) and Maximum Dry Density (MDD). The MDD is achieved at OMC.

2.3.4. Particle Size Distribution (PSD) Test

The distribution of coarse-grained soil is determined by the application of sieve analysis. The test sieves used were with the size 5.00 mm, 3.35 mm, 1.18 mm, 600 µm, 300 µm, 150 µm and 63 µm. The sieves were stacked up together with the largest opening size at the top and the pan under the smallest opening of sieves at the bottom. The sieving process was done by using a mechanical shaker and the proportions of soil left on each sieve were measured using the mass balance. A distribution curve was then plotted with the percentage of particles retained on each sieve. The sieve analysis can be carried out in either wet or dry conditions. In this research, the dry sieve analysis was selected.

2.3.5. Permeability Test

The permeability test was conducted using a constant head permeameter. The test involved applying a constant head of water on a compacted soil sample, measuring the volume of water passing through the sample and calculating the hydraulic conductivity or permeability of the soil. The test was carried out on both kaolin clay and crushed tile specimens at their respective OMC and MDD values to determine their permeability characteristics. The permeability coefficient or hydraulic conductivity of the soil was calculated using Darcy's law.

The falling head test was utilized to determine the coefficient of permeability of kaolin clay. In this test, the sample was placed in a permeameter with a diameter of 8.2 cm and a height of 10 cm. A manometer tube was connected to the permeameter to measure the head of water above the sample. The water was flowed through the sample by gravity, and the time taken for the water level in the manometer tube to fall a certain distance was recorded. The coefficient of permeability was calculated using Darcy's Law, which relates the flow of water to the hydraulic gradient and the properties of the soil.

2.3.6. Unconfined Compression Test (UCT)

Unconfined Compression Test (UCT) was conducted to obtain the unconfined compressive strength of the cohesive soils. This test is the simplest laboratory testing in determining the soil strength by imposing the axial load without lateral confining pressures.

2.3.7. Unconsolidated Undrained (UU) Triaxial Test

The strength parameters of kaolinitic clay enhanced with single enveloped crushed tile columns were determined through the 2.3.7 Unconsolidated Undrained (UU) Triaxial Test. A testing program was designed for UU triaxial tests of both kaolinitic clay and kaolinitic clay enhanced with enveloped crushed tile columns. A total of 21 specimens with varying area replacement ratios were tested. Table 3 shows the coding used for each sample and the corresponding testing program. In order to calculate the strength of kaolinitic enhanced with enveloped crushed tile columns, a confining pressure of 70, 140, and 280 kPa was applied to the sample via the chamber fluid until a 20 % strain was attained. The equipment was then carefully dismantled after the sample was removed.

2.3.8. Statistical Analysis

In this study, numerical analyses were conducted using Microsoft Excel 2010, and linear correlation analysis was utilized to assess the relationships between the independent and dependent variables. Error bars were incorporated to indicate statistically significant differences among the sample results.

3. Results and Discussion

3.1. Specific Gravity

The specific gravity of kaolinitic clay and crushed tile was determined using a small pycnometer. The specific gravity of kaolin was found to be 2.62, falling within the particle density range of most soils, which typically have specific gravities between 2.60 and 2.80 [12, 14, 17]. This suggests that kaolinite, with a reported specific gravity of 2.60, is likely a constituent mineral of kaolin. The specific gravity of crushed tile was measured as 2.57, which differs from the findings reported by Parminder et al. [21] and Yiosese et al., [22] who reported values of 2.24. These findings indicate that crushed tile has a lower apparent specific gravity than sand. Zaini et al. [23] attributed the low specific gravity of crushed tile to its high carbon content, as opposed to high iron content which would produce a high specific gravity. The specific gravity of crushed tile is a crucial factor in determining its quality. Yue et al. [24] have shown in their studies that a specific gravity value below 1.6 indicates poor material quality, which could be due to the presence of a high percentage of pore texture. Table 3 highlights the specific gravity of kaolinitic clay and crushed tile waste in comparison with the other researchers.

Table 3. Specific gravity of kaolinitic clay and crushed tile waste.

Researcher	Specific Gravity	
	Kaolinitic Clay	Crushed Tile Wase
Hasan et al., [7]	2.64	–
Zaini et al., [12]	2.64	–
Zaini et al., [14]	2.62	–
Parminder et al. [21]	–	2.24
Yiosese et al. [22]	–	2.24

3.2. Atterberg Limits

To enhance the condition of clay soil, adjustments to its moisture content can be made. The Atterberg Limit test was performed on kaolin to quantify the water required to attain its liquid limit (wL) and plastic limit (wp). The liquid limit graph was used to obtain the water content corresponding to a cone penetration of 20 mm, which was found to be 41.3 % for kaolin. The graph depicting penetration versus water content is presented in Fig. 2(a). The plastic limit of kaolinitic clay was 31.25 %, which is higher than that of crushed tile at 25.64 %. The plasticity index was calculated as the difference between the plastic limit and liquid limit, and for kaolin, it was 10.05 %, while for crushed tile, it was only 4.09 %. Classification of the soil was often based on the plasticity chart, as shown in Fig. 2(b), where the liquid limit was plotted as an ordinate versus the plasticity index. Based on this chart, kaolin was found to exhibit low plasticity characteristics, and the medium plasticity of kaolin and crushed tile was demonstrated in the figure. Therefore, kaolin can be classified as having low plasticity and is designated as ML.

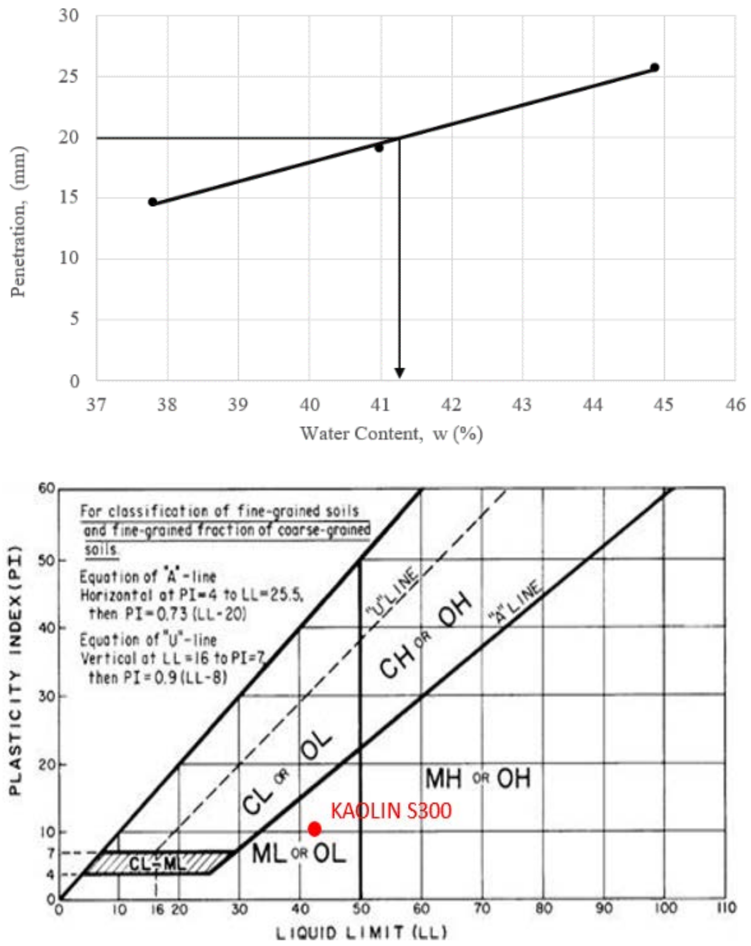

a)
b)

Figure 2. Atterberg limits of Kaolinitic specimen; a) liquid limit of kaolinitic clay and; b) classification of kaolinitic clay based on plasticity chart.

3.3. Standard Proctor Compaction

The relationships between the dry density and water content of kaolin and crushed tile were presented in Fig. 3(a) and Fig. 3(b), respectively. The MDD of kaolin and crushed tile was found to be 1.55 Mg/m^3 (15.20 kN/m^3) and 1.30 Mg/m^3 (12.75 kN/m^3), respectively, at an optimum moisture (w_{opt}) content of 18.0 % and 10.00 %. It is worth noting that kaolin exhibited a higher moisture content than crushed tile due to its high-water content and plasticity. Cabalar et al., [26] reported that when ceramic tile waste (crushed tile) was mixed with clay at a ratio of 30 %, the maximum dry density and optimum moisture content were found to be 1.88 Mg/m^3 (18.45 kN/m^3) and 12.73 %, respectively. This increase was attributed to the replacement of soil grains with higher specific gravity with waste ceramic tile grains having a relatively low specific gravity. Rezaei-Hosseinabadi et al., [27] and Rezaei-Hosseinabadi et al., [28] reported that low specific gravity and high air space content can significantly affect compaction characteristics. Furthermore, the low density of crushed tile makes it suitable for use in construction on low-bearing capacity foundations such as soft soils.

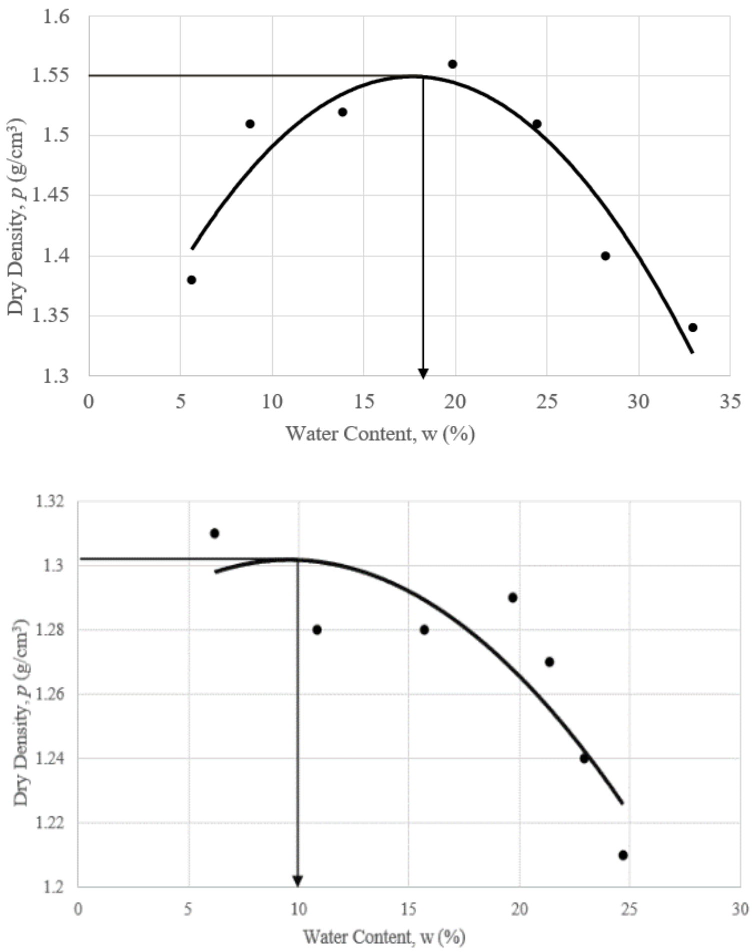

a)

b)

Figure 3. MDD and OMC of; a) Kaolinitic sample and; b) Crushed tile sample.

3.4. Morphology Analysis

A sieve was utilized to perform a sieve analysis of kaolin and crushed tile, and the resulting particle size distribution is presented in Fig. 4. The graph exhibits a well-graded distribution of kaolin particles, ranging from clay to fine silt. The kaolinitic clay particles were observed to have sizes ranging between 0.2 mm and 0.01 mm. Based on the American Association of State Highway and Transportation Officials (AASHTO) classification system, the kaolinitic clay sample was categorized as a clayey soil, belonging to Group A-7-6. Particle size analyses were conducted on crushed tile using the dry sieving method and sieve analysis. Majority of crushed tile particles were found to have sizes ranging between 10 mm and 0.063 mm, corresponding to fine gravel to fine sand sizes, and the size distribution was relatively well graded. The average coefficient of uniformity, Cu, for crushed tile was 60, and the average coefficient of curvature, Cc, was 2.67. Crushed tile with a Cu greater than 4 and Cc between 1 and 3 is classified as well-graded sand (SW) in accordance to the Unified Soil Classification System (USCS). In AASHTO, the soil classification of crushed tile falls under the A-1-A group, which corresponds to sand soil.

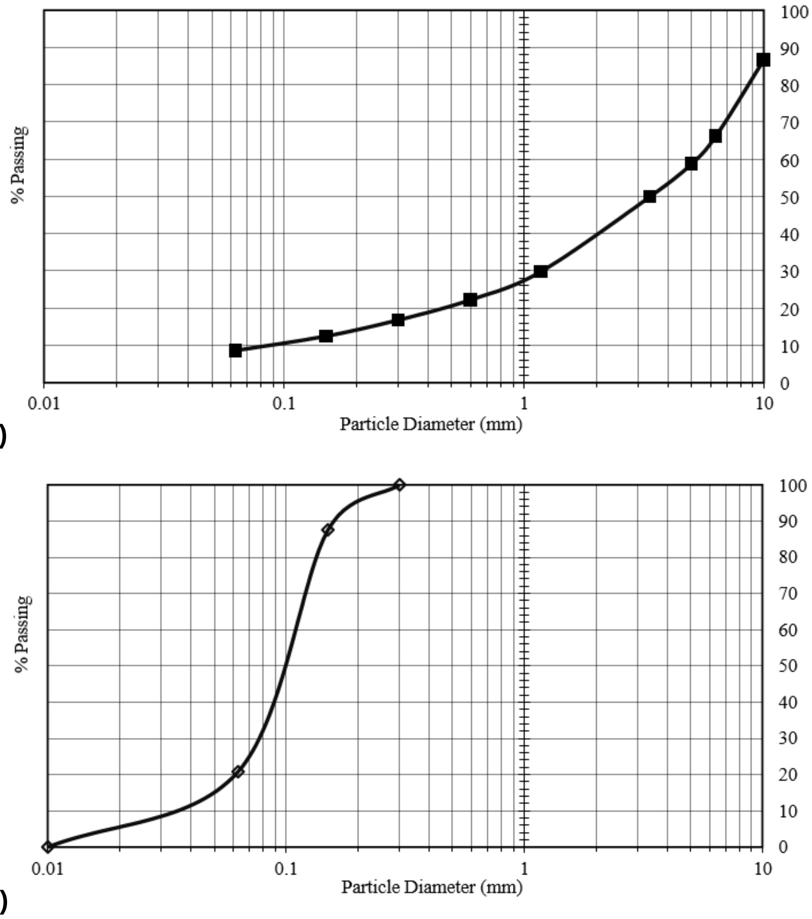

a)

b)

Figure 4. Particle size distribution of; a) Kaolinitic sample; b) Crushed tile sample.

3.5. Permeability

The coefficients of permeability for kaolinitic clay and crushed tile were determined using the constant head and falling head tests, and were found to be 2.61×10^{-8} m/s and 5.11×10^{-3} m/s, respectively. The obtained permeability coefficient for kaolin was considerably lower compared to that of crushed tile. The impermeable nature of fine-grained clay soil, including kaolin, is well documented in literature, which is often attributed to their insufficient drainage feature [14].

This study found that the coefficient values of permeability for crushed tile indicate a relatively high level of permeability, which is similar to soils that possess good drainage characteristics, such as clean sand. This high permeability is attributed to the higher maximum dry density obtained in this study. In comparison to Zaini and Hasan [12], the coefficient of permeability in this study is significantly higher, at 5.11×10^{-3} m/s at a dry density of 1.34 g/cm^3. The high fine particle content of crushed tile has a significant effect on permeability, causing the value to reduces as the smaller particle content increases.

3.6. Unconfined Compressive Strength

Table 4 provides a summary of the results of the Unconfined Compression Test (UCT) for the control sample and samples reinforced with 6 mm and 8 mm diameter single crushed tile columns at various column penetration ratios. The shear strengths were determined for area replacement ratios (CARR) of 15.79 % and 21.05 %, as well as height penetration ratios (CHPR) of 0, 0.33, 0.5, and 1.0. The shear strengths were 5.23 kPa, 6.79 kPa, 6.78 kPa, and 7.95 kPa for 6 mm and 8 mm diameter single crushed tile columns with 15.79 % of CARR and CHPR of 0, 0.33, 0.5, and 1.0. For the 21.05 % of CARR, the corresponding shear strengths were 5.23 kPa, 6.63 kPa, 6.75 kPa, and 7.18 kPa, respectively. In addition, the improvement in shear strength for 6 mm column diameter and a CARR of 21.05 % was 29.83 %, 29.64 %, and 52.00 %, while for 8 mm column diameter, the corresponding values were 26.76 %, 29.06 %, and 37.28 %.

The improvement in shear strength of specimens reinforced with crushed tile columns was analyzed and it was found that the improvement in shear strength was greater for 6 mm diameter specimens than for 8 mm diameter specimens. The reason for this is that the area replacement ratio of 8 mm diameter crushed tile columns is greater, which leads to vertical forces being applied to the columns and the columns bulging due to insufficient support from the remaining width of the specimen. This trend is consistent with the findings of previous researchers carried out by Zaini & Hasan [14] and Frikha et al., [29], who also reported that the decrease in shear strength improvement is due to the less confining stress in larger columns.

Table 4. Percentage of improvement shear strength of sample reinforced with crushed tile column.

Sample	Column Dia. (mm)	Column Height (mm)	CARR (%)	CHPR (%)	CVRR (%)	CHR-CDR (%)	UCS (kN/m^2)	AAS (%)	ASS (kN/m^2)	ISS (%)
K	–	–	–	–	–	–	10.46	6.88	5.23	0.00
K-CT6DH1	6	25.33	15.79	0.33	0.008	4.22	13.58	5.56	6.79	29.83
K-CT6DH2	6	38.00	15.79	0.5	0.012	6.33	13.56	5.58	6.78	29.64
K-CT6DH3	6	76.00	15.79	1.0	0.025	12.67	15.89	5.59	7.95	52.00
K-CT8DH1	8	25.33	21.05	0.33	0.015	3.17	13.25	5.57	6.63	26.76
K-CT8DH2	8	38.00	21.05	0.5	0.022	4.75	13.50	6.03	6.75	29.06
K-CT8DH3	8	76.00	21.05	1.0	0.044	9.50	14.36	6.67	7.18	37.28

Note: K, controlled sample; K-CT6D, single encapsulated with column diameter of 6mm and H1, H2, H3, Column Height of 25.33, 38.00 and 76.00, respectively, CARR, Column Area Replacement Ratio, CHPR, Column Height Penetration Ratio, CVRR, Column Volume Replacement Ratio, CHR-CDR, Column Height to Column Diameter Ratio, UCS, Unconfined Compressive Strength, AAS, Average Axial Strain, ASS, Average Shear Strength, ISS, Improvement of Shear Strength

3.7. Kaolinitic Clay Improvement due to the Column Area Replacement Ratio (CARR)

The research investigated the influence of CARR on the shear strength of kaolinitic clays. The study presented the interconnection between CARR and alterations in the strength of kaolinitic clay in Fig. 5. The results indicated a substantial improvement in shear strength when kaolinitic clay specimens were reinforced with enveloped crushed tile columns at various CARRR ranging from 15.79 % to 21.05 %. The shear strength increased from 10.46 kPa for the control sample to the maximum improvement of 15.89 kPa. Moreover, the ASS of a single enveloped crushed tile column with an CARR of 15.79 % applicable for K-CT6DH1, K-CT6DH2, and K-CT6DH3 was slightly greater than that of a single encapsulated crushed tile using 8 mm diameter column (CARR = 21.02 %) resulted in K-CT8DH1, K-CT8DH2, and K-CT8DH3.

Additionally, the use of single enveloped crushed tile columns with 6 mm column diameter resulted in higher ASS of kaolinitic clay compared to a single encapsulated crushed tile column with 8 mm column diameter. The study also found that the CARR substantially modify the strength improvement of kaolinitic clay, which is consistent with the findings of previous studies by Rezaei-Hosseinabadi et al. [27], and Rezaei-Hosseinabadi et al. [28]. The decline in the strength observed when the pillar was fully penetrated due to the significant portion of the soil was extracted from the specimen, disrupting the original condition of the soil.

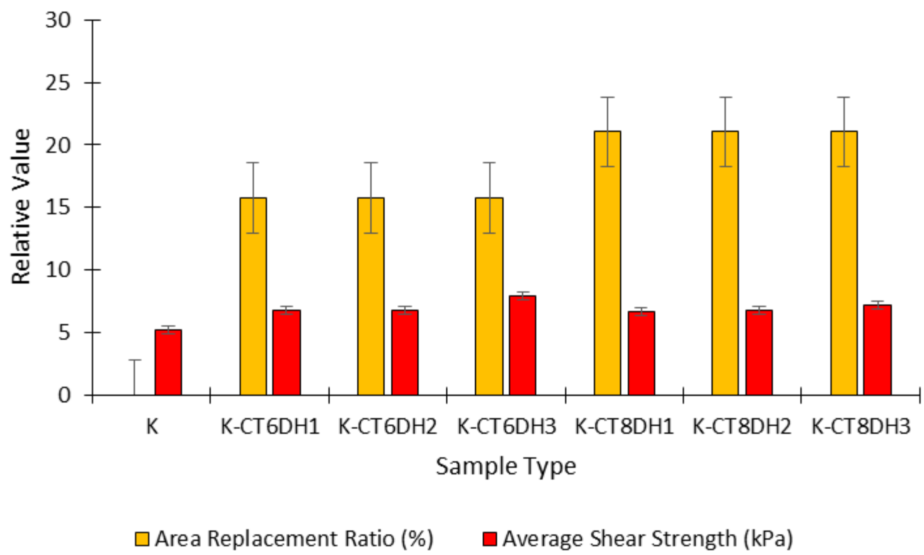

Figure 5. Relationship between the CARR with the ASS.

3.8. Kaolinitic Clay Improvement due to the Column Height Penetrating Ratio (CHPR)

This study investigated the effect of penetration height ratio (CHPR) on the average shear strength (ASS) of 6 mm and 8 mm diameter crushed tile columns, as depicted in Fig. 6. The results showed that increasing the CHPR led to a higher shear strength. However, the maximum shear strength values for a single column were determined to be 7.95 kPa for a 6 mm diameter and 7.18 kPa for an 8 mm diameter at a CHPR of 1.0. Furthermore, the study revealed that increasing the CHPR to 1.0 resulted in a 52.00 % increase in shear strength for a 6 mm diameter column, while the maximum increase in shear strength for an 8 mm diameter column occurred at a CHPR of 1.0 with a value of 37.28 %. Based on these findings, the critical CHPR was set to 1.0. Moreover, complete penetration occurs when the height penetration ratio of a crushed tile column is 1.0, meaning that the column will fully support the load when subjected to force. Conversely, height penetration ratios of 0.33 and 0.5 indicate partially penetrated columns. In such cases, the single crushed tile column supports the entire load, while the surrounding soil supports the remaining portion.

The increase in length of the crushed tile columns led to an increase in shear strength, as evidenced by the results. The highest increase in shear strength was observed when the CHPR was 1.0. Therefore, it can be inferred that the greater the CHPR compared to the column height, the greater the improvement in shear strength. Furthermore, the load-carrying capacity also increased when the CHPR was 1.0. However, it should be noted that the increment in shear strength was not solely attributable to the CHPR of single crushed tile columns. The percentage rise in shear strength was considered significant because the substitution of some of the soft clay with stiffer material, such as crushed tile, led to an increase in the CHPR of single crushed tile columns.

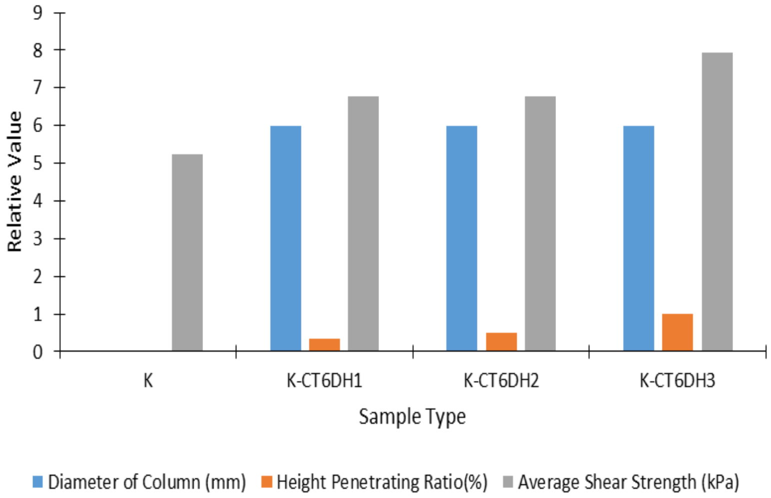

a)

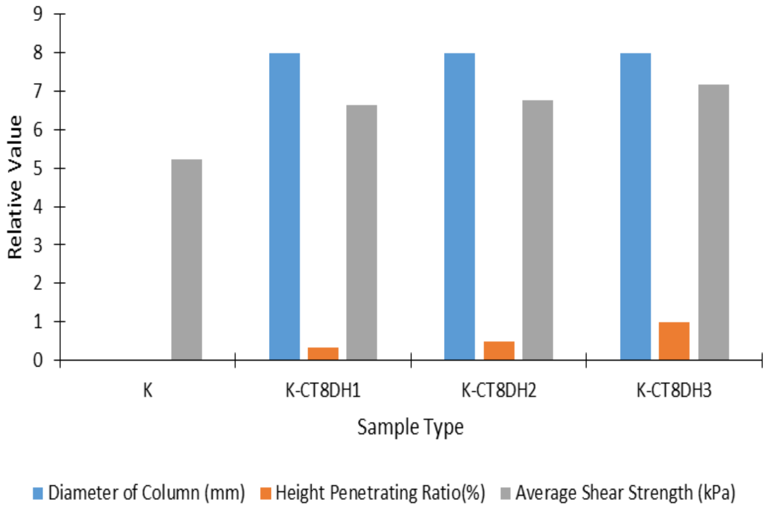

b)

Figure 6. Relationship between the CHPR with ASS; a) 6mm diameter column; b) 8mm diameter column.

3.9. Kaolinitic Clay Improvement due to the Column Height to Column Diameter Ratio (CHR-CDR)

Fig. 7 depict the variation of average shear strength (ASS) with respect to the height to column diameter ratio (CHR-CDR) for 6 mm and 8 mm crushed tile columns. It was observed that the shear strength increased as the CHR-CDR increased for both column diameters. For a 6 mm diameter column, the maximum shear strength of 7.95 kPa was achieved at a CHR-CDR of 12.67, which was a 52.00 % improvement over the other ratios tested (0.33 and 0.5). Similarly, for an 8 mm diameter column, the highest shear strength of 7.18 kPa was obtained at a CHR-CDR of 9.50, resulting in a 37.28 % improvement over the other ratios tested.

Changes in the column height and diameter resulted in variations of the CHR-CDR value, which was found to affect the shear strength of reinforced kaolinitic clay. Morever, the relationship between CHR-CDR and shear strength was not strictly linear due to the interconnections between CHR-CDR and various column dimensions. Fig. 7 illustrates that the maximum shear strength occurred at a CHR-CDR value of 1.0. Further increases in CHR-CDR value led to a reduction in the strength of the sample.

The findings of this study were consistent with previous research conducted by Zaini & Hasan [14], Rezaei-Hosseinabadi et al. [27], in demonstrating that the maximum improvement in shear strength occurred at the critical column length. According to Hasan et al. [7], the application of crushed tile columns for ground improvement had an influence on the level of strength enhancement in kaolinitic clay. The improvement in shear strength was attributed to the enhanced interlocking between the soil and the granules through the geotextile's surface adhesive, which improved the interface's shear properties.

While an increase in shear strength is observed, it is important to note that the improvement is not solely dependent on the CHR-CDR value of encapsulated crushed tile columns. Furthermore, the use of fully penetrating columns with a larger diameter was found to have a negative impact on the shear strength of the soil. This was attributed to a larger portions of soil being substitute by crushed tile particles, which disturbs the original state of the soil and weakens the structure and bonding between particles, resulting in a reduction in shear strength.

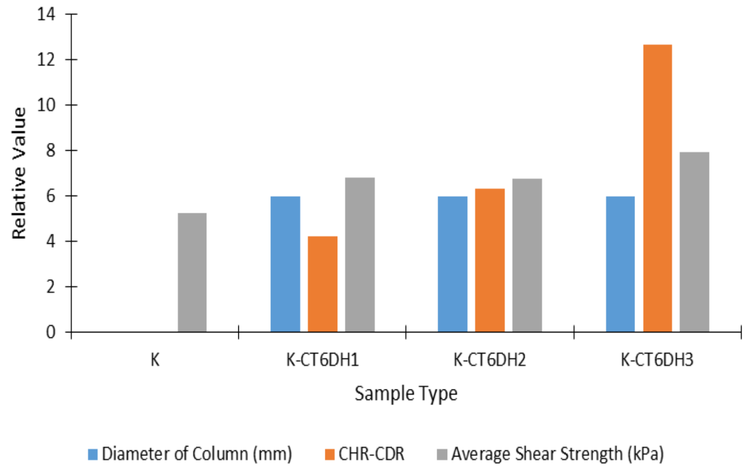

a)

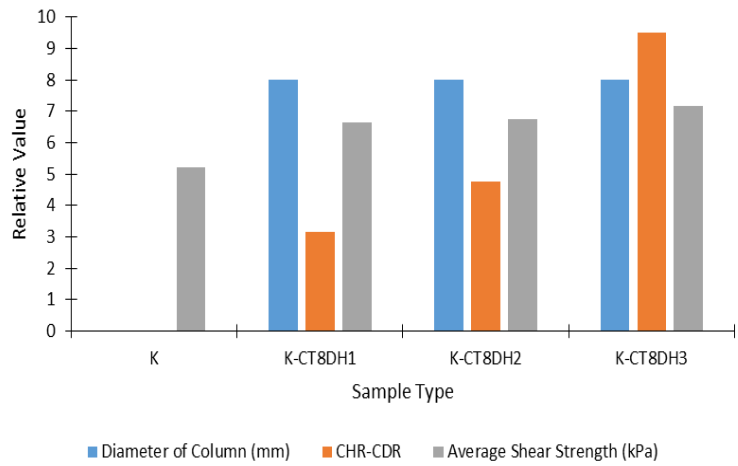

b)

Figure 7. Relationship between the CHR-CDR with ASS; a) 6mm diameter column; b) 8mm diameter column.

3.10. Kaolinitic Clay Improvement due to the Column Volume Replacement Ratio (CVRR)

Fig. 8 presents the average shear strength (ASS) versus volume replacement ratio (CVRR), which illustrates a substantial increase in the undrained shear strength of a kaolinitic specimen owing to the installation of a crushed tile column. Furthermore, Fig. 8 depicts the improvement in shear strength as a function of CVRR for 6 mm and 8 mm crushed tile columns. The results indicate that the highest shear strength is obtained at a CVRR of 0.025, with a value of 7.95 kPa and an increase of up to 52.00 % over the control sample. Similarly, for a crushed tile column with a diameter of 8 mm, the greatest improvement in shear strength occurs at a CVRR of 0.044, with the improvement in 6 mm diameter samples was found to be more pronounced than that of 8 mm diameter samples due to the minimal disturbance caused by drilling and extraction of a small quantity of kaolin from the specimens, as well as the higher confining stresses mobilized by the column. On the other hand, a substantial portion of the soil was extracted during the installation of an 8 mm diameter crushed tile column, leading to a smaller increase in shear strength. Additionally, the absence of confining pressure during the test caused a greater tendency for soil collapse.

The current study aligns with the findings of Hui-Teng et al. [7] and Zaini and Hasan [12] regarding the maximum shear strength improvement investigated in the study. The improvement in strength was attributed to the low value of the CARR, which has an effect on the area around the column. The interlocking and bonding between particles in the area were stronger because the kaolinitic clay was underpinned by the enveloped crushed tile column.

The stiffness of a column with smaller width increases with larger confining stresses. When subjected to a vertical load, the width of the sample that is left between the columns becomes too narrow to support the columns, leading to deformation or bulging. The friction, particle interconnection, and contact linkage between particles affect the shear resistance of soil. Under bending pressures, the volume of soil particles may swell or shrink due to interlocking. If the soil swells, the particle density reduces, resulting in a decrease in resistance, which leads to a reduction in maximum resistance as the shear stress reduces.

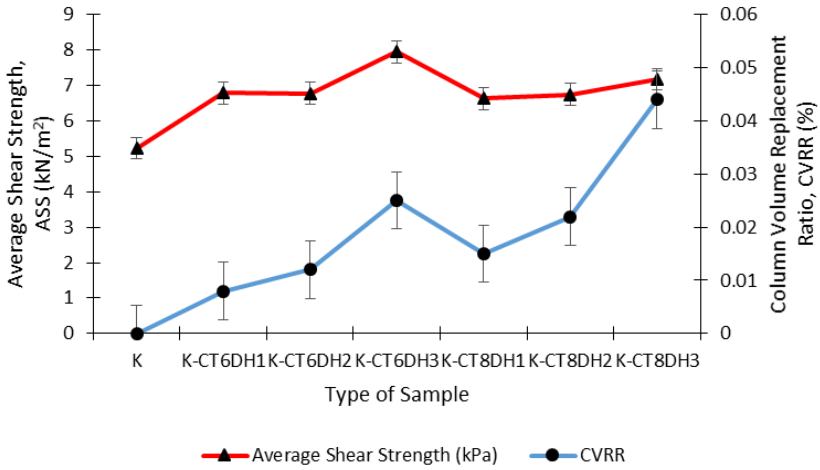

Figure 8. Relationship between the CVRR with ASS.

3.11. Shear Strength Parameters

The study involved conducting Unconsolidated Undrained (UU) tests to evaluate the shear strength of kaolinitic clay reinforced with single enveloped crushed tile columns. Samples of different penetration were examined, each subjected to varying confining pressures of 70 kPa, 140 kPa, and 280 kPa. The aim was to investigate the effective shear stress parameters for the kaolinitic column reinforced with various diameters of the crushed tile column at different values of CARR, CHPR, CHR-CDR, CVRR, cohesion, and friction angle, as presented in Table 3. The results revealed that the kaolinitic clay reinforced with enveloped crushed tile column exhibited a higher effective cohesion than the raw kaolinitic soil sample. In contrast, the effective friction angles showed minimal improvement since the difference from the raw kaolinitic clay was relatively similar. In general, the study demonstrated that reinforcing soft clay with encapsulated crushed tile column leads to noticeable improvements. The cohesion values for the kaolinitic clay and the altered samples with enveloped crushed tile columns were investigated. The cohesion for the kaolinitic clay was found to be 14.1 kPa. For the single column with a diameter of 6 mm and column heights of 25.33 mm, 38.00 mm, and 76.00 mm, the cohesion values were found to be 15.5 kPa, 25.3 kPa, and 14.7 kPa, respectively. Meanwhile, for the single column with a diameter of 8 mm, the cohesion values were 21.9 kPa, 26.3 kPa, and 22.4 kPa for the same column heights.

The highest cohesion value recorded in the study was 26.3 kPa for the K-CT8H2 sample, while the lowest value was 14.7 kPa for the K-CT6H3 sample. The ideal cohesion value for encapsulated crushed tile columns alone was discovered to be at a CHPR of 1.0. The data presented in Table 3 revealed that augmenting the confining pressure led to an enhancement in the cohesion value of the reinforced specimens in comparison to the control specimen. The research identified notable variations in the cohesion values of the reinforced specimens as opposed to the control specimen, signifying a rise in the cohesion value subsequent to the installation of the crushed tile column.

Cohesion is the internal molecular attraction that holds soil particles together and is a measure of the soil's resistance to deformation. A higher cohesion value indicates a stronger adhesive force between soil particles [29, 30]. According to Rezaie et al. [27, 28], the cohesion value significantly increases when the samples are reinforced with sand columns. According to the results obtained in this study, it is clear that the use of crushed tile columns with different diameters can enhance the cohesion value of the samples up to 26.3 kPa.

According to Table 5, the friction angle (φ) of the kaolinitic clay was 23.8°. For single encapsulated crushed tile columns with a 6 mm diameter and column heights of 25.33 mm, 36.00 mm, and 76.00 mm, the friction angles were recorded at 26.4°, 25.9°, 28.4°, respectively. With a column diameter of 8 mm with the same column heights as the 6 mm diameter column, the friction angles were recorded at 2°, 27.3°, 26.9° for the single encapsulated crushed tile columns. The K-CT6H3 sample exhibited the highest friction angle of 28.4°, whereas the K-CT6H2 sample had the lowest friction angle of 25.0°, according to the recorded data.

The study found that the ideal friction angle, which corresponds to the maximum strength improvement, was recorded at 27.3°. Although there was an increase in the friction angle with the installation of the crushed tile column, it was not significantly different from the friction angle of the control sample. The friction angle is a measure of the resistance of a soil to sliding and is defined as the angle between the Mohr-Coulomb failure envelope and the horizontal axis. Higher stresses lead to a higher friction angle. The granule size was reported to affect the behavior of the reinforced clayey soil, including its stiffness, friction angle, and shear strength characteristics, according to previous research [27]. In this investigation, the introduction of crushed tile columns with varying dimensions lead to an increase in both the shear stress and effective shear stress, thereby influencing the friction angle.

Table 5. Value of shear strength parameters.

Cell Pressure (kPa)	Column Dia. (mm)	Column Height (mm)	CARR	CHPR	CHR-CDR	CVRR	c (kPa)	Φ (°)
70 140 280	0	0	0	0	0	0	14.1	23.8
70 140 280	6	25.33	15.79	0.33	4.22	0.008	15.5	26.4
70 140 280	6	38.00	15.79	0.5	6.33	0.012	25.3	25.9
70 140 280	6	76.00	15.79	1.0	12.67	0.025	14.7	28.4
70 140 280	8	25.33	21.05	0.33	3.17	0.015	21.9	27.8
70 140 280	8	38.00	21.05	0.5	4.75	0.022	26.3	27.3
70 140 280	8	76.00	21.05	1.0	9.50	0.044	22.4	26.9

3.12. Linear Correlation Coefficient

In this study, correlations between engineering properties such as CARR, CHPR, CHR-CDR, and CVRR of delicate kaolin and varying diameter and height of column were established. These equations are essential in predicting the optimal model for granular column design. The statistical equation that correlate the parameters for the four studied parameters are presented in Table 6.

Based on the correlation equations presented in Table 6, it can be inferred that higher values of coefficient of determination (R^2 value) indicate that the level of variation in the four parameters studied can be predicted by considering the crushed tile as ground improvement granular column. The regression analysis conducted in this study revealed half of the variation in the parameters can be explained by the utilization of crushed tile column. Hence, the established relationship is the ideal model to forecast the optimal dimensions of granular column. The statistical analysis carried out in this study does not match a previous study due to the use of other alternative to obtain the R^2 value. However, both studies come to the same conclusion that the best design can be achieved by comparing a set of targeted models.

Table 6. Correlation coefficient of parameters studied.

Parameter	Correlation	Column Dia. (mm)	Linear Equation	R^2 Value
CARR	Shear Strength, S_u (kN/m^2)	6	S_u = 0.1231 CARR + 5.23	0.7579
		8	S_u = 0.0771 CARR + 5.23	0.9220
CHPR		6	S_u = 2.5736 CHPR + 5.5101	0.9245
		8	S_u = 1.8095 CHPR + 5.6197	0.7968
CHR-CDR		6	S_u = 0.2035 CHR-CDR + 5.5063	0.9264
		8	S_u = 0.1910 CHR-CDR + 5.6159	0.7994
CVRR		6	S_u = 102.5 CVRR + 5.5344	0.9186
		8	S_u = 41.426 CVRR + 5.6086	0.8043

4. Conclusions

This study examined the effects of crushed tile waste on the lateral load capacity of kaolinitic clay. Based on the outcome of the investigation, the following summary can be drawn:

1. According to the USCS, kaolinitic clay can be categorized as ML which is clayey silts with slight plastic. Kaolin was a clay with a low plasticity index, with a liquid limit of 41.30 % and a plasticity index of 10.05 %. Based on AASHTO, kaolinitic clay is classified as clay soil type A-7-6. Furthermore, the crushed tile is classified as SW, which means that it was well graded with a liquid limit of 29.73 % and a plasticity index of 4.09 %, indicating low plasticity. According to the AASTHO classification system, crushed tile is classified as A-1-a, which includes stone fragments, gravel, and sand.

2. Furthermore, the specific gravity of kaolinitic clay was found to be 2.62 and the specific gravity of the crushed tile waste was determined to be 2.57.

3. In addition, kaolinitic clay has a maximum dry density of 1.55 kg/m^3 and an optimal moisture content of 18.00 %. The crushed tile had a maximum dry density of 1.30 kg/m^3 and a moisture content of 10 %.

4. The shear strength of a column depends on the CHPR. A maximum increase in shear strength was observed when the CHPR was at 1.0, and a decrease in shear strength was observed when the column height decreased. When the CHPR was less than 1.0, the load-carrying capacity decreased. The increase in shear strength investigated in the study was not solely owing to the CHPR but also because of the substitution of stiffer material, such as crushed tile, for some of the soft clay. The maximum shear strength was achieved at a CHR-CDR of 12.67 for a column diameter of 6 mm and CHR-CDR of 9.5 for a column diameter of 8 mm.

5. Apart from the influence of crushed tile columns on the strength parameters of clay reinforcement, the confining pressure is also an important factor in determining the strength and compressibility of kaolinitic clay. Insufficient dispersion of excess pore water from the clay specimens was observed due to clogging phenomena between the clay and the crushed tile columns. The results of the experiments conducted in this study have provided evidence that the introduction of enveloped crushed tile columns can cause a change in the cohesion (c) and friction angle (ϕ) of kaolin clay samples from their original values of 14.1 kPa and 23.8°, respectively. The highest improvement was observed in the single enveloped crushed tile

column with 8 mm column diameter, where the cohesion increased up to 26.3 kPa and the friction angle increased up to 27.3°.

The study, therefore, concludes that the used of crushed tile waste firmly influenced the lateral load capacity of kaolinitic clay as an ideal ground improvement. In this study, it was found that the utilization of crushed tile as granular column was effective in improving the strength of kaolinitic clay soils. The strength improvement was up to 52.00 %, and the optimum enhancement was achieved with a utilization of crushed tile with a column diameter of 6 mm and column height of 76 mm. The correlation analysis showed that the level of variation in the four parameters studied (CARR, CHPR, CHR-CDR and CVRR) could be predicted by considering the crushed tile as granular material for ground improvement technique, with a higher coefficient of determination (R^2 value) indicating better predictability. This approach can lead to cost savings and promote the use of eco-friendly materials in soil improvement. Therefore, this particular study showed that the 6 mm column diameter and 76 mm column height of the crushed tile should be recommended as the most ideal column dimensions that can be used by practitioners to enhance the strength of kaolinitic clay for construction application. The technique of ground improvement by crushed tile waste is vital to improve the strength of weak soils especially clay during construction such as deep and shallow foundations. Ground improvement with crushed tile waste is now a very economical way of transforming weak soil into a suitable soil for construction purposes. Using this method, it is possible to construct infrastructure and buildings on soil with low specific gravity and high air void content, which would typically require expensive soil stabilization techniques. The use of granular columns reduces the need for excavation and replacement of weak soil, allowing significant cost savings and faster construction times.

References

1. Sheikhhosseini Lori, I., Toufigh, M.M., Toufigh, V. Improvement of poorly graded sandy soil by using copper mine tailing dam sediments-based geopolymer and silica fume. Construction and Building Materials. 2021. 281. Article no. 122591. DOI: 10.1016/j.conbuildmat.2021.122591
2. Tonini de Araújo, M., Tonatto Ferrazzo, S., Mansur Chaves, H., Gravina da Rocha, C., Cesar Consoli, N. Mechanical behavior, mineralogy, and microstructure of alkali-activated wastes-based binder for a clayey soil stabilization. Construction and Building Materials. 2023. 362. Article no. 129757. DOI: 10.1016/j.conbuildmat.2022.129757
3. Bagriacik, B. Utilization of alkali-activated construction demolition waste for sandy soil improvement with large-scale laboratory experiments. Construction and Building Materials. 2021. 302. Article no.124173. DOI: 10.1016/j.conbuildmat.2021.124173
4. Yadav, J.S., Tiwari, S.K. A study on the potential utilization of crumb rubber in cement treated soft clay. Journal of Building Engineering. 2017. 9. Pp. 177–191. DOI: 10.1016/j.jobe.2017.01.001
5. Hataf, N., Sayadi, M. Experimental and numerical study on the bearing capacity of soils reinforced using geobags. Journal of Building Engineering. 2018. 15. Pp. 290–297. DOI: 10.1016/j.jobe.2017.11.015
6. Temga, J.P., Madi, A.B., Djakba, S.B., Zame, P.Z. o., Angue, M.A., Mache, J.R., Nguetnkam, J.P., Bitom, L.D. Lime – and sand – stabilization of clayey materials from the Logone valley (Lake Chad basin) for their utilisation as building materials. Journal of Building Engineering. 2018. 19. Pp. 472–479. DOI: 10.1016/j.jobe.2018.06.003
7. Hui-Teng, N., Cheng-Yong, H., Yun-Ming, L., Abdullah, M.M.A.B., Ern Hun, K., Razi, H.M., Yong-Sing, N. Formulation, mechanical properties and phase analysis of fly ash geopolymer with ladle furnace slag replacement. Journal of Materials Research and Technology. 2021. 12. Pp. 1212–1226. DOI: 10.1016/j.jmrt.2021.03.065
8. Sabri, M.M., Shashkin, K.G., Zakharin, E., Ulybin, A.V. Soil stabilization and foundation restoration using an expandable polyurethane resin. Magazine of Civil Engineering. 2018. No. 6. Pp. 68–80. DOI: 10.18720/MCE.82.7
9. Sabri, M.M., Shashkin, K.G. Improvement of the soil deformation modulus using an expandable polyurethane resin. Magazine of Civil Engineering. 2018. No. 7. Pp. 222–234. DOI: 10.18720/MCE.83.20
10. Dudynov, S.V. Influence of biological additives on the properties of cement systems. Magazine of Civil Engineering. 2023. 118 (1). Pp. 11803. DOI: 10.34910/MCE.118.3
11. Bikash Subedi. Utilization of Crushed Ceramic Tile Wastes as Partial Replacement of Coarse Aggregate in Concrete Production. International Journal of Engineering Research and Technology. 2020. 9 (7). Pp. 1572–1584 DOI: 10.17577/ijertv9is070674
12. Zaini, M.S.I., Hasan, M. Effect of Optimum Utilization of Silica Fume and Lime on the Stabilization of Problematic Soils. International Journal of Integrated Engineering. 2023. 15 (1). Pp. 352–366. DOI: 10.30880/ijie.2023.15.01.032
13. Suksiripattanapong, C., Sakdinakorn, R., Tiyasangthong, S., Wonglakorn, N., Phetchuay, C., Tabyang, W. Properties of soft Bangkok clay stabilized with cement and fly ash geopolymer for deep mixing application. Case Studies in Construction Materials. 2022. 16. Article no. e01081. DOI: 10.1016/j.cscm.2022.e01081
14. Zaini, M.S.I., Hasan, M., Zolkepli, M.F. Influence of Alstonia Angustiloba tree water uptake on slope stability: A case study at the unsaturated slope, Pahang, Malaysia. Bulletin of the Geological Society of Malaysia. 2023. 75. Pp. 37–55. DOI: 10.7186/bgsm75202305
15. Hosseinpour, I., Soriano, C., Almeida, M.S.S. A comparative study for the performance of encased granular columns. Journal of Rock Mechanics and Geotechnical Engineering. 2019. 11 (2). Pp. 379–388. DOI: 10.1016/j.jrmge.2018.12.002
16. Zhang, M., Ma, D., He, J., Han, Y. Sulfate corrosion resistance of foundation concrete with nano-particles. Magazine of Civil Engineering. 2023. 119 (3). Article no. 11901. DOI: 10.34910/MCE.119.1
17. Supian, A.B.M., Jawaid, M., Rashid, B., Fouad, H., Saba, N., Dhakal, H.N., Khiari, R. Mechanical and physical performance of date palm/bamboo fibre reinforced epoxy hybrid composites. Journal of Materials Research and Technology. 2021. 15. Pp. 1330–1341. DOI: 10.1016/j.jmrt.2021.08.115
18. Hilal, N., Hadzima-Nyarko, M. Improvement of eco-efficient self-compacting concrete manufacture by recycling high quantity of waste materials. Environmental Science and Pollution Research. 2021. 28. Pp. 53282–53297. DOI: 10.1007/s11356-021-14222-9

19. Zanelli, C., Conte, S., Molinari, C., Soldati, R., Dondi, M. Waste recycling in ceramic tiles: a technological outlook. 2021. 168. Article no. 105289. DOI: 10.1016/j.resconrec.2020.105289
20. Zaini, M.S.I., Hasan, M., Yie, L.S., Masri, K.A., Putra Jaya, R., Hyodo, M., Winter, M.J. Effect of optimum utilization of silica fume and eggshell ash to the engineering properties of expansive soil. Journal of Materials Research and Technology. 2021. 14. Pp. 1401–1418. DOI: 10.1016/j.jmrt.2021.07.023
21. Parminder, S., Rakesh, K.S. Utilization Of Waste Ceramic Tiles As Coarse Aggregate In Concrete. Journal of Multidisciplinary Engineering Science and Technology (JMEST). 2015. 2 (11). Pp. 3294–3300.
22. Yiosese, A.O., Ayoola, A.R., Ugonna, M.C., Adewale, A.K. Partial Replacement of Coarse Aggregate with Broken Ceramic Tiles in Concrete Production. International Journal of Scientific & Engineering Research. 2015. 9 (8). Pp. 81–87.
23. Bollino, F., Giannella, V., Armentani, E., Sepe, R. Mechanical behavior of chemically-treated hemp fibers reinforced composites subjected to moisture absorption. Journal of Materials Research and Technology. 2023. 22. Pp. 762–775. DOI: 10.1016/j.jmrt.2022.11.152
24. Zhang, G., Chen, C., Sun, J., Li, K., Xiao, F., Wang, Y., Chen, M., Huang, J., Wang, X. Mixture optimisation for cement-soil mixtures with embedded GFRP tendons. Journal of Materials Research and Technology. 2022. 18. Pp. 611–628. DOI: 10.1016/j.jmrt.2022.02.076
25. Almada, B.S., da Silva Silveira Melo, H., Duarte, M.S., Aguilar, M.T.P., Garcia, D.C.S., Silva, G.J.B., dos Santos, W.J. Study of mechanical, durability and microstructural properties of cementitious composite with addition of different iron ore tailings from Brazil. Journal of Materials Research and Technology. 2022. 18. Pp. 1947–1962. DOI: 10.1016/j.jmrt.2022.03.070
26. Cabalar, A.F., Hassan, D.I., Abdulnafaa, M.D. Use of waste ceramic tiles for road pavement subgrade. Road Materials and Pavement Design. 2017. 18 (4). Pp. 882–896. DOI: 10.1080/14680629.2016.1194884
27. Rezaei-Hosseinabadi, M.J., Bayat, M., Nadi, B., Rahimi, A. Utilisation of steel slag as a granular column to enhance the lateral load capacity of soil. Geomechanics and Geoengineering. 2022. 17 (5). Pp. 1406–1416. DOI: 10.1080/17486025.2021.1940315
28. Rezaei-Hosseinabadi, M.J., Bayat, M., Nadi, B., Rahimi, A. Sustainable utilisation of steel slag as granular column for ground improvement in geotechnical projects. Case Studies in Construction Materials. 2022. 17. Article no. E01333. DOI: 10.1016/j.cscm.2022.e01333
29. Frikha, W., Bouassida, M., Canou, J. Parametric Study of a Clayey Specimen Reinforced by a Granular Column. International Journal of Geomechanics. 2015. 15 (5). Article no. 04014078. DOI: 10.1061/(asce)gm.1943-5622.0000419
30. Chaiyaput, S., Arwaedo, N., Kingnoi, N., Nghia-Nguyen, T., Ayawanna, J. Effect of curing conditions on the strength of soil cement. Case Studies in Construction Materials. 2022. 16. Article no. e01082. DOI: 10.1016/j.cscm.2022.e01082

Information about authors:

Muhammad Syamsul Imran Zaini, *PhD*
ORCID: https://orcid.org/0000-0002-7028-7129
E-mail: syamsulimran94@gmail.com

Muzamir Hasan, *PhD*
ORCID: https://orcid.org/0000-0002-2700-236X
E-mail: muzamir@ump.edu.my

Khairil Azman Masri, *PhD*
ORCID: https://orcid.org/0000-0003-0046-8669
E-mail: khairilazman@ump.edu.my

Received 15.04.2023. Approved after reviewing 22.08.2023. Accepted 23.08.2023.

Magazine of Civil Engineering. 2023. 123(7). Article No. 12305

Magazine of Civil Engineering

ISSN 2712-8172

journal homepage: http://engstroy.spbstu.ru/

Research article

UDC 691.3

DOI: 10.34910/MCE.123.5

Cementless binder consisting of high-calcium fly ash, silica fume and magnesium chloride

***K. Usanova*[1] ✉, *Yu.G. Barabanshchikov*[1], *S. Dixit* [2, 3, 4]**

[1] *Peter the Great St. Petersburg Polytechnic University, St. Petersburg, Russian Federation*

[2] *Division of Research, Uttaranchal University, Dehradun, India*

[3] *Division of Research and Development, Lovely Professional University, Phagwara, Punjab, India*

[4] *Khalifa University, Abu Dhabi, United Arab Emirates*

✉ *plml@mail.ru*

Keywords: fly ash, microsilica, silica fume, early strength agent, $MgCl_2$, X-ray diffraction analysis, strength, heat release, differential thermal analysis, heat of hydration, phase composition

Abstract. This work aims to study the effect of $MgCl_2$ additive on the strength, heat of hydration, and phase composition of hydration products of the binder consisting of high-calcium fly ash and silica fume. Fly ash from Berezovskaya thermal power plant, containing a lot of CaO_{free}, in combination with silica fume does not expand and exhibits the properties of a binder. However, the strength of this binder is low. The $MgCl_2$ additive significantly increases the hardening rate and the final strength of the mix. The compressive strength of 32×32×32 mm specimens from the paste at the age of 7 days is 15.2 MPa and 3.7 MPa with and without the $MgCl_2$ additive, respectively. Exothermic data show that silica fume inhibits CaO hydration from the first minutes of the reaction to 2 days, after which the process accelerates and proceeds evenly. The total value of the thermal effect for 10 days is 500 kJ per 1 kg of binder. The $MgCl_2$ additive does not increase this final value, however, it accelerates the release of heat in the initial periods, excluding the indicated stagnation period. The results of XRD and DTA showed that in the presence of $MgCl_2$, calcium hydrochloraluminate (Friedel's salt) is formed, which was not previously observed in the composition of binder hydration products.

Funding: Russian Science Foundation grant No. 21-19-00324, https://rscf.ru/project/21-19-00324/

Citation: Usanova, K., Barabanshchikov, Yu.G., Dixit, S. Cementless binder consisting of high-calcium fly ash, silica fume and magnesium chloride. Magazine of Civil Engineering. 2023. 123(7). Article no. 12305. DOI: 10.34910/MCE.123.5

1. Introduction

Fly ash is a finely dispersed material generated from the combustion of coal in thermal power plants. Numerous theoretical and practical studies, as well as world experience, show that industrial waste is a suitable raw material for replacing natural resources in the construction industry [1–4]. Fly ash is actively used in the concrete production as an additive [5–7], as a partial replacement for cement [8–10], as an artificial aggregate [11, 12] and as a binder for the production of geopolymers [13, 14]. A well-known solution is also the use of fly ash to obtain cementless binders [15, 16].

The fly ash properties directly depend on the type of coal burned. Combustion of anthracite or bituminous coals produces fly ash with a low CaO content. This fly ash is class F according to International Standard Specification ASTM C618. The combustion of brown coal produces fly ash with a CaO content of more than 10 %. This fly ash is class C according to ASTM C618.

The use of class C fly ash with a high content of CaO_{free} in concrete technology leads to a strong expansion and cracking of the material during the curing period. This prevents the use of high calcium fly ash in concrete production [17–19].

There are known methods for neutralizing the high calcium fly ash expansion in blended binders consisting of fly ash and cement. The silica fume additive in the dry mix causes shrinkage, which minimizes expansion and thus reduces crack development [20–22]. Another solution for neutralizing CaO_{free} is the co-grinding and hydrolysis of fly ash [23, 24]. It is possible to contain the expansion of dough from cement and fly ash by adding carbon fiber [25] or alkali-resistant glass fiber [26, 27].

The following ways to neutralize the expansion of a binder based only on high-calcium fly ash are known: pre-hydration, which reduces the amount of ettringite [28, 29], grinding, which accelerates the anhydrite and lime hydration [30], and cavitation technology [31].

The easiest way to neutralize fly ash expansion is to use silica fume additives. The study [32] proves the silica fume effectiveness in relation to the expansion of high-calcium fly ash from Berezovskaya thermal power plant during hydration. Expansion and cracking of the fly ash can be completely prevented by adding about 40 % microsilica to the fly ash. Such mixes do not have high strength [32]; therefore, they require the selection of hardening-accelerating admixture.

Chloride early strength agents are widely used in cement-based materials [33, 34]. Studies [35, 36] have shown that a certain amount of chlorides can effectively shorten the setting time of cement-based materials and improve the early strength.

The authors [37] studied the composition of waste rock, fly ash and cement in a ratio of 5:3:1 with the addition of chloride early strength agents. It found that NaCl and $CaCl_2$ promote early setting, while $MgCl_2$ reduces setting speed. The hydration heat increases if NaCl and $CaCl_2$ are used, but the hydration heat decreases if the addition of $MgCl_2$ is used.

Using chloride agents may cause reinforcement corrosion [38, 39]. It is known that free chloride ion moves inside the concrete and reduces the alkalinity of the pore solution, which causes decontamination and corrosion of the reinforcing steel in concrete [40]. But at the same time, the fixed chloride ion can react with $Ca(OH)_2$ and C_3A and form Friedel's salt ($C_3A \cdot CaCl_2 \cdot 10H_2O$), and the higher the chloride content in the solution, the more Friedel's salt will be generated [41, 42]. At the initial curing stage, Friedel's salt can effectively fill the gap between aggregates and improve the mechanical strength of the material [37].

Thus, the use of chloride agents in binders consisting of high-calcium fly ash and silica fume should reduce the content of free chloride ions by increasing the content of fixed chloride ions. In this case, the use of such a composition in concrete technology will be quite wide, for example, in the form of a cementless binder or in granular form, as a coarse aggregate of concrete.

The object of study is blended binders consisting of high-calcium fly ash from Berezovskaya thermal power plant and silica fume additive.

The work aims to study the effect of $MgCl_2$ additive on the strength, heat of hydration, and phase composition of hydration products of the binder based on high-calcium fly ash and silica fume.

Tasks of the research:

1. Experimental study of various early strength agents on their ability not to cause expansion in the composition of the cementless binder, consisting of high-calcium fly ash and silica fume.

2. Determination based on the results of X-ray Diffraction Analysis (XRD) what interactions occur in the "fly ash – silica fume – $MgCl_2$" system and how how these interactions affect the hydration.

3. Differential Thermal Analysis (DTA) of cementless binder specimens with different content of $MgCl_2$ additive.

4. Experimental study of the $MgCl_2$ additive on the heat release of cementless binder.

5. Experimental study of the effect of the $MgCl_2$ additive on the compressive strength of specimens from a mortar with polyfraction standard sand.

2. Materials and Methods

2.1. Materials

1. High-calcium fly ash from Berezovskaya thermal power plant (Krasnoyarsk Territory, Russia). The chemical composition of the tested specimens of fly ash is given in Table 1 [32].

Table 1. Chemical composition of fly ash.

CaO	SiO_2	Al_2O_3	Fe_2O_3	MgO	P_2O_5	SO_3	K_2O	Na_2O	Chlorine ion	C	Loss on ignition
42.2	26.8	6.49	6.09	7.05	<0.1	2.86	0.23	0.43	<0.05	2.33	3.44

The chemical composition of fly ash from the coal combustion of the Berezovsky deposit is characterized by a high content of CaOfree, which is 15.4 %. Fly ash from coals of the Berezovsky deposit is mineralogically represented mainly by silicates, aluminosilicates, and calcium ferrites, as well as calcium, magnesium and aluminium oxides (Table 2). Small amounts of TiO_2, MnO_2, and P_2O_5 are also present. Minerals such as brownmillerite, andradite, merwinite, grossular, and quartz are also identified. It should be noted that the fly ash contains a significant amount of unburned carbonaceous particles.

Fly ash from Berezovskaya thermal power plant sets and hardens when mixed with water. However, due to the presence of a large amount of free lime, its hardening is accompanied by strong expansion and cracking.

Table 2. Composition of fly ash according to X-ray diffraction analysis.

Crystal phases	Chemical Compound	Conditional Content [%]
Lime	Ca O	62.39
Graphite	C	12.81
Periclase	Mg O	7.3
Brownmillerite	$4CaO{\cdot}Al_2O_3{\cdot}Fe_2O_3$	3.71
Andradite	$3CaO{\cdot}Fe_2O_3{\cdot}3SiO_2$	3.62
Merwinite	$3CaO{\cdot}MgO{\cdot}2SiO_2$	3.39
Millosevichite	$Al_2(SO_4)_3$	1.97
Calcium Aluminum Oxide	$3CaO{\cdot}Al_2O_3$	1.92
Grossular	$3CaO{\cdot}Al_2O_3{\cdot}3SiO_2$	1.06
Aluminum Oxide	Al_2O_3	0.54
Yeelimite	$3CaO{\cdot}Al_2O_3{\cdot}CaSO_4$	0.51
Kilchoanite	$3CaO{\cdot}2SiO_2$	0.41
Quartz	SiO_2	0.38

The corresponding X-ray diffraction pattern is shown in Fig. 1.

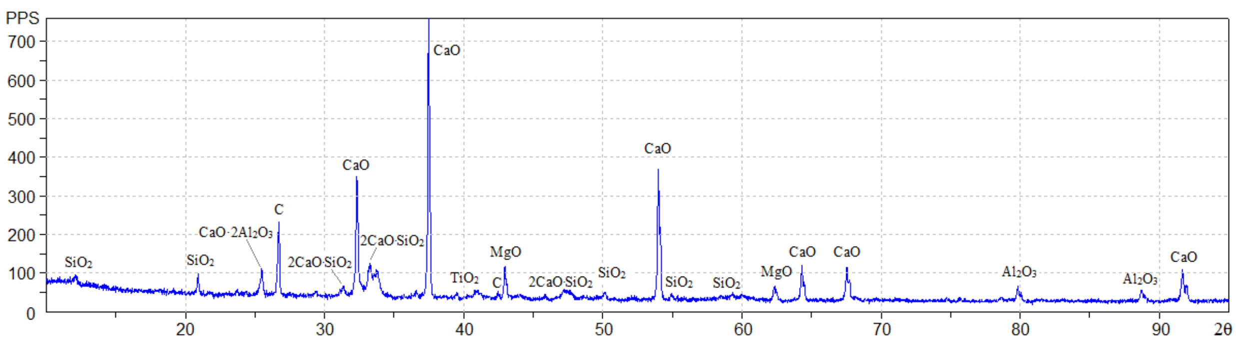

Figure 1. X-ray diffraction pattern of fly ash.

2. Silica Fume MKU-85. The additive is used to neutralize the expansion of fly ash.

3. Early strength agents: Al_2O_3, $Ca(OH)_2$, $CaCl_2$, Na_2SO_4, $MgSO_4$, K_2O, $MgCl_2$. Early strength agents are used to select an additive that increases the strength and water resistance of the binder, consisting of

fly ash from Berezovskaya thermal power plant and silica fume. The content of early strength agents and silica fume (MS) by weight of fly ash are presented in Table 3.

Table 3. Content of early strength agents and silica fume (MS) by weight of fly ash.

Type of additives	Al_2O_3	$Ca(OH)_2$	$CaCl_2$	Na_2SO_4	$MgSO_4$	K_2O	$MgCl_2$
Accelerator additive content [%]	21.4	21.2	7.0	11.5	11.5	7.7	12.2
MS content [%]	21.4	21.2	42.9	42.3	42.3	42.5	42.5
Water-fly ash ratio W/A	0.71	0.77	0.71	0.70	0.85	0.93	0.90

2.2. Influence of early strength agents on fly ash expansion in presence of silica fume

Expansion tests were carried out using Le Chatelier molds. Fly ash in the amount of 50 g, silica fume and early strength agents in the amount from Table 3 were taken for one Le Chatelier molds. First, the dry mixture was mixed by hand, and then water was slowly added until the consistency of all compositions was the same. The tests were carried out in accordance with EN 196-3:2016 Test Methods for Cement, Part 3: Determination of setting time and strength. Le Chatelier molds were placed on glass plates and filled with fly ash paste with additives in one go without compaction. Excess paste is cut off. Forms were covered from above with plates weighing 100 g and cured in air. The temperature was 20 ± 2 °C, relative air humidity was 45–55%. Unlike EN 196-3:2016, the samples were not boiled. The distance f between the ends of indicator arms was periodically measured with a caliper with an accuracy of 0.5 mm, and the difference $\Delta f = f - d$ was calculated, where d is the distance before the experiment.

2.3. Determination of compressive strength of specimens with early strength agents

The compressive strength was determined on specimens of a cubic shape with size of 32×32×32 mm. A total of 12 compositions based on a dry mixture of fly ash and silica fume in an amount of 30.4 % by weight of the fly ash were tested. The compositions differed in the type of early strength agents and their content. According to the results of testing the compositions in Le Chatelier moulds, three type of the early strength agents were selected with an expansion Δf < 5 mm: $MgSO_4$, $CaCl_2$ and $MgCl_2$. Each of the additives was used in four dosages: 1.5; 4.7; 8.2; 11.8 % by weight of fly ash. Early strength agents were introduced into the mixture in the form of an aqueous solution. The water content of the solution was considered in the calculation of the water/solid ratio (W/S). The water content in the finished mixture was selected so as to obtain mixtures with the same consistency. Therefore, the value of W/S was a characteristic of the water demand of the fly ash. 6 specimens of each composition were prepared. Demoulding of the specimens was carried out after 2 days. Immediately after demoulding, three out of 6 specimens were placed in water, and the other three were left to harden in sealed containers, which did not allow the specimens to dry out and exclude their contact with the outside air in a laboratory room with a temperature of 20 ± 2 °C. Specimens of both dry and wet hardening were tested for compressive strength after 7 days from the date of manufacture. Before testing, the state of the specimens was visually assessed, the presence of expansion and cracks.

2.4. X-ray Diffraction Analysis and Differential Thermal Analysis

The use of X-ray diffraction analysis and differential thermal analysis was aimed at establishing what interactions occur in the fly ash–silica fume–$MgCl_2$ system and how these interactions were related to expansion. XRD and DTA were performed on specimens of the mixes listed in Table 4.

Table 4. Compositions of paste.

Component	Components content in the composition of blended binder [%]		
	Mix 1	Mix 2	Mix 3
Fly ash from Berezovskaya TPP	100	70	64.7
Silica Fume MKU-85	-	30	27.7
$MgCl_2$	-	-	7.6
Water-solid ratio W/S	1.2	0.42	0.50

Specimens for XRD and DTA were prepared as follows. First, fly ash and silica fume were mixed in an automatic mortar mixer for 6 minutes, then the calculated amount of $MgCl_2$ solution with a density of 1.24 g/cm^3 and water were added, considering the amount of water in the additive solution. Specimens were stored above water in a closed container. After the end of the curing period, the specimens were crushed before passing through a sieve with mesh 0.25 mm and subjected to vacuum drying for 3 hours at a residual pressure of 3.3 Pa. The dried specimens were ground in an agate mortar until they passed through a 005 sieve.

Semiquantitative analysis of crystalline phases in the specimens was carried out on a Dron 7 X-ray diffractometer produced by JSC"E" Burevestnik"(Russia) with the following parameters: CuKα radiation, λ = 0.15406 Å, 2θ shooting range from 8° to 94° with a step of 0.02°, and an exposure of 3 and 5 s.

Differential thermal analysis was performed on the device"Termoscan-" produced by LLC"Analitpribo" (Russia). The specimens for DTA had a mass of about 0.7–0.8 g. The specimens were heated to a temperature of 950–1000 °C.

2.5. Heat of Hydration of mortar using Semi-Adiabatic Calorimetry

The test was carried out in accordance with EN 196-9:2010"Methods of testing cement part 9: heat of hydration—semi-adiabatic method".

The paste was placed in a thin-walled aluminum container and in a glass Dewar flask. A hot junction of a differential thermocouple and a control thermometer were placed in the center of the specimen reservoir. To determine the heat capacity, the specimen was supplied with an electric heater in the form of an insulated nichrome wire wound around the cylindrical surface of the specimen reservoir. The Dewar flask with a specimen, closed with a polystyrene foam stopper, with heater and thermocouple wires, was placed in the center of a heat-insulated thermostat case. To regulate the air temperature in the thermostat, it was equipped with a cooling device and a fan. During the experiments, the temperature of the air surrounding the thermos was maintained constant using a contact thermometer and an electronic thermostat. Fluctuations in the temperature of the medium relative to the average value were ±0.3 °C. Specimen temperature was recorded automatically every 30 min with an accuracy of 0.1 °C. The thermocouple readings were recorded by a"Terem-" multi-channel data logger every 30 minutes.

When measuring the exotherm of the specimen, the heating element was not used or was absent.

To obtain comparable results, the heat of hydration obtained by the semi-adiabatic method at an initial specimens temperature of 20 °C was recalculated to an isothermal hardening regime at a temperature of 20 °C using the reduced time hypothesis [43].

The heat of hydration was determined in the mix consisting of fly ash, silica fume, early strength agents and polyfraction standard sand on cylindrical specimens with diameter of 62 mm, high of 160 mm. Three mix of the mortar were tested (mixes Q1, Q4, Q5) with the same amount of fly ash, but with a different combination of additives (Table 5).

Table 5. Mixes and designation of specimens for determining heat of hydration and strength

Component	Material Consumption [kg/m^3]		
	Q1	Q4	Q5
Fly ash from Berezovskaya TPP	210	210	210
Silica fume MKU-85	-	90 (42.9 %)	90 (42.9 %)
$MgCl_2$ (dry)	-	-	24.8 (11.8 %)
Polyfraction standard sand	1645	1476	1451
Water	318	340	330
Total	2173	2116	2106

3. Results and Discussion

3.1. Evaluation of influence of early strength agents

The test results of early strength agents (Table 3) are shown in Fig. 2.

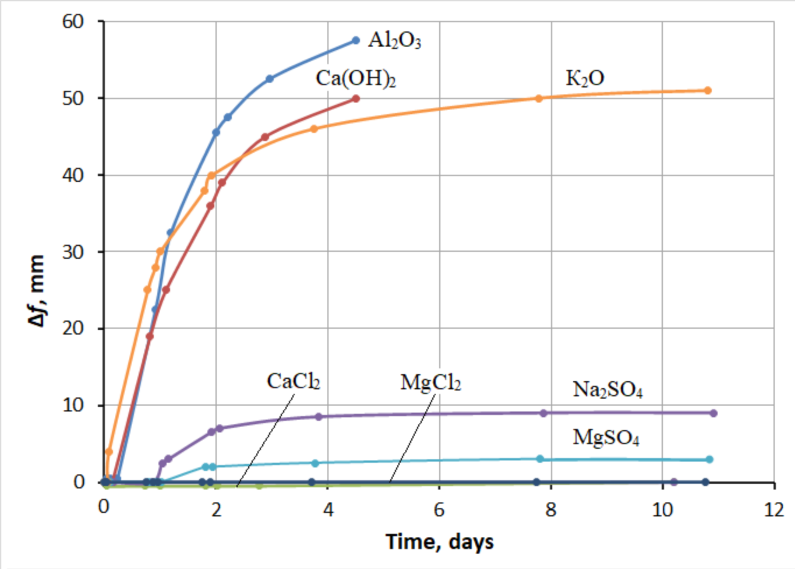

Figure. 2. Influence of early strength agents in complex with silica fume (MS) on fly ash paste expansion.

The high expansion of specimens with additives of Al_2O_3, $Ca(OH)_2$, K_2O is possibly associated with silica fume neutralization reactions, with the formation of $Al_2(SiO_3)_3$ in the case of aluminum oxide and MS, and with the formation of potassium and calcium hydrosilicates in the other two cases.

Additions of chloride and sulfate salts showed good results. Fly ash expansion with these additives was within the normal range for cement (10 mm). Chlorides showed a particularly high effect; expansion was almost non-existent. As shown below, this effect of chlorides was also retained during the aqueous exposure of the specimens. In connection with the action of these salts, it can be assumed that the specimen's expansion, especially during hardening in water, was caused by ettringite formation. Since it is known that the presence of chlorides slows down or stops the concrete expansion under the action of sulfate solutions. This is due to an increase in the solubility of calcium hydrosulfoaluminate in chloride solutions. However, X-ray diffraction analysis did not show the presence of significant amounts of ettringite in the hydration products. Therefore, the free lime hydration process was responsible for the expansion.

3.2. Compressive Strength and Water Resistance Test Results

The test results of specimens consisting of fly ash, MS, and early strength agents are presented in Table 6.

Table 6. Compressive strength (MPa).

Type of early strength agent		$MgSO_4$		$CaCl_2$		$MgCl_2$	
Curing		dry	water	dry	water	dry	water
Early strength agent content, % by weight of fly ash	1.5	8.2	0	5.8	0	2.9	0
	4.7	6.1	2.7	8.8	0	8.3	0
	8.2	4.4	1.2	7.9	1.53	9.8	1.92
	11.7	5	1.2	4.6	1.15	15.2	2.3

The strength of specimens with $MgSO_4$ decreased with increasing additive. The specimens hardened in water underwent significant expansion and cracking. When specimens hardened in dry conditions, these phenomena did not occur. The highest strength of 8.2 MPa was shown by specimens with a $MgSO_4$ content of 1.5 %.

Calcium chloride at dosages of 8.2 and 11.8 % caused a rapid thickening of the mix. As a result, the strength of these specimens was low. At the same time, these specimens did not have cracks and expansion during water hardening, in contrast to specimens with a lower $CaCl_2$ content. All specimens retained their shape and continuity under air conditions. The strength of dry hardening specimens with CaCl2 content of 4.7 % was the highest and amounted to 8.8 MPa; however, such specimens crumbled in water.

The $MgCl_2$ additive showed a relatively good result in compressing specimens hardened in dry conditions. The strength at an additive content of 11.8 % was 15.2 MPa. However, the strength dropped sharply to 2.3 MPa (Table 6) during the water hardening of specimens.

The appearance of specimens with $MgCl_2$ additive is shown in Fig. 3. It can be seen that the dry hardening specimens with a low content of magnesium chloride (1.5 %) underwent cracking. In water, specimens of this mix blurred, forming a liquid-like mass. Specimens with a high content of $MgCl_2$ (8.2–11.8 %) passed the test without cracking, both in air and in water; however, there was a slight expansion of the specimens in water. Since $MgCl_2$ is the best solution at this stage, we continued researching this supplement.

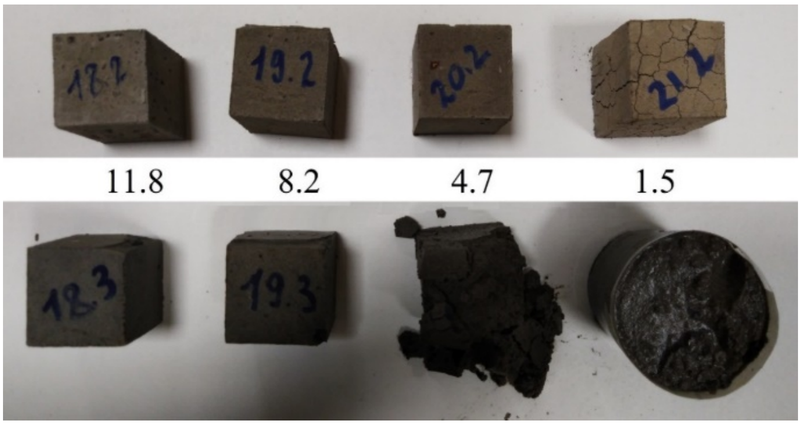

Figure 3. Specimens from fly ash, MS, and $MgCl_2$ additive in amount indicated in photo in % by weight of fly ash. Top row is with dry curing; bottom row is water curing.

3.3. Influence of magnesium chloride on phase composition of hydration products of binder

3.3.1. Results of X-ray diffraction analysis

X-ray patterns of specimens consisting of fly ash, silica fume (MS), and the $MgCl_2$ additive of mixes 1-3 (Table 4) after hydration are shown in Fig. 4, 5.

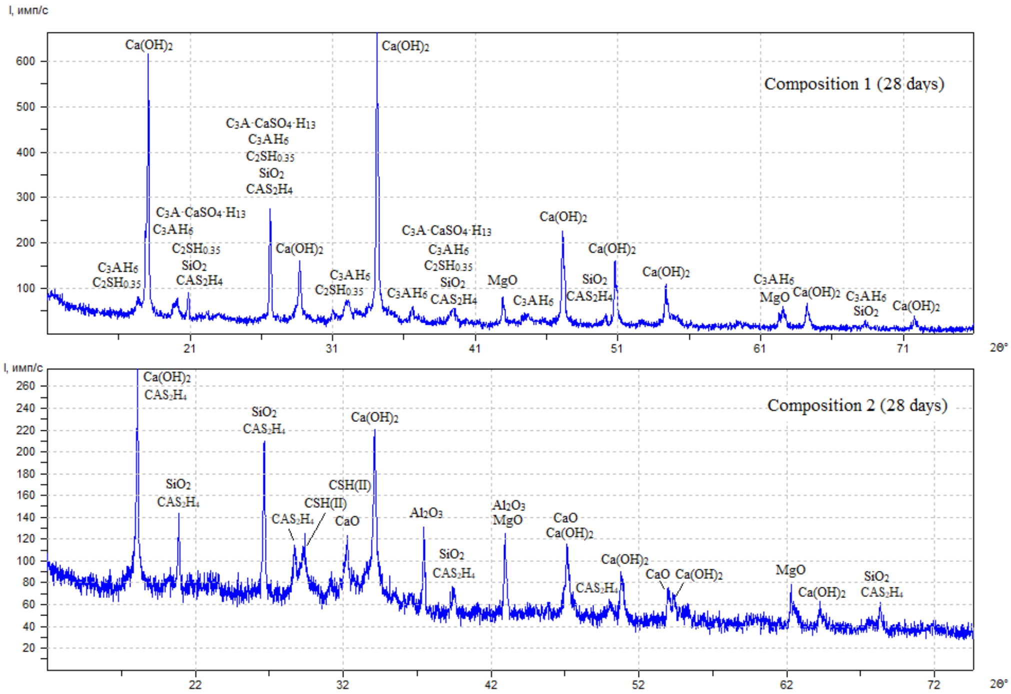

Figure 4. X-ray patterns of mixes 1 and 2 (Table 4) after hydration at age of 28 days.

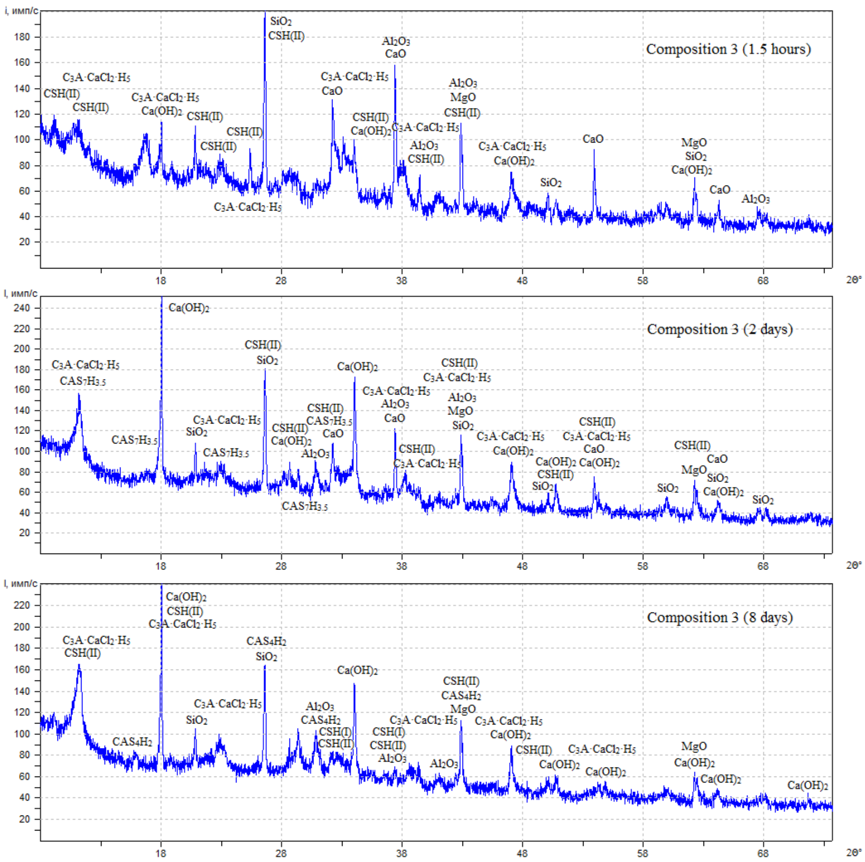

Figure 5. X-ray patterns of mix 3 (Table 4) after hydration at age of 1,5 hour, 2 days, and 8 days.

A semiquantitative analysis was carried out using the integral values of the intensity of the X-ray peaks. The obtained conditional values of the percentage of identified hydrated phases are given in Table 7.

Table 7. Crystalline phases of fly ash.

Phases	Chemical Compound	Mix 1 (28 days)	Mix 2 (28 days)	Mix 3		
				1.5 hours	2 days	8 days
Lime	CaO	-	12.8	27,3	10.8	-
Portlandite	$Ca(OH)_2$	85.4	41.8	12,5	32.3	34.1
Katoite	C_3AH_6	11.1	-	-	-	-
Calcium Aluminum Oxide Hydrate	C_4AH_{19}	-	-	-	5.6	-
Hydrocalumite	C_4AH_{13}	-	-	-	10.4	20.0
Gismondine	CAS_2H_4	-	27.5	40,2	18.9	25.4
Calcium Aluminum Silicate Hydrates	CAS_4H_2	-	-	-	-	3.2
Katoite silication	C_3ASH_4	-	2.7	-	6.2	
Calcium Silicate Hydrates	CSH(II)	-	15.2	-	1.6	2.1
Calcium Aluminum Oxide Sulfate Hydrate	$C_3A{\cdot}CaSO_4{\cdot}H_{13}$	3.5	-	-	-	-
Calcium Aluminum Oxide Chloride Hydrate	$C_3A{\cdot}CaCl_2{\cdot}H_{10}$	-	-	20.0	14.1	15.1

The following conclusions can be drawn from the data in Table 7.

1. In the absence of silica fume and $MgCl_2$ (mix 1), the interaction of fly ash with water for 28 days leads to the complete hydration of CaO_{free}. At the same time, calcium hydroxide is formed in an overwhelming amount from the hydration products of 85.4 % of the specimen's mass. Hydrosilicates in crystalline form are not found. There is C_3AH_6 (11.1 %) from calcium hydroaluminates. A small proportion (3.5 %) is the low sulfate form of calcium hydrosulfoaluminate.

2. The addition of silica fume to the fly ash (mix 2) slows down the hydration of the lime. This corresponds to the effect of siliceous admixture on the slaking rate of air-hardening lime. After 28 days of hydration, a significant amount of unreacted CaO_{free} (20.6 %) remains in the fly ash, and the content of $Ca(OH)_2$ is almost halved compared to mix 1, apparently as a result of the action of silica fume, as indicated by the significant content of the formed silicates and calcium aluminosilicates. The effect of silica fume on the hydration of high-calcium fly ash was considered by us in more detail in [32].

3. The effect of $MgCl_2$ (Mix 3) was investigated for three hydration periods. After 1.5 hours, a significant amount of unreacted CaO_{free} (36 %) and a small amount of $Ca(OH)_2$ remain in the mix. Calcium hydrosilicates are completely absent, which is explained by the short time for reactions and crystallization of hydration products. In subsequent periods, the content of lime decreases, and by 8 days, it is completely bound into hydrates, aluminates, and calcium aluminosilicates, which make up a significant proportion of the total number of neoplasms. Silicates are present in negligible quantities. Based on these data, it can be concluded that $MgCl_2$ accelerates the hydration of lime and its binding to silica. At the same time, the addition of magnesium chloride intensifies the formation of crystalline hydrates of calcium aluminosilicates, and hydrosilicates are formed to a greater extent in the X-ray amorphous state.

4. In the presence of $MgCl_2$, a new compound is found that has not previously appeared in the composition of hydration products; this is calcium hydrochloraluminate (Friedel's salt).

The content of Friedel's salt changes little with the age of the specimens. Friedel's salt here can be formed as a result of the replacement of sulfate ions in $C_3A{\cdot}CaSO_4{\cdot}H_{13}$, found in mix 1, with chloride ions:

$$2Cl^- + 3CaO{\cdot}Al_2O_3{\cdot}CaSO_4{\cdot}13H_2O \rightarrow 3CaO{\cdot}Al_2O_3{\cdot}CaCl_2{\cdot}10H_2O + SO_4^{2-} + 3H_2O,$$

or when interacting with tricalcium hydroaluminate

$$3CaO{\cdot}Al_2O_3{\cdot}6H_2O + MgCl_2 + Ca(OH)_2 + 4H_2O = 3CaO{\cdot}Al_2O_3{\cdot}\ CaCl_2{\cdot}10H_2O + Mg(OH)_2.$$

Also, a semiquantitative X-ray diffraction analysis was carried out for specimens consisting of fly ash, MS, and the magnesium chloride additive, which were previously tested for strength (see Table 6). The XRD results are shown in Fig. 4, 5, and Table 8.

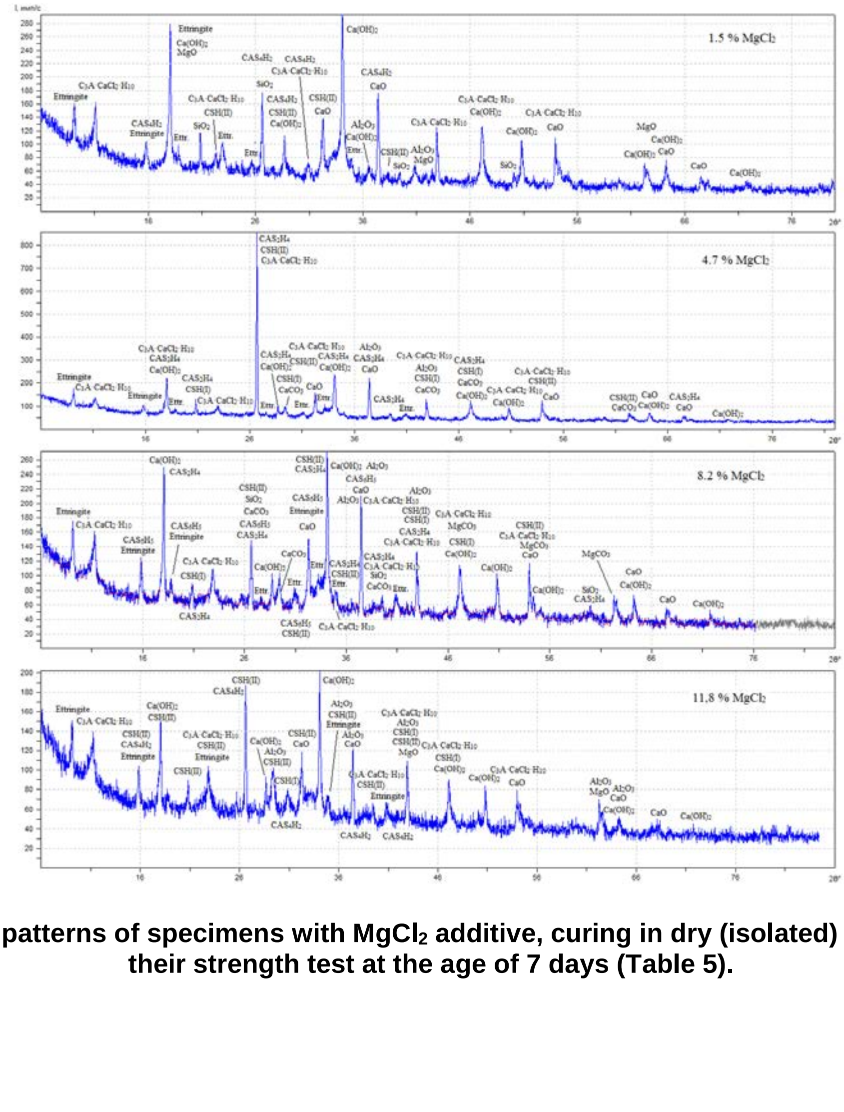

Figure 6. X-ray patterns of specimens with $MgCl_2$ additive, curing in dry (isolated) conditions, after their strength test at the age of 7 days (Table 5).

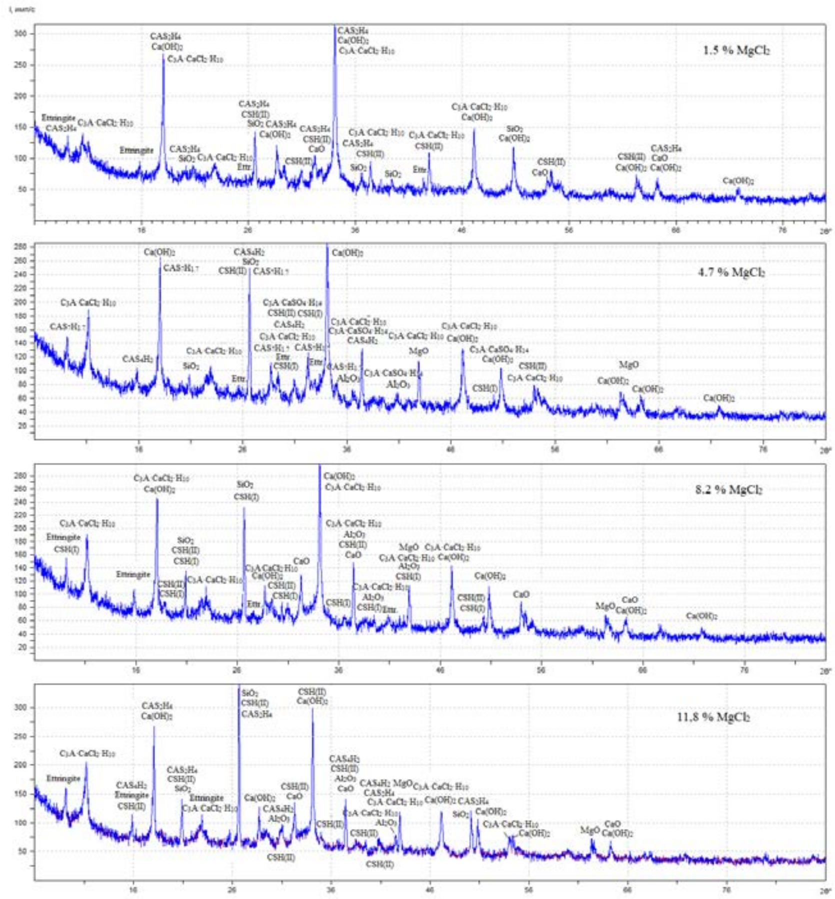

Figure 7. X-ray patterns of specimens with $MgCl_2$ additive, curing in water, after their strength test at the age of 7 days (Table 4).

Table 8. Conventional values of percentage of identified phases.

Phases	Chemical Compound	Curing	Content of $MgCl_2$, % by weight of fly ash			
			1.5	4.7	8.2	11.8
Portlandite	$Ca(OH)_2$	dry	52.6	26.0	31.8	37.2
		in water	70.2	32.9	36.1	42.9
Lime	CaO	dry	23.7	21.7	20.9	17.5
		in water	11.0	14.3	17.7	21.5
Calcium Aluminum Oxide Chloride Hydrate	$C_3A{\cdot}CaCl_2{\cdot}H_{10}$	dry	6.0	3.5	18.3	19.4
		in water	3.9	21.1	14.7	6.1
Calcium Aluminum Hydroxide Hydrate	C_4AH_{13}	dry	8.7	-	-	-
		in water	-	-	-	-
Calcium Aluminum Silicate Hydrates	CAS_xH_y	dry	7.0	34.5	24.2	16.8
		in water	12.7	31.1	26.8	11.7
Calcium Silicate Hydrate	CSH(II)	dry	2.0	14.2	4.9	9.2
		in water	2.2	0.7	4.7	18.3

The main phases identified in the specimens (Table 8) are lime, calcium hydroxide, calcium hydrochloraluminate, and a significant amount of calcium aluminosilicates of the composition CAS_2H_4, CAS_4H_2, CAS_6H_5, $CAS_7H_{1,7}$, which in Table 5 are denoted by the general formula CAS_xH_y. The effect of $MgCl_2$ on other compounds' content manifests differently depending on the concentration. The content of $Ca(OH)_2$ decreases by almost 2 times with an increase in the content of $MgCl_2$ from 1.5 to 4.7 % by weight of fly ash, both in dry and water curing of specimens. At the same time, the content of calcium hydroaluminosilicates increased 5 times during dry hardening and 2.5 times during water hardening. The content of $C_3A{\cdot}CaCl_2{\cdot}H_{10}$ in this range of magnesium chloride concentrations decreased from 6 to 3.5 % during dry curing, and, on the contrary, it increased from 3.9 to 21.1 % during water curing. With a further increase in the concentration of $MgCl_2$ from 4.7 to 11.8 %, the content of $Ca(OH)_2$ moderately increases, and the content of calcium aluminosilicates decreases for both hardening methods. The calcium hydrochloraluminate formation increases significantly with an increase in the concentration of $MgCl_2$ during dry curing but decreases when the specimens are placed in water. The residual amount of lime can be a little dependent on the $MgCl_2$ content and hydration conditions. Thus, the magnesium chloride assistive promotes the formation of calcium hydrochloraluminate and the redistribution of free lime towards the formation of calcium hydroaluminosilicates instead of $Ca(OH)_2$.

3.3.2. Results of differential thermal analysis

Differential thermal analysis data confirm the XRD results. DTA curves for mixes 2 and 3 at different ages (Table 4) are shown in Fig. 8.

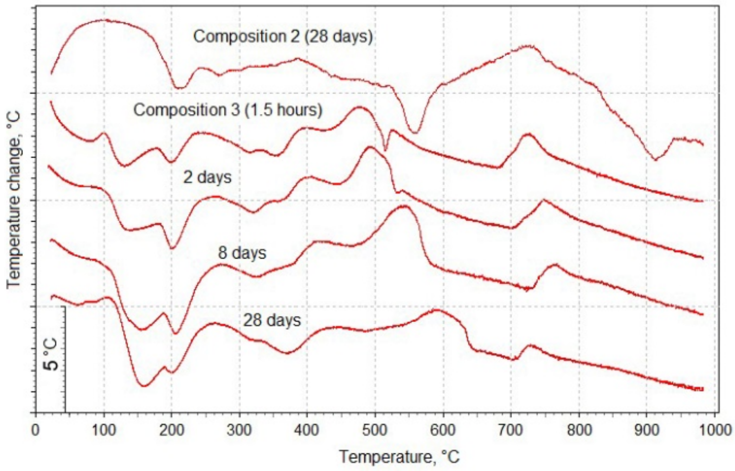

Figure 8. DTA curves of specimens from mixes 2 (without $MgCl_2$ additive) and 3 with 11.8% $MgCl_2$ additive at different ages.

The thermogram of mix 2 shows 3 pronounced endothermic peaks at 210, 560, and 915 °C. The first of them may correspond to the loss of interlayer water in the tobermorite. The effects at 560 and 915 °C refer to the decomposition of $Ca(OH)_2$ and $CaCO_3$, respectively. Other thermograms show several effects caused by $MgCl_2$ influence. These are endothermic peaks with increasing intensity as the specimens' curing period increases, in the temperature range of 130–160 °C. In this temperature range, adsorbed and hydrosilicates and AFm-phases usually lose interlayer water. Thus, $MgCl_2$ promotes the formation of these phases, which also follows from the XRD results. The endothermic peak at 200 °C noted on all thermograms can be attributed to C_4AH_{13}, which is stable in $Ca(OH)_2$ solutions at CaO concentrations higher than 1.08 g/L. This effect may also be associated with dehydrating the CAS_2H_4 compound or other calcium alumina hydrosilicates.

The endothermic effect at 320°C is associated with the presence of C_3AH_6, and the effect at 360 °C is associated with the dehydration of C_3ASH_4. A wide depression in the temperature range of 400–500 °C, shifting to the right with the age of the specimens, presumably indicates the presence of calcium hydrosilicates with a $CaO:SiO_2$ ratio of more than 1,3.

The formation of $C_3A{\cdot}CaCl_2{\cdot}H_{10}$ in this system can be evidenced by endothermic effects at 155, 200–210, and 320 °C. Literature data show similar temperature peaks for this compound. The thermogram of the synthesized calcium hydrochloraluminate [44] shows endothermic peaks at 215 and 330 °C. In work [45], three endothermic peaks were found for the Friedel salt obtained due to hydrothermal synthesis: the peak at 35 °C is due to a structural transition, the peak at 155 and 340 °C corresponds to the loss of interlayer water and hydroxyl condensation, respectively.

The thermograms of mix 3 (Fig. 8) show two exothermic peaks. The first one, with an increase in the age of the specimens, shifts towards a higher temperature, from 475 to 590 °C, and is superimposed on the effect of $Ca(OH)_2$ dehydration, overlapping the heat costs for the decomposition of portlandite. Since mix 2 did not show a similar effect, the addition of $MgCl_2$ can be considered responsible for it. Unfortunately, it has not yet been possible to decipher this effect. The second exothermic peak at 725–765 °C is characteristic of all thermograms, including mix 2 without $MgCl_2$ addition. The most probable in this case is the burnout of unburned carbon particles.

The thermograms shown in Fig. 9 characterize the effect of the magnesium chloride amount on the phase composition of the fly ash – silica fume specimens.

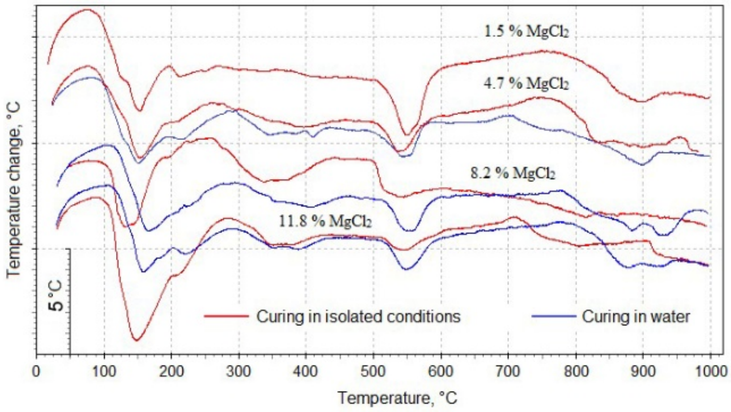

Figure 9. DTA curves of specimens with different MgCl2 content.

As can be seen from Fig. 9, the obtained DTA curves basically repeat the shape of the previous thermograms. That is, in qualitative terms, we have the same data as in the analysis of Fig. 6. It is noteworthy here that with an increase in the $MgCl_2$ content, the depth of the endothermic peak at 150 °C sharply increases, which once again confirms the intensive growth of aluminate hydrates and calcium aluminosilicates in the presence of $MgCl_2$. In this case, the amount of $Ca(OH)_2$ formed decreases, as evidenced by the decreasing depth of the endothermic peak at 550 °C. This is more pronounced during dry curing of the specimens.

3.4. Influence of magnesium chloride on heat generation of fly ash-silica fume binder

The heat generation of the mortar (binder + polyfraction standard sand) per 1 kg of fly ash at a temperature of 20 °C, depending on the mix, is shown in Fig. 10.

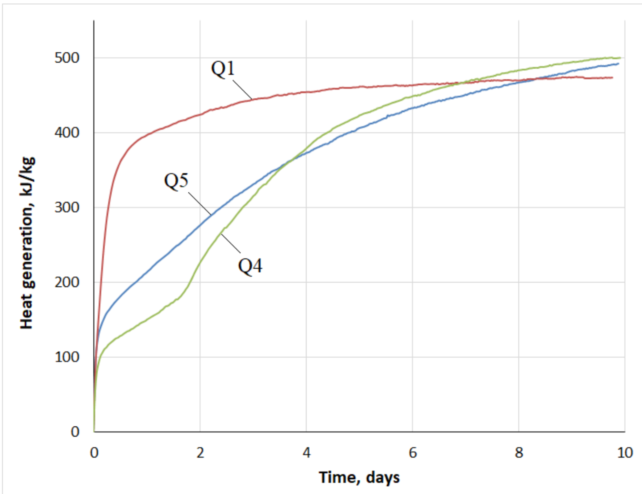

Figure 10. Heat generation of fly ash mortar per 1 kg of fly ash at temperature of 20 °C, depending on the mix: Q1 is without additives; Q4 is with additive of 42.9 % MS; Q5 is with additives of 42.9% MS and 11.8 % $MgCl_2$.

Pure fly ash (curve Q1) reacted very violently with water due to the slaking of free lime. Approximately 1 day after the intense heat release, the process slowed down sharply and ended by the fourth day. In the presence of silica fume (curve Q4), a sharp slowdown of the heat release process was observed. By the end of the second day, the reaction rate increased again, and on the 10th day, the heat release was higher than that of pure fly ash. The addition of $MgCl_2$ compensated for the retarding effect of silica fume and increased the heat release in the first 3 days, giving a smoother curve with a moderate increase in exotherm. Starting from day 4, the heat release curves for the mixes Q4 and Q5 were parallel and very close to each other, with a slight excess of the mix Q4 over Q5. By the end of the experiment, the mix Q5 also overtaked pure fly ash in terms of the total thermal effect.

The heat of hydration experiments require a certain amount of time to prepare the mix and the specimens. In our case, this time was about 30 min. Additional tests were carried out to determine the heating in the first hour of hydration. The mixes of the test are given in Table 9.

Table 9. Test mixes for determining the temperature in the initial period of hydration.

Component	Material Consumption [kg/m^3]		
	t1	t2	t3
Fly ash from Berezovskaya TPP	30	30	30
Silica fume MKU-85	-	12.9 (42.9 %)	12.9 (42.9 %)
$MgCl_2$ (dry)	-	-	3.54 (11.8 %)
Water	19.5	27.9	30.2
Total	49.5	70.8	76.64

Fly ash or a thoroughly mixed fly ash and MS were placed at the bottom of the Dewar flask. The $MgCl_2$ additive was introduced in the paste with mixing water. A closed container with water or an additive solution, suspended on a thin thread, was placed above the dry mixture inside a Dewar flask. The water-solid ratio was 0.65. A closed thermos and a glass thermometer with a division value of 0.1 °C were kept for 1 day in a room with a constant temperature. Before the start of the experiment, the temperature of the dry mix in a thermos was measured and taken as the initial temperature of the specimens. The dry mix in a thermos was closed with prepared water and quickly stirred with the end of a thermometer, fixing the temperature. The first reading was taken 30 s after the moment of shuttering. Each composition was tested twice, and the average value was taken. The results of measuring the temperature of the fly ash-silica fume paste are shown in Fig. 11.

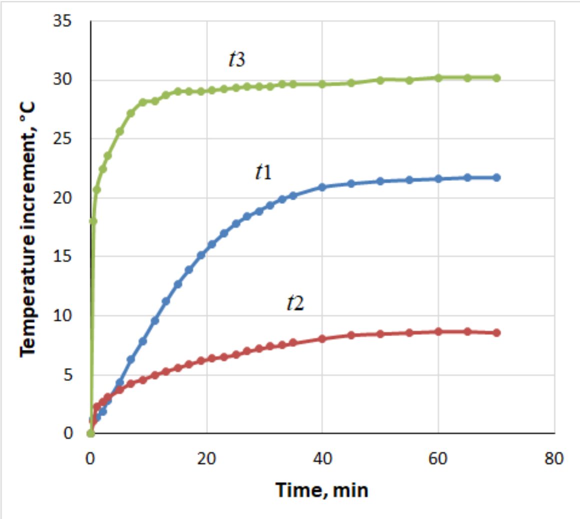

Figure 11. Temperature increment of specimens depending on mix: t1 is fly ash without additives; t2 is fly ash with addition of 42.9% MS; t3 is fly ash with additions of 42.9% MS and 11.8 $MgCl_2$%.

Fig. 11 shows that the temperature of the fly ash (mix t1) for 1 hour of hydration increased by 21.6 °C against the initial one. In the presence of silica fume (mix t2), the hydration rate decreased sharply, and the temperature of the paste increased only by 8.7 °C. Here, the same regularity of the silica fume influence was observed as in the initial period of hardening of the mortar (Fig. 10). Such an effect of silica fume was explained by a decrease in the transfer rate in solutions [46]. The introduction of the $MgCl_2$ additive resulted in an extremely sharp temperature jump in the first seconds after mixing. The temperature increase after 30 s was 18 °C, and after 10 min was 28.2 °C.

This characterizes magnesium chloride as a powerful early strength agent of fly ash-silica fume binder.

3.5. Effect of magnesium chloride on the mortar strength

The specimens consisting of fly ash, silica fume, polyfraction standard sand, and magnesium chloride (Table 5) tested for heat release were also tested for compressive strength at the age of 28 days. Specimens of a cubic form, in 3 pieces per test, had dimensions of 7×7×7 cm. The specimens were stored in a laboratory room with a temperature of (20 ± 2) °C, for the first 7 days in covered forms and the rest of the time in a desiccator above water. Testing hydraulic press PGM-50MG4 with a maximum force of 50 kN was used for testing. During the test, the loading rate was maintained (50±10) kPa/s.

The results of determining the compressive strength of the specimens are shown in the diagram in Fig. 12.

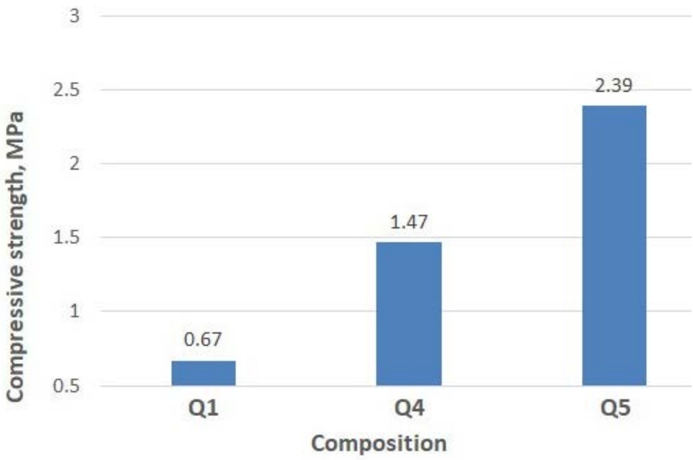

Figure 12. Compressive strength test results of specimens.

From Fig. 12, it can be seen that adding silica fume to the fly ash increased the strength of the specimens by more than 2 times, and adding $MgCl_2$ increased the strength by another 63 %. Authors [36] also obtained greater strength of specimens based on cement and fly ash at high dosages of $MgCl_2$ additive.

The low strength of the tested compositions of the mortar; however, it must be borne in mind that the binder-sand ratio in these solutions ranges from 1:5 to 1:7.

4. Conclusions

This paper presented the results of an experimental studies conducted to evaluate the influence of magnesium chloride additive on a cementless binder consisting of high-calcium fly ash and silica fume. The following key conclusions were drawn from this study:

1. Silica fume added to the high-calcium fly ash of Berezovskaya thermal power plant in an amount of about 40 % eliminates its expansion due to CaO hydration. A mix of fly ash and silica fume exhibits the properties of a binder. Early strength agents can significantly increase the binder strength. However, some agents restore the fly ash expansion despite the silica fume presence.

Of the early strength agents tested, magnesium and calcium chloride showed virtually no expansion, and $MgSO_4$ showed expansion within the normal range for Portland cement. The highest compressive strength of these three additives was provided by $MgCl_2$ (15.2 MPa at the age of 7 days with an additive content of 11.8 %).

2. X-ray Diffraction Analysis showed the following results:

2.1. The interaction of pure fly ash with water in 28 days leads to complete hydration of CaO_{free}. In this case, calcium hydroxide is formed in most hydration products. C_3AH_6 is present in calcium hydroaluminates. The addition of silica fume to the fly ash slows down the hydration of lime. After 28 days of hydration, a significant amount of unreacted CaO_{free} (about 20 %) still remains in the fly ash, and the content of $Ca(OH)_2$ is almost halved.

2.2. The effect of $MgCl_2$ was investigated for three hydration periods. After 1.5 hours, a significant amount of unreacted CaO_{free} (36 %) and, accordingly, a small amount of $Ca(OH)_2$ remain in the composition of the binder. In subsequent periods, the content of lime decreases, and by 8 days, it is completely bound into hydrates, aluminates, and calcium aluminosilicates, which make up a significant proportion of the total number of neoplasms. The XRD results show that $MgCl_2$ accelerates the hydration of lime and its binding to silica. At the same time, the addition of magnesium chloride intensifies the processes of formation of crystalline hydrates of calcium aluminosilicates.

With the introduction of $MgCl_2$, calcium hydrochloraluminate (Friedel's salt) is formed, which has not previously been observed in the composition of the hydration products of the binder. The content of $3CaO{\cdot}Al_2O_3{\cdot}CaCl_2{\cdot}10H_2O$ changes little with the age of the specimens.

2.3. The main phases identified in specimens consisting of fly ash, silica fume, and different $MgCl_2$ content at the age of 9 days are lime, calcium hydroxide, calcium hydrochloraluminate, and a significant amount of calcium aluminosilicates of the composition CAS_2H_4, CAS_4H_2, CAS_6H_5, $CAS_7H_{1,7}$. The effect of $MgCl_2$ on other compounds' content manifests differently depending on the concentration. The content of $Ca(OH)_2$ decreases by almost 2 times, both during dry and water curing of specimens, if the $MgCl_2$ content increases from 1.5 to 4.7 % by weight of fly ash. This is accompanied by a sharp increase in the amount of calcium hydroaluminosilicates. With a further increase in the $MgCl_2$ content from 4.7 to 11.8 %, the $Ca(OH)_2$

content increases moderately, and the content of calcium aluminosilicates decreases. The calcium hydrochloraluminate formation increases significantly with an increase in the concentration of $MgCl_2$ during dry curing but decreases when the specimens are placed in water. Thus, the magnesium chloride promotes the calcium hydrochloraluminate formation and the redistribution of free lime towards the formation of calcium hydroaluminosilicates instead of $Ca(OH)_2$.

3. In the DTA curves, with an increase in the $MgCl_2$ content, the depth of the endothermic peak at 150 °C increases sharply, which confirms the intensive growth of aluminate hydrates and calcium aluminosilicates in the presence of $MgCl_2$.

4. Pure fly ash reacts very violently with water due to the slaking of free lime. During the first day, 85 % of the heat is released from the final total value of the released heat in the experiment for 10 days. There is a sharp slowdown in the process of heat release in the presence of silica fume in the initial period of hardening. The thermal effect was only 30% of the final value by the end of the first day. The addition of $MgCl_2$ partially compensates for the retarding effect of silica fume. In this case, 44 % of the heat from the final value is released during the first day. It should be noted that the final value of the total heat release is approximately the same in all three cases.

5. The addition of $MgCl_2$ to the mortar with polyfraction standard sand increases the compressive strength by 63 %.

References

1. Petrov, V.V., Protsenko, A.E., Sapozhnik, K.R. Solid-cabide tool waste recycling technology. Construction Materials and Products. 2022. 5(3). Pp. 27–34. DOI: 10.58224/2618-7183-2022-5-3-27-34
2. Zakrevskaya, L.V., Gavrilenko, A.A., Kapush, I.R., Lyubin, P.A. Creating ground concrete and strengthening substrates using mining waste. Construction Materials and Products. 2022. 5 (3). Pp. 35–44. DOI: 10.58224/2618-7183-2022-5-3-35-44
3. Kashapov, R.N., Kashapov, N.F., Kashapov, L.N., Klyuev, S.V., Chebakova, V.Yu. Study of the plasma-electrolyte process for producing titanium oxide nanoparticles. Construction Materials and Products. 2022. 5 (5). Pp. 70–79. DOI: 10.58224/2618-7183-2022-5-5-70-79
4. Kashapov, R.N., Kashapov, N.F., Kashapov, L.N., Klyuev, S.V. Plasma electrolyte production of titanium oxide powder. Construction Materials and Products. 2022. 5 (6). Pp. 75–84. DOI: 10.58224/2618-7183-2022-5-6-75-84
5. Vatin, N., Barabanshchikov, Yu., Usanova, K., Akimov, S., Kalachev, A., Uhanov, A. Cement-based materials with oil shale fly ash additives. IOP Conf Ser Earth Environ Sci. IOP Publishing Ltd. 2020. 578 (1). Article no. 012043. DOI: 10.1088/1755-1315/578/1/012043
6. Barabanshchikov, Yu., Usanova, K., Akimov, S., Uhanov, A. Influence of Electrostatic Precipitator Ash “Zolest-Bet” and Silica Fume on Sulfate Resistance of Portland Cement. Materials. 2020. 13(21). Article no. 4917. DOI: 10.3390/ma13214917
7. Barabanshchikov, Y., Usanova, K. Influence of High-Calcium Oil Shale Ash Additive on Concrete Properties. Lecture Notes in Civil Engineering. 2021. 150 LNCE. Pp. 23–34. DOI: 10.1007/978-3-030-72404-7_3
8. Raju, S., Rathinam, J., Dharmar, B., Rekha, S., Avudaiappan, S., Amran, M., Usanova, K., Fediuk, R., Guindos, P., Ramamoorthy, R.V. Cyclically Loaded Copper Slag Admixed Reinforced Concrete Beams with Cement Partially Replaced with Fly Ash. Materials. MDPI. 2022. 15(9). Article no. 3101. DOI: 10.3390/ma15093101
9. Teixeira, E.R., Mateus, R., Camoes, A., Braganca, L., Branco, F.G. Comparative environmental life-cycle analysis of concretes using biomass and coal fly ashes as partial cement replacement material. Journal of Cleaner Production. 2016. 112. Pp. 2221–2230. DOI: 10.1016/j.jclepro.2015.09.124
10. Amran, M., Fediuk, R., Murali, G., Avudaiappan, S., Ozbakkaloglu, T., Vatin, N.I., Karelina, M., Klyuev, S., Gholampour, A. Fly ash-based eco-efficient concretes: A comprehensive review of the short-term properties. Materials. 2021. 14(15). Article no. 4264. DOI: 10.3390/ma14154264
11. Öz, H.Ö., Yücel, H., Güneş, M., Köker, T. Fly-ash-based geopolymer composites incorporating cold-bonded lightweight fly ash aggregates. Construction and Building Materials. 2021. 272. Pp. 121963. DOI: 10.1016/j.conbuildmat.2020.121963
12. Narattha, C., Chaipanich, A. Effect of curing time on the hydration and material properties of cold-bonded high-calcium fly ash–Portland cement lightweight aggregate. Journal of Thermal Analysis and Calorimetry. 2021. 145(17). Pp. 2277–2286. DOI: 10.1007/s10973-020-09730-8
13. Yang, S., Zhao, R., Ma, B., Si, R., Zeng, X. Mechanical and fracture properties of fly ash-based geopolymer concrete with different fibers. Journal of Building Engineering. 2023. 63. Part A. Article no. 105281. DOI: 10.1016/j.jobe.2022.105281
14. Korniejenko, K., Łach, M., Marczyk, J., Ziejewska, C., Halyag, N.P., Mucsi, G. Fly ash as a raw material for geopolymerisation-mineralogical composition and morphology. IOP Conf Ser Mater Sci Eng. 2019. 706(1). Article no. 012006. DOI: 10.1088/1757-899X/706/1/012006
15. Anees Ahmed, A.A., Lesovik, R., Lesovik, V., Fediuk, R., Klyuev, R., Amran, M., Ali, M., de Azevedo, A.R.G., Vatin, N. Demolition Waste Potential for Completely Cement-Free Binders. Materials. 2022. 15(17). Article no. 6018. DOI: 10.3390/ma15176018
16. Salamanova, M., Murtazaev, S.-A., Saidumov, M., Alaskhanov, A., Murtazaeva, T., Fediuk, R. Recycling of Cement Industry Waste for Alkali-Activated Materials Production. Materials. 2022. 15. Article no. 6660. DOI: 10.3390/ma15196660
17. Xu, G., Shi, X. Characteristics and applications of fly ash as a sustainable construction material: A state-of-the-art review. Resources, Conservation and Recycling. 2018. 136. Pp. 95–109. DOI: 10.1016/j.resconrec.2018.04.010
18. Zhang, N., Yu, H., Gong, W., Liu, T., Wang, N., Tan, Y., Wu, C. Effects of low- and high-calcium fly ash on the water resistance of magnesium oxysulfate cement. Construction and Building Materials. 2020. 230. Article no. 116951. DOI: 10.1016/j.conbuildmat.2019.116951
19. Fan, W.J., Wang, X.Y., Park, K.B. Evaluation of the Chemical and Mechanical Properties of Hardening High-Calcium Fly Ash Blended Concrete. Materials. 2015. 8(9). Pp. 5933–5952. DOI: 10.3390/ma8095282

20. Goenawan, V., Antoni, A., Hardjito D. A Preliminary Study on Cracking Tendency of Cement Paste Incorporating High Calcium Fly Ash. Applied Mechanics and Materials. 2015. 815. Pp. 158–163. DOI: 10.4028/www.scientific.net/AMM.815.158
21. Dhole, R., Thomas, M.D.A., Folliard, K., Drimalas, T. Sulfate resistance of mortar mixtures of high-calcium fly ashes and other pozzolans. ACI Mater Journal. 2011. 108(6). Pp. 645–654.
22. Antiohos, S., Tsimas, S. Investigating the role of reactive silica in the hydration mechanisms of high-calcium fly ash/cement systems. Cement and Concrete Composites. 2005. 27 (2). Pp. 171–181. DOI: 10.1016/j.cemconcomp.2004.02.004
23. Korpa, A., Seiti, B., Xhaxhiu, K., Mele, A., Trettin, R. Processing of high sulphate and free lime calcareous coal fly ash for producing high volume blended cements and complying grade products employed in civil engineering. Zastita materijala. 2014. 55(3). Pp. 251–258. DOI: 10.5937/ZasMat1403251K
24. Tsimas, S., Moutsatsou-Tsima, A. High-calcium fly ash as the fourth constituent in concrete: problems, solutions and perspectives. Cement and Concrete Composites. 2005. 27. 2. Pp. 231–237.
25. Klyuev, S.V., Bratanovskiy, S.N., Trukhanov, S.V., Manukyan, H.A. Strengthening of concrete structures with composite based on carbon fiber. Journal of Computational and Theoretical Nanoscience. 2019. 16(7). Pp. 2810–2814. DOI: 10.1166/jctn.2019.8132
26. Chen, B., Liu, J. Effect of fibers on expansion of concrete with a large amount of high f-CaO fly ash. Cement and Concrete Composites 2003. 33(10). Pp. 1549–1552.
27. Klyuev, S.V., Kashapov, N.F., Radaykin, O.V., Sabitov, L.S., Klyuev, A.V., Shchekina, N.A. Reliability coefficient for fibreconcrete material. Construction Materials and Products. 2022. 5 (2). Pp. 51–58. DOI: 10.58224/2618-7183-2022-5-2-51-58
28. Anthony, E.J., Bulewicz, E.M., Dudek, K., Kozak, A. The long term behaviour of CFBC ash–water systems. Waste Management. 2002. 22(1). Pp. 99–111. DOI: 10.1016/s0956-053x(01)00059-9.
29. Blondin, J., Iribarne, A., Iribarne, J., Anthony, E.J. Hydration of combustion ashes — a chemical and physical study. Fuel. 2001. 80(6). Pp. 773–784.
30. Sheng, G., Li, Q., Zhai, J., Li, F. Self-cementitious properties of fly ashes from CFBC boilers co-firing coal and high-sulphur petroleum coke. *Cement and Concrete Research.* 2007. 37(6). Pp. 871–876. DOI: 10.1016/j.cemconres.2007.03.013
31. Domanskaya, I., Oleynik, V., Minyazev, D. ICSC Problems and Perspectives of high-calcium fly ash from heat power plants in the composition of “green” building materials. E3S Web of Conferences. 2016. 6. Article no. 01014. DOI: 10.1051/e3sconf/20160601014
32. Barabanshchikov, Y., Usanova, K. Influence of Silica Fume on High-Calcium Fly Ash Expansion during Hydration. Materials. 2022. 15(10). Article no. 3544. DOI: 10.3390/ma15103544
33. Li, Z., Lu, D., Gao, X. Analysis of correlation between hydration heat release and compressive strength for blended cement pastes. Construction and Building Materials. 2020. 260. Article no. 120436. DOI: 10.1016/j.conbuildmat.2020.120436
34. Ghadir, P., Razeghi, H.R. Effects of sodium chloride on the mechanical strength of alkali activated volcanic ash and slag pastes under room and elevated temperatures. Construction and Building Materials. 2022. 344(2). Article no. 128113. DOI: 10.1016/j.conbuildmat.2022.128113
35. Li, J., Huang, Ya., Li, W., Guo, Ya., Ouyang, Sh., Cao, G. Study on dynamic adsorption characteristics of broken coal gangue to heavy metal ions under leaching condition and its cleaner mechanism to mine water. Journal of Cleaner Production. 2021. 329. Article no. 129756. DOI: 10.1016/j.jclepro.2021.129756
36. Chen, S., Du, Z., Zhang, Z., Zhang, H. Effects of chloride on the early mechanical properties and microstructure of gangue-cemented paste backfill. Construction and Building Materials. 2020. 235. Article no. 117504. DOI: 10.1016/j.conbuildmat.2019.117504
37. Ouyang, S., Huang, Y., Wu, L., Yin, W., Yang, x., Wang, J., Wang, G., Li, J., Lei, Y. Effects of chlorides on setting time, hydration heat and hydration products of fresh slurry of cemented paste backfill. Case Studies in Construction Materials. 2022. 17. Article no. e01462. DOI: 10.1016/J.CSCM.2022.E01462
38. Khan, I., François, R., Castel, A. Prediction of reinforcement corrosion using corrosion induced cracks width in corroded reinforced concrete beams. Cement and Concrete Research. 2014. 56. Pp. 84–96. DOI: 10.1016/j.cemconres.2013.11.006
39. Cheewaket, T., Jaturapitakkul, C., Chalee, W. Initial corrosion presented by chloride threshold penetration of concrete up to 10 year-results under marine site. Construction and Building Materials. 2012. 37. Pp. 693–698. DOI: 10.1016/j.conbuildmat.2012.07.061
40. Chen, Sh., Shui, Z., Sun, T., Gao, X., Guo, C. Effects of sulfate and magnesium ion on the chloride transportation behavior and binding capacity of Portland cement mortar. Construction and Building Materials. 2019. 204(7). Pp. 265–275. DOI: 10.1016/j.conbuildmat.2019.01.132
41. Shi, Z., Geiker, M.R., Lothenbach, B., De Weerdt, K., Frreiro, S., Enemark-Rasmussen, K., Skibsted, J. Friedel’s salt profiles from thermogravimetric analysis and thermodynamic modelling of Portland cement-based mortars exposed to sodium chloride solution. Cement and Concrete Composites. 2017. 78. Pp. 73–83. DOI: 10.1016/j.cemconcomp.2017.01.002
42. Yuan, Q., Shi, C., De Schutter, G., Audenaert, K. Chloride binding of cement-based materials subjected to external chloride environment – A review. Construction and Building Materials. 2009. 23(1). Pp. 1–13. DOI: 10.1016/j.conbuildmat.2008.02.004
43. Zaporozhets, I.D., Okorokov, S.D., Pariyskiy, A.A. Teplovydeleniye betona [Heat Liberation by concrete]. Moscow: Stroyizdat, 1966. 314 p. (rus)
44. Heller, L., Ben-Yair, M. Effect of chleride solutions on Portland cement. Journal of Applied Chemistry. 1966. 16(8).
45. Rapin, J.Pp., Renaudin, G., Elkaim, E., Francois, M. Structural transition of Friedel’s salt $3CaO{\cdot}Al_2O_3{\cdot}CaCl_2{\cdot}10H_2O$ studied by synchrotron powder diffraction. Cement and Concrete Research. 2002. 32(4). Pp. 513–519. DOI: 10.1016/S0008-8846(01)00716-5
46. Lobo, C., Cohen, M.D. Hydration of type K expansive cement paste and the effect of silica fume: I. Expansion and solid phase analysis. Cement and Concrete Research. 1992. 22(5). Pp. 961–969.

Information about authors:

Kseniia Usanova,
ORCID: https://orcid.org/0000-0002-5694-1737
E-mail: plml@mail.ru

Yuriy Barabanshchikov, *Doctor of Technical Sciences*
ORCID: https://orcid.org/0000-0001-7011-8213
E-mail: ugb@mail.ru

Saurav Dixit,
E-mail: sauravarambol@gmail.com

Received 16.07.2023. Approved after reviewing 22.08.2023. Accepted 23.08.2023.

Magazine of Civil Engineering

ISSN 2712-8172

journal homepage: http://engstroy.spbstu.ru/

Research article

UDC 691.3

DOI: 10.34910/MCE.123.6

Self-compacting concrete with finely dispersed additives and superplasticizer

D.S. Dyussembinov[1], ***T. Awwad***[2, 3], ***Y.Y. Sabitov***[1], ***A.A. Zhumagulova***[1], ***Zh.A. Shakhmov***[1], ***Zh. Kaliyeva***[1], ***D.O. Bazarbayev***[1] ✉

[1] L.N. Gumilyov Eurasian National University, Astana, Republic of Kazakhstan

[2] Kazakh Leading Academy of Engineering and Construction Inc., Almaty, Republic of Kazakhstan

[3] Emperor Alexander I St. Petersburg State Transport University, St. Petersburg, Russian Federation

✉ *phdd84@mail.ru*

Keywords: self-compacting concrete, silica fume, compressive strength, slump-flow, fly ash, plasticizing additive

Abstract. This article investigates the features, qualitative characteristics, and structure of self-compacting concrete (SCC). In particular in this article we present the results of research into the influence of finely dispersed fillers with superplasticizer on physical and mechanical properties of self-compacting concrete. By developing the optimum compositions of different types of concrete, we determined the compressive strength of self-compacting concrete. We proved that plasticizing additive MasterGlenium ACE (Admixture Controlled Energy) significantly liquefies concrete mixture, which allows obtaining self-compacting concrete. The influence of finely dispersed fillers and plasticizers on the density of the concrete mixture was also studied. During the research the effectiveness of the complex application of silica fume (SF) and plasticizer was identified. The results of the research confirm the effect of the amount of fine aggregate and the amount of ACE affecting the workability of the concrete mixture and its strength.

Acknowledgments: The authors of the project express deep gratitude to the Research and Production Center of L.N. Gumilyov Eurasian National University “ENU-Lab” for the provided laboratory base for research work.

Citation: Dyussembinov, D.S., Awwad, T., Sabitov, Y.Y., Zhumagulova, A.A., Shakhmov, Zh.A., Kaliyeva, Zh., Bazarbayev, D.O. Self-compacting concrete with finely dispersed additives and superplasticizer. Magazine of Civil Engineering. 2023. 123(7). Article no. 12306. DOI: 10.34910/MCE.123.6

1. Introduction

At present, high-rise buildings are being built extensively worldwide, and the advancement of infrastructure necessitates the use of materials that are capable of high performance [1]. Self-compacting concrete (SCC) has superior characteristics that increase efficiency and improve working conditions by eliminating the need for vibration and compaction. SCC is appropriate for use in structures with dense reinforcement without requiring vibration, and it contributes to achieving a superior surface finish [2]. As a rule, compared to vibrated concrete, SCC has a significantly higher content of finely dispersed phase [3, 4]. Therefore, the flowability of the concrete mixture should be high enough to facilitate the release of concrete from the air contained in it, create optimal adhesion between steel and concrete even with a high degree of reinforcement, and reduce the risk of defects (for example, the accumulation of coarse aggregate) [5]. On the other hand, self-compacting concrete must have a good adhesion capacity of individual components and prevent delamination of the mixture [6].

In order to simultaneously achieve the required flowability and adhesion capacity of the components, a rational ratio of the composition and the amount of finely dispersed phase, water and liquefaction plasticizers should be observed. The amount of water must be determined in such a way that it exactly corresponds to the water consumption of the finely dispersed phase and moistens the surface of the concrete mixture [7–9].

The addition of dusty materials (limestone flour or fly ash) leads to an improvement in the flowability of the mixture [10, 11]. However, too high a content of very small particles under the same conditions leads to a decrease in its flowability. In this case, the finely dispersed phase leads to a change in water consumption, and the changed composition, as a rule, entails a change in the properties of the freshly prepared concrete mixture [12]. The additional water consumption simultaneously affects the flowability of the concrete mixture and the adhesion of the concrete components. This can lead to the fact that while increasing the flowability of the concrete mixture, the adhesion between its components decreases, which will make the structure of concrete unstable. Results of early studies it is shown that a change in the amount of water added by ± 3 l/m may be sufficient to cause settling, separation, air involvement or low flowability of the concrete mixture. While the water affects the flowability and adhesion of the components of the concrete mixture and can lead to segregation, the use of a liquefier regulates its flowability [3, 13, 14].

Currently, in the production of self-compacting concrete, liquefiers of a new generation, the so-called plasticizing additives based on polycarboxylate, are used almost exclusively [15, 16]. One of them is a highly reducing and superplasticizing additive based on polycarboxylate ester – MasterGlenium ACE [17]. Reducing the need for water through the use of MasterGlenium ACE allows us to eliminate the above shortcomings and immediately create strong self-compacting concrete mixtures [17–20].

In addition, positive effects of industrial waste, silica fume, and fly ash together with superplasticisers have been studied and experimentally confirmed in works by Y. Utepov et.al. [21], and D. Akhmetov et.al. [22].

Thus, the object of the research is use of finely dispersed fillers from man-made waste and superplasticizing additive based on polycarboxylate ester – MasterGlenium ACE.

The goal is researching the effect of different types of finely dispersed fillers from man-made waste and chemical additives on the workability of self-compacting concrete and the strength of the concrete matrix.

The research objectives:

- research of raw materials and methods to determine the flowability of the concrete mixture and the strength of the cured concrete;
- analysis of fine fillers from man-made waste (SF and fly ash) in combination with plasticizer ACE effect on the flowability of SCC and determination of its strength.

Research were carried out on the basis of the laboratory of the L.N. Gumilyov Eurasian National University to determine the effect of fine aggregates with a superplasticizer on the physical and mechanical properties of self-compacting concrete.

2. Materials and Methods

Concrete compositions were developed to investigate the effect of various types of finely dispersed fillers, such as fly ashes [23] and silica fume [24] in combination with the ACE superplasticizer, on the workability of self-compacting concretes and the compressive strength of the concrete matrix (Table 1). In the experiment were used Portland cement type CEM II/A-S 42.5N, sand with size modulus 2.23 and coarse aggregate fraction of 5 mm. The amount of fillers was taken in relation to the cement binder in percentage.

Table 1. Composition of the tested concrete

Composition	Cement, kg	Sand, kg	Coarse gravel, Kg	ACE, %	SF, %	Water, litre	Fly ash %
Control sample without additives	300	800	1150	-	-	180	-
ACE	300	820	1180	<1	-	135	-
Silica fume (SF) ACE	300	850	1200	<1	<10	135	-
ACE fly ash	300	800	1150	<1	-	135	<2

After determining the flowability and compressive strength of concrete, optimal compositions of different types of concrete were developed:

– composition without additives – Type 1;
– composition with ACE plasticizer – Type 2;
– composition with ACE plasticizer and silica fume – Type 3;
– composition with ACE plasticizer and fly ash – Type 4.

Concrete testing was carried out in the laboratory of Research and Production Center of L.N. Gumilyov Eurasian National University “ENU-Lab”. For a control sample, a composition without additives was taken – Type 1.

2.1. Additive superplasticizer

Admixture Controlled Energy (ACE) series of additives are products of BASF (Germany) [25], the main purpose of which is to reduce energy costs in the construction industry. ACE can be used to produce concrete with high strength, density and surface quality. Allows to produce flowable and highly flowable concrete mixes, including self-compacting mixes. The additive used meets the requirements of Standard of Organization 70386662-310-2014 [26].

Technical data of the additive are shown in Table 2.

Table 2. Technical data Master Glenium ACE 430.

Technical data	Size
Form	Liquid
Color	Light brown or brown
Density (at 20 ºC)	1.06 ± 0.02 g/cm^3
Dry residue	29 ± 2 %
Hydrogen index (at 20 ºC), pH	3.5-7.5
Cl-ion content, in wt. %	<0.1 %
Guaranteed shelf life	1 year from the date of manufacture

2.2. Industrial waste fly ash

The granulometric composition of ash significantly affects the quality of concrete. Ash studies have shown that three groups of substances can be distinguished in the composition of ash and slag:

– Vitreous;
– Crystalline;
– Organic.

The vitreous substance is represented by spherical formations subjected to hydration. The organic part is a type of coke and semi-coke. The crystalline phase of ash consists of grains of quartz, mullite, hematite, kaolinite and feldspar. Thus, the composition of the ash of hydro-removal in mineralogical composition is partially similar to the composition of clinker, which confirms the effectiveness of its use. The chemical composition of the ash, presented in Table 3, also confirms the similarity.

Ashes from the heat and power plant of Astana city were taken as fly ashes.

Table 3. Chemical composition of fly ash.

Mineral content in %							
SiO_2	Al_2O_3	CaO	MgO	Fe_2O_3	SO_3	Alkali metals	Ash residue
51.5	17.4	12.4	1.9	6.2	3	1.3	6.3

2.3. Silica fume

It is known that silica fume is an effective additive for high-strength concretes, including in the form of an organomineral additive [27]. It is obtained by high-temperature processing of starting materials containing silica. The processing is related to the process of sublimation of silicon oxides. During the condensation of sublimation products in the cooling process, a finely dispersed colloid-like, mostly amorphous material is formed. The predominant particle size of silica fume is from 2...3 to 0.01 micrometres. X-ray phase analysis established the presence of silicon oxide in the silica fume in the form of coesite, which gives it a high chemical activity in an aqueous medium. This is a highly baric modification of silica – SiO_2. The average density is 2.95...3 g/cm^3, the hardness is 7.5...8 on the Mohs scale. When the pressure decreases, it turns into quartz. In this case, the presence of coesite in the silica fume is unlikely [28, 29].

Silica fume is a by-product of metallurgical production in the smelting of ferrosilicon and its alloys, formed as a result of the reduction of high purity quartz by carbon in electric [27, 30, 31]. In the process of smelting silicon alloys, some part of the silicon monoxide SiO passes into a gaseous state and, undergoing oxidation and condensation, forms an extremely fine product in the form of spherical particles with a high content of amorphous silica. When smelting 1 ton of ferrosilicon alloys, about 300 kg of silica fume is released. As the silicon content of the alloy increases, the amount of silicon dioxide SiO_2 increases [27, 30, 31].

To research the impact of industrial waste, the silica fume produced from the Aksu Ferroalloy Plant (Pavlodar city) was taken. Table 4 shows the chemical composition of silica fume waste.

Table 4. Chemical composition of silica fume, in percentage.

SiO_2	Al_2O_3	Fe_2O_3	CaO	MgO	Na_2O	K_2O	C	Si
86-92	0.6-0.8	0.4-0.7	0.9	0.8-1	0.6-0.8	1.2-1.4	0.9-1.2	0.2-0.3

To determine the qualitative characteristics of self compacting concrete, researches were carried out in accordance with Russian State Standard GOST R 58002-2017/EN 12350-8: 2010 “Testing fresh concrete – Part 8: Self compacting concrete – Slump-flow test”. The standard establishes the procedure for determining the blurring and time t_{500} [32].

The slump-flow and time t_{500} were used to assess the flowability and fluidity of the self compacting concrete mixture in the absence of obstacles. Based on the cone sediment measurement tests described in Russian State Standard GOST R 57809-2017/EN 12350-2:2009 [33], the results of which are an indicator of the filling capacity of the self compacting concrete mixture. Time t_{500} is an indicator of the spread rate and relative viscosity of the self compacting concrete mixture. The concrete mixture was formed into a cone, after removing the cone, the time was measured from the moment the cone began to move upwards to the spread of the concrete mixture to a diameter of 500 mm, that is, this is the time t_{500}. Then the largest diameter of the spread and another diameter perpendicular to it were measured. The average value is a blurring. The devices corresponded to Russian State Standard GOST R 57809-2017/EN 12350-2:2009 [33]. The base plate on which the concrete mixture flows and on which the flowability determination is performed, was made in the form of a flat steel plate with an area of at least 900×900 mm in the plan.

The center of the plate is marked with a cross, the lines of which are parallel to the edges of the plate and circles with a diameter of (210±1) mm and (500±1) mm, the centers of which coincide with the central point of the plate. All lines are not wider than 2 mm and no deeper than 1 mm according to the regulatory and technical documentation. To measure the blur, a tape measure (measuring tape) with a length of 5,000 mm and with a length division of not more than 1 mm was used.

To determine the slump-flow, the base plate was installed on a flat horizontal surface that is not subject to vibration or shock. With the help of the level, the upper surface was checked for horizontality. The platform and cone were wiped with a wet cloth, preventing excessive moisture on the surface of the plate and inside the cone. Placed the cone in the center inside a 210-millimeter circle on the base plate and held it in place, pressing the legs on the legs. Filled the cone at one time without mechanical sealing and removed the excess from the top of the cone. We withstood the cone of 30 seconds, after which we raised the cone in one motion in 2 seconds, without preventing the concrete mixture from slump-flowing. The stopwatch was turned on immediately after the cone broke away from the base plate and recorded the time during which the spreading concrete mixture first touched the 500-millimeter circumference mark. After the melting of the concrete mixture stabilized on its own without affecting the slab or concrete mixture, the melting diameter of the mixture was measured and recorded as d_1 with rounding to 10 mm. Then the spread of the spread at right angles to d_1 was measured and fixed as d_2. During the studies, the difference between d_1 and d_2 was not more than 30 mm.

The slump-flow, the mean of d_1 and d_2 rounded to the nearest 10 mm, was determined by the formula:

$$SF = \frac{(d_1 + d_2)}{2},$$

in the methodology, the following are taken as the main designations: SF is slump-flow; d_1 is the largest diameter of the spreading of the slump-flow, mm; d_2 is spreading of the slump-flow at an angle of 90 degrees to d_1, mm.

Time t_{500} is indicated in the report with rounding to the nearest 0.5 s.

The preparation and test process are presented in Fig. 1a) and 1b).

(a) Cone loading **b) Slump-flow test**

Figure 1. Preparation for the slump-flow test.

The compressive strength of self compacting concrete was determined according to Interstate Standard GOST 10180-2012 Concretes. Methods for compressive strength determination using reference specimens [34]. Tests were carried out on 100×100×100 mm specimens, prepared in advance by forming them into forms without vibration compaction and bayoneting. Sample preparation is shown in Fig. 2 a). The age of the samples during the test is 28 days.

a) Sample preparation **b) Compressive strength test**

Figure 2. Determination of compressive strength.

The compression test is shown in Fig. 2 b), the samples were tested on a press of the automatic brand CONTROLS (Pilot) 500 kN. Compressive strength from one series was defined as the arithmetic mean of the tested samples.

3. Results and Discussions

The following study conducted research on fresh and hardened concrete mixtures containing different proportions of pumice powder, fly ash, and slag as partial replacements for Portland cement. The results showed that using more than 30 % pozzolanic materials in the binary blended Portland cement mixtures resulted in a significant decline in both the fresh and hardened test results. To improve the properties of self-compacting concrete (SCC) containing pumice, a ternary blended cement replacement with pumice and silica fume (SF) was developed. Incorporating SF substantially enhanced the properties of the mixtures [35]. Another study which focused on the influence of variation in cement characteristics on workability and strength of SCC with fly ash and slag additions came to the result that the characteristics of cements and admixtures have a strong influence on the properties of self-compacting concrete (SCC), and even small variations in these materials can have a significant impact on these properties. Generally, adding fly ash (FA) to cement increased their slump values, especially when using SP1. For SP2, the slump values of all cements increased with an increase in FA to a certain extent and then remained constant [36].

In our study research of the properties of self compacting concrete and the effect of finely dispersed fillers in combination with a plasticizer on it. BASF (Germany) ACE (Admixture Controlled Energy) was used as a super plasticizer. The results of the research show (Table 5) that the ACE additive significantly liquefies the concrete mixture allowing for self compacting concrete.

Table 5. Research of workability.

Composition	ACE %	SF %	Fly ash	W/C ratio	Grade by slump-flow cone	Time from	
						t_{500}	Total
Type 1	0	0	0	0.6	P 4	7	8
Type 2	0.5	-	0	0.45	P 4	5	10
	1		0		P 5	3	11
	1.5		0		P 6	2.5	12
Type 3	0.5	10	0	0.45	P 4	6	10
	0.5	15	0		P 4	6.5	10
	0.5	20	0		P 4	7	9
	1	10	0		P 5	4	7
	1	15	0		P 4	5	9
	1	20	0		P 4	5	9
	1.5	10	0		P 5	4	11
	1.5	15	0		P 5	4	11
	1.5	20	0		P 4	4	8
Type 4	0.5	0	2	0.45	P 4	5	10
	0.5	0	4		P 4	6	9
	0.5	0	6		P 4	6	7
	1	0	2		P 5	3	11
	1	0	4		P 4	4	9
	1	0	6		P 4	5	9
	1.5	0	2		P 5	3	11
	1.5	0	4		P 5	4	10
	1.5	0	6		P 4	4	10

The obtained results show that regardless of the amount of finely dispersed fillers, the flowability of the concrete mixture increases with an increase in the ACE plasticizer, and with a small amount of plasticizer, the flowability difference is large according to Fig. 3.

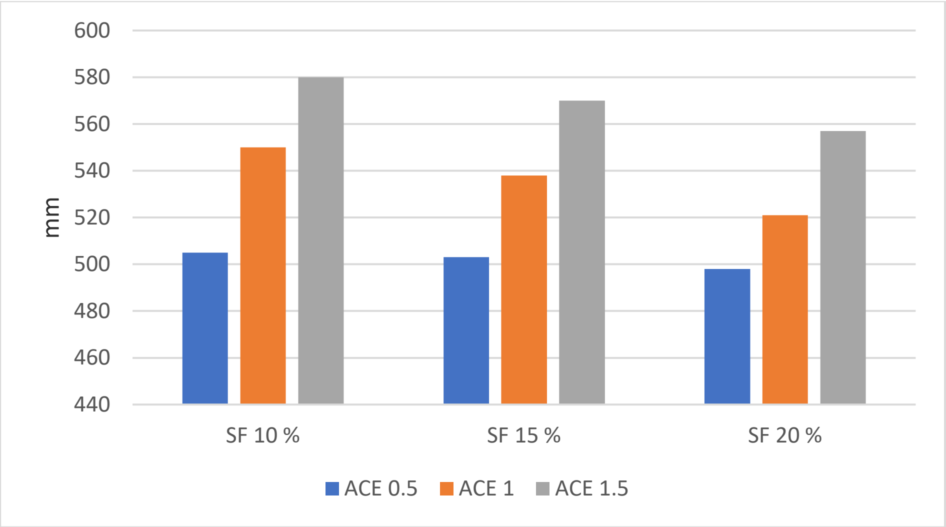

Figure 3. The diameter of the cone blur with a different number of SF and ACE.

Fig. 3 shows that as the amount of ACE plasticizer increases, the flowability of the concrete mixture increases. If we compare the slump-low diameter of the composition SF 10 % with the SF 20 % with ACE 0.5 %, then we see an increase in flowability by 1.4 %. The difference in the slump-flow of the cone of the composition of SF 10 % with SF 20 % with ACE 1.5 % is 4 %. This shows the effect of the plasticizer on the flowability of the finely dispersed SF filler.

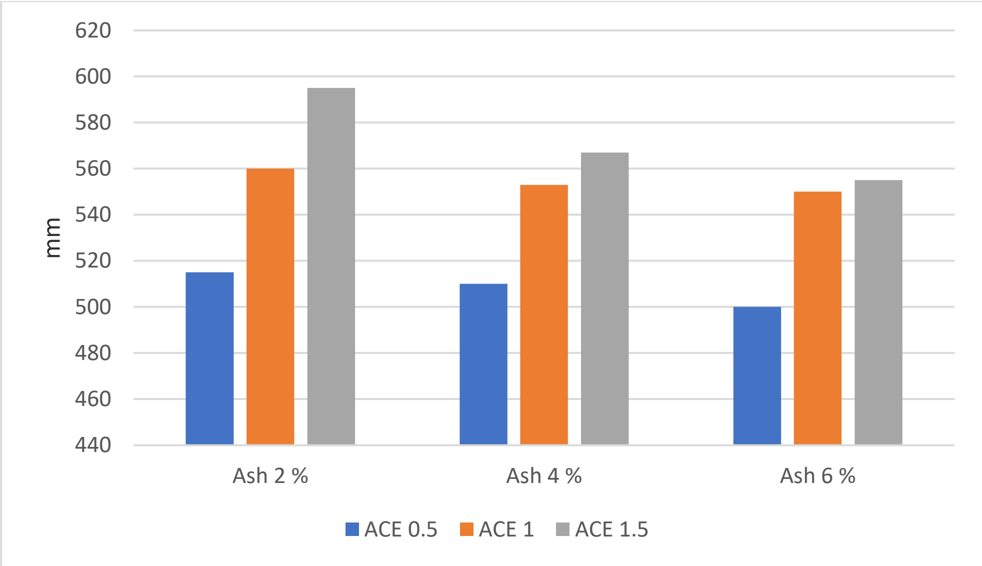

Figure 4. The diameter of the cone slump-flow with different amounts of fly ash and ACE.

The results of Fig. 4 show that the change in flowability depends on the amount of ash and confirms formulations where the amount of ACE plasticizer is 1 % and 1.5 % with an ash content of 6 %, the difference in flowability is 0.9 %. With 1 % ACE and 1.5 ACE and 4 % fly ash the difference in workability was 2.65 % which is almost three times higher than the composition with 6 % fly ash. Consequently, increasing the amount of hydro removal ash reduces the workability of the concrete mixture.

The following researches were carried out to determine the effect of finely dispersed fillers and plasticizers on the density of the concrete mixture. As is known, the workability of the concrete mixture, depending on the production circumstances (transportation, delay in laying time, compaction method and other factors), is often associated with the water consumption of the concrete mixture [37]. The results of experiments to determine the effect of ACE additives and finely dispersed fillers on the water consumption, density of the concrete mixture are presented in Table 6.

Table 6. Influence of finely dispersed fillers and plasticizers on the density of the concrete mixture at the maximum content of finely dispersed fillers and ACE plasticizer of 1.5 %.

Composition	Water consumption W/C	Average density, kg/m^3
Type 1	0.6	2250
Type 2	0.45	2300
Type 3	0.45	2350
Type 4	0.45	2250

From Table 6 it can be seen that the density of the composition with ash, even with the use of the ACE plasticizer (Type 4), does not increase with respect to the composition of Type 1, and unlike the composition with silica fume under the same conditions, the increase in density from the Type1 sample was 4.4 %.

Thus, the research carried out the effectiveness of silica fume SF in combination with the plasticising additive ACE. It is proved that with increase of ACE amount up to 1.5 % the flowability of concrete mixture significantly increases. It is also confirmed that the flowability of the concrete mixture decreases considerably with the increase of the fly ash.

To determine the effect of the investigated finely dispersed fillers and plasticizer on the strength properties of the self-compacting concrete, comparative tests of Type 1, Type 2 Type 3 and Type 4 with different quantities of components were carried out. All compressive strength values are given together with the scaling factors. The results of the compressive strength properties of the test specimen are shown in Table 7.

Table 7. Quality characteristics of the control sample.

Composition	W/C ratio	Compressive strength, MPa	Density, kg/m^3
Reference sample Type1	0.6	25	2235

The results of statistical processing of data on the test of self-compacting concrete are shown in Fig. 5, 6, 7.

The results of the compressive strength tests of the concrete specimens, 10 cm cubes, are shown in Fig. 7 with an age of 28 days.

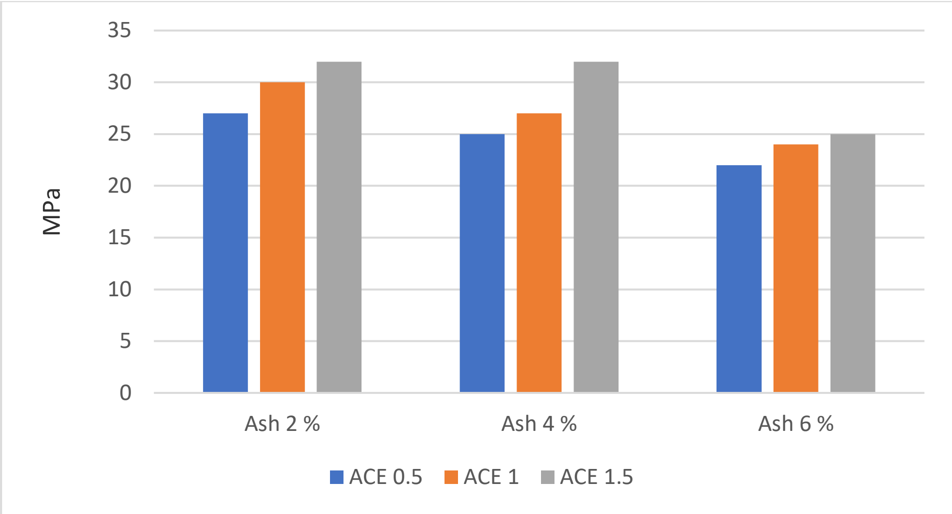

Figure 5. Compressive strength of self-compacting concrete in the fly ash.

The research shows a decrease in strength with increasing hydro removal ash and an increase in strength with increasing ACE plasticizer. Fig. 5 shows the compressive strength increase of the 2 % and 4 % hydro removal ash in the presence of 1.5 % ACE plasticizer in contrast to the 6 % hydro removal ash which shows a strength decrease of 22 %. This confirms the research that the effect of the plasticizer decreases with increasing amounts of ash is shown Fig. 5.

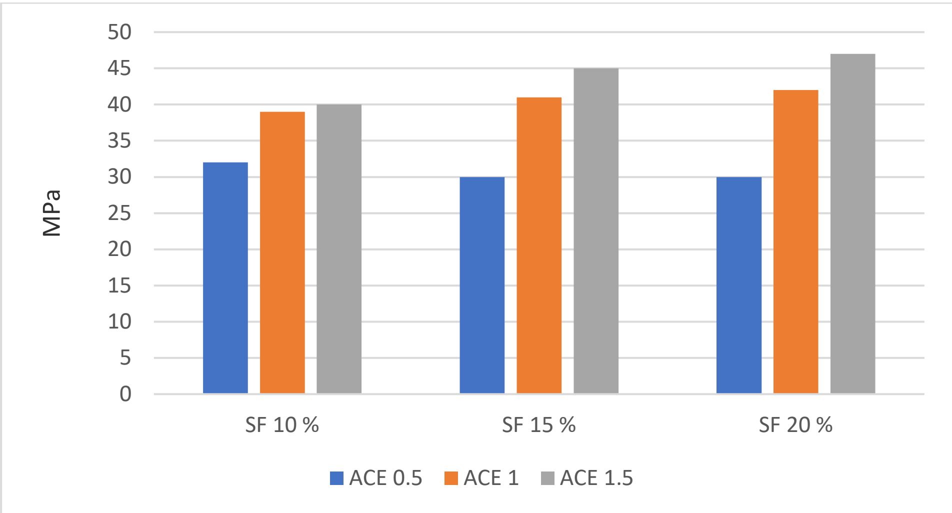

Figure 6. Compressive strength of self-compacting concrete on silica fume (SF).

The research of the compressive strength of concrete on the basis of SF showed positive results with different compositions. In the process of compressive strength testing, the compressive strength growth pattern was determined with increasing amount of ACE and stable growth of compressive strength with increasing composition of SF. According to Fig. 6 with composition of SF 10 % and ACE 0.5 % the result was 32 MPa, and with SF 20 % and ACE 0.5 % it was 30 MPa and increase of compressive strength of the sample of the first composition by 6.5 %. At composition SF 10 % and ACE 1.5 the compressive strength is obtained 40 MPa, and at SF 20 % and ACE 1.5 the compressive strength is increased up to 47 MPa. In a comparative analysis, the results show the opposite dynamics and with the increase in the amount of SF (subject to an increase in the amount of plasticizer ACE) the increase in compressive strength of the concrete is 17.5 %.

Thus, the conducted research confirms the effectiveness of the integrated use of SF and plasticizer, and it can also be assumed that SF has activity that is manifested in the process of hydration when combined with a plasticizer.

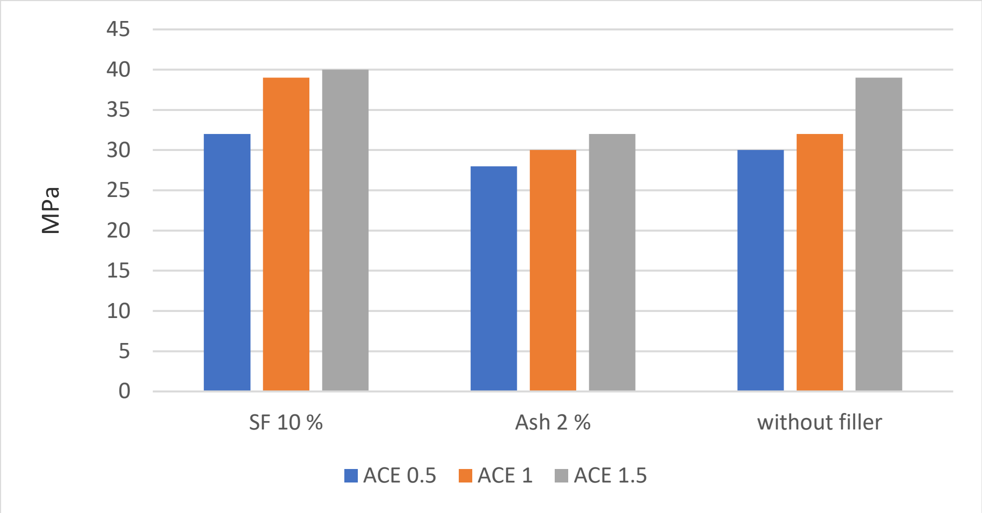

Figure 7. Comparative analysis of the compressive strength of self-compacting concrete Type 2, Type 3, Type 4, with a minimum amount of filler.

The comparative analysis presented in Fig. 7 shows the dynamics of compressive strength growth depending on the fillers and the ACE plasticizer. The results showed that with a minimum ash content the samples have the lowest strength in the three positions of the amount of ACE plasticizer 0.5 %, 1 %, 1.5 %. This research confirms that ash has no activity, and the increase in strength is due to the presence of a plasticizer in its composition. However, it must be recognized that a finely dispersed filler in the form of ash with its optimal ratio in comparison with a sample without a filler improves the flowability of the concrete mixture and increases the strength of the control sample type 1 by 28 %.

Research of concrete with silica fume SF with a minimum amount of it increases its strength in contrast to a sample without a filler, which indicates an additional activity of SF, which depends on the amount of ACE plasticizer. The compressive strength of a sample with SF at an ACE of 1.5 % is 40 MPa, and a sample without a filler with the same amount of ACE has a strength of 39 MPa. Thus, the Type 3 sample has a strength higher than the Type 2 sample by 2.5 % and, compared to the Type 1 control sample, Type 3 is 60 % higher than the Type 1 control sample, Type 2 and 56 % higher than the Type 1 control sample.

A comparative analysis of the compressive strength index with finely dispersed fillers, fly ash 4 %, SF 15 %, with different ACE plasticizer indicators of 0.5, 1, 1.5 (in %) are presented in Fig. 8.

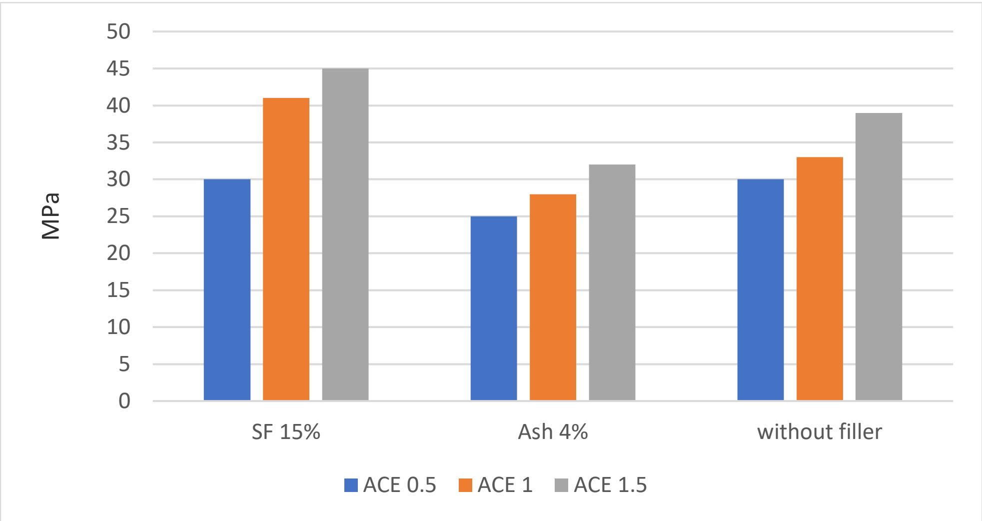

Figure 8. Comparative analysis of the compressive strength of self-compacting concrete Type 2, Type 3, Type 4, with an average amount of filler.

The research of the compressive strength of concrete, presented in Fig. 8, show an increase in the strength of a Type 3 sample based on SF by 15 % at ACE 0.5 % of 30 MPa, and at ACE 1 % – 41 MPa, which is 36.7 % more. Accordingly, the strength at ACE increased by 1.5 % to 45 MPa, which amounted to an increase in strength from a grade with ACE 0.5 % by 50 %. In contrast to the samples with SF silica the samples with fly ash did not show significant strength increase.

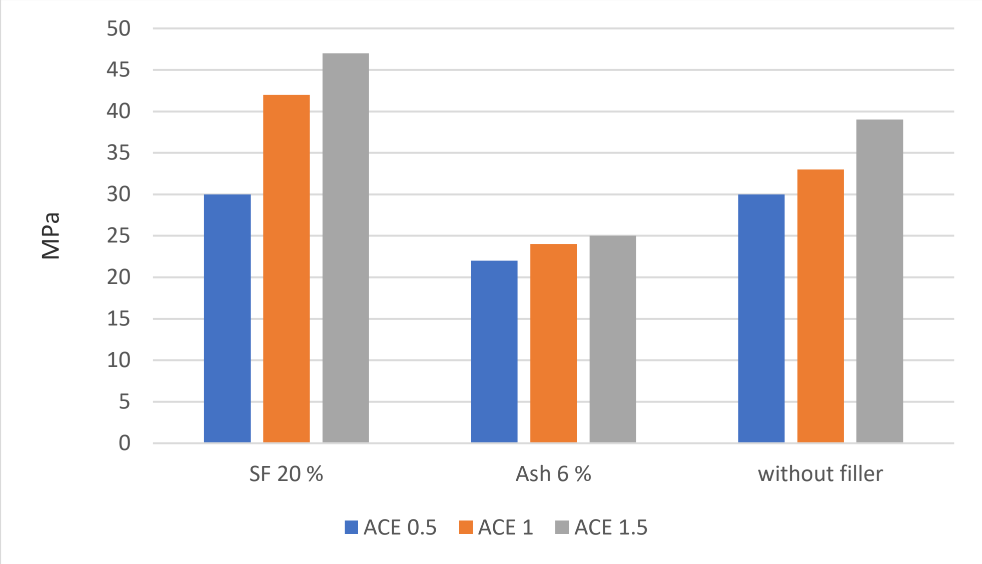

Figure 9. Comparative analysis of the compressive strength of self compacting concrete Type2, Type 3, Type 4, with the maximum amount of filler.

Fig. 9 shows the maximum amount of finely dispersed fillers. According to the analysis of the quality of the samples obtained, it is possible to note a maximum decrease in the strength of samples based on hydraulic removal ash. These results may indicate that the use of finely dispersed filler of fly ash is unacceptable in the amount of 6 % of the mass of cement. However, samples based on SF in the amount of 20 % continue to increase the strength of concrete. Thus, with an increase in the ACE plasticizer from 0.5 % to 1.5 %, the strength increased by 56.7 %, which indicates that the dynamics of strength growth continues to grow.

Thus, the use of fly ash is effective only with a ratio to cement of not more than 4 %, with an increase in the ratio, the strength of concrete decreases. The optimal content in the concrete mixture of SF is also established. The compressive strength of samples based on SF, with the condition of using plasticizers, increases regardless of its amount.

4. Conclusions

1. Researches of a concrete mixture based on finely dispersed SF fillers in combination with ACE and fly ash in combination with the ACE plasticizer were carried out. The results showed the effect of the amount of finely dispersed filler and amount of ACE on workability and compressive strength of concrete mixture.

According to the results of the research, the effectiveness of the use of fly ash was confirmed, but the dependencies affecting the flowability of the concrete mixture were also revealed. Thus, an increase in the ash of hydro-removal of more than 4 % reduces the flowability of the concrete mixture and significantly reduces the strength. The qualitative characteristics of self compacting concrete with different amounts of SF and ACE were also determined. The obtained results show maximum blowing efficiency of SF 15 % and ACE 1.5 %, which can be explained not only by the flowability of the cement binder, but also by the finely dispersed filler, as it is active in the hydration process of the concrete.

However, the research also showed an increase in the compressive strength of the self compacting concrete with an increase in the amount of SF. At SF 20% and ACE 1.5 %, the strength was 47 MPa, which is 4.5 % higher than the sample with SF 15 % and ACE 1.5 %, which indicates an increase in strength with an increase in the amount of SF. To obtain a more mobile concrete, this composition has a low grade index of P4 for the slump-flow of the cone, while the grade by the slump-flow for the composition of SF 15 % and ACE 1.5 % is P5.

2. The recommendations reflect the results of empirical research methods; choosing the maximum effective amount of finely dispersed fillers and plasticizer for both fly ash and SF is based on the results of research and analysis.

References

1. Kharun, M., Koroteev, D.D. Heat treatment of self-compacting high-strength concrete in cast in situ construction using infrared rays. Materials Science Forum. 2019. 972. Pp. 84–90. DOI: 10.4028/www.scientific.net/MSF.972.84
2. Kharun, M., Nikolenko, Y.V., Stashevskaya, N.A., Koroteev, D.D. Thermal treatment of self-compacting concrete in cast-in-situ construction. Key Engineering Materials. 2017. 753. Pp. 315–320. DOI: 10.4028/www.scientific.net/KEM.753.315
3. Faraj, R.H., Mohammed, A.A., Omer, K.M. Self-compacting concrete composites modified with nanoparticles: A comprehensive review, analysis and modeling. Journal of Building Engineering. 2022. 50. Article no. 104170. DOI: 10.1016/j.jobe.2022.104170.
4. Suprakash, A.S., Karthiyaini, S., Shanmugasundaram, M. Future and scope for development of calcium and silica rich supplementary blends on properties of self-compacting concrete – A comparative review. Journal of Materials Research and Technology. 2021. 15. Pp. 5662–5681. DOI: 10.1016/j.jmrt.2021.11.026
5. Benaicha, M., Jalbaud, O., Hafidi Alaoui, A., Burtschell, Y. Porosity effects on rheological and mechanical behavior of self-compacting concrete. Journal of Building Engineering. 2022. 48. Article no. 103964. DOI: 10.1016/j.jobe.2021.103964
6. Geiker, M., Jacobsen, S. Self-compacting concrete (SCC). Developments in the Formulation and Reinforcement of Concrete. Elsevier, 2019. Pp. 229–256. DOI: 10.1016/B978-0-08-102616-8.00010-1
7. Carro-López, D., González-Fonteboa, B., Martínez-Abella, F., González-Taboada, I., de Brito, J., Varela-Puga, F. Proportioning, fresh-state properties and rheology of self-compacting concrete with fine recycled aggregates. Hormigón y Acero. 2018. 69(286). Pp. 213–221. DOI: 10.1016/j.hya.2017.04.023
8. Elemam, W.E., Abdelraheem, A.H., Mahdy, M.G., Tahwia, A.M. Optimizing fresh properties and compressive strength of self-consolidating concrete. Construction and Building Materials. 2020. 249. Article no. 118781. DOI: 10.1016/j.conbuildmat.2020.118781
9. Bahraman, M., Asadollahfardi, G., Salehi, A.M., Yahyaei, B. Feasibility study of using wash water from ready mixed concrete plant and synthetic wastewater based on tap water with different total dissolved solid to produce self-compacting concrete. Journal of Building Engineering. 2021. 41. Article no. 102781. DOI: 10.1016/j.jobe.2021.102781
10. Kraus, R.N., Naik, T.R., Ramme, B.W., Kumar, R. Use of foundry silica-dust in manufacturing economical self-consolidating concrete. Construction and Building Materials. 2009. 23 (11). Pp. 3439–3442. DOI: 10.1016/j.conbuildmat.2009.06.006
11. Singh, A., Mehta, P.K., Kumar, R. Performance of binary admixtures (Fly Ash and Silica Fume) on Self Compacting concrete. Materials Today: Proceedings. 2022. 58. Part 3. Pp. 970–977. DOI: 10.1016/j.matpr.2022.02.489
12. Ortigara, Y.V.B., Lintz, R.C.C., Pimentel, L.L., Rodrigues Simões Ortigara, M.C., Jacintho, A.E.P.G. de A., Gachet, L.A., Fontanini, P.S.P. Influence of the use of sanitary ware waste in self-compacting concrete production. Materials Today: Proceedings. 2022. 65. Part 2. Pp. 511–519. DOI: 10.1016/j.matpr.2022.03.065
13. Sonebi, M., Yahia, A. Mix design procedure, tests, and standards. Self-Compacting Concrete: Materials, Properties and Applications. 2020. Pp. 1–30. DOI: 10.1016/B978-0-12-817369-5.00001-5
14. Badgujar, S., Kumar Dwivedi, A. Microstructural analysis of Self-Compacting Concrete– A review. Materials Today: Proceedings. 2022. 65. Part 2. DOI: 10.1016/j.matpr.2022.04.185
15. Sulakshna Sanjay, S., Pal, A., Kishor Chakraborty, S., Ali Khan, H. Reduction of shrinkage of self compacting concrete using polycarboxylate ether as shrinkage reducing admixture. Materials Today: Proceedings. 2022. 60. Part 1. DOI: 10.1016/j.matpr.2022.01.316
16. Schmidt, W., Brouwers, H.J.H., Kühne, H.-C., Meng, B. Influences of superplasticizer modification and mixture composition on the performance of self-compacting concrete at varied ambient temperatures. Cement and Concrete Composites. 2014. 49. Pp. 111–126. DOI: 10.1016/j.cemconcomp.2013.12.004
17. Sainz-Aja, J.A., Carrascal, I.A., Polanco, J.A., Sosa, I., Thomas, C., Casado, J., Diego, S. Determination of the Optimum Amount of Superplasticizer Additive for Self-Compacting Concrete. Applied Sciences. 2020. 10(9). Pp. 3096. DOI: 10.3390/app10093096
18. Boukendakdji, O., Kadri, E.-H., Kenai, S. Effects of granulated blast furnace slag and superplasticizer type on the fresh properties and compressive strength of self-compacting concrete. Cement and Concrete Composites. 2012. 34(4). Pp. 583–590. DOI: 10.1016/j.cemconcomp.2011.08.013.
19. Tangadagi, R.B., M, M., Seth, D., S, P. Role of mineral admixtures on strength and durability of high strength self compacting concrete: An experimental study. Materialia. 2021. 18. Pp. 101144. DOI: 10.1016/j.mtla.2021.101144.
20. Vivek, S.S., Dhinakaran, G. Durability properties of self-compacting concrete using mineral admixtures. Case study II. Handbook of Sustainable Concrete and Industrial Waste Management. Elsevier, 2022. Pp. 407–418.
21. Utepov, Y., Akhmetov, D., Akhmatshaeva, I. Effect of fine fillers from industrial waste and various chemical additives on the placeability of self-compacting concrete. Computers and Concrete. 2020. 25 (1). Pp. 59–65. DOI: 10.12989/CAC.2020.25.1.059
22. Akhmetov, D., Aniskin, A., Utepov, Y., Root, Y., & Kozina, G. Determination of Optimal Fibre Reinforcement Parameters for Self-Compacting Concretes. Tehnički Vjesnik. 2020. 27 (6). Pp.1982–1989. DOI: 10.17559/TV-20200630163212
23. Raghavendra, T., Jawad, F., Gurunandan, M., Vageesh, H.P. Application of fly ash in flowable fills and self-compacting concretes. Handbook of Fly Ash. Elsevier, 2022. Pp. 611–656.
24. Saba, A.M., Khan, A.H., Akhtar, M.N., Khan, N.A., Rahimian Koloor, S.S., Petrů, M., Radwan, N. Strength and flexural behavior of steel fiber and silica fume incorporated self-compacting concrete. Journal of Materials Research and Technology. 2021. 12. Pp. 1380–1390. DOI: 10.1016/j.jmrt.2021.03.066
25. MasterGlenium ® ACE 430. URL: www.master-builders-solutions.ru (date of application: 29.04.2022).
26. Standard of Organization 70386662-310-2014 Super plasticising additives for concrete and mortar MasterGlenium series (Glenium) BASF. 2014URL: http://a-ing.ru/upload/iblock/6ca/sto-70386662_310_2014-masterglenium.pdf (date of application: 6.06.2022).
27. Massana, J., Reyes, E., Bernal, J., León, N., Sánchez-Espinosa, E. Influence of nano- and micro-silica additions on the durability of a high-performance self-compacting concrete. Construction and Building Materials. 2018. 165. Pp. 93–103. DOI: 10.1016/j.conbuildmat.2017.12.100
28. Saint-Jalmes, A., Peugeot, M.L., Ferraz, H., Langevin, D. Differences between protein and surfactant foams: Microscopic properties, stability and coarsening. Colloids and Surfaces A: Physicochemical and Engineering Aspects. 2005. 263(1-3 SPEC. ISS.). Pp. 219–225. DOI: 10.1016/j.colsurfa.2005.02.002
29. Bergna, H.E. Colloid Chemistry of Silica An Overview. 141994. 2022 p. ISBN: 82.200.168.84.

30. Lewis, R., Fidjestøl, P. Microsilica as an Addition. Lea's Chemistry of Cement and Concrete. Elsevier, 2019. Pp. 509–535.
31. Gesoglu, M., Güneyisi, E., Asaad, D.S., Muhyaddin, G.F. Properties of low binder ultra-high performance cementitious composites: Comparison of nanosilica and microsilica. Construction and Building Materials. 2016. 102. Pp. 706–713. DOI: 10.1016/j.conbuildmat.2015.11.020
32. Russian State standard GOST R 58002-2017/EN 12350-8 – Testing fresh concrete – Part 8: Self-compacting concrete – Slump-flow test.
33. Russian State standard GOST R 57809-2017/EN 12350-2:2009 Testing fresh concrete. Part 2. Slump test. URL: https://docs.cntd.ru/document/1200157288 (date of application: 14.05.2022).
34. Interstate standard GOST 10180-2012 Concretes. Methods for strength determination using reference specimens.
35. Bani Ardalan, R., Joshaghani, A., Douglas Hooton, R. Workability retention and compressive strength of self-compacting concrete incorporating pumice powder and silica fume. Construction and Building Materials. 2017. 134. Pp. 116–122. https://doi.org/10.1016/j.conbuildmat.2016.12.090
36. Almuwbber, O, Haldenwang, R, Mbasha, W, Masalova, I. The influence of variation in cement characteristics on workability and strength of SCC with fly ash and slag additions. Construction and Building Materials. 2018. 160. Pp. 258–267. DOI: 10.1016/j.conbuildmat.2017.11.039
37. Meko, B., Ighalo, J.O., Ofuyatan, O.M. Enhancement of self-compactability of fresh self-compacting concrete: A review. Cleaner Materials. 2021. 1.Article no. 100019. DOI: 10.1016/j.clema.2021.100019

Information about authors:

Duman Dyussembinov, *PhD in Technical Sciences*
ORCID: https://orcid.org/0000-0001-6118-5238
E-mail: dusembinov@mail.ru

Talal Awwad, *PhD*
ORCID: https://orcid.org/0000-0002-6487-2428
E-mail: dr.awwad.gfce@gmail.com

Yerlan Sabitov, *PhD in Technical Sciences*
E-mail: e_sabitov@mail.ru

Adiya Zhumagulova, *PhD in Technical Sciences*
ORCID: https://orcid.org/0000-0002-6310-2501
E-mail: zaaskarovna@gmail.com

Zhanbolat Shakhmov, *PhD*
ORCID: https://orcid.org/0000-0003-1680-5287
E-mail: zhanbolat8624@mail.ru

Zhanar Kaliyeva, *PhD in Technical Sciences*
ORCID: https://orcid.org/0000-0001-9033-2065
E-mail: zhanna-080477@mail.ru

Daniyar Bazarbayev, *PhD*
ORCID: https://orcid.org/0000-0001-8547-5440
E-mail: phdd84@mail.ru

Received 08.06.2022. Approved after reviewing 03.10.2023. Accepted 04.10.2023.

Magazine of Civil Engineering. 2023. 123(7). Article No. 12307

Magazine of Civil Engineering

ISSN 2712-8172

journal homepage: http://engstroy.spbstu.ru/

Research article

UDC 697.921: 533.697

DOI: 10.34910/MCE.123.7

Vortex zones in an exhaust hood in front of an impermeable plane

***A.M. Ziganshin*[1] ✉, *K.I. Logachev*[2], *J.R. Kareeva*[1]**

[1] *Kazan State University of Architecture and Engineering, Kazan, Russian Federation*

[2] *V.G. Shukhov Belgorod State Technological University, Belgorod, Russian Federation*

✉ *ziganshin.arslan@gmail.com*

Keywords: local exhaust ventilation, exhaust hood, vortex zone, numerical calculation, impermeable plane

Abstract. The paper presents the results of the study of the flow to the ventilation exhaust device in a form of a circular exhaust hood with a flange, located in front of an impermeable plane. Local exhaust devices are the most rational type of localization of harmful substances in industrial and civil buildings. However, they consume a large amount of energy, so the ways to increase their efficiency are relevant and are the subject of numerous studies around the world. One of the promising ways to reduce the aerodynamic drag of such devices is shaping their inlet sharp edges by the outlines of vortex zones. However, when the hood is located above an impermeable plane, the outlines are not known. This study is carried out numerically, so at the first stage the adequacy of the computation model is demonstrated by comparing it with the known data on the resistance of this kind of devices. Furthermore, the dependences for the local drag coefficient are constructed for the flange dimensions in the range d/R = 0.5; 1.5; 2.5; 5 and distances to the impermeable plane in the range s/R = 0.5; 1; 2; 5. The authors found the outlines of both the first vortex zone, formed at flow separating from the sharp edge of the flange, and the second vortex zone, formed at the point of the flange connection to the exhaust channel. The plotted curves showed that the zones sizes are significantly dependent on the distance s/R. The property of geometric similarity for the first vortex zone was found, which will make it possible to construct the first vortex zone using the dependence for the scale factor without numerical simulation. The constructed outlines of the vortex zones will be further used to develop shaped designs of ventilation exhaust hoods.

Funding: grant of Russian Federation President, Project No.NS-25.2022.4.

Citation: Ziganshin, A.M., Logachev, K.I., Kareeva, J.R. Vortex zones in an exhaust hood in front of an impermeable plane. Magazine of Civil Engineering. 2023. 123(7). Article no. 12307. DOI: 10.34910/MCE.123.7

1. Introduction

The use of local exhaust ventilation significantly increases the efficiency of removal of pollutants emitted in various processes. However, their operation requires a large amount of energy, which is primarily spent to air moving. Depending on the construction of the exhaust system, the required degree of exhaust is provided by a different amount of air. The open local exhaust systems such as exhaust inlets, hoods are characterized by large amounts of air and therefore a very significant energy consumption to overcome the resistance in the network. The efficiency of such systems depends significantly on the distance to the source of effluents: the higher efficiency at a lower flow rate of air removed is achieved for the smaller distance. Usually, the source of effluents is located on the surrounding impermeable plane and it significantly affects the flow to the exhaust. The source of effluents can be a heated part located on a machine tool or conveyor [1], foundry processes [2, 3], joints in welding process [4] or painting process during spray painting of parts extended in space [5, 6], etc. The intrinsic momentum of such pollutants significantly affects the velocity field of the exhaust device, but it is also important to know the velocity field of exhaust. However, the emitted pollutants can be often considered passive and having no significant influence on the exhaust velocity field. For example, these are diffusive sources of solvent vapor emitted from the painted surface during manual painting and drying [7], vapors of various liquids during drying of construction, plant and other materials [8], fine-dispersed dust emissions [9], aerosols [10]. In this case, the flow in the supply-exhaust system is almost completely determined by the exhaust operation. And it is clear that the presence of an impermeable wall will affect both the velocity field and the outlines of vortex zones (VZs) formed by flow separation at the inlet of such an exhaust. The previous studies on the flow to the circular exhaust showed that two VZs are formed here - the first one when the flow is separated from the sharp edge of the hood, and the second at the point of the hood connection to the channel; moreover, found were the laws for the outlines of the vortex zones and velocity field [11]. It was also shown that the most effective is the design with the hood inclination angle of 90°, i.e. for an exhaust with a flange. So the object of research is the outlines of vortex zones in the circular flanged exhaust hood under the influence of the impermeable plane placed in front of it.

To increase the efficiency and reduce the energy consumption of local exhaust devices, one can use various ways of hiding the source of harmful emission and limiting the area of air flow to the exhaust: curtains [12], flanges at the exhaust and their improvement, for example, by increasing the shielding ability of the flange by placing a supply channel inside it through which the supply stream flows out. Such a design is often called the Aaberg exhaust and is still actively studied [13] and improved in different ways, e.g. by swirling the inflow jet [14]. Methods for capturing emitted pollutants are also being improved, for example by using sound waves to aggregate aerosol particles and increase the efficiency of local exhausts [15]. For example, the numerical assessment of velocity field was carried out for several exhaust hood designs [16], and the corrected formula of axial air flow rate was found. The authors believe that this result also improves the efficiency of local exhaust ventilation, since it clarifies the necessary flow rate removed from the exhaust, although it is clear that during the air removal, there is no actual jet flow, and therefore the axis, so it is important to know not only the velocity at the geometric axis, but also the entire field of velocities in front of the exhaust. Therefore, the velocity and its components in the entire field in front of the exhaust are important when considering the pollutants' removal by exhaust. Nevertheless, in this paper one can also see the formation of vortex zones at the exhaust inlet, although the authors do not pay due attention to it.

Now the reduction of aerodynamic resistance of elements is considered as an efficient approach to improve the efficiency of ventilation systems. A well-known method of reducing resistance of various duct fitting elements consists in installing baffles and blades, which reduce pressure gradients and thus occurring energy losses for flows collisions and creation of separation zones. But these studies are still actual, and such devices are being developed and optimized for different types of ventilation elements – bends [17, 18], tees [19–21], the optimal angle of screen slope in them is being studied [22]. The results obtained show the possibility of reducing the aerodynamic resistance, the level of which depends on the type and size of the duct fitting element, as well as on the flow rate and the ratio of air flow rates for elements with separation or merging of flows. The disadvantage of this method is the complication of the element construction and, the corresponding increase in its cost. Therefore, its application is usually limited by economic considerations. Another way to reduce pressure losses in the elements is smoothing of sharp edges at bends, taps and other junctions, where the flow has a strong deformation and therefore the greatest energy losses. The most common and well-studied method of smoothing is to replace the sharp corner with part of a circle, and the larger circle radius results in a greater resistance reduction. Modern studies continue to optimize the shape of the smoothing curve.

There are examples of finding the optimal spline shape for S-shaped duct section [23], topological optimization of the shape of bends, tees [24, 25] or the so-called biomimetic optimization, when the outlines taken from nature are used for smoothing – the flow of rivers or the growth of plant stems for tees [26, 27], tongue-shaped elbows [25]. These methods also show the possibility of reducing aerodynamic drag, the different level of which depends on the specific design of the element and its parameters. However, this method is not often used in real conditions, where the space placement of ventilation networks is usually limited, because the size of the part improved in this way is more than that of the standard unsmoothed one. The method of installing a shaping insert inside the element does not have the mentioned disadvantage, but the element construction becomes more complicated. For example, inserts of different shapes in unit consisting of an elbow and a tee are investigated in [28], and it is shown that a decrease in resistance is obtained for several cases of the ratio of flow rates through the unit. For the insert, several known profiles from automobile and aircraft construction are chosen.

A specific combination of the described two methods can be considered as profiling the element wall according to the outlines of the vortex zone that occurs when the flow separates from the sharp edge. This does not increase the size and does not complicate the construction of the element, since no additional parts are introduced. But this method has a deeper meaning – the outline for the shape is not chosen conventionally (a circle, ellipse or Bézier curve), but it is the outline of the vortex zone. In other words, the shaped wall replaces the vortex zone formed in this place of the duct fitting element. Therefore, the profile does not cause the additional narrowing of the channel and deformation of the flow, but only prevents the formation of the flow separation and the associated energy losses.

The outlines of the vortex zones were used to improve the designs of free circular exhaust hoods [29]. This improvement has shown the possibility of reducing the aerodynamic drag by up to 40 % as compared to the original non-shaped ones. Which indicates a significant, but not dominant, contribution of shaping to resistance. The work [29] shows a reduction in the resistance of the inlet sections of freely located exhaust flanged hoods by almost 98 %, by eliminating the second reason – the blockage of the flow resulting from the vortex zone. That is, it is possible to estimate the contribution of the first shaping method to the section resistance at the level of 40 %, and the second – about 58 %. However, the use of the second method increases the dimensions of the system. In practice, in cramped conditions for the placement of elements of ventilation systems, this method is rarely used.

The problem of flow to the flanged exhaust hood in front of impermeable plane was previously solved by the method of discrete vortices [30], and the outlines of the first and second vortex zones (VZs) were found. But due to peculiarities of the mathematical apparatus, the outlines of the second VZ are defined only up to the point of maximum VZ width, and further it extends parallel to the channel wall. However, from general considerations, it is usually assumed that the flow behind the separation zone should occupy the whole channel cross section, so there is a point of closure of the vortex zone to the wall or, in a more general, three-dimensional case – points where the jets of the main flow, surrounding the vortex zone, touch the wall. To develop the improved designs of local exhaust hoods, it is necessary to determine the outlines of VZs along its entire length. This can be done using the methods of computational fluid dynamics, which have shown a fairly good convergence with both the method of discrete vortex in determining the outlines of VZs, and with experimental data on the outlines of VZs and the local drag coefficients (LDC). Such studies for an exhaust hood located freely in space are also presented in [11, 29].

So since the flanged exhaust hood is frequently used for pollutants removal from the impermeable planes and that plane influenced on the flow and the vortex zones, which can be used to shaping and reduce its aerodynamic resistance. It is relevant to find regularities for the full length outlines of the vortex zones for this case.

Therefore, the purpose of the presented paper is to determine the outlines of both the first and the second VZs along their entire length, for the construction of an exhaust hood with an inclination angle of 90°. The objectives to be achieved is to validate the obtained solution and construct the dependences of LDC on the exhaust pipe design and compare with the known data from the reference book [31]; to plot the relationship between the outlines of VZs and both the length of the flange of the exhaust hood, and the distance to the impermeable wall.

2. Methods

The ANSYS Fluent software package is used in this study [32]. The problem is solved in the axisymmetric turbulent formulation. The geometry of the computational domain and its main dimensions are shown in Fig. 1 (for the variant of the problem with dimensions s/R = 2, d/R = 1.5).

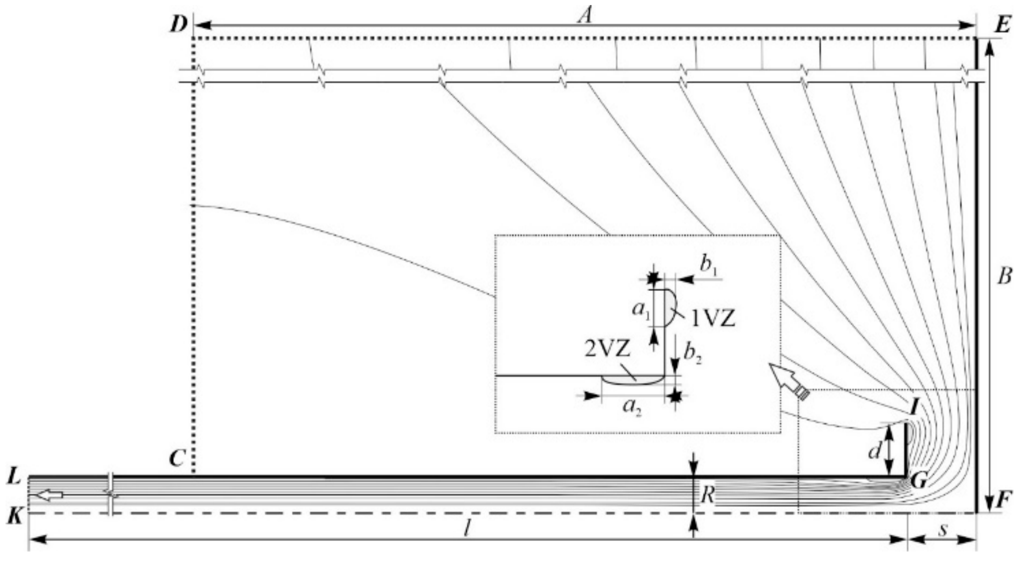

Figure 1. Geometry of the computational domain, streamlines, main dimensions for the variant s/R = 2, d/R = 1.5.

The problem is solved for the hood dimensions d/R = 0.5; 1.5; 2.5; 5 and distances to the impermeable plane s/R = 0.5; 1; 2; 5, where R = 50 mm is the channel radius. For the illustration purposes Fig. 1 also shows the streamlines of the resulting flow. It can be seen that two vortex zones are formed. The first vortex zone (1VZ) is formed at flow separation from the sharp edge of the hood and the second one (2VZ) is formed at flow separation in the point of the hood connection to the exhaust channel. The lengths of vortex zones are a_1 and a_2, respectively, and their widths are b_1 and b_2. Boundary conditions (BC) (Fig. 1) are as follows: a section of external boundary CDE is the free boundary modeled using the "Pressure Inlet" BC with overpressure equal to zero; EF, LGI are impermeable walls (BC "Wall"); KF is the symmetry axis (BC "Axis"); LK is the boundary through which air is removed (BC "Velocity Inlet") with the velocity v_{x0} = 50 m/s. This velocity is assumed to achieve self-similarity and developed turbulent flow regime (Re = $2.9 \cdot 10^5$).

Earlier in [30], a validation for the CFD numerical model has already been performed for the exhaust hood with a flange inclination angle of 0°, i.e. for a circular exhaust opening, and the most adequate combination of the Reynolds Stress Turbulence Model (RSM) with the Enhanced Wall Treatments (EWT) was shown. Therefore, the same combination is used here.

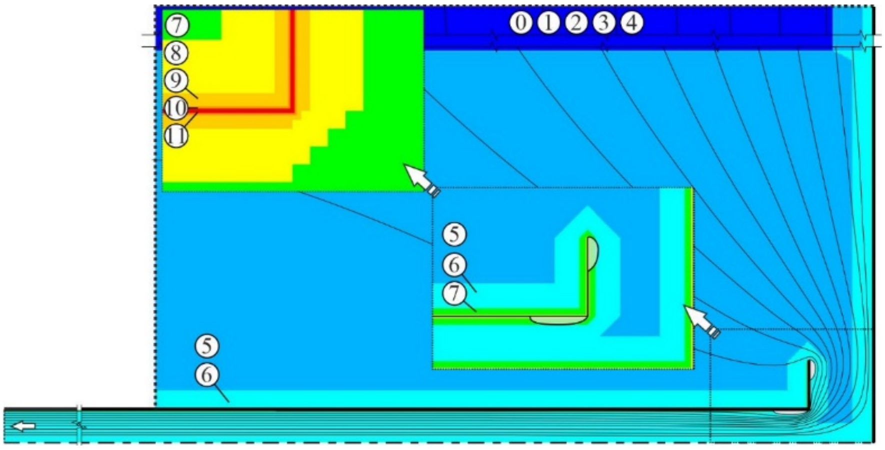

Figure 2. Visualization of adaptation steps for the variant s/R = 2, d/R = 1.5.

To test for grid convergence, each problem underwent a series of computational grid refinement (adaptation) steps when solved (showing with color regions on Fig. 2). The first 4 stages were carried out over the entire computational domain, further the area of refinement was reduced and included part of the area in front of the hood, near the impermeable wall and the channel (No.5). And further, for proper resolution of the boundary layer by the computational grid, refinement was carried out at the solid boundaries – the impermeable plane and the channel walls (adaptations 6 to 11).

Following the results of numerical solution of each refinement stage for each of the investigated geometries, LDC was calculated using the method described in detail in [33]. As a result of numerically obtained distribution of total pressure along the length of the channel, the average value of specific pressure friction loss R (Pa/m) is determined and the zone of non-physical deformation of the pressure field is excluded due to the impact of the boundary condition to determine the channel length l_C (m). Then the LDC value is defined as:

$$\zeta = \frac{P_1^{\text{tot}} - P_2^{\text{tot}} - \Delta P_{\text{fr}}}{P^{\text{dyn}}}, \tag{1}$$

where P_1^{tot} and P_2^{tot} are the total pressure in the section in front of the hood is taken equal to zero, and in the channel section near the outlet boundary, but unaffected by the deformation due to the imposed boundary condition, respectively, $\Delta P_{fr} = R \cdot l_c$ is the pressure loss for friction, $P^{\text{dyn}} = \rho \cdot v_{x0}^2 / 2$ is the dynamic pressure.

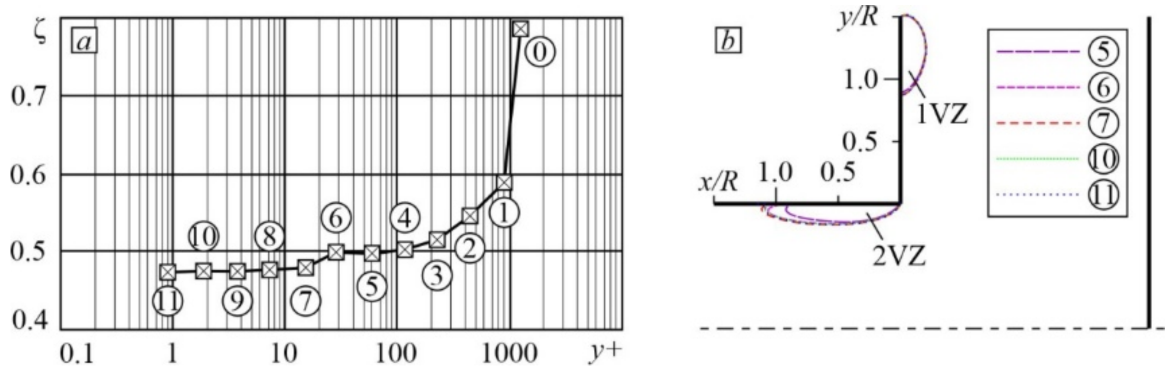

Figure 3. Grid dependence study: a) local drag coefficient; b) vortex zones outlines.

Figure 3a shows the change in LDC during computational grid refinement, which is characterized by dimensionless distance (taking maximum value at all impermeable boundaries at the computational domain) $y+ = \rho \cdot v_\tau \cdot y_p / \mu$, where $v_\tau = \sqrt{\tau_w / \rho}$ is friction velocity, y_p is distance from the center of the near-wall cell to the wall, ρ is density and μ is dynamic viscosity of air at this point, τ_w is shear stress at the wall at this place. It can be seen that with refinement of grid cells and correspondingly decrease of $y+$, LDC changes significantly (5 %–30 %) until $y+$ values are about 30 (adaptation No. 6), then starting from adaptation No.7 ($y+$ <20) the difference between the LDC values does not exceed 0.4 %.

Fig. 3b shows the change in the outlines of the vortex zones (VZ) for several stages of adaptations. The outlines of both the first and second vortex zones for adaptations from No. 7 to No. 11 coincide with each other. This means that there is no grid dependence, so further for all problems a similar refinement process is carried out and the solution on the computational grid No. 11 is taken as the final one. Parameters of computational grids of the last adaptations for different geometries are somewhat different, but are of the same order: sizes of the minimum cell (along solid boundaries) are about 0.01 mm, sizes of the maximum cell (in the underflow area away from exhaust) are about 3 mm, total number of cells is about 2.5 million pcs.

3. Results and Discussion

Numerical solution of all above mentioned designs of the exhaust hood with the flange length d/R = 0.5; 1.5; 2.5; 5 was carried out, for each of them the variants of distances to the impermeable plane s/R = 0.5; 1; 2; 5 were calculated. As a result, the local drag coefficients (LDC) were determined using the calculated pressure field.

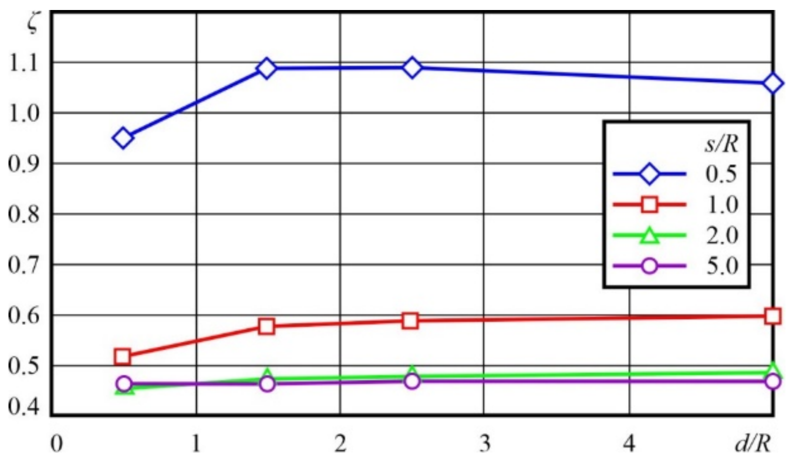

Figure 4. Dependence of local drag coefficient on d/R for various s/R.

When the obtained values are presented as a dependence of ζ on the hood flange length d/R (Fig. 4), one can see that with an increase in d/R, the LDC value increases to d/R ≈ 1.5. Further, for d/R > 1.5, the LDC value stops changing, which indicates the absence of LDC dependence on flange length in the case of long flanges. This is explained by the peculiarities of formation of the first vortex zone, which at such flange lengths closing on it, and further the 2VZ forms separately. It is known that for shorter flanges, the vortex zones merge into one. Nevertheless, for the shortest investigated d/R =1 and d/R =1.5 there seems to be an influence of the first VZ on the second one. In contrast to the case of a free hood [29], where there is no such dependence for the considered case of a 90° inclination angle. At the same time, there is a significant dependence of LDC on s/R for small distances from the impermeable wall (s/R = 0.5 and s/R = 1). This dependence practically disappears for distances s/R > 2: the curves for s/R = 2 and s/R = 5 practically coincide. This implies that the aerodynamic drag is significantly affected by the impermeable wall at distances less than $2R$.

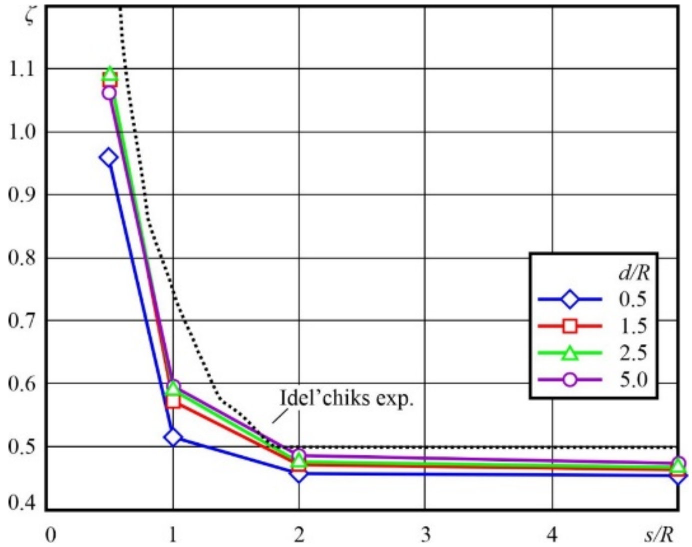

Figure 5. Dependence of local drag coefficient on s/R for various d/R.

To compare the obtained results with the known data [31], we plotted the relationship between LDC and s/R for exhaust designs with different hood flange lengths d/R (Fig. 5). The experimental data [31] (Idel'chiks exp.) are also plotted in Fig. 4. It can be seen that the hood with the smallest flange length (d/R = 0.5) is characterized by somewhat lower resistance than for the other sizes, which is apparently explained by lower constriction and deformation of the flow at small flange lengths. For other flange sizes, the LDC change curve is almost the same. Comparison with the data of [31] shows satisfactory convergence (average difference of about 5 %) of the numerical solution data and the known experimental study. This once again confirms the adequacy of the computation model.

The results of the numerical calculation were used to construct the outlines of the first (1VZ) and second (2VZ) vortex zones for each of the investigated geometries (Fig. 6). The numerically found outlines are shown with solid lines. For comparison, the outlines found by the discrete vortex method (DVM) [30] are also plotted there as dashed lines, and for the exhaust hood with d/R = 5 the outlines for the case of the absence of impermeable wall ($s/R = \infty$) [29] are shown as dashed line (numerical solution) and dashed-dotted line (DVM).

Although quantitatively the sizes of the first vortex zone found numerically and by DVM are somewhat different, qualitatively the outlines and their size behavior with a change in s/R is similar. For long hoods ($d/R \geq 2.5$) the smallest dimensions of VZ (both length and width) are observed at the smallest of investigated distances s/R = 0.5. In this case, the influence of the impermeable wall has a constraining character, limiting the development of the vortex zone. The 1VZ outline in the absence of an impermeable wall, plotted for the case d/R = 5 (dashed line $s/R = \infty$) shows significantly larger dimensions than those for small s/R. At s/R = 2 the difference between the outlines is 12.2 %, and at s/R = 5 it does not exceed 6.5 %. Thus, the size of 1VZ increases with an increase in distance s/R from 0.5 to 2, and then decreases again for s/R = 5, tending to the size of VZ without an impermeable wall. It can be seen that 1VZ at the smallest distance s/R = 0.5 has a flatter outline, with the smallest width of VZ. 2VZ behaves similarly and at s/R = 5 is no longer significantly different from the case of a free exhaust hood (dashed line $s/R = \infty$). So, the influence of the wall on VZ disappears at distances of the order of s/R = 5. For a better understanding of the regularities of changes in the dimensions of VZ, the graphs for the length a_1/R and a_2/R and widths b_1/R and b_2/R of the first and second VZ, respectively, are plotted.

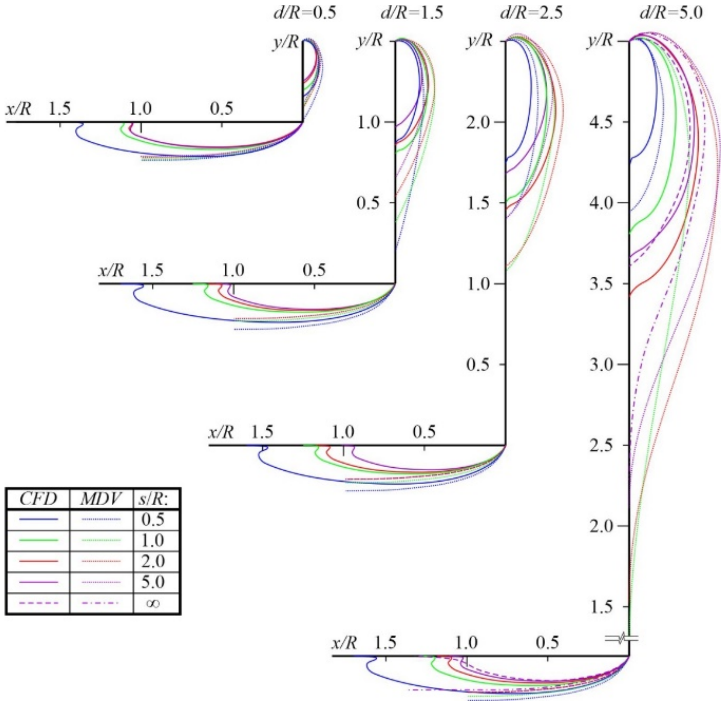

Figure 6. Outlines of vortex zones for various d/R and changing of s/R.

For the main dimensions of VZ (length a and width b) plotted the dependencies for the hood of the studied designs d/R when changing the distance to the impermeable plane s/R. The first VZ is considered in Fig. 7.

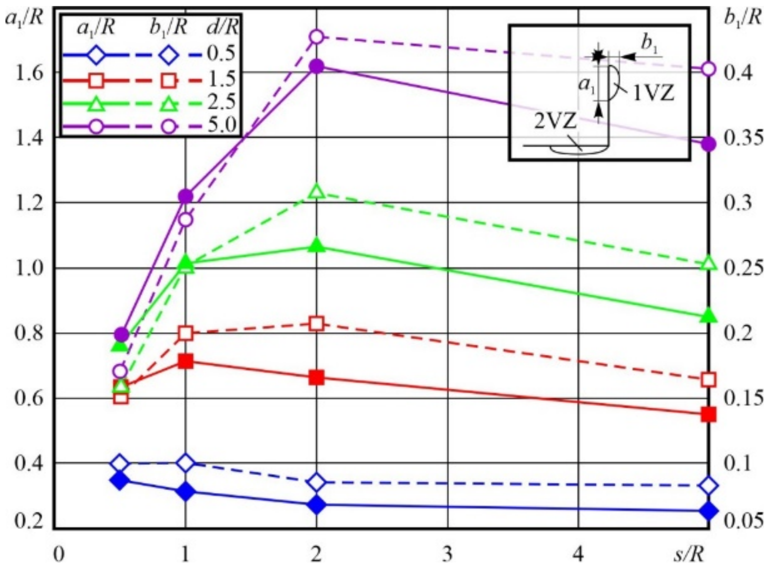

Figure 7. Dependencies of 1VZ dimensions on s/R and d/R.

It can be seen that for each exhaust design (d/R = const), except for the smallest of investigated (d/R = 0.5) with an increase in distance to impermeable surface (s/R) both VZ dimensions increase (mainly up to s/R = 2) and then a smooth decrease is observed. This can be explained by the fact that at small distances, the impermeable plane limits the development of VZ. When the limiting effect decreases, VZ begins to increase, and its size becomes larger than the size of VZ for exhausts without impermeable plane, because the flow velocity when flowing around the sharp edge of the hood flange is significantly higher, due to the presence of impermeable plane. As the distance is further increased, the velocity decreases, resulting in a smooth decrease in the size of VZ to the size of VZ in the absence of an impermeable plane. This states that there are two mechanisms of influence of the impermeable plane on the size of 1VZ – the "damping" mechanism, which leads to a decrease in size, despite the presence of the second mechanism – the mechanism "accelerating" the flow in the area of formation of VZ, which leads to an increase in its size. In general, it can be concluded from Fig. 6 that the "damping" effect of the impermeable plane ends at a distance of about $2R$, and as d/R decreases, this peak shifts toward smaller s/R distances. For the exhaust hood design with the smallest of the investigated hood flange lengths (d/R = 0.5), the above described dependence can be traced, but has not so pronounced character.

For the second VZ, the patterns of changes in the main dimensions are shown in Fig. 8.

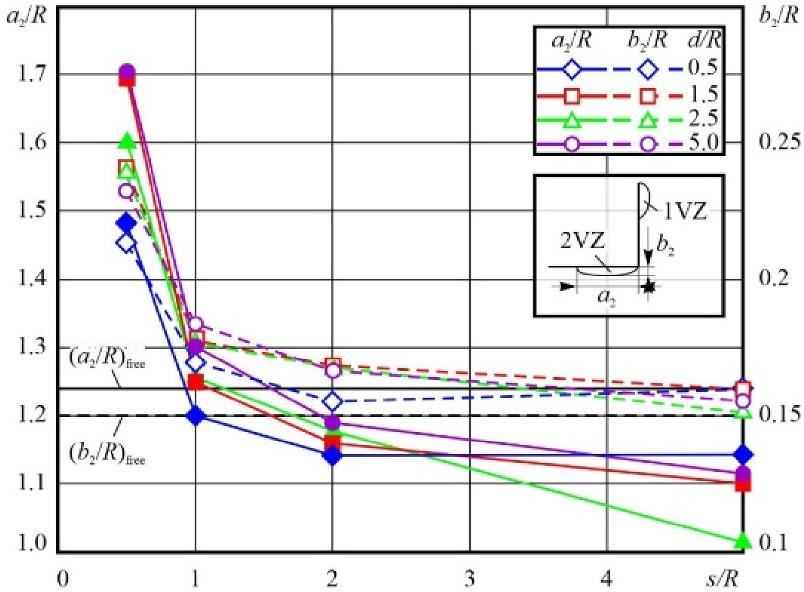

Figure 8. Dependencies of 2VZ dimensions on s/R and d/R.

Both 2VZ sizes decrease as the distance to the impermeable plane increases. This can also be explained by a decrease in the mechanism "accelerating" the flow in the region of 2VZ formation. Decrease of flow velocity, and flow around a sharp inlet edge leads to decrease of sizes of vortex zone. It may be noted that the main decrease in size (by about 20÷40 %) occurs when the distance increases in the range of 0.5 < s/R < 2. Further, the decrease in VZ dimensions is not so significant (about 5 %). Moreover, if 1VZ is characterized by such a change of dimensions, in which they tend to different values for each value of d/R, then for 2VZ for all exhaust hood designs, the dimensions tend to the same value, which is close to the values of dimensions without impermeable plane – $(a_2/R)_{free}$ and $(b_2/R)_{free}$. This is in a good agreement with the earlier studies [11, 22], where it is shown that 1VZ is characterized by a dependence on the size of the exhaust flange, and 2VZ is not characterized.

When analyzing the changes in the 1VZ outlines, their geometric similarity was found, as previously for the case of an exhaust hood located freely [22]. This is expressed in the fact that taking one of the lines of VZ outline as a base line (in this case it is an outline for d/R = 2.5), by multiplying the coordinates of the base line by the scale factor k_{VZ} one can obtain coordinates of 1VZ outlines for other cases (other dimensions of the flange d/R and other distances to the impermeable plane s/R). The dependencies for the scaling factor were constructed using the 1VZ dimensions found from the numerical solution (Table 1).

Table 1. Dependencies for k_{VZ} on d/R and s/R.

s/R	$k_{VZ} = f(d/R)$
0.5	$k_{VZ} = -0.06 \cdot d/R^2 + 0.4548 \cdot d/R + 0.2583$
1	$k_{VZ} = -0.0587 \cdot d/R^2 + 0.5201 \cdot d/R + 0.0603$
2	$k_{VZ} = -0.0334 \cdot d/R^2 + 0.4681 \cdot d/R + 0.0193$
5	$k_{VZ} = -0.0192 \cdot d/R^2 + 0.4026 \cdot d/R + 0.1025$

The behavior of the multipliers in the regression equations can be used to judge that there is a dependence of both k_{VZ} and the 1VZ outlines on the distance to the impermeable plane.

Fig. 9 shows the outlines of 1VZ – the original ones obtained numerically (dashed line), and those found using k_{VZ} (solid line).

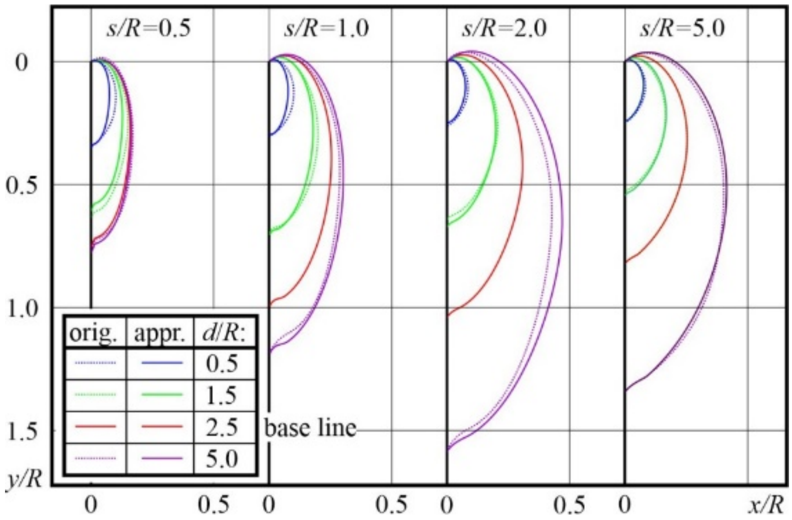

Figure 9. Geometric similarity of the outlines of the first vortex zone.

It can be seen that the 1VZ outlines obtained using the scale factor k_{VZ} (solid lines) coincide well with the original ones found numerically (dashed lines), the difference between them does not exceed 9 %. The exception is the version of the exhaust design with the smallest of the investigated hood flange lengths d/R, at the two smallest of the investigated distances s/R = 1 and 2, where the difference is of the order of 25 %. This indicates some change in the character of the flow in this case, but since for all other designs the use of k_{VZ} shows good results, it can be concluded that in developing improved designs of this type of exhaust, it is necessary to check the efficiency of profiling also for small flange lengths. For the 2VZ outlines, as in the case of free exhausts, no geometric similarity is observed. At the same time, as shown earlier, the 2VZ dimensions for distance s/R > 1 are weakly dependent on design and distance. Therefore, when developing shaped hoods, it will be necessary to check the necessity of using the found outlines for each case, as well as one universal profile, to which, as these studies have shown, the 2VZ outlines tend - the case of a free exhaust hood.

4. Conclusions

The conducted numerical studies of the flow to the ventilating exhaust with an inclination angle of 90°, made it possible to make the following conclusions:

1. To obtain adequate results, both in resistance and in VZ outlines, it is necessary to carry out refinement of computational grid cells in the flow area up to values of parameter $y+\approx 60$, and further to refine along all solid boundaries up to values of parameter $y+\approx 1$.

2. The dependence of the local drag coefficient (LDC) is obtained not only on the distance s/R, but also on various flange sizes d/R.

3. VZ outlines for exhaust hood designs with the flange length d/R = 0.5; 1.5; 2.5; 5 and for distances to the impermeable plane s/R = 0.5; 1; 2; 5 have been constructed. Their comparison with those found by the method of discrete vortices has shown satisfactory convergence. So, the detailed outlines for 2VZ were obtained.

4. The dependences of the main dimensions of VZ were plotted. The dimensions of 1VZ increase significantly with an increase in flange d/R, and increase with an increase in distance up to s/R = 2, and then decrease and tend to the dimensions of 1VZ for a free exhaust. The dimensions of 2VZ depend slightly on d/R, and decrease sharply with increasing distance s/R = 2, further changes being insignificant.

5. Geometric similarity for 1VZ is found, and dependencies for the scale factor are constructed to find the outlines of 1VZ, in the size ranges investigated, without involving numerical simulation. There is no geometric similarity for 2VZ.

The obtained results show a significant dependence of both the resistance and the outlines of VZ on the presence of an impermeable plane. So, it should be definitely taken into account for distances $s/R \le 2$. The found outlines of VZ will make it possible to develop improved designs of exhaust hoods with inclination angle of 90°, located in front of the impermeable plane, shaped by the outlines of VZ.

References

1. Kulmala, I., Hynynen, P., Welling, I., Säämänen, A. Local ventilation solution for large, warm emission sources. The Annals of occupational hygiene. 2007. 51(1). Pp. 35–43. DOI: 10.1093/annhyg/mel049
2. Huang, Y., Wang, Y., Liu, L., Nielsen, P. V., Jensen, R.L., Yang, X. Performance of constant exhaust ventilation for removal of transient high-temperature contaminated airflows and ventilation-performance comparison between two local exhaust hoods. Energy and Buildings. 2017. 154. Pp. 207–216. DOI: 10.1016/j.enbuild.2017.08.061
3. Huang, Y., Wang, Y., Liu, L., Nielsen, P.V., Jensen, R.L., Yan, F. Reduced-scale experimental investigation on ventilation performance of a local exhaust hood in an industrial plant. Building and Environment. 2015. 85. Pp. 94–103. DOI: 10.1016/j.buildenv.2014.11.038
4. Flynn, M.R., Susi, P. Local exhaust ventilation for the control of welding fumes in the construction industry--a literature review. The Annals of occupational hygiene. 2012. 56 (7). Pp. 764–76. DOI: 10.1093/annhyg/mes018
5. Madsena, U., Fontaine, J.R., Nielsenc, P. V., Aubertin, G., Breum, N.O. A Numerical Study of Dispersion and Local Exhaust Capture of Aerosols Generated from a Variety of Sources and Airflow Conditions. AIHAJ. 1996. 57 (2). Pp. 134–141. DOI: 10.1202/0002-8894(1996)057<0134:ANSODA>2.0.CO;2
6. Liu, F., Zhang, T.T., Zhang, H., Huo, Q., Wang, J., Long, Z., Liu, J. Removing painting-generated VOCs in a commercial airplane hangar with multiple portable exhaust hoods. Building and Environment. 2021. 196 (January). Pp. 107797. DOI: 10.1016/j.buildenv.2021.107797
7. Qi, Y., Shen, L., Zhang, J., Yao, J., Lu, R., Miyakoshi, T. Species and release characteristics of VOCs in furniture coating process. Environmental Pollution. 2019. 245. Pp. 810–819. DOI: 10.1016/j.envpol.2018.11.057
8. Cao, W.-x., You, X.-y. The inverse optimization of exhaust hood by using intelligent algorithms and CFD simulation. Powder Technology. 2017. 315. Pp. 282–289. DOI: 10.1016/j.powtec.2017.04.019
9. Zamalieva, A.T., Ziganshin, M.G., Potapova, L.I. Ob jeffektivnosti sushhestvujushhih metodov ciklonnoj fil'tracii pri osazhdenii melkodispersnyh chastic klassov PM10, PM2,5 [The analysis of efficiency of use of a cyclonic filtration for sedimentation of fine particles]. News of KSUAE. 2017. 42 (4). Pp. 415–423.
10. Bilalov, M.I., Ziganshin, M.G. Estimates of the influence of the solar irradiation spectrum energy on the intensity of heat treatment of solid waste with hexavalent chromium. IOP Conference Series: Materials Science and Engineering. 2019. 481. Pp. 012044. DOI: 10.1088/1757-899X/481/1/012044
11. Logachev, K.I., Ziganshin, A.M., Averkova, O.A., Logachev, A.K. A survey of separated airflow patterns at inlet of circular exhaust hoods. Energy and Buildings. 2018. 173 (6). Pp. 58–70. DOI: 10.1016/j.enbuild.2018.05.036
12. Wang, J., Huo, Q., Zhang, T., Liu, F., Wang, S., Ma, Z., Jiang, S. Performance evaluation for a coupled push – pull ventilation and air curtain system to restrict pollutant dispersion in a factory building. Journal of Building Engineering. 2021. 43 (January). Article no. 103164. DOI: 10.1016/j.jobe.2021.103164
13. Zhang, J., Wang, J., Gao, J., Cao, C., Lv, L., Xie, M., Zeng, L. Critical velocity of active air jet required to enhance free opening rectangular exhaust hood. Energy and Buildings. 2020. 225. Article no. 110316. DOI: 10.1016/j.enbuild.2020.110316
14. Zhao, R., Qian, H., Liu, L., Zheng, X. Comprehensive performance evaluation of a novel Aaberg exhaust system reinforced by a swirling jet. Building and Environment. 2020. 167. Article no. 106451. DOI: 10.1016/j.buildenv.2019.106451
15. Vekteris, V., Tetsman, I., Mokshin, V. Investigation of the efficiency of the lateral exhaust hood enhanced by aeroacoustic air flow. Process Safety and Environmental Protection. 2017. 109. Pp. 224–232. DOI: 10.1016/j.psep.2017.04.004
16. Pinelli, M., Suman, A. A numerical method for the efficient design of free opening hoods in industrial and domestic applications. Energy. 2014. 74. Pp. 484–493. DOI: 10.1016/j.energy.2014.07.014
17. Yin, Y., Li, A., Wen, X., Zhang, J., Zhang, X., Guo, J., Li, J., Zhang, W., Che, J. Resistance reduction of an elbow with a guide vane based on the field synergy principle and viscous dissipation analysis. Journal of Building Engineering. 2022. 54. Article no. 104649. DOI: 10.1016/j.jobe.2022.104649
18. Solodova, E.E. Osobennosti chislennogo modelirovaniya techeniy v Z-obraznykh otvodakh sistem ventilyatsii i konditsionirovaniya zdaniy i sooruzheniy [Features of flows numerical modeling in z-shaped elbows of ventilation and air conditioning systems of buildings and structures. News of KSUAE. 2021. 55 (1). Pp. 71–84. DOI: 10.52409/20731523_2021_1_71
19. Yin, Y., Wen, X., Zhang, J., Li, A. Geometric parameters optimization of low resistance T-junction with guide vanes in HVAC system. E3S Web of Conferences. 2022. 356. Article no. 02056. DOI: 10.1051/e3sconf/202235602056
20. Shopayeva, A., Safiullin, R. CFD-modeling of flow in confluence nodes of ventilation units of multi-storey buildings. IOP Conference Series: Materials Science and Engineering. 2020. 890. Pp. 012157. DOI: 10.1088/1757-899X/890/1/012157
21. Gao, R., Liu, K., Li, A., Fang, Z., Yang, Z., Cong, B. Study of the shape optimization of a tee guide vane in a ventilation and air-conditioning duct. Building and Environment. 2018. 132. Pp. 345–356. DOI: 10.1016/j.buildenv.2018.02.006
22. Yin, Y., Chen, K., Qiao, X., Lin, M., Lin, Z., Wang, Q. Mean Pressure Distributions on the Vanes and Flow Loss in the Branch in a T Pipe Junction with Different Angles. Energy Procedia. 2017. 105. Pp. 3239–3244. DOI: 10.1016/j.egypro.2017.03.718
23. Srinivasan, K., Balamurugan, V., Jayanti, S. Shape optimisation of curved interconnecting ducts. Defence Science Journal. 2015. 65 (4). Pp. 300–306. DOI: 10.14429/dsj.65.8353
24. Courtais, A., Lesage, F., Privat, Y., Frey, P., Latifi, A. razak. Adjoint system method in shape optimization of some typical fluid flow patterns. Computer Aided Chemical Engineering. 2019. 46. Pp. 871–876. DOI: 10.1016/B978-0-12-818634-3.50146-6
25. Demirel, G., Acar, E., Celebioglu, K., Aradag, S. CFD-driven surrogate-based multi-objective shape optimization of an elbow type draft tube. International Journal of Hydrogen Energy. 2017. 42 (28). Pp. 17601–17610. DOI: 10.1016/j.ijhydene.2017.03.082
26. Gao, R., Zhang, H., Li, A., Liu, K., Yu, S., Deng, B., Wen, S., Li, A., Zhang, H., Du, W., Deng, B. A novel low-resistance duct tee emulating a river course. Building and Environment. 2018. 144 (June). Pp. 295–304. DOI: 10.1016/j.buildenv.2018.08.034
27. Gao, R., Liu, K., Li, A., Fang, Z., Yang, Z., Cong, B. Biomimetic duct tee for reducing the local resistance of a ventilation and air-conditioning system. Building and Environment. 2018. 129 (September 2017). Pp. 130–141. DOI: 10.1016/j.buildenv.2017.11.023
28. Li, A., Chen, X., Chen, L. Numerical investigations on effects of seven drag reduction components in elbow and T-junction close-coupled pipes. Building Services Engineering Research and Technology. 2015. 36 (3). Pp. 295–310. DOI: 10.1177/0143624414541453
29. Logachev, K.I., Ziganshin, A.M., Averkova, O.A. On the resistance of a round exhaust hood, shaped by outlines of the vortex zones occurring at its inlet. Building and Environment. 2019. 151. Pp. 338–347. DOI: 10.1016/j.buildenv.2019.01.039

30. Logachev, K.I., Ziganshin, A.M., Huang, Y., Wang, Y., Averkova, O.A., Popov, E.N., Gol'tsov, A.B., Tiron, O. V. Investigating changes in geometric dimensions of vortex zones at the inlet of an exhaust hood set over a plane. Building and Environment. 2022. (May). Pp. 109377. DOI: 10.1016/j.buildenv.2022.109377
31. Idel'chik, I.E., Steinberg, M.O. Handbook of Hydraulic Resistance. 3rd Edn. . Boca Raton, FL, CRC Press, 1994. 790 s. ISBN: 0-8493-9908-4.
32. ANSYS® Academic Research Mechanical and CFD, Release 18.2.
33. Logachev, K.I., Ziganshin, A.M., Averkova, O.A. Simulations of dust dynamics around a cone hood in updraft conditions. Journal of Occupational and Environmental Hygiene. 2018. 15 (10). Pp. 715–731. DOI: 10.1080/15459624.2018.1492137

Information about authors:

Arslan Ziganshin, *Doctor of Technical Sciences*
ORCID: https://orcid.org/0000-0001-7335-7797
E-mail: ziganshin.arslan@gmail.com

Konstantin Logachev, *Doctor of Technical Sciences*
ORCID: https://orcid.org/0000-0003-0632-6784
E-mail: kilogachev@mail.ru

Julia Kareeva, *PhD in Technical Sciences*
ORCID: https://orcid.org/0000-0002-9497-349X
E-mail: jkareeva2503@gmail.com

Received 13.04.2023. Approved after reviewing 25.09.2023. Accepted 27.09.2023.

Magazine of Civil Engineering

ISSN 2712-8172

journal homepage: http://engstroy.spbstu.ru/

Research article

UDC 691.16+620.162

DOI: 10.34910/MCE.123.8

Intrinsic self-healing potential of asphalt concrete

S.S. Inozemtcev [1] ✉ , ***E.V. Korolev*** [2] , ***T. Do*** [1]

[1] *Moscow State University of Civil Engineering (National Research University), Moscow, Russian Federation*

[2] *St. Petersburg State University of Architecture and Civil Engineering, St. Petersburg, Russian Federation*

✉ *inozemtsevss@mail.ru*

Keywords: self-healing, intrinsic potential, asphalt concrete, bitumen

Abstract. In the work, the influence of temperature, the time of its exposure, as well as the structural properties of bitumen and the test conditions for asphalt concrete on its intrinsic potential for self-healing was studied. Asphalt concrete samples from two types of bitumen with different group compositions were produced and tested under uniaxial compression and split. The intrinsic self-healing potential of asphalt concrete increases with an increase in temperature and exposure time. The greatest effect of temperature on the intrinsic self-healing potential corresponds to values close to the bitumen softening temperature. Temperature is a factor of double action: if there is a sufficient amount of maltene fraction in the bituminous matrix of asphalt concrete, it improves healing; in the absence of the maltene fraction, the high temperature is a condition for the aging of the binder. Aromatic compounds among maltenes are of greater importance in self-healing. The dimensions, condition of the samples, and features of the formation of defects are factors that affect intrinsic self-healing.

Funding: Russian Science Foundation grant no. 22-79-10051, https://rscf.ru/project/22-79-10051/

Citation: Inozemtcev, S.S., Korolev, E.V., Do, T. Intrinsic self-healing potential of asphalt concrete. Magazine of Civil Engineering. 2023. 123(7). Article no. 12308. DOI: 10.34910/MCE.123.8

1. Introduction

Asphalt concretes are operated under variable mechanical and thermal loads, due to which cracks occur in the material causing premature failure of pavements [1]. Functional modifiers in asphalt mixes are used to improve the performance of asphalt concrete. Ordinary additives improve the ability of asphalt concrete to resist dynamic impacts [2], delaying the onset of cracking. There is a new type of additives that provide self-healing of asphalt concrete, eliminate some of the defects at the stage of operation and preserve the functionality of the material. A lot of research [4–6] is aimed at developing new solutions that allow creating effective self-healing asphalt concrete.

The problem in the development of such asphalt concretes is the thermoplastic nature of the binder and the technological features of the production of the material. Since the technology of using thermoplastic bitumen as part of asphalt concrete mixture includes the stage of heating to a temperature above 100 °C when mixing the components, the use of microorganisms as a healing agent is impossible. Also, the process of compacting the asphalt mixture can prematurely destroy the capsules of the healing agent. Therefore, the technology for using an encapsulated healing agent must take these factors into account.

After cooling of the asphalt concrete mixture, the bitumen hardens, and the elastic properties prevail in the asphalt concrete. The type of defects in asphalt concrete depends on the conditions in which it is operated. At high temperatures, plastic deformations occur, and at low temperatures, cracks form due to brittleness. Cracks occur in the asphalt concrete matrix or at the binder-aggregate interface. Defects are formed at the microscale level at the initial stage, and then they combine into macrocracks [7].

Intrinsic self-healing potential is an important aspect to consider when developing self-healing methods for asphalt concrete. The intrinsic self-healing potential is the ability of a material to restore the state of the structure, due to the nature and characteristics of the substance of which it is composed. For asphalt concrete, this ability is determined by the thermoplastic nature of the bituminous binder. Therefore, when developing an effective solution for self-healing asphalt concrete, it must be taken into account that partial restoration of the state of the structure may be due to the bitumen's intrinsic self-healing potential.

Analysis of scientific studies [4–17] shows that the effectiveness of asphalt concrete self-healing depends on controllable factors, which are regulated by prescription parameters, and on uncontrollable factors, which are determined by the operating conditions of the pavement (Fig. 1).

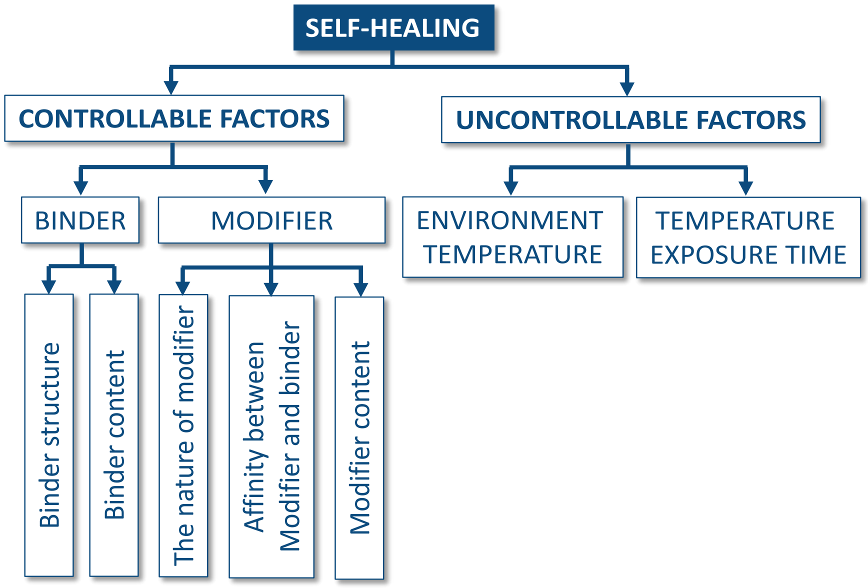

Figure 1. Decomposition of factors affecting the self-healing of asphalt concrete.

Recipe and technological parameters of asphalt concrete production, which are controlled at the stage of designing the composition of the asphalt concrete mixture, are controllable factors [5, 7]. Controlling the self-healing ability of asphalt concrete is achieved through two main components: bitumen and special modifiers [6–11].

The ability to independently eliminate defects in the structure is determined by the thermoplastic properties of bitumen and is provided by spontaneous entanglement of the molecule [8]. Also, the intergrowth of molecules in bitumen occurs at the molecular level due to reversible hydrogen bonding [9] with the formation of new crosslinks and chains [10, 11]. These processes determine intrinsic self-healing potential for bitumen in asphalt concrete, which depends on the binder content in the mixture and its group composition.

The use of various kinds of modifiers to intensify self-healing is a solution that determines its effectiveness [12–16]. In this case, the nature of the modifier used and its degree of affinity with bitumen will affect the efficiency of self-healing and the mechanism of this process. For example, an encapsulated rejuvenator is able to increase bitumen intrinsic potential self-healing by changing its group composition [12, 13]. And the encapsulated polymer modifier acts as a gluing agent, forming new structural bonds [14, 15].

Environment temperature and its exposure time are uncontrollable factors that affect the self-healing of asphalt concrete. The influence of temperature is due to the thermoplastic properties of bitumen in asphalt concrete, when the viscoelastic flow contributes to the closure of microcracks and prevents their growth. In this case, the intensity of this process depends on the intermolecular distance and the rate of thermal motion of molecules, which naturally increases with increasing temperature rise.

An important condition for the occurrence of self-healing during operation at high temperatures is the absence of significant plastic deformations. With temperature rise, the kinetic energy of the rotational and vibrational motion of the molecules of the binder increases, which leads to an increase in the distance between the molecules. The consequence of this is an increase in the volume of the material and a decrease in the viscosity of the thermoplastic material [16, 17]. In this case, a contact can occur in the defect (crack) zone if its surfaces are sufficiently close, which, as a result, contributes to their spontaneous coalescence.

It should be noted that when special additives are used in the composition of asphalt concrete, including components sensitive to healing effects, the properties and nature of these components will be an additional factor influencing the ability of self-healing [3, 18, 19]. Therefore, studies to establish the degree of influence of temperature, the time of its exposure, the composition of bitumen on the intrinsic self-healing potential of asphalt concrete, taking into account the type of testing of samples, are relevant.

In this article, the goal is to study the influence of these factors (Fig. 1) on the intrinsic self-healing potential of asphalt concrete, to achieve which the tasks of studying the influence of the temperature of the medium and the time of its action on asphalt concrete samples during the healing period after the strength test were solved. The problem of assessing the influence of the composition of bitumen and test methods on the intrinsic self-healing potential of asphalt concrete was also solved.

2. Materials and Methods

Mechanical behavior of self-healing stone mastic asphalt (SMA) mixtures is examined experimentally. The materials and tests methods used in this study are summarized in sections 2.1 and 2.2 respectively.

2.1. Materials

Bitumens BND 60/90 (Russian State Standard GOST 22245-90 Viscous petroleum road bitumen. Specifications) with a softening point of 51 °C (BND(1)) and 60 °C (BND(2)) (ASTM D36/D36M-20, EN 1427:2015) are used as a binder for asphalt concrete. BND(2) bitumen is obtained from BND(1) by aging for 8 hours at 160 °C. The basis of the binder aging technique complies with the test conditions in accordance with the Russian State Standard GOST 18180-72 Petroleum bitumen. Method for determination of change of mass after heating (EN 12607-2). The group composition of bitumen (referred to as SARA) is presented in Table 1.

Table 1. Bitumen composition SARA.

Bitumen	SARA, %			
	Saturates	Aromatics	Resins	Asphaltenes
BND (1)	7.1	38.5	32.2	22.2
BND (2)	6.5	32.9	38.5	22.1

Note: Method for Determining SARA described in the section 2.2

The SMA mixtures were prepared following the aggregate gradation presented in Table 2. The binder content is 7 % over the mineral part of the mixture, resulting in an air void content of 3 %. 0.3 % by weight of the mixture of cellulose fibers Viatop-66 is used as a stabilizing additive to prevent bitumen drainage.

Table 2. Sieve grain analysis (particle size distribution).

Parameter	Value								
Sieve size, mm	15	10	5	2.5	1.25	0.63	0.315	0.16	0.071
Passing, %	92.3	58.8	33.0	21.7	18.4	16.5	14.7	12.7	10.6

SMA cylindrical specimens with a height and diameter of 71.4 mm were manufactured, by placing the required mass of the mixture into a mold (inner height is 160 mm and inner diameter are 71.4 mm) and compacting it in two stages (Russian State Standard GOST 12801-98). The form, heated to 90...100 °C, is filled with an asphalt concrete mixture, installed on a vibrating platform, firmly fixed on it with a special device. The mixture in the mold is vibrated for 3.0 ± 0.1 min at a frequency of 2900 ± 100 min^{-1}, an amplitude of 0.40 ± 0.05 mm and a vertical load on the mixture of 30 ± 5 kPa, which is transferred to the mixture with the help of a load hung on the form. After vibrating, the mold with the sample is removed from the vibrating platform, placed on the press plate for additional compaction under pressure 20.0 ± 0.5 MPa and maintained at this pressure for 3 minutes. Then the load is removed and the sample is removed from the mold with a squeeze tool.

The main properties of SMA are summarized in Table 3.

Table 3. Main properties of SMA with different bitumen.

Parameter	Method	Unit	Standard limit	Value for bitumen	
				BND(1)	BND(2)
Average density	Russian State Standard GOST 12801-98	g/cm^3	–	2.43	2.44
Air void		%	1.5…4.5	3.0	3.0
Water saturation		%	1.0…4.0	1.9	1.2
Compressive strength at 20 °C		MPa	> 2.2	3.3	3.2
Compressive strength at 50 °C		MPa	> 0.65	1.1	0.9
Coefficient of internal friction		–	> 0.93	0.93	0.97
Shear bond at 50 °C		MPa	> 0.18	0.56	0.57
Tensile strength at 0 °C		MPa	2.5…6.0	2.6	2.5
Water resistance (long exposure)		–	> 0.85	0.92	0.90

2.2. Test methods

SARA was determined by thin layer chromatography with a flame ionization detector and with Chromarod TM type SIII quartz rods in accordance with IP 469 using an Iatroscan Mark V analyzer.

Determination of the main properties of SMA was carried out in accordance with the methods specified in Russian State Standard GOST 12801-98 Materials on the basis of organic binders for road and airfield construction. Test methods.

The effect of temperature and the structure of the binder on the self-healing of SMA were studied on cylinder samples, which were tested under two loading schemes to determine the strength: in compression and splitting.

Cylinder samples (diameter – 71.4 mm, height – 71.4 mm) were used to determine the compressive strength. Compression was carried out after thermostating the samples at a temperature of 20 °C. Thermostating of the samples was carried out in a climatic chamber for 4 hours. The compression rate corresponded to a press plate movement of 3 mm/min. During loading, the maximum load that the sample could withstand was recorded. Compression strength was calculated using the formula:

$$R_c = \frac{P}{S} \cdot 10^{-2}, \tag{1}$$

where P is maximum compression load, N; S is load distribution area, cm^2, 10^{-2} is conversion factor to MPa.

Samples-half-cylinders with a radius and thickness of 35.7 mm were sawn from standard samples-cylinders to determine the ultimate strength in splitting. Splitting was carried out after thermostating the samples at a temperature of –20 °C. Thermostating of the samples was carried out in a climatic chamber for 4 hours. The loading rate corresponded to the movement of the press plate of 3 mm/min. During loading, the maximum load that the sample could withstand was recorded. Split strength was calculated using the formula:

$$R_b = \frac{P}{2RT}, \tag{2}$$

where P is maximum breaking load, N; T is half-cylinder sample width, cm, R is half-cylinder sample radius, cm.

After the destruction of the semi-cylinder samples, the two parts were combined, pressing the fracture surfaces to each other with rubber bands.

For healing, the samples were placed in a drying chamber. The duration of recovery and the temperature of the medium were set in accordance with the two-factor experimental plan.

Two-factor composite experimental design was implemented. Temperature (X_1, °C) and exposure time (X_2, day) are selected as predictors. It was also proved during the research that polynomial regression model [20]:

$$Y = B_0 + B_1 X_1 + B_2 X_2 + B_{12} X_1 X_2 + B_{11} X_1^2 + B_{22} X_2^2, \tag{3}$$

is suitable (hypothesis test for adequacy by means of F -criterion) as a description.

Zero levels $\left(X_{0i}\right)$ and half-variations $\left(l_i\right)$ for experimental designs are summarized: X_{01} = 45 °C; X_{02} = 7 days; l_1 = 15 °C; l_2 = 3 days.

After the healing period, the specimens were re-thermostated at 20 °C or –20 °C and tested in compression or splitting, respectively.

3. Results and Discussion

Currently, there is no single approach to assess the effect of self-healing in materials. In most cases, the calculation of the relative change in strength after a rest period is used. However, this approach can not show the ability of the material to heal for various loading schemes and test conditions.

In this work, the residual strength approach was used to evaluate the effect of intrinsic self-healing potential $\left(HP\right)$.

$$HP = \frac{R_h - R_1}{R_0}, \tag{4}$$

where R_h is strength after healing, MPa; R_0 is strength before healing, MPa; R_1 is residual strength, MPa. Residual strength was measured by repeated testing on samples after determining R_0.

The results of determining the strength indicators of asphalt concrete under various loading schemes and various healing conditions are presented in Table 4.

Table 4. SMA strength for various test schemes.

#	X_1, °C	X_2, day	Strength, MPa											
			SMA based BND(1)						SMA based BND(2)					
			Compression			Splitting			Compression			Splitting		
			R_0	R_1	R_h	R_0	R_1	R_h	R_0	R_1	R_h	R_0	R_1	R_h
1	30	4			1.64			0.05			1.91			0.34
2	60	4			2.12			0.41			1.97			0.87
3	30	10			1.82			0.21			1.98			0.37
4	60	10			2.11			0.65			1.88			0.29
5	23.8	7	3.36	1.32	1.60	1.95	–	0.01	3.17	1.85	1.90	1.74	–	0.05
6	66.2	7			2.03			0.32			1.94			1.24
7	45	2.75			1.73			0.06			2.02			0.29
8	45	11.24			1.75			0.31			1.92			0.48
9	45	7			1.81			0.23			1.95			0.54

Strength indicates a greater fragility of asphalt concrete based on BND(2) bitumen, which is due to a lower content of aromatic compounds. This is explained by the fact that BND(2) contains less maltenes, including aromatic compounds that reduce hardness and increase fluidity. And resins, which are viscosity and hardness, are contained in BND (2) more [21]. Residual strength is absent for samples tested in splitting. At the same time, the residual compressive strength is 58 % of the strength of asphalt concrete based on BND(2) and 40 % of the strength of asphalt concrete based on BND(1). This is probably due to the influence of the group composition of bitumen on the deformative properties of asphalt concrete. Asphalt concrete based BND(1), where the concentration of paraffin-naphthenic and aromatic compounds is higher, is prone to large deformations, therefore, after a compression test, deformation and displacement of structural elements occur, which contributes to the formation of a less stable structure [22]. These factors must be taken into account when choosing a method for determining the ability of self-healing.

The healing characteristics were calculated using the strength, on the basis of which the regression equations were obtained, reflecting the dependence of the intrinsic self-healing potential on the temperature and time of its exposure during the rest period.

For asphalt concrete based on BND(1), the equations are:

$$HP_{C1} = 14.7 + 5.09X_1 + 0.76X_2 - 1.35X_1X_2 + 1.17X_1^2 + 0.09X_2^2, \tag{5}$$

$$HP_{B1} = 12.0 + 7.95X_1 + 4.86X_2 + 1.05X_1X_2 + 0.12X_1^2 + 0.79X_2^2 \quad (6)$$

and for asphalt concrete based on BND(2) bitumen, the equations are:

$$HP_{C2} = 3.2 + 0.05X_1 - 0.66X_2 - 1.23X_1X_2 - 0.55X_1^2 - 0.23X_2^2, \quad (7)$$

$$HP_{B2} = 30.7 + 15.27X_1 + 2.07X_2 - 8.72X_1X_2 + 2.39X_1^2 - 5.06X_2^2, \quad (8)$$

where HP_{Ci} and HP_{Bi} are the intrinsic self-healing potential of specimens during compression and splitting tests, respectively.

The dependencies under study are graphically presented in Fig. 2 for asphalt concrete based on BND(1) and in fig. 3 for asphalt concrete based on BND(2).

a) **b)**

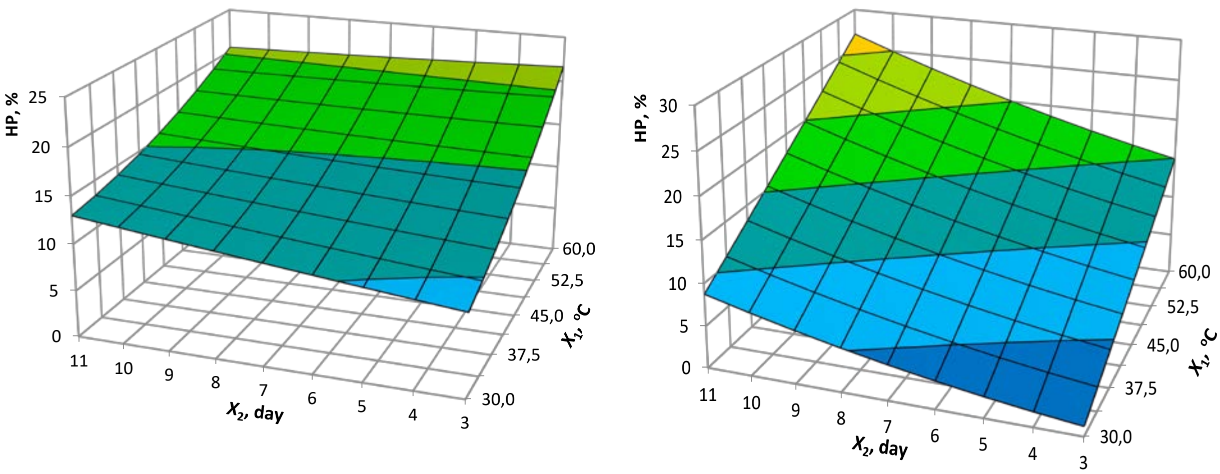

Figure 2. For asphalt concrete based on BND(1) graphical representation of equations: a – compression test (5); b – split test (6).

a) **b)**

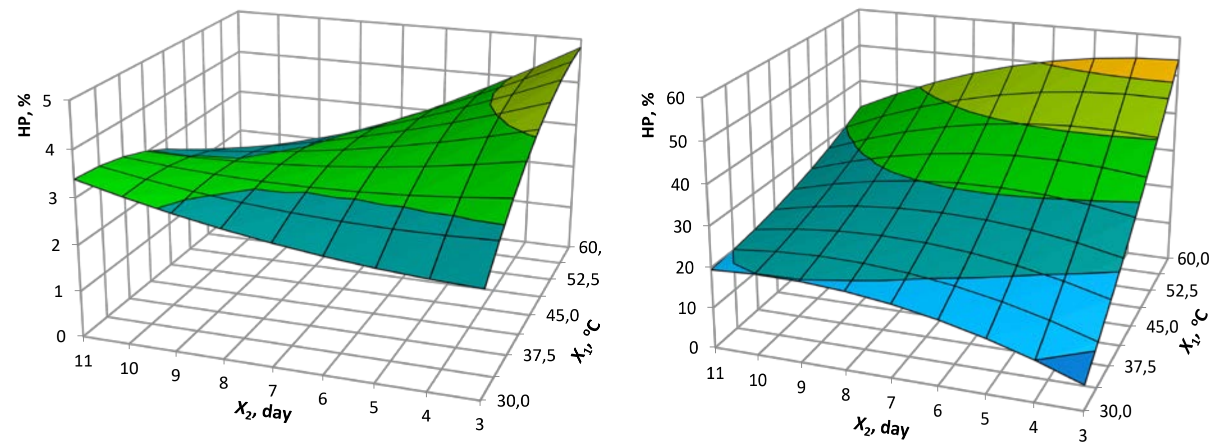

Figure 3. For asphalt concrete based on BND(2) graphical representation of equations: a – compression test (7); b – split test (8).

An analysis of the obtained mathematical models, which describe changes in the intrinsic self-healing potential with temperature and time of its action, shows that the studied factors have a different effect on samples made on the basis of bitumen with different group composition and tested under different conditions.

The temperature factor has a positive effect on the intrinsic self-healing potential of asphalt concrete: with an increase in temperature to the bitumen softening point, an increase in strength after self-healing is observed. This effect is due to a change in the rheological properties of the matrix, a decrease in the viscosity of bitumen, and an increase in the mobility of molecules. In such a state, the probability increases that the molecules spontaneously entangle with each other and grow together through the restoration of specific bonds [9, 23]. The intensity of this process depends on the intermolecular distance and the rate of thermal motion of molecules, which naturally increases with increasing temperature. In this case, a contact that promotes their spontaneous entangle can occur when the surfaces of the defect (crack) are sufficiently close. Consideration of a defect with the involvement of the Laplace pressure is a theoretical justification for the implementation of the self-healing mechanism. In this case, the defect is represented as two surfaces, between which there is a gas phase. The Laplace pressure arises on each surface, which is directed into the internal volume of the phase that forms the surface of the defect. This pressure prevents spontaneous self-healing.

It should be noted that temperature is a factor of double action. Temperature can be a factor that improves recovery, and can negatively affect the ability to self-heal. If there is a sufficient amount of maltene fraction in the bituminous matrix of asphalt concrete (Fig. 2), the temperature has a positive effect on the healing process. But with its deficiency, temperature is a condition for the aging of the binder and does not contribute to the process of spontaneous entangle of molecules (Fig. 3). The intrinsic self-healing potential for asphalt concrete based on BND(2) is significantly less than for asphalt concrete based on BND(1).

The double action effect of the influence of temperature is obvious with an increase in the time of its exposure. The time factor for asphalt concrete based on BND(1) is positive, however, at elevated temperatures, its positive effect decreases. Under conditions of lower content of light fractions in bitumen, the temperature exposure time is a negative factor influencing the intrinsic self-healing potential. In this case, the maximum values of the intrinsic self-healing potential of asphalt concrete correspond to the boundary of the studied factor space – exposure for 3 days. This is due to the aging of the binder and a decrease in the maltene part of bitumen, in which asphaltene-resin complexes are dissolved, which contributes to the deterioration of rheological properties and a decrease in the mobility of molecules.

It should be noted that the ability of bitumen to self-heal is a sensitive property, because a decrease in the content of paraffin-naphthenic and aromatic compounds by 13.5 % leads to a significant change in the degree of influence of temperature and the time of its exposure. Taking into account the differences in the group compositions of the bitumen used (Table 1), it can be concluded that a higher content of light fractions has a positive effect on intrinsic self-healing potential. When choosing bitumen and designing an asphalt concrete mixture, it is necessary to take into account the physical and chemical processes of the interaction of the binder with mineral components, as a result of which the fractions are redistributed, and the amount of free bitumen will also affect self-healing.

Intrinsic self-healing potential differs significantly when testing asphalt concrete samples using different loading schemes and testing temperatures. The test temperature affects the state of asphalt concrete at the time of loading. When tested under conditions of negative temperature, elastic properties prevail in asphalt concrete, and the sample does not deform during loading, but brittle breaks into two parts with a clear contour of the defect surfaces. When the sample is compressed at 20 °C, the work at failure is partially spent on deformation and the elastoplastic properties appear. At the same time, samples after compression are characterized by residual strength, since the maximum fixed load does not destroy all structural bonds in asphalt concrete. The main crack across the sample is formed during splitting, so there is no residual strength. Thus, the testing scheme affects the type of defects in the samples and creates different initial conditions for further self-healing.

It should be noted that when testing samples of asphalt concrete for splitting, the intrinsic self-healing potential is greater than when testing under compression for each type of bitumen. Since the determination of the splitting strength was carried out at a temperature of –20 °C, the asphalt concrete sample was brittle, which ensured good contact of the fracture planes during self-healing (Fig. 4).

a) **b)**

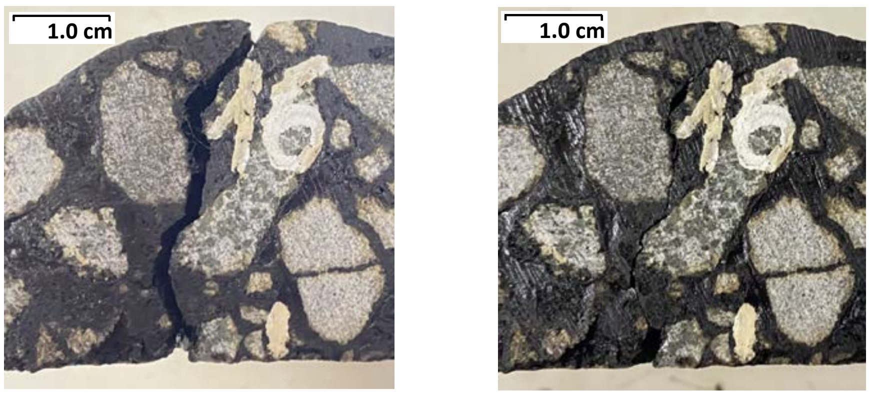

Figure 4. Asphalt concrete sample before (a) and after (b) self-healing.

Pictures of asphalt concrete samples show that defects have angular edges. The surfaces of the defect are easily joined to each other during the healing process, which will contribute to better self-healing. After healing, the defect on the front surface of the sample remains visible to the naked eye, but the strength is high.

The reason for the increased values of intrinsic self-healing potential are two main aspects. First of all, this is the brittle state of the material and the nature of the defect formed during splitting. When the sample is destroyed, the formed surfaces of the main crack have a similar relief without significant deformations, which contributes to their good joining during the rest period. Secondly, the gap between the surfaces of the defect contributes to their heating during thermostating, and during heating in the volume of the sample, a certain temperature gradient is formed. Thus, the dimensions of the tested samples, the state of the samples during testing, the features of the formation of defects are factors that affect self-healing. These factors should be taken into account when developing new ways to implement self-healing technology and a unified method for measuring self-healing indicators.

The group composition of bitumen is used to calculate the Colloidal Instability Index (CII), which is the ratio of the sum of the concentrations of asphaltenes and saturates to the sum of the concentrations of resins and aromatic compounds:

$$CII = \frac{A_s + S}{R + A_r}, \tag{9}$$

where: A_s is the weight percent of asphaltenes; S is the weight percent of saturates; R is the weight percent of resins; and A_r is the weight percent of aromatics.

This index characterizes the peptizing ability and its lower values indicate a greater stability of the bitumen structure. It was noted in [24] that lower CII values correspond to higher self-healing rates, because molecules with a less branched structure are more mobile. For the studied bitumens, the CII values differ insignificantly, for BND(1) it is 0.41, and for BND(2) it is 0.40. Thus, it is aromatic compounds that are dominant in the issue of bitumen self-healing among maltenes. This may be due to the sequence of transition of individual fractions of bitumen into the melt with increasing temperature: aromatic compounds have a lower softening point, so their molecules are more involved in free thermal motion than resin molecules.

Also, the amphoteric nature of bitumen and aromaticity affect the formation of chains in the structure and the ability to interact in several places [25]. According to [25], an increase in the acid-base surface energy and a decrease in the Lifshitz-van der Waals surface energy occur in bitumen with a low content of amphoteric substances and a high content of aromatic compounds. This confirms the importance of the influence of a higher concentration of aromatic compounds on diffusion, molecular mobility and, consequently, self-healing [26–28].

It should be noted that this article does not take into account the influence of the ratio of bulk and structured bitumen in the volume of asphalt concrete. However, it is obvious that the interaction of mineral components with bitumen will contribute to the redistribution of binder fractions [29]. The intensity of these physical and chemical processes will also affect the ability of self-healing. Therefore, this issue is relevant for further research in the field of self-healing asphalt concrete.

4. Conclusions

Temperature is a factor of double action: if there is a sufficient amount of maltene fraction in the bituminous matrix of asphalt concrete, it has a positive effect on healing; with a lack of maltene fraction, temperature serves as a condition for the aging of the binder and does not contribute to self-healing. The ability of bitumen to self-heal is a sensitive property, because a decrease in the content of paraffin-naphthenic and aromatic compounds by 13.5 % leads to a significant change in the degree of influence of temperature and the time of exposure to it. The maximum recovery of strength after thermal exposure at a temperature of 60 °C is 27 % and 55 % for asphalt concrete based on BND(1) and BND(2) bitumen, respectively.

The greatest effect of temperature on the intrinsic self-healing potential corresponds to values close to the softening point of the applied bitumen. However, under such conditions, asphalt concrete loses its bearing capacity, deforms excessively and cannot be used. Therefore, using the ability of bitumen molecules to spontaneously entangle as a mechanism for self-healing is difficult.

For the studied bitumens, the Colloidal Instability Index values differ insignificantly, for BND(1) it is 0.41, and for BND(2) it is 0.40. Aromatic compounds have a dominant role in the self-healing of bitumen among maltenes: aromatic compounds have a lower softening point, so their molecules are more involved in free thermal movement than resin molecules.

The dimensions of the tested samples, the state of the samples during testing, the features of the formation of defects are factors that affect self-healing. These factors should be taken into account when developing new ways to implement self-healing technology and a unified method for measuring self-healing indicators.

References

1. Yang, T., Jia, Y., Pan, Y., Zhao, Y. Evaluation of the Low-Temperature Cracking Performance of Recycled Asphalt Mixture: A Development of Equivalent Fracture Temperature. Buildings. 2022. 12. 1366. DOI: 10.3390/buildings12091366
2. Teltayeva, B.B., Rossib, C.O., Izmailovaa, G.G., Amirbayeva, E.D., Elshibayeva, A.O. Evaluating the effect of asphalt binder modification on the low-temperature cracking resistance of hot mix asphalt. Case Studies in Construction Materials. 2019. 11. e00238. DOI: 10.1016/j.cscm.2019.e00238
3. Inozemtcev, S., Korolev, E. Review of road materials self-healing: problems and perspective. IOP Conference Series: Materials Science and Engineering. 2020. 855. 12010. DOI: 10.1088/1757-899X/855/1/012010
4. Anupam, B.R., Sahoo, U.C., Chandrappa, A.K. A methodological review on self-healing asphalt pavements. Construction and Building Materials. 321. 2022. 126395. DOI: 10.1016/j.conbuildmat.2022.126395
5. Varma, R., Balieu, R., Kringos, N. A state-of-the-art review on self-healing in asphalt materials: Mechanical testing and analysis approaches. Construction and Building Materials. 310. 2021. 125197. DOI: 10.1016/j.conbuildmat.2021.125197
6. Nalbandian, K.M., Carpio, M., González, Á. Analysis of the scientific evolution of self-healing asphalt pavements: Toward sustainable road materials. Journal of Cleaner Production. 2021. 293. 126107. DOI: 10.1016/j.jclepro.2021.126107
7. Leegwater, G., Tabokovi´c, A., Baglieri, O., Hammoum, F., Baaj, H. Terms and Definitions on Crack-Healing and Restoration of Mechanical Properties in Bituminous Materials. Proceedings of the RILEM International Symposium on Bituminous Materials. 2021. RILEM Bookseries 27. DOI: 10.1007/978-3-030-46455-4_6
8. Mouillet, V., De la Roche, C., Chailleux, E., Coussot, P. Thixotropic Behavior of Paving-Grade Bitumens under Dynamic Shear. Journal of Materials in Civil Engineering. 2012. 24 (1). Pp. 23–31. DOI: 10.1061/(ASCE)MT.1943-5533.0000354
9. Phillips, M.C. Multi-step models for fatigue and healing, and binder properties involved in healing. In: Eurobitume workshop on performance related properties for bituminous binders, 1998, Luxembourg. Paper no. 115.
10. Fisher, H. Self repairing materials – dream or reality? Natural Science. 2010. 2 (8). Pp. 873–901. DOI: 10.4236/ns.2010.28110
11. Qui, J., Van de Ven, M.F.C., Wu, S., Molenaar, A.A.A. Investigation of self healing capability of bituminous binders. Road Materials Pavement Design. 2009. 10 (1). Pp. 81–94. DOI: 10.1080/14680629.2009.9690237
12. Xua, S., Liua, X., Tabaković, A., Lin, P., Zhang, Y., Nahar, S., Lommerts, B.J., Schlangena, E. The role of rejuvenators in embedded damage healing for asphalt pavement. Materials & Design. 2021. 202. 109564. DOI: 10.1016/j.matdes.2021.109564
13. Zheng, Y. Evaluation of sunflower oil's healing effect in bituminous materials. IOP Conf. Ser.: Mater. Sci. Eng. 2019. 493. 012021. DOI: 10.1088/1757-899X/493/1/012021
14. Inozemtcev, S., Jelagin, D., Korolev, E., Partl, M.N., Fasil, H., Do, T.T. Experimental and numerical study on SMA modified with an encapsulated polymeric healing agent. Materials and Structures. 2022. 55. 230. DOI: 10.1617/s11527-022-02059-8
15. Inozemtcev, S., Korolev, E. Sodium alginate emulsions for asphalt concrete modifiers encapsulating: structural rheological properties. Magazine of Civil Engineering. 2021. 101 (1). 10104. DOI: 10.34910/MCE.101.4
16. Bueno, M., Kakar, M.R., Refaa, Z., Wortlitschek, J., Stamatiuo, A., Partl, M.N. Modification of Asphalt Mixtures for Cold Regions Using Microencapsulated Phase Change Materials. Nature Research: Sci Rep. 2019. 9 (1). 20342. DOI: 10.1038/s41598-019-56808-x
17. Bekele, A., Ryden, N., Gudmarsson, A., Birgisson, B. Effect of Cyclic low temperature conditioning on Stiffness Modulus of Asphalt Concrete based on Non-contact Resonance testing method. Construction and Building Materials. 2019. 225. Pp. 502–509. DOI: 10.1016/j.conbuildmat.2019.07.194
18. Liu, J., Zhang, T., Guo, H., Wang Z., Wang X. Evaluation of self-healing properties of asphalt mixture containing steel slag under microwave heating: Mechanical, thermal transfer and voids microstructural characteristics. Journal of Cleaner Production. 2022. 342. 130932. DOI: 10.1016/j.jclepro.2022.130932
19. Shirzad, S., Hassan, M.M., Aguirre, M.A., Cooper, S.Jr., Mohammad, L.N., Negulescu I.I. Laboratory Testing of Self-Healing Polymer Modified Asphalt Mixtures Containing Recycled Asphalt Materials (RAP/RAS). MATEC Web of Conferences. 2019. 271. 03003. DOI: 10.1051/matecconf/201927103003
20. Yang, W., Yang, J., Kim, R. Multiple Quadratic Polynomial Regression Models and Quality Maps for Tensile Mechanical Properties and Quality Indices of Cast Aluminum Alloys according to Artificial Aging Heat Treatment Condition. Advances in Materials Science and Engineering. 2023. 2023. 7069987. DOI: 10.1155/2023/7069987
21. Holý, M., Remisova, E. Analysis of influence of bitumen composition on the properties represented by empirical and viscosity test. Transportation Research Procedia. 2019. 40. Pp. 34–41. DOI: 10.1016/j.trpro.2019.07.007
22. Wei, H., Hu, B., Wang, F., Zheng, J. Influence of temperature on deformation failure and acoustic emission characterisation of asphalt concrete under uniaxial compression. International Journal of Pavement Engineering. 2022. DOI: 10.1080/10298436.2022.2038380
23. Qiu, J., Van de Ven, M.F.C., Wu, S., Yu, J., Molenaar, A.A.A. Investigating the Self Healing Capability of Bituminous Binders. Road Materials and Pavement Design. 2009. 10. 81–94. DOI: 10.1080/14680629.2009.9690237
24. Kim, Y.R., Little, D.N., Benson, F.C. Chemical and mechanical evaluation of healing mechanism of asphalt concrete. Journal of Association Asphalt Paving Technologists. 1990. 59. Pp. 240–275.
25. Little, D.N., Lytton, R.L., Williams, D., Kim, R.Y. An analysis of the mechanism of microdamage healing based on the application of micromechanics first principles of fracture and healing. Journal of the Association of Asphalt Paving Technologists. 1999. 68. Pp. 501–542.

26. Sun, D., Yu, F., Li, L., Lin, T., Zhu, X.Y. Effect of chemical composition and structure of asphalt binders on self-healing. Construction and Building Materials. 2017. 133. Pp. 495–501. DOI: 10.1016/j.conbuildmat.2016.12.082
27. Abadeen, A.Z.U., Hussain, A., Kumar, V.S., Murali, G., Vatin, N.I., Hassan, Riaz H. Comprehensive Self-Healing Evaluation of Asphalt Concrete Containing Encapsulated Rejuvenator. Materials (Basel). 2022. 15 (10):3672. DOI: 10.3390/ma15103672
28. Qiu, J. Self Healing of Asphalt Mixtures: Towards a Better Understanding of the Mechanism. Thesis, Delft University of Technology. 2012.
29. Faheem, A.F., Bahia, H.U. Modeling of Asphalt Mastic in Terms of Filler-Bitumen Interaction. Road Materials and Pavement Design. 2010. Road Materials and Pavement Design. 11 (sup1). Pp. 281–303. DOI: 10.1080/14680629.2010.9690335

Information about authors:

Sergei Inozemtcev, *PhD in Technical Sciences*
ORCID: https://orcid.org/0000-0002-2965-0846
E-mail: inozemtsevss@mail.ru

Evgeniy Korolev, *Doctor of Technical Sciences*
ORCID: https://orcid.org/0000-0003-0815-4621
E-mail: korolev@nocnt.ru

Toan Do,
E-mail: trongtoan007@gmail.com

Received 03.04.2023. Approved after reviewing 03.10.2023. Accepted 03.10.2023.

Magazine of Civil Engineering

ISSN 2712-8172

journal homepage: http://engstroy.spbstu.ru/

Research article

UDC 69.07

DOI: 10.34910/MCE.123.9

Lateral bracing and steel shear wall integration in steel high-rises

M.F.K. Al Shamaa ✉, ***A.J.H. Al Shimmeri***, ***A. Lazem***

Civil Engineering Department, University of Baghdad, Baghdad, Iraq

✉ *mushriqf@coeng.uobaghdad.edu.iq*

Keywords: steel plate shear walls, lateral stiffness, lateral strength, braced frames

Abstract. In high-rise building structures, the designers tend to utilize tube systems, or their combination with other structural frame systems, as an efficient lateral resisting structural system. The drawbacks of tube systems include the effect of shear lag and the architectural problems arising from the closely spaced columns. These drawbacks can be remedied by using exterior braces (concentric bracing system), which provide high shear stiffness in combination with the tubes. Since in high-rise building structures control of bending drift is so difficult and complicated, utlizing the exterior braces is regarded as a practical method due to its high shear and bending stiffenesss. In so doing, in this paper, an innovative concept was investigated in which steel plate shear walls are utilized at the two extreme bays of a frame, and giant exterior braces are used between the shear walls. These two walls act as strong moment arms against the overturning moment and, because of their high stiffness, absorb most of the produced shear; consequently, the shear lag effect diminishes. The obtained results indicate that in the proposed system, the lateral displacement is diminished by around 2.13 times; consequently, the axial forces and bending moments in columns are reduced considerably by about 30 % and 50 %, respectively, demonstrating this system's high effectiveness.

Citation: Al Shamaa, M.F.K., AlShimmeri A.J.H., Lazem A. Lateral Bracing & Steel Shear Wall Integration in Steel High-rises. Magazine of Civil Engineering. 2023. 123(7). Article no. 12309. DOI: 10.34910/MCE.123.9

1. Introduction

Human has always been fascinated by tall buildings and high-rise towers. In ancient civilizations, tall structures were used for defensive purposes and symbolic and ceremonial applications. The growth and development of new high-rise structures with residential and commercial applications began in the 1880s [1]. Till now, several approaches have emerged to control the drift of the tall building, including dampers (passive, active, or semi-active) (Fisco and Adeli [2, 3]);(Nie et al [4]);(Farzampour et al [5]); (Zhao et al [6]); Qiu [7]);(Meghdadaian and Ghalehnovi [8]); (Al-Rumaithi et al [9]);(Ghamari et al. [10–12]);(AL-Shamaa et al [13])(Arshadi et al [14]);(Maddahi et al [15]); the TMDs (Smith et al. [16]);(Jin and Doloi [17]); (Lin et al., [18]);(Farghaly and Salem Ahmed [19]); (Kim [20]);(Giaralis and Petrini [21]);(Khaleel and AL-Shamaa [22]);(Zhang [23]); which improve a structure’s behavior and performance against wind and explosion, are typically considered as semi-active or passive control mechanisms (Moon et al. [24]); (Shayanfar et al.[25]). Fig. 1 illustrates some of the systems for steel structures. (Taranath [26]), stated that the use of tube systems has been deemed effective for tall buildings of the following order.

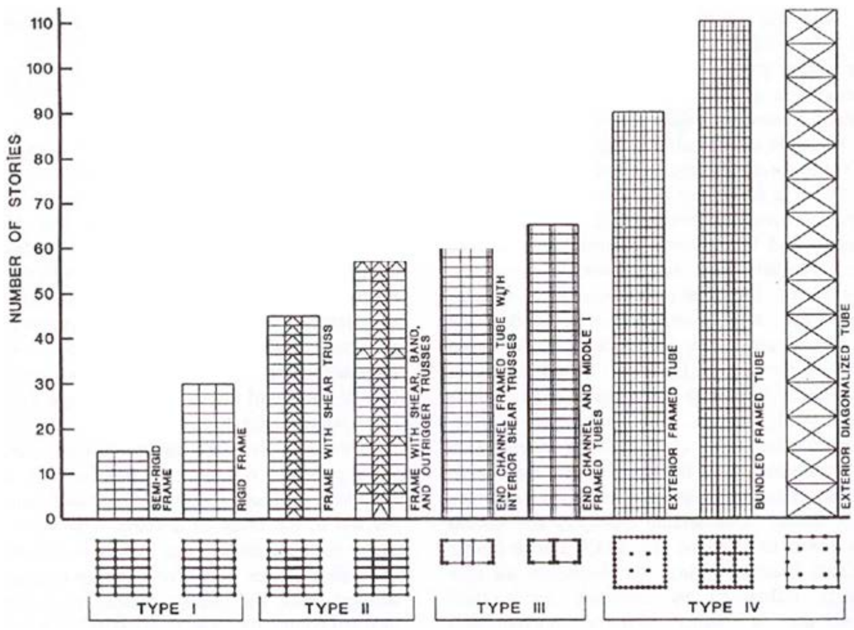

Figure 1. Systems tall buildings [26].

Tube systems are the developed versions of traditional rigid frames. The goal of using this structural form is to transfer most of the lateral load-resisting material to the structure's perimeter to maximize the flexural rigidity of the structure. The tube systems' strength and lateral stiffness are provided by using deep beams and closed columns. Practically, to achieve the optimum geometry and structural system in steel structures, the distance between the columns is set between 1.5 and 3.00 m, and the depth of the spandrels is considered between 0.9 and 1.5 m [26]. Although the tube systems withstand the entire lateral load, the gravity loads are divided among the peripheral and interior columns. When the structure is subjected to a lateral load, the peripheral frames in the direction of loading act as a web, and the frames normal to the loading direction act as a flange [26].

The main drawback of the tubes in controlling the lateral displacement stems from the flexibility of the beams of this system. This flexibility of the beams causes a non-uniform distribution of the axial stresses of the first-story columns according to Fig. 2, which is known as the “shear lag effect”. Another shortcoming of this system is related to the architectural aspects, i.e., the closely spaced peripheral columns. In addition, the problem associated with the closely-spaced columns becomes more apparent in tall buildings where the first stories have parking and commercial applications. These problems are remedied to a large extent by using giant exterior braces.

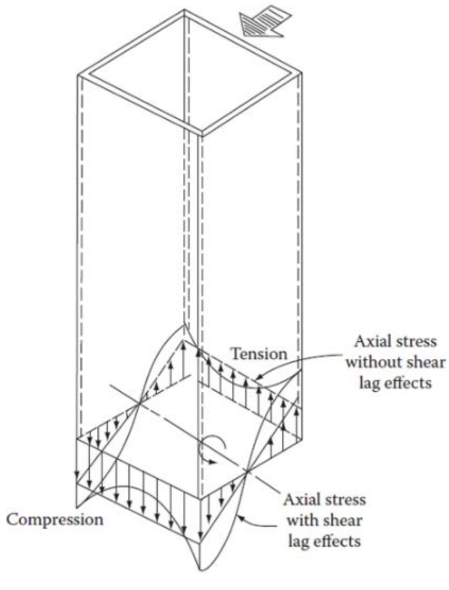

Figure 2. Shear lag effect [26].

By adding the giant exterior braces to the tubes, as shown in Fig. 3, the stiffness and rigidity of the system increase considerably.

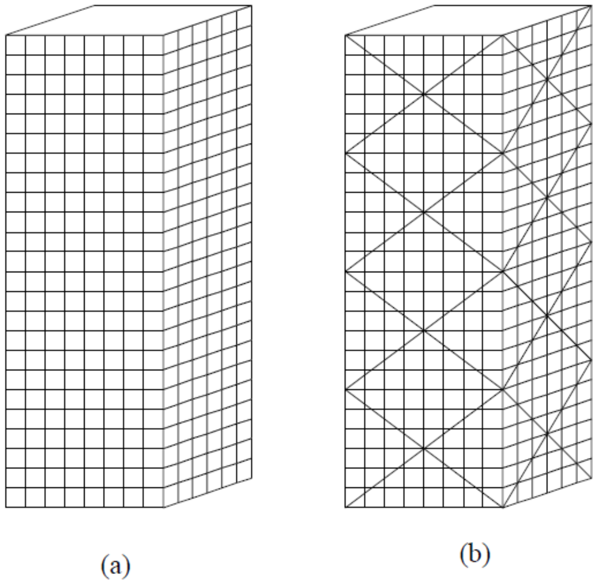

Figure 3. a) Structural framed tube b) exterior diagonalized tube.

By employing diagonal members, more considerable distances between the columns and smaller sections for beams and columns can be used [26]. Also, in the exterior diagonalized tubes, a significant portion of shear is withstood by the diagonal members, which makes the axial stresses of the first story more uniform and therefore reduces the shear lag. Employing these diagonal elements, the system behaves more like a pure cantilever system. This behavior is displayed in Fig. 4. Given the above statements, adding giant exterior braces improves the behavior of a tube system. In this regard, by taking advantage of the benefits of tubes and exterior braces in combination with steel plate shear walls, an innovative system will be introduced and analyzed, improving the structure's behavior.

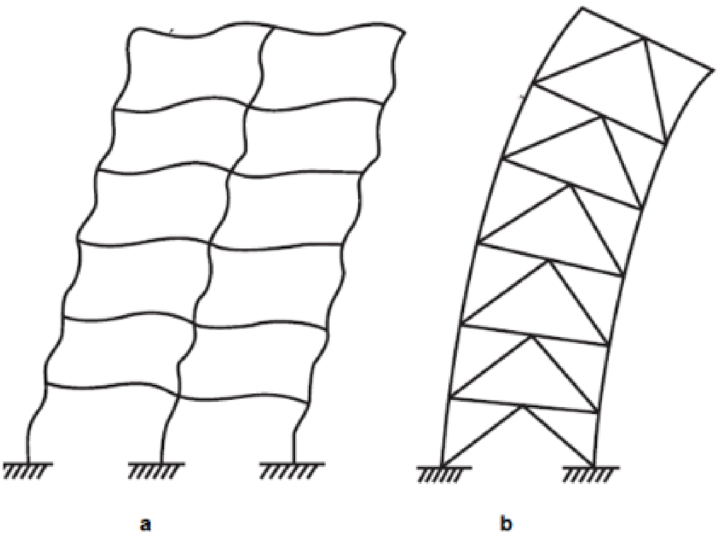

Figure 4. Shear and bending deformations [26].

To achieve a higher stiffness for a structure, usually concentric braces are used, because concentric diagonal braces have higher shear stiffness relative to other types of braces. However, researchers have demonstrated that a steel plate shear wall has greater shear stiffness and lateral strength relative to concentric braces. Considering the same amount and type of material, the stiffness of a shear wall can be 1.7 to 2 times and its ultimate strength can be 1.5 to 2 times that of a concentric brace [26]. The braces are connected to the exterior frame through gusset plates. The failure and rupture of welds in gusset plates resulting from stress concentration or faulty welding prevents the braces from participating in lateral load bearing. However, in steel plate shear walls, the steel plate is continuously attached to the peripheral frame, which reduces the amount of stress concentration. Therefore, the probability of eliminating the steel plate from participation in the carrying of lateral load is much less than the gusset plate weld failure; thus, the use of steel plate shear walls is safer. The higher stiffness and strength of a steel plate shear wall relative to a brace is due to its load-carrying mechanism.

The post-buckled state of a slender plate loaded in pure shear is stable due to the development of tension-field action. In other words, following the deformation of a plate due to shear buckling, some secondary stresses are produced which tend to restore the plate to an equilibrium state. As a result of these stresses, the sudden buckling that normally occurs in column and beam elements is not observed in plates; and after shear buckling, plates exhibit a large loading capacity [27]. Although the occurrence of buckling in beam elements considerably reduces their load-carrying capacity, a Steel Plate Shear Wall (SPSW) withstands under applied loads in tension and compression in both diagonal directions.

By referring to Fig. 5, it can be realized that by the addition of steel SPSW at the two extreme bays of the frame, shear lag may diminish significantly. Also, the compressive stresses developed in slender SPSWs are generally very small in comparison to the tensile stresses and are typically ignored in analysis and design, thus, the SPSW web acts as a tensile brace. Due to the connection of the steel plate to the boundary elements, the produced stresses are distributed to it, and the beams and columns bordering the steel plate have a greater participation in carrying the lateral load. In addition, the presence of the wall at the two extreme bays of the frame, as illustrated in Fig. 6, produces a strong resistive moment arm against the overturning moment. The existence of the braces between the two walls causes the walls to act in tandem; and with the elimination of these braces, because of the flexibility of the beams, the axial forces will not be transferred properly. Besides the above advantages, SPSW has enhanced the redundancy of the structure, which is effective in reducing lateral deflections. In addition to the above advantages, the overall material weight of the structure will decrease, but, we know that the material weight, although important, is not the only factor that impacts cost. It is a reasonable metric to use for assessing cost, but it is not the only one. The numerical models in the subsequent sections will demonstrate the behavior of the proposed system. The main disadvantage of the proposed system, from an architectural point of view, is the usage of the shear walls at the corner spans. Of course, one should bear in mind that this is just a theoretical study and could have practical applications where certain circumstances demand.

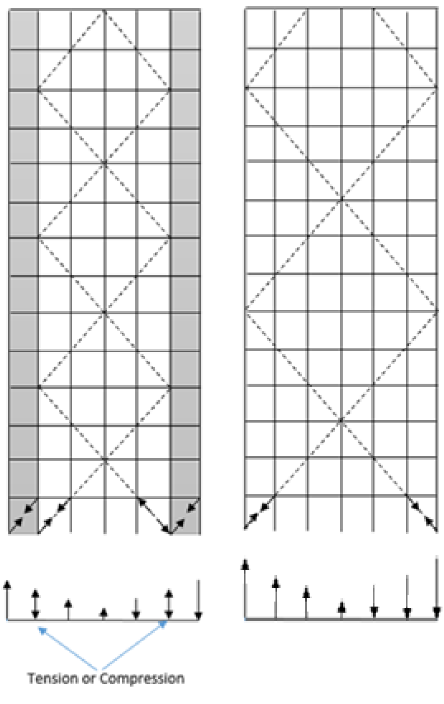

Figure 5. The SPSW impact on the reduction of shear lag.

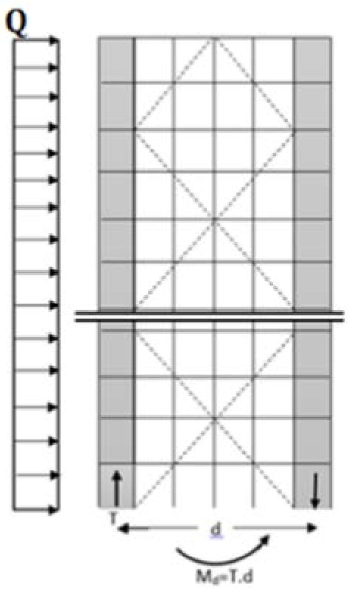

Figure 6. Moment arm resisting the overturning moment.

2. Methods

2.1. Numerical study

Since the analysis of high-rise buildings is time-consuming, to introduce the proposed system and to evaluate its behavior, the intended analyses will be performed in two series. In the first series of analyses, the proposed system will be analyzed as a 2D system subjected to a uniformly distributed load (simplified wind load) to highlight its effectiveness and superiority relative to the other systems. Also, since the analyses are preliminary, some simplifying assumptions were considered. Also, the unit less load is selected for the magnitude of lateral load which the value of the uniform load is equal to Q. In these analyses, the sections selected in all the models are such that the same amount of material is obtained for each system. In the second series of analyses, a real structure is designed and analyzed three-dimensionally under real wind and seismic loads to achieve more realistic results.

Parametric studies were performed for all of the numerical models. For this purpose, the uniform lateral load selected as Q would have the same dimension as axial load, shear force, etc. The parameter Q and the displacement in the said figures are normalized and hence the displacement of each structural system at the same story level is obtained relative to one another concerning the induced uniform lateral load Q. Moreover, the lateral displacement is a function of the dimension of the modulus of elasticity, the moment of inertia of beams and columns, and beam and column lengths.

2.2. Numerical models of Series 1

In the first series of analyses and investigations, four types of 2D structural systems with 40, 60, 80, and 100 stories have been investigated to evaluate and compare their behaviors with each other. In these system designations, M indicates the sole moment frame, M-B shows the combination of flexural frame and exterior braces, M-S specifies the combination of moment frame and steel plate shear wall, and M-B-S indicates the combination of moment frame and exterior braces with steel plate shear walls. By considering the rigidities of the beams and columns, the shear stiffness of the frame at each story is determined approximately from Eq. (1). It should be mentioned that the K values used in Eq. (1) ignore beam shear deformations, joint rigid offsets, and joint deformation [28].

$$K_i = \frac{24E}{h_i^2\left[\frac{2}{\sum k_c} + \frac{1}{\sum k_{bb}} + \frac{1}{\sum k_{bt}}\right]}. \quad (1)$$

In this equation, E is the modulus of elasticity, h is the story height, $\sum K_c$ is the sum of the stiffness values of columns, and $\sum K_{bt}$ and $\sum K_{bb}$ are the sums of the stiffness values of beams at the upper and lower stories, respectively. By considering the moments of inertia of the beams and columns based on Fig. 7 as well as an equal height for the stories, the stiffness of each story in terms of the elasticity modulus (E) is obtained as $K_i = 0.06E$. Also, the shear stiffness of the braces at each story is calculated from Eq. (2), where A is the section area, L is the brace length, n is the number of diagonal braces and α is the brace angle.

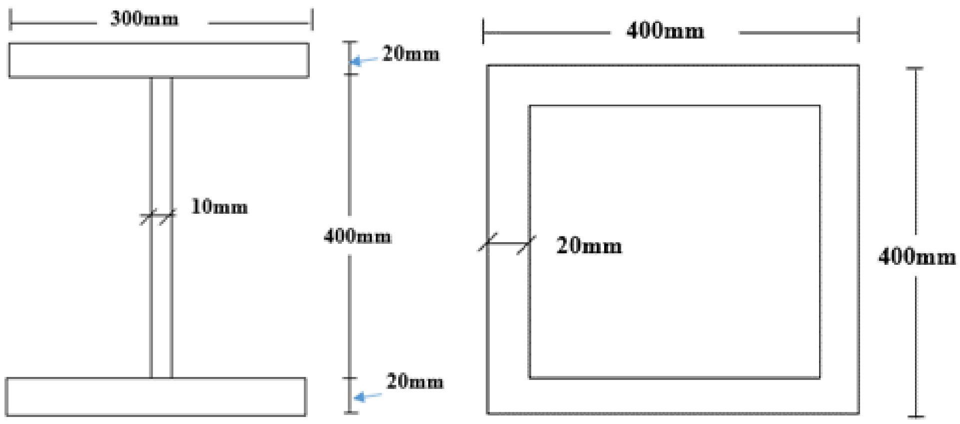

Figure 7. Beam and column geometries.

$$K_{brace} = n\frac{EA}{L}\cos^2\alpha, \quad (2)$$

where, E is the modulus of elasticity n is the number of the diagonal brace elements, α is the angle of the brace with the horizon, and L is the length of the brace.

By equating the stiffness values of the braces and the moment frame at each story, the cross-sectional area of the braces will be equal to $n\frac{E.A}{L}\cos^2 0.79 = 0.06E.$ Accordingly, the cross of $A = 45.48$ cm² was obtained. Therefore, the section of 2UNP100 was selected. Knowing that the stiffness of SPSW is determined as:

$$K_w = \frac{Ebt}{4h}, \tag{3}$$

where, t is the thickness of the infill plate, E is the modulus of elasticity, h is the height of SPSW, and b is the length of the infill plate. By equivalent the stiffness of the SPSW and brace, the thickness of the SPSW is obtained as 3 mm. Substituting the $h,\ b,\ t$ and E to Eq. (3) gives the $K_w = 0.08E.$

Thus, with the same amount and type of material, the shear stiffness of a SPSW is 1.33 times $\left(\frac{K_w}{K_{brace}} == \frac{0.08E}{0.06E} = 1.33\right)$ greater than that of braces. So the shear stiffness of the proposed system is expected to be higher than that of the other examined systems; while, with the increase in structure height, bending stiffness dominates. To prove this claim, the analysis results of the models, obtained by the finite element method are discussed.

2.3. Numerical Models of Series 2

In the second series of analyses, a 3D numerical models of a 40-story executive office building has been examined. This structure has been designed and constructed for a wind load according to Fig. 8, and for a seismic load with a base acceleration of 0.35 g. In this structure, the dead load equals 5.5 kN/m^2, the live load for general use spaces equals 2.0 kN/m^2, and the live load for floors equals 5.0 kN/m^2 have all been considered. The building is 40x40 m with the center-to-center distance between the peripheral columns is 4 m, Fig. 8. So, the distance between the C2 columns are 16 m.

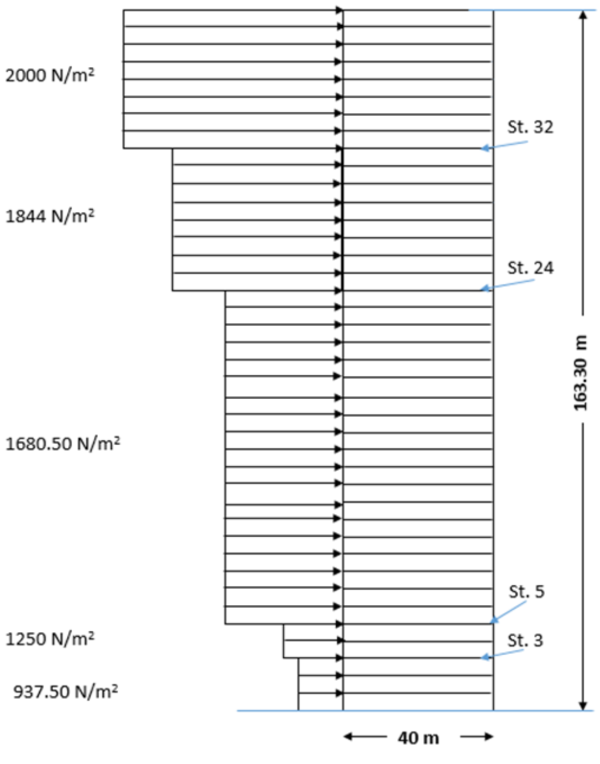

Figure 8. Distribution of wind force at various heights.

The slable thickness of the structure was 170mm. Also, during the design of the structure for seismic loading, the structure was designed under acceleration of 0.8g m/s^2. Also, the spectrum analysis was used to design of the structures. In the design computations of this structure, it has been demonstrated that the wind load governs the design Therefore, this structure will be analyzed for wind load by using the proposed system. The specifications of the structure have been presented in Fig. 9. It should be noted that there are practical issues with using box sections in SPSW construction. The box sections generally need to be filled with concrete or have large internal stiffeners to adequately transfer the web plate force to the column.

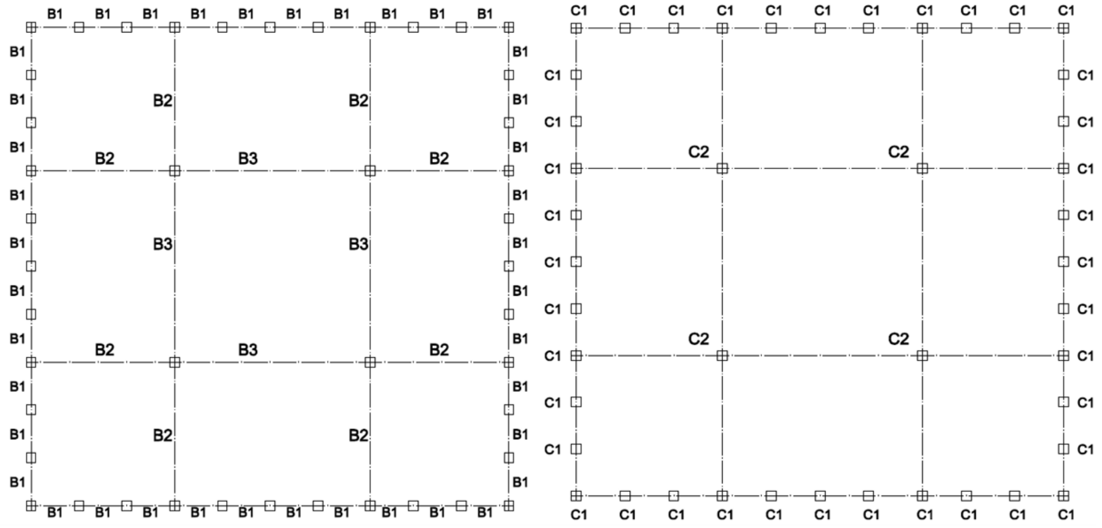

Figure 9. Plan views of beam and column layouts.

3. Results and Disscusion

3.1. Discussion on results of Series 1

3.1.1 Displacement and the drift ratio

As was mentioned before, the lateral displacement control of tall structures is one of the most important factors in determining the right system for a particular high-rise structure. The lateral displacements of various frame systems versus the number of stories have been plotted in Fig. 10.

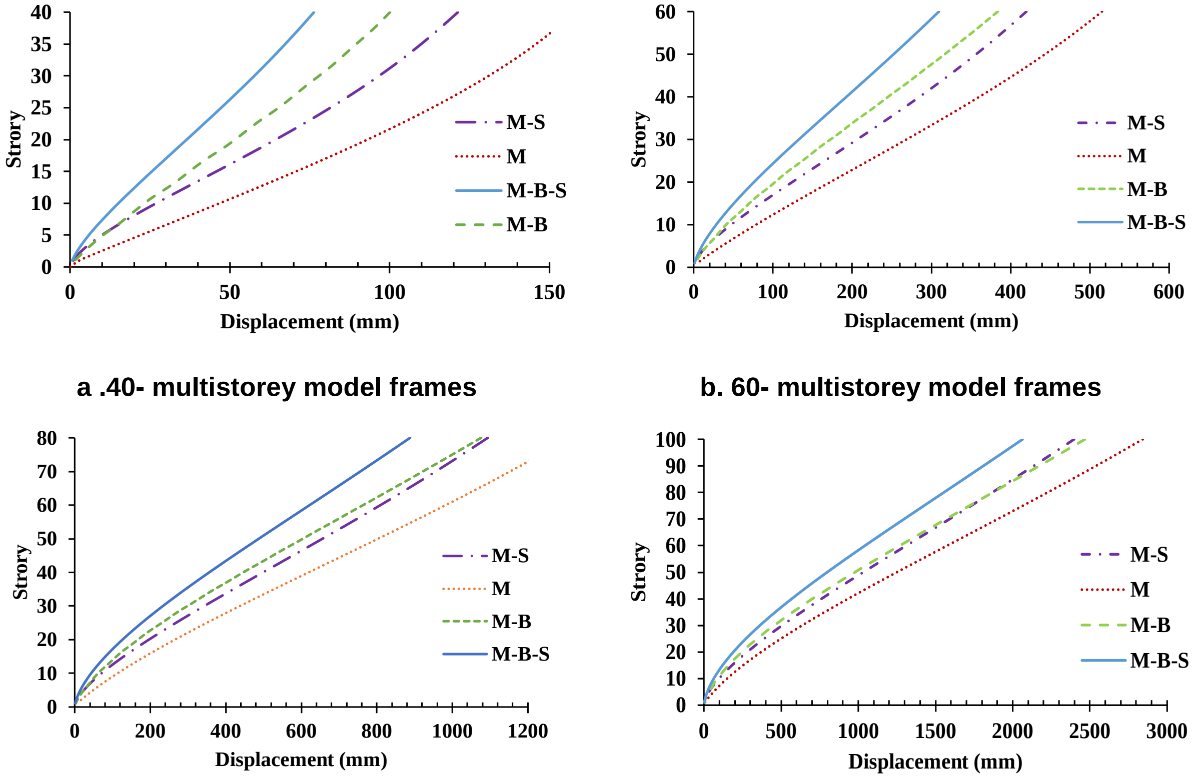

a .40- multistorey model frames **b. 60- multistorey model frames**

c. 80- multistorey model frames **d. 100- multistorey model frames**

Figure 10. Relative displacements of the multi story model frames.

It is observed that the proposed system has the least amount of lateral displacement. Among all the considered systems, the least amount of lateral displacement belongs to the M-B-S system (the proposed system), followed by the M-B system (the moment frame with the exterior braces), the M-S system (the moment frame in conjunction with the steel plate shear wall) and finally the M system (the moment frame alone). The comparison between the drift ratios (horizontal drift to story height) of structures in Fig. 11 shows the better performance of the proposed system relative to the other systems. In comparing the 40-story structures, the M-B system has a lower drift, relative to the M-S system; but in 60 and 80 stories, the drift ratios are close to each other and at mid-stories the M-B have a lower drift, relative to the M-S system. This behavior is reversed at higher stories. In comparing the 100-story structures, the M-B system has almost similar drifts up to 30 stories, relative to the M-S; and at higher stories the M-S system has a lower drift, relative to the M-B system.

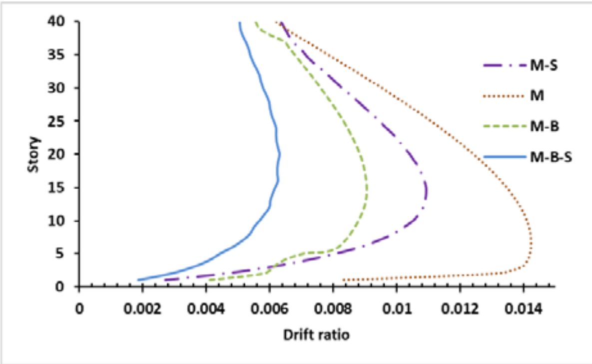

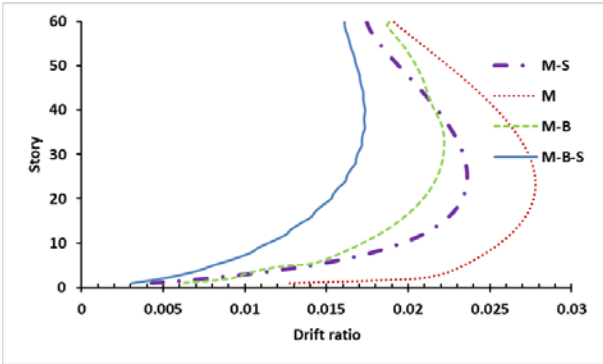

a .40- multistorey model frames **b. 60- multistorey model frames**

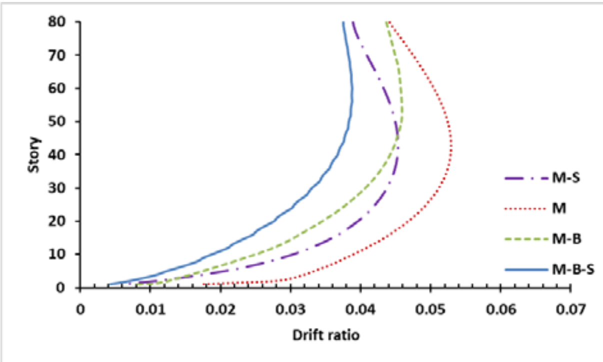

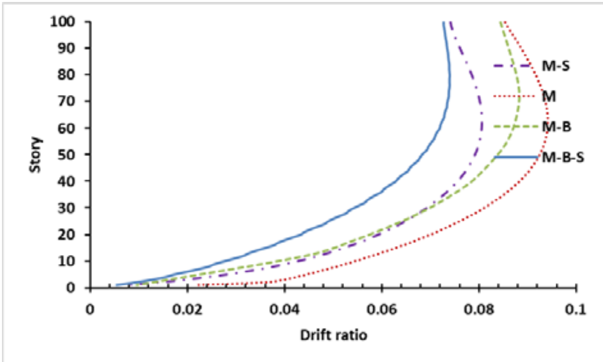

c. 80- multistorey model frames **d. 100- multistorey model frames**

Figure 11. Relative drift ratios of the multi story model frames.

In Fig. 12, the lateral displacements of the systems have been divided by the lateral displacements of the moment frames to yield the percent reduction in the displacement of a system relative to a moment frame. These results better illustrate the effectiveness of a system. A comparison of these results shows a 20 to 50 % in 40-story, 20 to 60 % in 60-story, 20 to 67 % in 80-story and 20 to 73 % in 100-story reduction in the lateral displacement of the proposed system. With this percentage of lateral displacement reduction, a lesser amount of material will be needed to control the frame displacement and thus the system will be more economical.

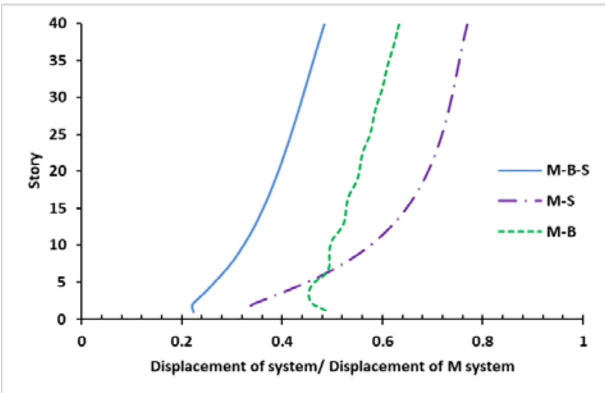

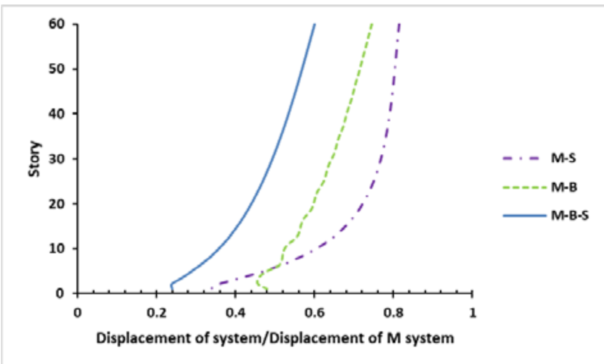

a .40- multistorey model frames **b. 60- multistorey model frames**

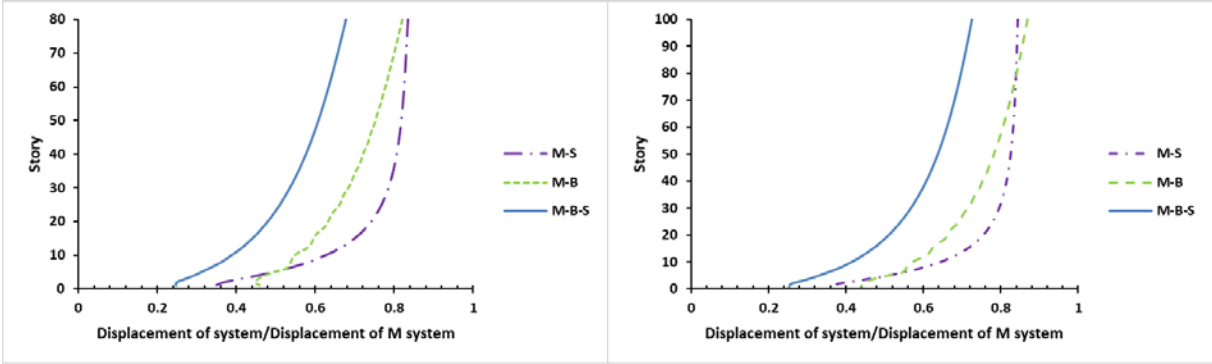

c. 80- multistorey model frames **d. 100- multistorey model frames**

Figure 12. Comparison of displacement ratios of different systems with respect to story numbers.

3.1.2 Axial force in columns

By applying the lateral wind load, axial forces and a bending moment are produced in a column. The axial forces produced in windward columns and leeward columns are tensile and compressive forces, respectively, with their absolute values being equal. Also, an axial force of almost zero magnitude is obtained for the middle column in all the models. In Fig. 13, the axial force in the windward column has been plotted versus the number of stories for all the mentioned systems. The results indicate that in almost all the structures, the largest axial force is obtained in the system containing the steel plate shear wall at the lower stories; however, at the higher stories, the structure has a better performance. In the M-B system, the sudden changes of the axial force at higher stories are clearly observed. Also, the axial force in the columns of the lower stories in the proposed system's 40-story structures is greater than that in the M-B and M systems; however, at the fourth story (almost the mid height of the structure), the said values become equal and from this level on up, the lowest amount of axial force is produced in the columns of the proposed system. Of course, at the very top stories, the forces in the windward columns are compressive forces resulting from the stresses applied by the steel plate shear wall to those columns. The same trend can be seen in the 60, 80 and 100-story models. The reduction of axial force in the proposed system, with respect to the M-S system, will definitely lead to the reduction of the base plate and foundation dimensions, which is important from the perspective of structure economics and work execution issues. In addition, by reducing the axial force in a column, smaller sections can be used.

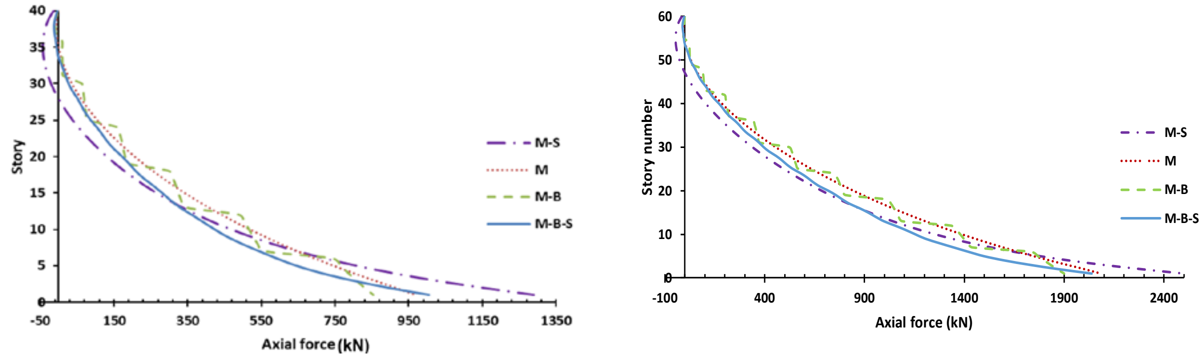

a .40- multistorey model frames **b. 60- multistorey model frames**

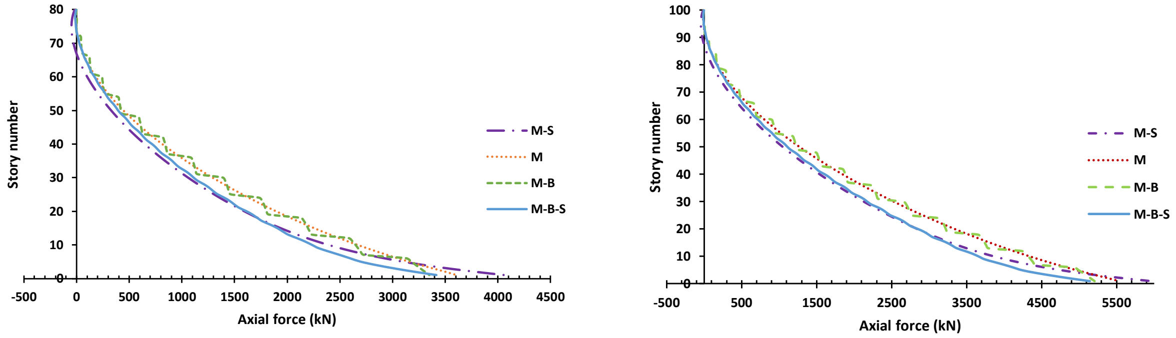

c. 80- multistorey model frames **d. 100- multistorey model frames**

Figure 13. Maximum axial force in each corner column.

3.1.3 Bending moment and shear force in columns

Besides the axial force, the bending moment and shear force are also important in sizing the columns. The shear forces and bending moments produced in the columns of each system have been shown in Fig. 14. The results indicate that, with regards to the bending moment produced in the columns, the proposed system performs better in all the structures (40, 60, 80 and 100 stories). In system M-B, the bending moment rises and falls abruptly; and this case is also true for relative displacements. In all the diagrams, the largest bending moment is generated in the sole bending frame (system M).

As observed in the Fig. 15, regarding the maximum shear forces produced in the corner columns, the structural performance and the obtained results are the same as those related to the maximum bending moments. So, these results indicate the superiority of the proposed system, which produces the least amount of bending moment and shear force in the columns. This is because the lateral shear is endured by the exterior brace and the shear wall; and working together, they eliminate the irregularity and the sudden fluctuations in the bending moment and shear force. Also, since the shear stiffness of the steel plate shear wall is much higher than that of the brace and frame, the wall absorbs more of the lateral shear force and improves the system behavior. Also, the performance of the diagonal tension field of the shear wall causes a more uniform distribution of stresses at the bases of the first story columns and a reduction of the shear lag, because it counteracts the axial forces in those columns.

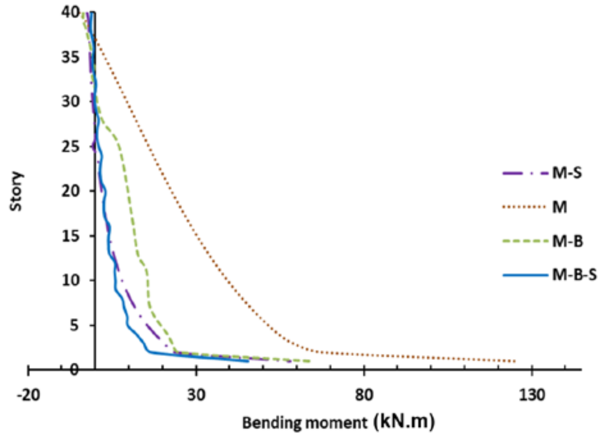

a .40- multistorey model frames

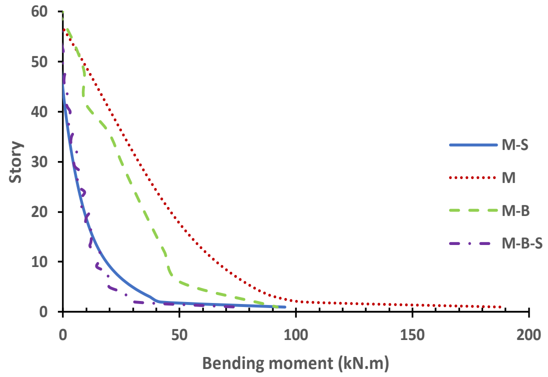

b. 60- multistorey model frames

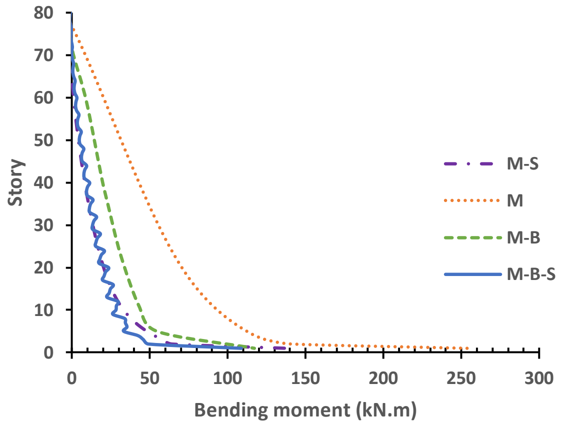

c. 80- multistorey model frames

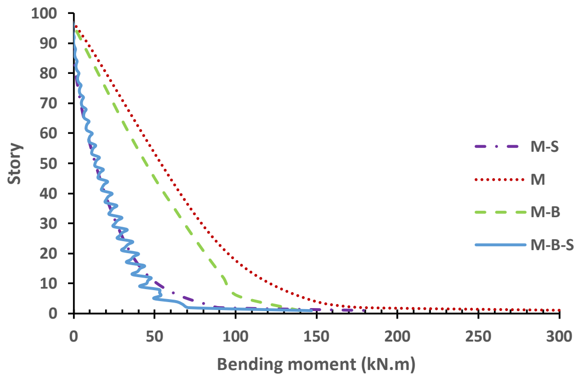

d. 100- multistorey model frames

Figure 14. Maximum bending moment in each corner column.

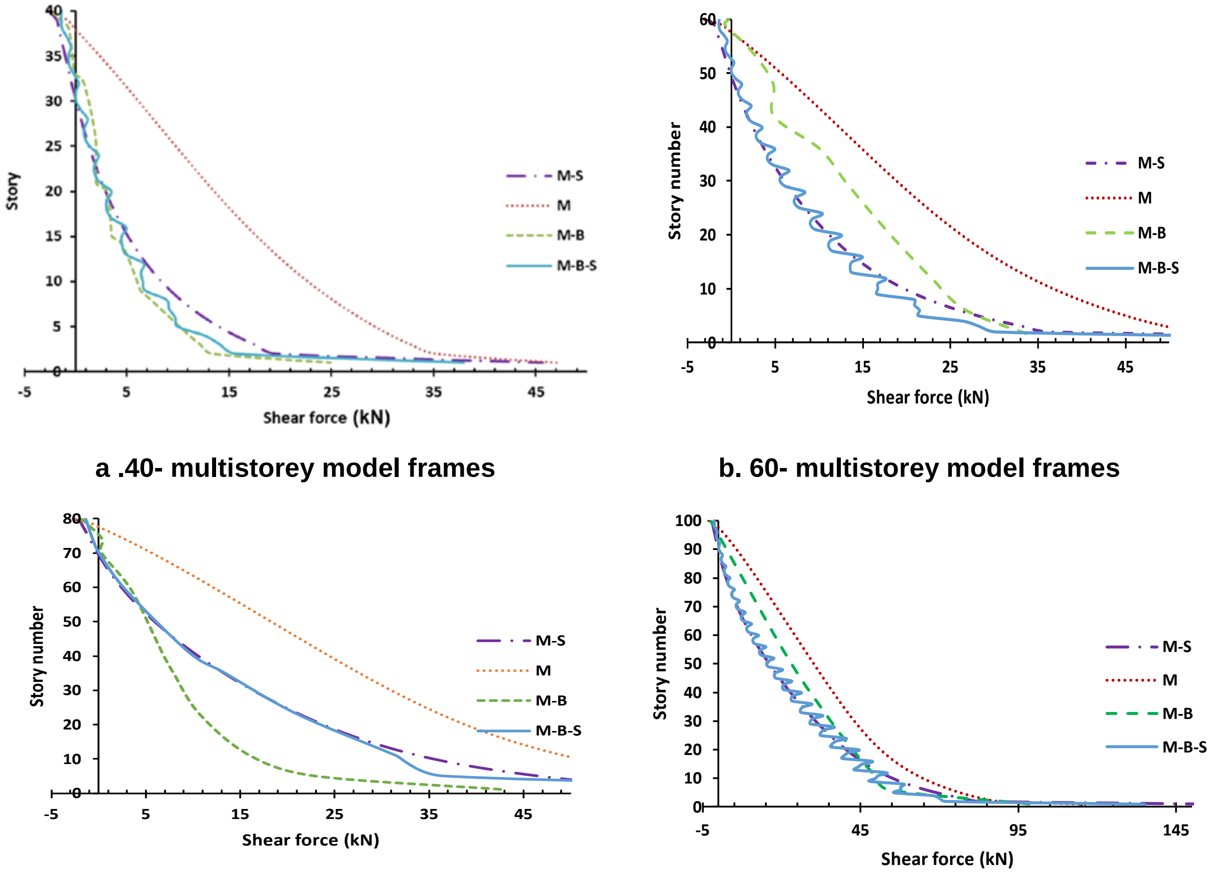

a .40- multistorey model frames **b. 60- multistorey model frames**

c. 80- multistorey model frames **d. 100- multistorey model frames**

Figure 15. Maximum shear force in each corner column.

3.2. Discussion on results of Series 2

After parametric study of the proposed system in the previous sections, its effectiveness is evaluated when utilized in an actual structure, as introduced in section 4-1. Fig. 16 shows that by applying the proposed concept, the lateral displacements are reduced.

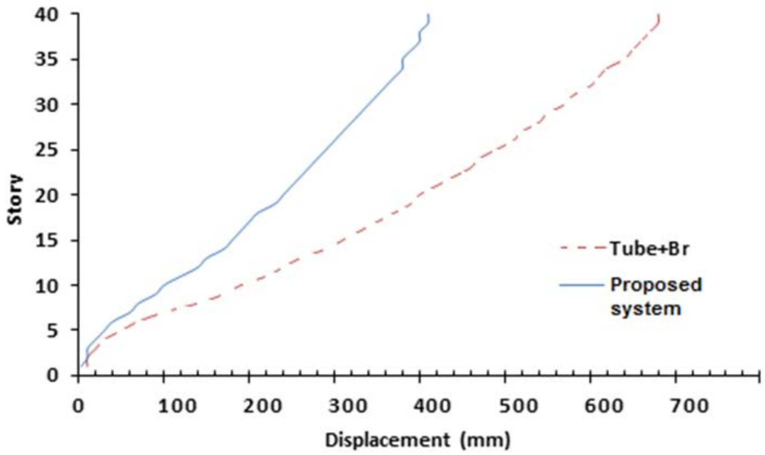

Figure 16. Comparison of displacements of the proposed system with that of the existing structure.

Moreover, as was claimed before, the proposed system reduces the shear lag effect. In Fig. 17 and 18, the axial forces in the columns of the first story have been shown for comparing the shear lag effects. This comparison indicates a more uniform distribution of forces in the proposed system. In other words, in the proposed system, the shear lag effect has diminished considerably, relative to the other two systems.

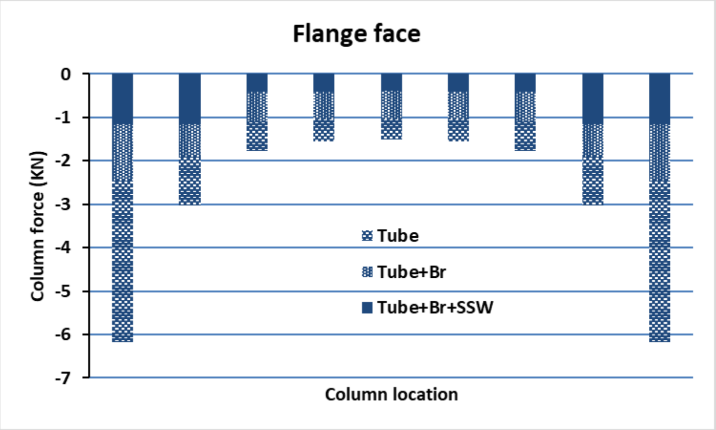

Figure 17. Comparison of shear lag effects in tube system flanges.

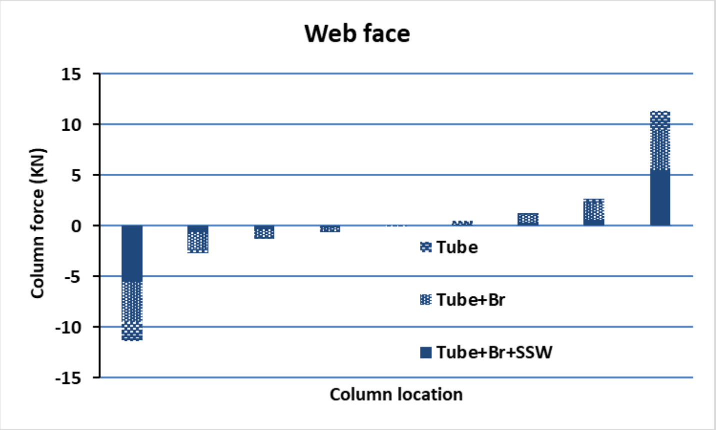

Figure 18.Comparison of shear lag effects in tube system webs.

4. Conclusions

In this paper, the behavior of steel tall buildings employing a combined lateral bracing and steel plate shear wall system was investigated. Combining the SPSW and bracing system allows advantages of both systems regarding increasing the stiffness and strength. The finding can be summarized as follows:

- The combination of tubes, giant braces, and steel plate shear walls was proposed as a new approach that exploits the advantages of all these systems.
- The numerical results indicate that by employing the proposed system, the lateral displacement and drift of the structure diminish by around 2.13 times.
- In addition, due to the high shear stiffness of the SPSW, the wall absorbs a significant portion of the lateral shear; thus, the forces produced in the beams and columns diminish substantially.
- By using the combined system, the maximum bending moment in the columns was reduced by around 50 %.
- Results indicated that by using the combined system, the shear force in the columns was reduced by around 30 %. The effect of the system on structures with lower heights is greater than that on the taller buildings.
- Moreover, in this system, the shear lag may diminish considerably. Therefore, the obtained results indicate that the proposed system can be used as an economical, effective, and safe system.

References

1. Chudoba, M. The Tall Building and Urban Space: In light of two modernist case studies. Architectural Research in Finland. 2021. 5 (1). Pp. 83–97. DOI: 10.37457/arf.11325
2. Fisco, NR., Adeli, H. Smart structures: part II—hybrid control systems and control strategies. Scientia Iranica. 2011. 18 (3). Pp. 275–284. DOI: 10.1016/j.scient.2011.05.034
3. Fisco, NR., Adeli, H. Smart structures: part II—hybrid control systems and control strategies. Scientia Iranica. 2011. 18 (3). Pp. 285–295. DOI: 10.1016/j.scient.2011.05.035
4. Nie, JG., Zhu, L., Fan, JS., Mo, YL. Lateral resistance capacity of stiffened steel plate shear walls. Thin-Walled Structures. 2013. 67. Pp. 155–167. DOI: 10.1016/j.tws.2013.01.014

5. Farzampour, A., Laman, JA., Mofid, M. Behavior prediction of corrugated steel plate shear walls with openings. Journal of Constructional Steel Research. 2015. 114. Pp. 258–268. DOI: 10.1016/j.jcsr.2015.07.018
6. Zhao, Q., Sun, J,. Li, Y., Li, Z. Cyclic analyses of corrugated steel plate shear walls. The Structural Design of Tall and Special Buildings. 2017. 26(16). e1351. DOI: 10.1002/tal.1351
7. Qiu, J., Zhao, Q., Yu, C., Li, Z. Experimental studies on cyclic behavior of corrugated steel plate shear walls. Journal of Structural Engineering. 2018. 144 (11). 04018200. DOI: 10.1061/(asce)st.1943-541x.0002165
8. Meghdadaian, M., Ghalehnovi, M. Improving seismic performance of composite steel plate shear walls containing openings. Journal of Building Engineering. 2019. 21. Pp. 336–342. DOI: 10.1016/j.jobe.2018.11.001
9. Al-Rumaithi, A., Al-Shamaa, M.F., Karkush, M.O. Probability concepts of transfer load to the foundation of container structure. InIOP Conference Series: Materials Science and Engineering. 2020. 901(1). 012007. DOI: 10.1088/1757-899x/901/1/012007
10. Ghamari, A., Haeri, H., Khaloo, A,, Zhu, Z. Improving the hysteretic behavior of Concentrically Braced Frame (CBF) by a proposed shear damper. Steel and Composite Structures, An International Journal. 2019. 30(4). Pp. 383–92. DOI: 10.1016/j.jcsr.2021.106672
11. Ghamari, A., Almasi, B., Kim, CH., Jeong, SH,. Hong, KJ. An innovative steel damper with a flexural and shear–flexural mechanism to enhance the CBF system behavior: an experimental and numerical study. Applied Sciences. 2021. 11(23). 11454. DOI: 10.3390/app112311454
12. Ghamari, A., Kim, C., Jeong, S.H. Development of an innovative metallic damper for concentrically braced frame systems based on experimental and analytical studies. The Structural Design of Tall and Special Buildings. 2022. 31(8): e1927. DOI: 10.1002/tal.1927
13. AL-Shamaa, M.F., Sheikha, A.A., Karkush, M.O., Jabba, M.S., Al-Rumaithi, A.A. Numerical modeling of honeycombed geocell reinforced soil. Modern Applications of Geotechnical Engineering and Construction: Geotechnical Engineering and Construction 2021. Pp. 253–263. DOI: 10.1007/978-981-15-9399-4_22
14. Arshadi, H., Kheyroddin, A., Nezhad, AA. High-strength steel effects on the behavior of special shear walls. Magazine of Civil Engineering. 2022. 111 (3). 11102. DOI: 10.1016/j.istruc.2019.11.002
15. Maddahi, M., Gerami, M., Naderpour, H. Effect of uncertainties of shear wall on reliability of rehabilitated structure. Magazine of Civil Engineering. 2023. 117(1). 11701. DOI: 10.24200/sci.2020.54252.3668
16. Smith, J., Nguyen, T. Autonomous and cooperative robotic behavior based on fuzzy logic and genetic programming. Integrated Computer-Aided Engineering. 2007. 14 (2). Pp. 141–159. DOI: 10.3233/ica-2007-14203
17. Jin, X., Doloi, H. Modeling risk allocation in privately financed infrastructure projects using fuzzy logic. Computer-Aided Civil and Infrastructure Engineering. 2009. 24 (7). Pp. 509–524. DOI: 10.1111/j.1467-8667.2009.00609.x
18. Lin, C., Chen, C., Wang, J. Vibration control of structures with initially accelerated passive tuned mass dampers under near-fault earthquake excitation. Computer-Aided Civil and Infrastructure Engineering. 2010. 25 (1). Pp. 69–75. DOI: 10.1111/j.1467-8667.2009.00607.x
19. Farghaly, A., Salem, M. Optimum design of TMD system for tall buildings. International Scholarly Research Notices. 2012. 2012. DOI: 10.5402/2012/716469
20. Kim, S. Seismic response control of adjacent buildings coupled by semi-active shared TMD. International Journal of Steel Structures. 2016. 16. Pp. 647–656. DOI: 10.1007/s13296-016-6030-0
21. Giaralis, A., Petrini, F. Wind-induced vibration mitigation in tall buildings using the tuned mass-damper-inerter. Journal of Structural Engineering. 2017. 143 (9). 04017127. DOI: 10.1061/(asce)st.1943-541x.0001863
22. Khaleel AI, AL-Shamaa MF. Experimental Investigation on the Structural Behavior of Double Channel Castellated Steel Beams. E3S Web of Conferences. 2021. 318. 03009. DOI: 10.1051/e3sconf/202131803009
23. Zhang, W., Liu, S., Shokrabadi, M., Dehghanpoor, A., Taciroglu, E. Nonlinear seismic fragility assessment of tall buildings equipped with tuned mass damper (TMD) and considering soil-structure interaction effects. Bulletin of Earthquake Engineering. 2022. 20 (7). Pp. 3469–3483. DOI: 10.1007/s10518-022-01363-6
24. Moon, K., Connor, J., Fernandez, J. Diagrid structural systems for tall buildings: characteristics and methodology for preliminary design. The structural design of tall and special buildings. 2007. 16 (2). Pp. 205–230. DOI: 10.1002/tal.311
25. Shayanfar, M., Broujerdian, V., Ghamari, A. Numerically and parametrically investigating the cracked steel plate shear walls (SPSWs). Iranian Journal of Science and Technology, Transactions of Civil Engineering. 2020. 44. Pp. 481–500. DOI: 10.1007/s40996-019-00250-6
26. Taranath, B. Structural analysis and design of tall buildings: Steel and composite construction. CRC press, 2016. DOI: 10.1201/b11248
27. Broujerdian, V., Ghamari, A., Zolghadr, R. Investigating a combinatorial lateral resisting system for tall buildings. Iranian Journal of Science and Technology, Transactions of Civil Engineering. 2019. 43. Pp. 697–709. DOI: 10.1007/s40996-019-00233-7
28. Zalka, K. Structural analysis of regular multi-storey buildings. CRC Press; 2012. DOI: 10.1201/b12326

Contacts:

Mushriq Al Shamaa,
ORCID: https://orcid.org/0000-0001-8332-8607
E-mail: mushriqf@coeng.uobaghdad.edu.iq

Ahmad Jabbar Hussain Al Shimmeri,
E-mail: dr.ahmadalshimmeri@coeng.uobaghdad.edu.iq

Adnan Lazem,
E-mail: adnan.lazem@coeng.uobaghdad.edu.iq

Received 15.02.2023. Approved after reviewing 19.10.2023. Accepted 04.11.2023.

Magazine of Civil Engineering. 2023. 123(7). Article No. 12310

Magazine of Civil Engineering

ISSN 2712-8172

journal homepage: http://engstroy.spbstu.ru/

Research article

UDC 697.1:628.8

DOI: 10.34910/MCE.123.10

Temperature mode of a room at integrated regulation of split systems

O.D. Samarin

Moscow State University of Civil Engineering (National Research University), Moscow, Russian Federation

samarin-oleg@mail.ru

Keywords: microclimate, temperature, heat balance, heat gain, regulation, integral algorithm, transmission coefficient, civil engineering, building, construction industry

Abstract. The article considers simplified mathematical formulation and problem solution of internal air temperature changing. The room is equipped with automated local heating and cooling systems under variable thermal influences. At the same time, the study does not pay attention to the influence of the background general exchange system of supply and exhaust mechanical ventilation. It is shown that the main differential equation connecting the most important components of the heat flow in the room for the case under consideration belongs to the class of Emden-Fowler equations. The article provides an analysis of this equation, obtains the structure and variants of its asymptotic solutions. They describe the time dependence of the room air temperature deviation from the setpoint and the expression for the time moment at which the maximum temperature deviation is observed, with an abrupt change in the heat flow and regulation of the equipment of local heating and cooling system according to the integral law. Calculations were carried out to confirm the obtained dependencies using a numerical solution of the original differential equation by the Runge-Kutta method, as well as by comparing them with the results of field measurements in one residential building in Moscow. It is noted that the structure of the analytical solution and the type of dimensionless complexes constructed by reducing the equation to a dimensionless form directly follow from the properties of the Emden-Fowler differential equations. The obtained ratios are proposed to be used for an approximate assessment of the non-stationary thermal regime of an air-conditioned room served by local heating-cooling systems controlled by the integral law. Moreover, these ratios can be used for determination of the necessary characteristics of the regulator, including on the basis of multivariate calculations with a change in the parameters of the problem.

Citation: Samarin, O.D. Temperature mode of a room at integrated regulation of split systems. Magazine of Civil Engineering. 2023. 123(7). Article no. 12310. DOI: 10.34910/MCE.123.10

1. Introduction

This paper studies the pattern of change in the temperature of the indoor air in a room equipped with automated local heating and cooling systems under variable disturbing thermal effects in the absence of the influence of a background unregulated positive pressure ventilation.

The necessary combination of indoor microclimate parameters should be maintained primarily based on the needs of ensuring a comfortable and safe living environment and implementing technological processes carried out within the premises. In order to stabilize the hydrothermal regime in actual practice, certain automatic control systems are mainly used for climate equipment, while taking into account the inherent heat stability of the premises. At the same time, the nearly always present variable nature of heat losses and heat gains in the building makes the problem under consideration materially unsteady.

It should be noted that the behavior of the internal temperature when air conditioning the premises, depending on the nature of thermal disturbances and the method of regulating the heat and cold supply, has already attracted the attention of a number of researchers. For instance, even educational and reference literature materials contain some of the most simplified solutions to the problem under consideration. Nevertheless, more serious works have recently emerged, including [1–3], which are devoted mainly to the variable thermal regime during the operation of external networks of the heat supply system. However, the approaches contained in them may be considered rather complex, yet for the same reason the results obtained there are very complex as well, resulting in their little use for engineering calculations. Another modern trend in this area is the increasing use of computer modelling when studying and analyzing unsteady regimes. From this point of view, some foreign works may present certain interest, in which approaches of this type have become the most characteristic in recent years, among which [4, 5] are worth noting. In addition, in the field under consideration, there is a number of solutions associated with specific objects operating in limited areas under specific conditions, including underground structures in harsh climatic conditions [6] or for external enclosing structures with heat-conducting inclusions [7]. An earlier publication by the author [8] devoted to the development of a very simple solution for the propagation of a temperature wave in a thick-walled cylinder may also be noted. Moreover, the authors of some studies in this area tend to solve the inverse problem - the determination of the thermophysical parameters of a material based on the study of temperature fluctuations [9] or thermography methods [10]. The works [11–16] consider modeling of processes in the premises as a whole. Thus, the authors of [11] give a fairly complete consideration of the thermal and humidity regime of the premises, but it applies only to a specific building and is mainly experimental in nature, and [12] presents a very detailed multi-parameter simulation-type computational model, applicable to the cold period of the year with the heating on only. Publications [13–16] may also be considered as comprehensive, in particular, the articles [13–14] are devoted to using the principles of fuzzy logic when organizing indoor climate management, and [15–16] mostly employ the methods of automatic control theory, however, the results obtained therein are still unsuitable for use in engineering practice due to their complexity. Finally, there are also studies based on the general principles of building engineering systems management and implementation of power-saving engineering solutions that are possible under given conditions, for example, [17–19], and precisely because of their general nature, they also lack specific dependencies that are of interest to us

That being said, it should be noted that recent engineering practice indicates a gradual expansion of the use of local heating and cooling systems in the premises, in particular, of the “chiller system” type to maintain the air temperature and fence surfaces at the required level during the warm season. Their operation involves full recirculation of the heated or cooled airflow and therefore does not affect the overall air balance in the premises. This way, the mechanical supply and exhaust general ventilation mainly functions as a sanitary and hygienic system ensuring the necessary purity of the internal air; heating or cooling the inflow, when provided, plays a secondary role, making it possible to reduce the load on local systems in the conditions under consideration as much as possible. The same is true for the installation of radiant heating and cooling systems, especially those heating or cooling ceilings.

In [20], the author obtained a sufficiently general analytical solution to the problem of changing temperature of the indoor air in the premises serviced by an air conditioning system using the law of astatic control for climate control equipment [21]. The corresponding dependence may be represented as a sufficiently better convergent series in powers of a certain independent variable, for which a dimensionless group, including the characteristic parameter of the corresponding differential equation and the period of time that has elapsed since the occurrence of thermal exposure is used. Nevertheless, there is merit in considering the possibility of simplification and further generalization of this solution while maintaining its physical validity [21]. This will provide additional opportunities for its analysis and comparison with existing analogues, and at the same time identify the limits when such a simplification is acceptable. Therefore, we can find the scope of these simplified options for engineering calculations with no losses in accuracy of calculations. In addition, it should be taken into account that for the time being local heating and cooling systems often are the only systems which are regulated, bearing the main burden of assimilating heat gains and compensating for heat losses, while the general exchange inflow plays only the background role at a minimum level. Thus, the possibility of adapting the solution obtained to the specified conditions must be assessed.

The relevance of the proposed study then lies in the feasibility of exploring relatively simple and at the same time physically reasonable analytical dependencies for the behavior of the internal temperature in the premises with climate control equipment such as split systems, regulated under the law of astatic control. We need to take into account the values of surplus heat, the characteristics of the enclosing structures and the controller, and the relationship of all listed parameters and the largest temperature deviation from a given level. The formulas obtained should be written in a fairly simple form, suitable for using in engineering practice, but at the same time, be of satisfactory accuracy and allow for multivariate evaluation calculations, to allow for the analysis of the thermal regime of the premises and the synthesis of the appropriate climate control equipment automation system. In this case, this will allow application of the results achieved for a quite wide range of objects of a similar class [21].

Thus, the aim of the paper is to construct simplified analytical methods for calculating the change in the temperature of the indoor air served by local automated split heating and cooling systems in the absence of a background unregulated inflow. The following items may be considered as study objectives:

– compilation of the basic differential equation describing the general balance of convective heat in the air conditioned premises, taking into account the simultaneous operation of automated climate control systems;
– analysis of this equation, bringing it to the dimensionless form and constructing its possible analytical solutions, including asymptotic solutions, in the form of end formulas with an abrupt change in the values of surplus heat and using the law of astatic control for regulating heating and cooling systems;
– confirmation of the dependencies obtained by comparing their variants with the exact solution in the form of an infinite series, obtained by the author in [20], and with the data of experimental measurements for the typical representative premises;
– identifying the limits of applicability of various options for asymptotical solutions based on a comparison of the discrepancies given by them with the typical error of engineering calculations and their initial data.

2. Methods

Let us consider the regime where abrupt heat surpluses in the amount of Q_{in}, *W*, are compensated by a local cooling system (for example, of a split-system type), which assimilates the amount of heat Q_c, W, at each moment of time. In this case, the system is regulated as per the law of astatic control, depending on the current deviation of the indoor air temperature t_{in} from the specified initial value (setpoint) $t_{in.0}$: $\theta_{in} = t_{in} - t_{in.0}$,°C. With that in mind, we consider that the background general ventilation does not function or its influence may be neglected. In most cases, this is achievable, since the air exchange in split systems in the premises is usually kept as low as possible to a minimum for reasons of energy saving, which is determined by the sanitary standard for the supply of outdoor air based on the number of people present in the premises. In this case, the general equation for the heat balance of the premises after replacing $z = \sqrt{\tau}$ may be written as [20]:

$$\frac{\mathrm{d}^2\theta_{in}}{\mathrm{d}z^2} + Cz\theta_{in} = 0 \ . \tag{1}$$

Here, $C = \dfrac{4K_c}{B}$ – is the characteristic parameter of the equation, $c^{-3/2}$, where K_c is the equivalent transmission ratio of the automated system, W/(K·s), over the channel "$t_{in} \rightarrow$ derivative of Q_c"; parameter B, W·s$^{1/2}$/K, may be calculated using the formula:

$$B = \sum \left[A_m \sqrt{\lambda c \rho} \right]_i \ . \tag{2}$$

Here, λ, c and ρ are the thermal conductivity, W/(m K), specific heat capacity, J/(kg K), and the density of the material of the layer of the *i*-th solid fence facing the inside of the premises, for example, external and internal walls and partitions, as well as interflooring, respectively; A_m is the area of each of the enclosing structures listed, m^2. Thus, in this case, the expression for C differs from that obtained in [20], since another way of compensating for surplus heat in the premises is considered.

The differential equation (1) is nonlinear equation of the second order and is classified as an Emden-Fowler equation, the general form of which may be written as follows [22–24]:

$$\frac{\mathrm{d}^2 y}{\mathrm{d}z^2} + Cz^n y^m = 0 \ . \tag{3}$$

Similar equations arise in a number of physical and economic applications. Thus, (1) is a special case of (3) with m = 1, n = 1. However, the challenge lies in the fact that with m = 1, there is no end analytical solution (2) in elementary functions [22–24].

The equation (1) can be obtained from the common equation of convective heat balance for indoor air within the framework of its single-are model can be shown here as follows [24]:

$$Q_{in} + G_s c_a \left(t_s - t_{in}\right)/3.6 - Q_c - B\sqrt{\tau}\,\frac{\mathrm{d}t_{in}}{\mathrm{d}\tau} = 0\,, \tag{4}$$

where G_s is mass flow rate, kg/h, of the supply air which is usually considered as equal to the value of the exhaust flow rate G_{ex} due to the almost instantaneous stationary state of the air equilibrium of the room compared to the heat equilibrium; c_a is specific heat of air equal to 1.005 kJ/(kg·K); t_{in} is indoor air temperature, °C; t_s is inflow temperature, °C. Equation (4) contains an additional term of Q_c, representing the value of the regulated heat flow, W, from local cooling systems, which is designed to compensate for heat input. For the same reason, it is now assumed in (4) that $t_s = \mathrm{const}$.

If the value of t_{in} is automatically supported by a control unit implementing a continuous integral law with the necessary change in the value of Q_c, the additional constraint equation the most conveniently written in this form:

$$\frac{\mathrm{d}Q_c}{\mathrm{d}\tau} = K_c\left(t_{in} - t_{in.0}\right). \tag{5}$$

Using the concept of θ_{in}, and differentiating (4) term by term by τ for the possibility of substituting expressions (5) there, we can write (4) in the canonical form (1) considering $G_s = 0$ because when using split systems, general air exchange is minimized and for it we can assume $t_s = \mathrm{const}$.

Let us consider a slightly different approach to solution (1) compared to that adopted in [20], namely, we will perform certain transformations to initially reduce it to the dimensionless form and single out its singularities to simplify further integration. Bearing in mind some general properties of the Emden-Fowler equations [22], [23], [24],in particular, the presence of a critical point with $z = 0$, let us initially present the solution in the form of the product $\theta_{in} = zf\left(z\right)$, and after its substituting into (1), obtain an equation for the function selected $f\left(z\right)$:

$$\frac{\mathrm{d}^2 f}{\mathrm{d}z^2} + \frac{2}{z}\frac{\mathrm{d}f}{\mathrm{d}z} + Czf = 0\ . \tag{6}$$

If we now make a substitution of variables in the form of $x = Cz^3$, where x will obviously already be a dimensionless quantity, we find the end equation for $f\left(x\right)$:

$$9x\frac{\mathrm{d}^2 f}{\mathrm{d}x^2} + 12\frac{\mathrm{d}f}{\mathrm{d}x} + f = 0\,. \tag{7}$$

With the inverse transformation, we obtain $z = \left(\frac{x}{C}\right)^{1/3}$. It is easy to see that (7) no longer contains the parameter C, meaning that the assumption made concerning the form of representation of the independent variable is correct. As the initial conditions with $\tau = 0$ for the original equation (1), we obviously need to take $\theta_{in} = 0$ and $\mathrm{d}\theta_{in}/\mathrm{d}z = 2Q_{in}/B$, from which it turns out for (7) that $f(0) = 1$, since the singularity with $z = 0$ was singled by representing $\theta_{in} = zf\left(z\right)$, and similar to $\mathrm{d}f/\mathrm{d}x = 1/12$.

We can note that with small x the first term in (7) may be neglected, and it becomes an equation of the first order with separable variables, the solution to which has the form of $f = \exp\left(-x/12\right)$ and, thus, the asymptotic approximation of the solution for the initial moments of time takes the form of:

$$\theta_{in} = \frac{2Q_{in}}{B}\left(\frac{x}{C}\right)^{1/3}\exp\left(-x/12\right) = \frac{1.26Q_{in}}{\sqrt[3]{K_c B^2}}\,x^{1/3}\exp\left(-x/12\right). \tag{8}$$

It is easy to see that the first two expansion terms of the function f in a Taylor series coincide with those for the exact solution obtained in [20] by the method of undetermined coefficients

$$\exp(-x/12) = 1 - x/12 + \ldots \; . \tag{9}$$

Now, assigning a certain value $\frac{\mathrm{d}^2 f}{\mathrm{d}x^2} = a$, we write down the differential equation from (7) for the following approximation:

$$\frac{\mathrm{d}f}{\mathrm{d}x} + \frac{f}{12} + \frac{3ax}{4} = 0 \, . \tag{10}$$

This is a linear inhomogeneous equation of the 1st order, which may be integrated completely in elementary functions, from which, taking into account the initial condition, we obtain:

$$f = (1 - 108a)\exp(-x/12) + 108a\left(1 - \frac{x}{12}\right). \tag{11}$$

In particular, with a = 1/252 we find:

$$f = \frac{4}{7}\exp(-x/12) + \frac{3}{7}\left(1 - \frac{x}{12}\right) \, . \tag{12}$$

This value of a corresponds to $\frac{\mathrm{d}^2 f}{\mathrm{d}x^2}$ for the first approximation approximately at x = 6.72. It can be demonstrated that the first three terms in the expansion of this function already coincide with the exact solution:

$$\exp(-x/12) = 1 - x/12 + x^2/504 - \ldots \; . \tag{13}$$

However, calculations show that the best agreement with the exact solution with x < 10 is achieved for a = 1/312. If we calculate the x derivative of the product $x^{1/3} f$, where f is taken in accordance with (12), we find:

$$\frac{\mathrm{d}}{\mathrm{d}x}\left(x^{1/3} f\right) = \frac{1}{21x^{2/3}}\left[(4 - x)\exp(-x/12) + 3 - x\right]. \tag{14}$$

Equating (14) to zero, we find that at the maximum point x = 3.43, which coincides with the value of 3.48 for the exact solution if the error is no more than 1.5 percent [20]. In this case, the largest value of the complex itself $x^{1/3} f$ is 10/9, just as in [20].

3. Results and Discussion

For illustrative purposes, Figure 1 shows the graphs of the expressions obtained for the function of f – exponential approximation (thick solid line) and dependence (12) (dotted line). For comparison, the solid thin line shows the behavior of the direct computational solution of the original differential equation (7), found using a computer program with Runge-Kutta method of the 4th order. It coincides with the exact solution in the form of an infinite series given in [20] up to the line thickness.

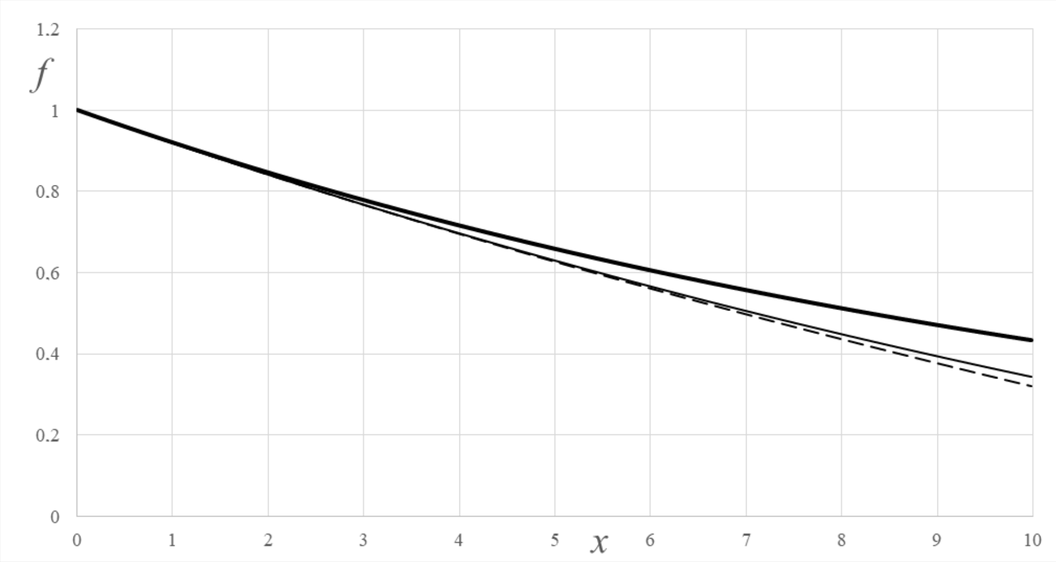

Figure 1. Graphs of the function f for various options of its representation.

Similarly, Figure 2 shows the graphs of the product $x^{1/3} f$,i.e., the desired dimensionless temperature. It can be seen that the accuracy of the expression (12) is good and, taking into account its simplicity and physical validity, it can be recommended for use in calculations.

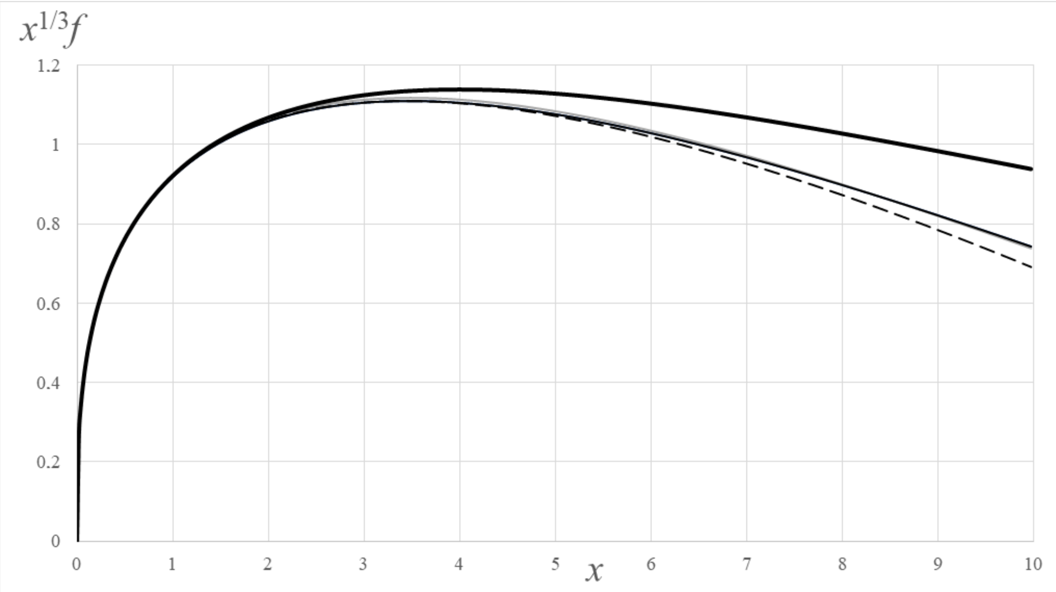

Figure 2. Graphs of dependence of the product $x^{1/3} f$ for various options of its representation.

Additional confirmation and justification of the presented mathematical model can be obtained experimentally. Figure 3 shows a comparison of the theoretical dependence for $x^{1/3} f$ (solid line) using (12) and the data obtained from direct temperature measurements in the premises served by a split cooling system. In reality, its control was implemented in a positional way, but due to the high switching rate, it approached astatic control. The abrupt rise in heat input was simulated by turning on a convective electric heater with Q_{in} = 500 W, and the value of B was determined taking into account the actual thermal parameters of building materials in the enclosures and the geometric dimensions of the premises [25]. Their area was 14 m^2, height from floor to ceiling was 3 m, depth from the outer wall could be considered equal to 6 m, internal structures had a total area of 64 m^2. They were made of reinforced concrete with a density of 1,200 kg/m^3. One must bear in mind that under the conditions considered, this entire area should be taken into account, since during the experiment the temperature wave propagates in one direction only. The outer wall was made of lightweight concrete with a density of 500 kg/m^3 and an area of 7 m^2 including a window with an area of 1.8 m^2. Then we obtain B = 2,4000 W·s $^{1/2}$/K from the expression (2).

To measure t_{in} a Testo 0560 1110 thermometer with a division value of 0.1° was used, which was installed in the center of the room at a height of 1 m from the floor. When processing the results in order to reduce the temperature to the dimensionless form in accordance with (6), its value was divided by the $\frac{1.26Q_{in}}{\sqrt[3]{K_c B^2}}$, and the parameter *x* was determined by the expression $Cz^3 = \frac{4K_c}{B}\tau^{3/2}$. as noted earlier. The best agreement between the theoretical and experimental dependences is observed at K_c = 2 W/(K·s), which is shown in Figure 3. Thus, when combining theoretical and experimental methods, it is possible to identify the mathematical model and determine the actual values of its certain parameters, while establishing their values antecedently may prove to be difficult.

The dashed dot shows the data of full-scale measurements of the non-stationary thermal regime of the room, which is equipped with the automated air heating system under similar control conditions given in [26] (dotted line), after normalization by the magnitude of the maximum temperature deviation. It can be seen that in the begin after the appearance of the thermal disturbance, experimental measurements give a similar nature of dependence, which further confirms the theoretical provisions of the proposed work. In the future, the discrepancy begins to increase, since in [26] the regulator, in addition to the integral, also had a proportional component, so the temperature there fades faster.

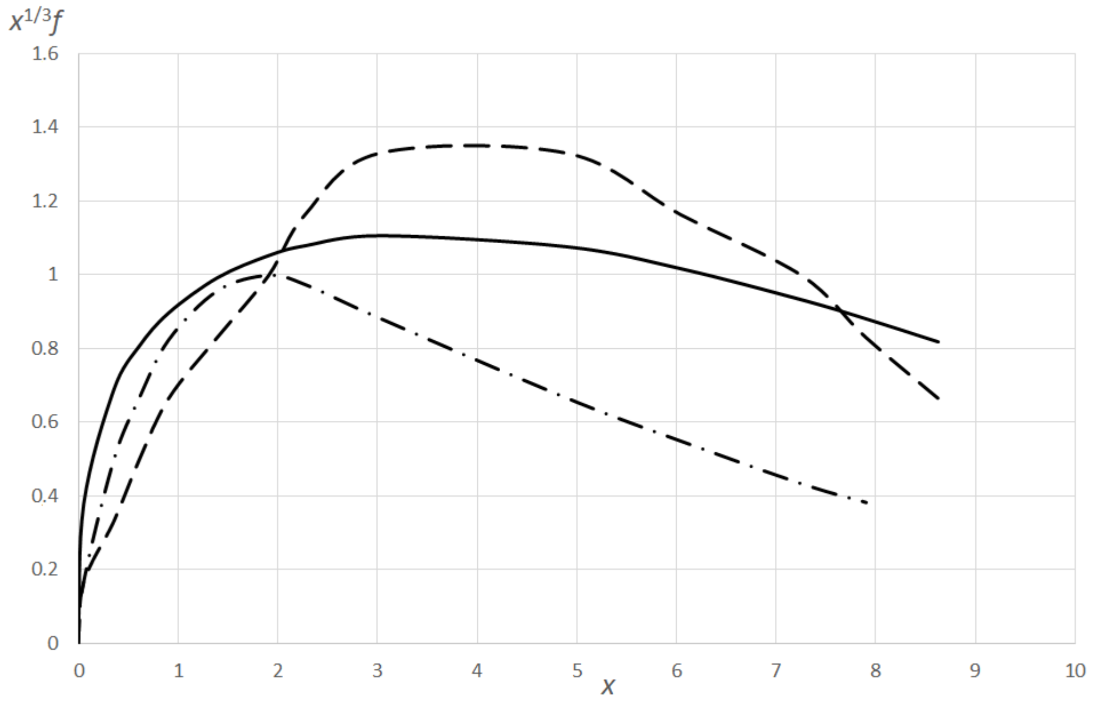

Figure 3. Dependence of θ_{in} on time for the calculated premises with automatic keeping of t_{in} (solid line, taking into account expression (12); dotted line, experiment; dashed dot, measurement data [26])).

Note that, for the general nature of dependence (10) shown in Figure 3, one can find a significant similarity between the relationships that are given, e.g. by the authors of [12] and [13] under similar initial conditions, and the observed temperature deviations from the initial values generally correspond to the level noted in [27] for similar regimes. Finally, the general concept of the approach considered and certain elements of the mathematical arrangement and solution to the problem under study are consistent with the results presented in publications [11], [14] and a number of other materials, allowing us to assume that the results of the proposed study are quite reliable and justified.

The results achieved additionally confirm the reliability of the previously found accurate analytical solution in the form of an infinite series [20]. It takes into account the thermal stability of enclosing structures during the propagation of a temperature wave in their material and the characteristics of the controller, as well as demonstrates its applicability when installing split systems and lacking background general ventilation.

4. Conclusion

1. The premises under consideration had automated climate control equipment such as split systems when regulated under the law of astatic control in the absence of a background unregulated inflow. It was proved that for such premises, the asymptotic variants of the analytical solution obtained in the paper describing the behavior of the value t_{in} describe the actual process of heating or cooling quite well, at least for not too large values of τ under the conditions of an abrupt thermal disturbance.

2. It was established that the core of the identified dependence for t_{in} may be expressed in an explicit form through the product of power and exponential functions from a dimensionless group, including the value $\tau^{3/2}$. This allows analyzing the problem quite easily and further synthesizing the automation system for climate control equipment by selecting numerical coefficients in the solution.

3. It was noted that the form of representation of the analytical solution in the dimensionless form and the composition of the dimensionless group used as an independent variable are naturally obtained in accordance with the properties of the original differential Emden–Fowler equation.

4. Experiments using full-scale measurements for the typical representative premises confirmed that the discrepancy between the actual and calculated values of t_{in} lies within the measurement accuracy limits and the typical error of engineering calculation.

5. We propose to use the variants of dependencies found in this paper for an approximate analytical assessment of the behavior of the internal temperature in the air conditioned premises in unsteady conditions with local heating and cooling systems equipped with an integrative controller to check the comfort and safety of the living environment, the possibilities of implementing the technological process, to identify the required parameters of the regulator, including on the basis of multivariate calculations with a change in the initial data.

References

1. Rafalskaya, T. Safety of engineering systems of buildings with limited heat supply. IOP Conference Series: Materials Science and Engineering. 2021. 1030. 012049. DOI: 10.1088/1757-899X/1030/1/012049
2. Rafalskaya, T.A. Simulation of thermal characteristics of heat supply systems in variable operating. Journal of Physics: Conference Series. XXXV Siberian Thermophysical Seminar, STS 2019. 2019. 1382. 012140. DOI: 10.1088/1742-6596/1382/1/012140
3. Mansurov, R.Sh., Rafalskaya, T.A., Efimov, D.I. Mathematical modeling of thermal technical characteristics of external protections with air layers. E3S Web of Conferences. 22nd International Scientific Conference on Construction the Formation of Living Environment, FORM 2019. 2019. 97. 06007. DOI: 10.1051/e3sconf/20199706007
4. De Rosa, M., Bianco, V., Scarpa, F., Tagliafico, L.A. Modelling of energy consumption in buildings: an assessment of static and dynamic models. Russian Journal of Construction Science and Technology. 2016. 2(1). Pp. 12–24. DOI: 10.15826/rjcst.2016.1.002
5. Liu, C.-S. An integral equation method to recover non-additive and non-separable heat source without initial temperature. International Journal of Heat and Mass Transfer. 2016. 97. Pp. 943–953. DOI: 10.1016/j.ijheatmasstransfer.2016.03.003
6. Stetjukha, V.A. Energy efficiency of underground structures in harsh climatic conditions. Magazine of Civil Engineering. 2023. 117(1). Article no. 11710. DOI: 10.34910/MCE.117.10
7. Belous, A.N., Kotov, G.A., Belous, O.E., Garanzha, I.M. Calculation of heat resistance of external enclosing structures with heat-conducting inclusions. Magazine of Civil Engineering. 2022. 113(5). Article No. 11313. DOI: 10.34910/MCE.113.13
8. Samarin, O.D. The periodic temperature oscillations in a cylindrical profile with a large thickness. Magazine of Civil Engineering. 2019. 85(1). Pp. 51–58. DOI: 10.18720/MCE.85.5
9. Li, N., Chen, Q. Experimental study on heat transfer characteristics of interior walls under partial-space heating mode in hot summer and cold winter zone in China. Applied Thermal Engineering. 2019. 162. 114264. DOI: 10.1016/j.applthermaleng.2019.114264
10. Marino, B.M., Muñoz, N., Thomas, L.P. Estimation of the surface thermal resistances and heat loss by conduction using thermography. Applied Thermal Engineering. 2017. 114. Pp. 1213–1221. DOI: 10.1016/j.applthermaleng.2016.12.033
11. Korniyenko, S.V., Dubov, I.A., Nazarov, K.R. Field study of thermal comfort in dwelling during the winter, mid-season and summer. Magazine of Civil Engineering. 2023. 121(5). Article no. 12101. DOI: 10.34910/MCE.121.1
12. Bilous, I.Yu., Deshko, V.I., Sukhodub, I.O. Building energy modeling using hourly infiltration rate. Magazine of Civil Engineering. 2020. 4 (96). Pp. 27–41. DOI: 10.18720/MCE.96.3
13. Faouzi, D., Bibi-Triki ,N., Draoui, B., Abène, A. Modeling a fuzzy logic controller to simulate and optimize the greenhouse microclimate management using Mathlab Simulink. International. Journal of Mathematical Sciences and Computing. 2017. 3(3). Pp. 12–27. DOI: 10.5815/ijmsc.2017.03.02
14. Latif, M., Nasir, A. Decentralized stochastic control for building energy and comfort management. Journal of Building Engineering. 2019. 24. 100739. DOI: 10.1016/j.jobe.2019.100739
15. Ryzhov, A., Ouerdane, H., Gryazina, E., Bischi, A., Turitsyn, K. Model predictive control of indoor microclimate: existing building stock comfort improvement. Energy Conversion and Management. 2019. 179. Pp. 219–228. DOI: 10.1016/j.enconman.2018.10.046
16. Serale, G., Capozzoli, A., Fiorentini, M., Bernardini, D., Bemporad, A. Model predictive control (MPC) for enhancing building and HVAC system energy efficiency: problem formulation, applications and opportunities. Energies. 2018. 11(3). 631. DOI: 10.3390/en11030631

17. Belussi, L., Barozzi, B., Bellazzi, A., Danza, L., Devitofrancesco, A., Ghellere, M., Guazzi, G., Meroni, I., Salamone, F., Scamoni, F., Scrosati, C., Fanciulli, C. A review of performance of zero energy buildings and energy efficiency solutions. Journal of Building Engineering. 2019. 25. 100772. DOI: 10.1016/j.jobe.2019.100772
18. Sha, H., Xu, P., Yang, Z., Chen, Y., Tang, J. Overview of computational intelligence for building energy system design. Renewable and Sustainable Energy Reviews. 2019. 108. Pp. 76–90. DOI: 10.1016/j.rser.2019.03.018
19. Kharchenko, V., Boyarchuk, A., Brezhnev, E., Andrashov, A., Ponochovnyi, Y. Monte-Carlo simulation and availability assessment of the smart building automation systems considering component failures and attacks on vulnerabilities. Advances in Intelligent Systems and Computing. 2019. 761. Pp. 270–280. DOI: 10.1007/978-3-319-91446-6_26
20. Samarin, O.D. Raschet temperatury vozdukha v pomeshchenii po bezrazmernym parametram pri integralnom regulirovanii klimaticheskikh sistem [Calculation of indoor air temperature using dimensionless parameters for integrated climate control systems]. Vestnik MGSU. 2021. 16(4). Pp. 486–492.(rus) DOI: 10.22227/1997-0935.2021.4.486-492.
21. Samarin, O.D. Thermal mode of a room with integrated regulation of microclimate systems. Magazine of Civil Engineering. 2022. 116(8). Article no. 11610. DOI: 10.34910/MCE.116.10
22. Carillo, S., Zullo, F. Ermakov-Pinney and Emden-Fowler equations: new solutions from novel Bäcklund transformations. Theoretical and Mathematical Physics. 2018. 196(3). Pp. 1268–1281. DOI: 10.4213/tmf9508
23. Pikulin, S.V. The Thomas-Fermi problem and solutions of the Emden-Fowler equation. Computational Mathematics and Mathematical Physics. 2019. 59(8). Pp. 1292–1313. DOI: 10.1134/S0044466919080131
24. Pikulin, S.V. Parametrization of solutions to the Emden-Fowler equation and the Thomas-Fermi model of compressed atoms // Computational Mathematics and Mathematical Physics. 2020. 60(8). Pp. 1315–1328. DOI: 10.31857/S004446692008013X
25. Samarin, O.D. Thermal mode of a room with integrated regulation of cooling systems. Magazine of Civil Engineering. 2021. 103(3). 10312. DOI: 10.34910/MCE.103.12
26. Lysak, O. Analysis of the temperature distribution in a space heated by a dynamic (fan) storage heater. Eastern-European Journal of Enterprise Technologies. 2017. Vol. 3. 8 (87). Pp. 17–25. DOI: 10.15587/1729-4061.2017.103778
27. Odineca, T., Borodinecs, A., Korjakins, A., Zajecs, D. The impacts of the exterior glazed structures and orientation on the energy consumption of the building. IOP Conference Series: Earth and Envi-ronmental Science. 2019. 290(1). P. 012105. DOI: 10.1088/1755-1315/290/1/012105

Information about authors:

Oleg Samarin, *PhD in Technical Sciences*
ORCID: https://orcid.org/0000-0003-2533-9732
E-mail: samarin-oleg@mail.ru

Received 16.11.2022. Approved after reviewing 16.10.2023. Accepted 16.10.2023.